UNIVERSITÁ DEGLI STUDI
DI MODENA E REGGIO EMILIA

Dottorato di ricerca in Physics and Nanosciences
Ciclo XXVIII

The role of mechanical and thermodynamical properties in the activity of biological systems

Candidato: Mattia Sacchi
Relatore (Tutor): Prof. Andrea Alessandrini
Direttore del Dottorato: Prof. Marco Affronte

Contents

Abstract

Historically, the fields of structural biology and physiology have tended to overlook materials-science approaches when investigating biological matter. However, studies of the physical - mechanical and thermodynamical, but also optical and/or magnetic - properties of biological systems and the investigation of how these features responds to changing environmental factors, provides opportunities to improve understanding of functional and physiological processes at all scales, from molecular and nanoscale to the macroscale.

The emergence of biological materials science is due, in part, to the advent of regenerative medicine, as this discipline needs biomaterials that interact with the body in a specific, predictable manner. In parallel, the development of new technologies - both theoretical/computational and experimental - allows researchers the possibility to use new tools to study, in great detail, the structural properties of biological materials, whether cells, tissue samples or complete organs.

In this experimental work we exploit Atomic Force Microscopy (AFM) - combined with other different and complementary techniques, like Micropipette Aspiration Technique (MAT) and Fourier Trasformed Infrared Spectroscopy (FTIR) - to study and characterize different biological samples, in order to have a better insight on their mechanical and thermodynamical properties, according to the specific target of application, which spaces from pharmacology to regenerative medicine and to tissue engineering.

In particular, atomic force microscope (AFM) can perform, beyond the bare imaging of surfaces, very sophisticated analyses based on the possibility to measure the forces acting between the probing tip and the sample surface, or some other quantities strictly connected to the details of the interaction force such as the cantilever resonance frequency shift or/and the phase lag between the driving signal and the cantilever response, when in non-contact or intermittent-contact mode. These operating modes are grouped under the common hat of Atomic Force Spectroscopy (AFS).

After an introduction where the state of the art and the main motivations for this work are pointed out (**Chapter 1**), we present and describe the investigated materials (**Chapter 2**), as well as the employed experimental techniques (**Chapter 3**). The complete methods and protocols used for our characterization are reported in **Chapter 4**.

In **Chapter 5** we present the results concerning the effect of molecules

of pharmacological interest like neurosteroids (allopregnanolone (Allo), isoallopregnanolone (isoAllo), pregnenolone sulfate (Preg-S)) on model lipid membranes. Mechanical and thermodynamical modification due to the presence of the neurosteroids are remarked and contextualized in the framework of the "raft hypothesis".

In **Chapter 6** the effects of neurosteroids' enantiomers (*ent*-Allo and *ent*-isoAllo) on model lipid bilayers are studied in order to evaluate the enantiospecific properties of the membrane.

Chapter 7 deals with the effects of the neurosteroids Allo and dehydroepiandrosterone (DHEA) - which are proved to have a neuroregenerative function - on cells relevant for the central nervous system, whether regarding the cytoskeleton reorganization or modifications in the mechanical properties.

Chapter 8 deals with the topographical and mechanical characterization of fibrin+keratinocytes samples for regenerative medicine and, in particular, for corneas transplantations. Data emerging from the characterization of the bare fibrin are for the first time analyzed in the context of the poroelastic theory and indentation modulation measurements are also presented.

Finally, in **Chapter 9** the results obtained in this work are briefly summarized and the main conclusions are presented, as well as future perspectives.

Until now, three papers have been produced out of this work:

1) **Sacchi M**, Balleza D, Vena G, Puia G, Facci P, Alessandrini A (2015), *Effects of neurosteroids on a model lipid bilayer including cholesterol: an Atomic Force Microscopy study*, Biochim. Biophys. Acta 1848(5): 1258-67;

2) Balleza D, **Sacchi M**, Vena G, Galloni D, Puia G, Facci P, Alessandrini A (2015), *Effects of neurosteroids on a model membrane including cholesterol: a micropipette aspiration study*, Biochim. Biophys. Acta 1848(5): 1268-76;

3) Balleza D, **Sacchi M**, Morelli F, Battaglioli M, Puia G, Facci P, Alessandrini A, *Effect of the neurosteroid pregnenolone sulfate on model lipid bilayers: hypothesis on a role for the lipid bilayer in its mechanism of action*, manuscript in preparation.

Chapter 1

Introduction

1.1 Neurosteroids and model lipid bilayers

1.1.1 Motivations

An increasing number of works in biophysics and in cell biology are nowadays devoted to the relevant role that lipid components of the biological membrane can have on the activity of membrane proteins, by both specific [1] and non-specific mechanisms that consider the bilayer as a continuum [2, 3, 4]. The non-specific roles of lipids are related to both their mechanical properties through their relevant role in the conformational transitions of membrane proteins (considering for example mechanical spring constants of the bilayers and lateral pressure profile) and to the lateral heterogeneity of membranes, according to the so-called "raft hypothesis" [5, 6].

The neurosteroid allopregnanolone (in the following: Allo), has been demonstrated to potentiate GABA-evoked currents by the $GABA_A$ receptor activation at low nanomolar concentrations and to activate the $GABA_A$ receptor at higher concentrations [7]. Many studies report on the possible interaction of Allo with the lipid bilayer [8], although a well established understanding on this aspect is still lacking and the possible effects of Allo on the mechanical parameters characterizing the membrane have not yet been considered. As a consequence, the possible contribution of lipid bilayer properties on the behavior of the receptors has largely been neglected apart very few works in the literature [9]. For these reasons, the effect of Allo on a pure lipid model system is worthwhile being investigated, also considering that the concentrations we used in our work (in the nanomolar range) are functionally relevant for the $GABA_A$ receptor.

In the debate on the possible effects of drugs on biological membranes, stereoisomers' activity is usually considered a fundamental guideline to distinguish between a specific effect on membrane proteins and an aspecific action on the lipid bilayer physical properties [10, 11]. More generally, if colligative properties are considered, enantiomers of the same molecule should not produce different effects on an achiral environment. Accordingly, if two enantiomers change differently the activity of a membrane

protein, the mechanistic explanation should foresee a specific interaction of the drug with the membrane protein. However, it is not trivial to study the complete effect of a molecule on a lipid bilayer, because it could affect properties which are not easy to study experimentally, such as the lateral pressure profile inside the bilayer [12], a property still waiting for an appropriate experimental technique able to provide its measurement. In general terms, it is important to stress that the lipid bilayer cannot be considered an achiral environment, especially if cholesterol is one of the components [13]. Accordingly, the same effect of two enantiomers on a lipid bilayer must be experimentally investigated. Dealing with the phase organization of lipid bilayers, it is for example important to study if isomers of the drugs could differently alter the phase state of the bilayer inducing the prevalence of one phase over other coexisting phases.

We decided to work also with iso-allopregnanolone (isoAllo), an isoform of Allo (not its mirror image, but a diastereoisomer, differing in the orientation of an OH group) which is known to be a non-competitive antagonist of Allo with regard to $GABA_A$ receptors [14]. Thus, the two isoform molecules represent a very interesting test case to investigate if their different pharmacological properties at the level of a membrane protein could be somehow also related to differential effects on the lipid components of the membrane. In the past, the different effects of Allo and isoAllo on lipid bilayers have already been considered, albeit at higher concentrations than what we used in the present work [15, 16].

Potentiating steroids of the $GABA_A$ receptor, like Allo, are uncharged and highly lipophilic molecules: their accumulation in the membrane is likely relevant to their action because binding sites for anesthetic neuroactive steroids were identified recently within transmembrane domains of the $GABA_A$ receptor [17]. By contrast, the most potent GABA-antagonist steroids are sulfated at carbon 3 of the steroid A-ring [18, 19]. The anionic charge of sulfated steroids keeps this class of neurosteroid from passing directly through the plasma membrane, at least at sufficiently low concentrations [20], but some of the sulfated stereoids exhbit voltage dependent block of $GABA_A$ receptors [21], suggesting the possibility of physical voltage-dependent translocation of the molecule across the bilayer, as occurs with other charged lipophilic molecules [22, 23]. However, results obtained in [24] showed that the interaction between charged neurosteroids and cell plasma membrane apparently does not result in a voltage-dependent charge movement of the anionic sulfate group itself, but in an alteration of the membrane capacitance. It is possible that these membrane interactions are important for the modulation of membrane channels, most notably the $GABA_A$ receptor and the NMDA receptor.

In this work we chose to investigate pregnenolone sulfate (Preg-S), a neurosteroid that negatively modulates the $GABA_A$ receptor, as a testing molecule to understand the effects of the charged sulfated group on a pure lipid bilayer.

1.1.2 State of the art

Drugs are specific chemicals or proteins that interact with the binding site on their specific targets to alter cellular functions. The original idea of drug targeting was put forward at the beginning of the $20th$ century with the pioneering work of Ehrlich [25]; reinforced by numerous subsequent works [26, 27, 28, 29, 30] this concept became the "pharmacology's big idea" [31] and still nowadays it remains the bedrock of biomedical research, especially in the context of drug discovery.

Drug targets are typically macromolecules that have discrete structural motifs that allow a very complete and complicated classification [32, 33]; each drug target irrespective of its classification has at least one recognition, or binding site, for its ligand (receptor) or substrate (enzyme) that are often associated with a variety of scaffold proteins and/or signaling pathways that are not only necessary for their physiological actions but also aid in defining the response at that target with the engagement of different pathways often being a function of particular cell and tissue type [34].

The mechanism of specific interaction between drug molecules and membrane proteins, which represents the most common class of drug targets, has been demonstrated in many cases and the binding sites for many ligands and their receptors have been clearly identified [35, 36]. However, in many cases, several conformational states are introduced to reproduce theoretically the kinetic behavior of drug/protein interaction and the introduced states are often difficult to identify experimentally. This quite complicate picture can be somehow simplified by considering, in addition to the specific drug/receptor interaction, an aspecific interaction between the drug and the lipid bilayer in which the protein receptor is hosted [37, 38].

When dealing with non-specific bilayer properties [39] the lipid bilayer is typically considered as a continuum medium, characterized by certain mechanical properties [3]. These include bilayer thickness, compressibility, lateral pressure profile, and surface charge [40, 41]. Properties of a lipid bilayer could vary both as a consequence of changes in environmental parameters such as pH and temperature, but also, and probably in a more effective way, by modifications of the lipid bilayer components.

Drugs, besides interacting specifically with membrane proteins, can also adsorb to the lipid bilayer affecting its properties. When the drug molecules remain confined at the lipid bilayer/water interface, the interaction is considered as an adsorption process, whereas it can be considered as an uptake process when the molecules are able to get inside the bilayer. The different between the two cases is ofter related to the hydrophilic character of the drug.

Many investigations demonstrated that the activity of many integral membrane proteins changes with changes in the bulk properties of the surrounding lipid bilayer or with changes in the lipid composition of the bilayer [42, 43]. This means that a transmembrane protein which accomplishes its function by a conformational change involving the lipid/protein interface will be influenced, as far as its functionality is concerned, by the lipid bi-

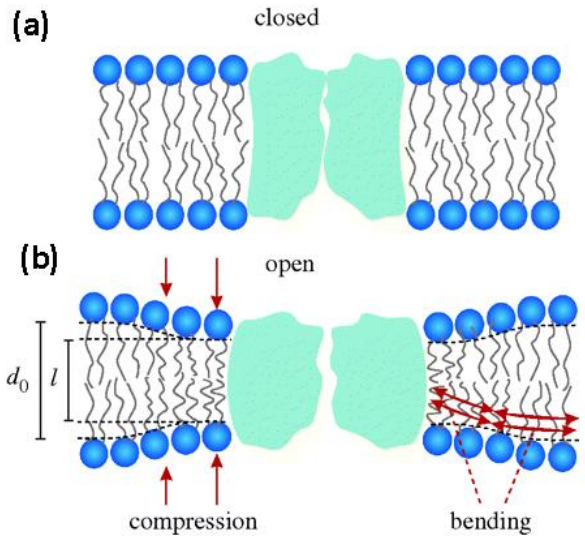

Figure 1.1: Hydrophobic coupling between a bilayer-spanning membrane protein (ion channel) and host lipid bilayer. A local lipid bilayer deformation causes a change in the protein conformational state and viceversa. For simplicity, there is no hydrophobic mismatch in the closed state. Modified from [45].

layer's properties (Figure 1.1) [1]. In particular, if a lipophilic drug is able to affect the physical properties of lipid bilayers, ion channels can experiment the preference for different conformation, either open or closed [41, 44]. From this point of view the aspecific interaction between the drug and the lipid bilayer, mediated by the lipid bilayer properties, can somehow justify the complex kinetic behavior already mentioned and the introduction of several conformational state for the membrane protein could be only artificial and without a real physical meaning. Complex kinetic schemes could be explained in this case by the introduction of a open, a closed and a desensitized state.

Dealing with the possible role of drugs in affecting the functional activities of biological membranes by an aspecific mechanism, one of the most studied effect is the interplay between anesthetics and lipid bilayers [12, 46, 47, 48, 49]. Anesthetics have many actions on lipid bilayers [50, 51, 52]. Purely hydrophobic anesthetics will preferentially be located in the lipid membrane hydrocarbon core; they thicken membranes and increase their surface tension [53]. They also change lateral pressure profiles in membranes [12]. Anesthetics may decrease the phase transition temperatures of bilayer membranes [54, 55, 56] or produce lateral phase separation [57]. Also the membrane electrical properties such as membrane dielectric constant [58] or surface dipole potentials [59] can be changed by anesthetics.

The longstanding debate between the specific effects of anesthetics on membrane proteins and their indirect action, mediated by changes they may produce in the lipid bilayer properties, has its roots in the Meyer-Overton rule. This rule states that the activity of anesthetics is strongly related to

their partition coefficient in lipid bilayers. Among the mechanisms related to aspecific interactions, the lateral pressure profile change across the lipid bilayer has been proposed as a way to affect efficiently the equilibrium distribution of the membrane proteins in their different conformational states and the rate constants for their transitions [37].

Another interesting class of molecules whose interactions with lipid bilayers could be relevant for their activity is exemplified by neurosteroids (NSs) [60] which are endogenous molecules able to modulate the activity of ion channels and relevant in the propagation of electrical signals in the nervous system [61]. Their action is typically explained by an allosteric interaction with a membrane protein, i.e., the $GABA_A$ receptor Cl channel, that, affecting the receptor conformational states, produces variation in the channel open time that ultimately results in a changed activity [62, 63]. Their activity is usually detected at very low concentrations (in the nM range) and this aspect initially suggested a highly specific interaction with the corresponding membrane proteins [8].

Evidences for a specific NS binding site on $GABA_A$ receptors (Figure 1.2) were provided by several groups: using site-directed mutagenesis, single residues in the receptor protein that influence NS regulation of GABA receptor have been identified [64, 65, 66]. However, NSs are strongly lipophilic and, according to their structure, in some cases they have a partition coefficient which can produce a micromolar concentration inside the lipid bilayer from a nanomolar concentration in aqueous solution [67]. In this case, a highly specific docking mechanism would not be required to explain their effect at a very low water concentration. Moreover, it has been found that their docking site to the membrane protein could be located in their intramembraneous portion [8]. Accordingly, the effects of NSs could be also related to their partition and diffusion inside the lipid bilayer. It is also well known that, at high concentrations, NSs which modulate the activity of $GABA_A$ receptors can, independently from the GABA presence, activate

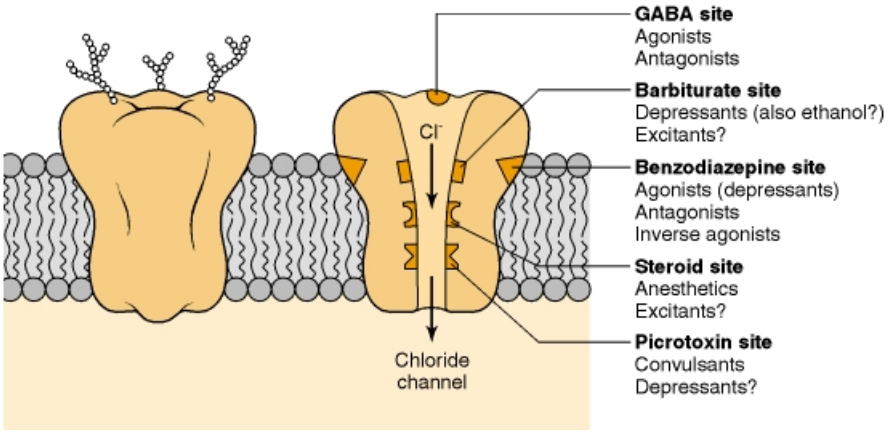

Figure 1.2: Structural model of the $GABA_A$ receptor. The cut-away view demonstrates targets for a variey of compounds that influcence the receptor complex. From [70].

the receptors [68]. This direct gating effect of the NS has typically slow kinetics which has been connected to its accumulation in the lipid bilayer [69]. The gating kinetics could be attributed both to the required increase of NS concentration inside the bilayer to bind the channels and to the increasing modification of the lipid bilayer properties as the NS concentration inside the bilayer increases.

As already stated, the non-specific roles of lipids are related to the mechanical properties of the lipid bilayer that are relevant in the conformational transitions of membrane proteins, but also to the so called "lateral heterogeneity" of membranes. Specific domains with a lateral extension in the order of tens of nanometers could be present in the membrane [71]. Many proteins could preferentially partition in these domains and the partitioning could affect their interactions and their activation or deactivation of signaling pathways [5, 72]. The membrane organization in nanometer-sized lipid aggregates could be related to its thermodynamic conditions [73] considering also the non-equilibrium situation of a biological cell membrane. The interaction of drugs with the membrane could in turn affect its thermodynamics and alter the bilayer organization [74]. These changes could have strong effects on the activity of membrane proteins which preferentially associate with specific domains. Accordingly, it would be very important to study how the insertion of exogenous molecules in a lipid bilayer affects its thermodynamics.

This aspect represents an issue that is not new [75, 76], but it has received a strong burst after the so called "raft hypothesis" (Figure 1.3) was introduced in the biological community [77] and it is far from being resolved. In the first introduced models of the biological membrane, the lateral heterogeneity in the organization of the membrane regarded mainly the possibility of phase segregation or the presence of different phase domains such as in the case of solid ordered domains (S_o, also gel phase) coexisting with the liquid disordered phase (L_d, also liquid crystalline). The raft hypothesis shifted the attention to the possibility of another phase separation in biological membranes. The new idea is related to the possibility of a phase separation between two liquid domains in the biological membrane, the liquid ordered (L_o) phase and the L_d one [72]. In this case, relevant roles are played by the presence of sterols such as cholesterol in the membrane and by their preferred interactions with specific lipids. Many membrane proteins seem to have the tendency to segregate into one of the two phases and the segregation of different proteins in the same domain is considered as the basic mechanism by which many signaling pathways could be activated [5, 71, 78].

In this scenario, any mechanism able to produce an alteration of the bilayer phase properties could be relevant for the normal operation of a biological membrane[72]. However, the detection of phase separation between different liquid phases in biological membranes remains still elusive [79]. The elusive character of these domains in biological membranes is now ascribed to their small lateral dimensions (in the order of a few tens of nanometers)

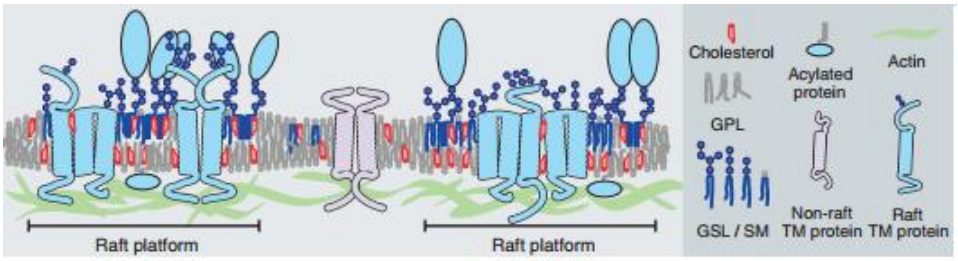

Figure 1.3: The plasma membrane of cells contain combination of glycosphingolipids and protein receptors organized in glycolipoprotein microdomains called lipid rafts. Lipid rafts are responsible for the lateral heterogeneity in cell membranes. Picture is taken from [5].

and to their dynamic aspects (lifetime in the order of milliseconds) [80]. The raft hypothesis stimulated a plethora of studies trying to elucidate if specific membrane proteins could be considered raft-associated. In cases where this association is possible, it can be concluded that any modification of the bilayer affecting the thermodynamics of raft domains can also affect protein function. A very interesting breakthrough was the realization that specific thermodynamic properties could play important roles in the organization and consequently in the activity of a biological membrane. In particular, the proximity, in physiological conditions, of the biological membrane to a critical point or to several critical points emerged as an intriguing possibility in this research field [81]. Around physiological temperature, the membrane is thought to be, due to its lipid composition, just above its critical condition [74]. In this situation, fluctuations in lipid composition could explain both the small lateral dimensions of the domains and their dynamic organization. Moreover, it was demonstrated that lipid bilayer model systems composed of three different lipid types, one low-melting lipid type, one high-melting lipid type and cholesterol, could be considered representative of much more complex bilayers in eukaryotic cells [82] and useful information could be obtained studying these model systems.

The role of thermodynamics in the behavior of a membrane brings about considerations also on the possibility that a dopant in the bilayer could alter the thermodynamics of the system and impair the regular formation of domains. This aspect could be particularly relevant in the case of proximity of the membrane to a critical point or in general to a miscibility border. Accordingly, the longstanding discussion on the interactions between drugs and lipids in the membrane [83] was enriched with a new viewpoint related to the thermodynamical aspects of lipid bilayers near critical points [37]. In fact, the simple insertion of a drug could change the bilayer position in the phase diagram affecting the domain organization as a consequence of a changed distance from the miscibility border and could consequently affect the activity of membrane proteins. Even if a mechanistic view of the process leading from the presence of the drug in the membrane to changes in its functions is not completely clear, it is evident that further studies of

the interaction of drugs with membranes deserve great attention. This is particularly true for highly lipophilic drugs such as some anesthetics and neurosteroids.

1.2 Neurosteroid's enantiomers

1.2.1 Motivations

As already stated in the previous Paragraph, when evaluating the modulation of membrane bound receptors by steroids, it is necessary to consider both the direct actions of the steroid caused by its binding to the receptor of interest and the indirect actions of the steroid on receptor function caused by steroid alteration of the membrane environment. A priori there is no reason to disregard the possibility that both types of steroid-mediated effects may be occurring simultaneously.

Distinguishing between the direct and indirect effects of steroids on membrane receptor function can be difficult. One potential way to make the distinction relies on a stereochemical approach based on the fact that enantiomers (non-superimposable mirror images of optically active molecules-steroids and *ent*-steroids in this case) have mirror image shapes but identical physicochemical properties. Because enantiomers have mirror image shapes and receptors have well-defined and structurally maintained binding pockets, receptors generally can discriminate between ligands of different shapes. Hence, it is more probable than not, that binding of a ligand to its receptor will be enantioselective (i.e., one enantiomer will bind more effectively than the other enantiomer). By contrast, membrane lipids present a dynamic environment that does not maintain structurally well-defined binding sites for steroids. Hence, in the membrane, the physiochemical properties of the steroid, not it's absolute configuration (one enantiomer or the other), will be the dominant factor that determines the degree to which the steroid affects membrane properties. Since both enantiomers have identical physicochemical properties, their effects on membrane properties will be essentially equivalent (non-enantioselective). Therefore, the direct receptor binding and indirect membrane perturbation effects of the steroid on receptor function could potentially be distinguished by differences in the magnitude of enantioselectivity observed for each mechanism of receptor modulation.

The lack of enantiospecific interactions is by no means obvious a priori, as phospholipids and cholesterol are chiral molecules known to display enantiospecific interactions. The enantiospecificity of the interactions of steroid anesthetics with lipid bilayers has not been studied a lot, while there exists a conspicuous body of literature showing the correlation of the anesthetic potency of steroids with the effects on hydration and the structure and function of model proteins and peptides [15, 84]. Morover, to our knowledge, an AFM-based study of the effects of enantiomers of supported lipid bilayers is still lacking.

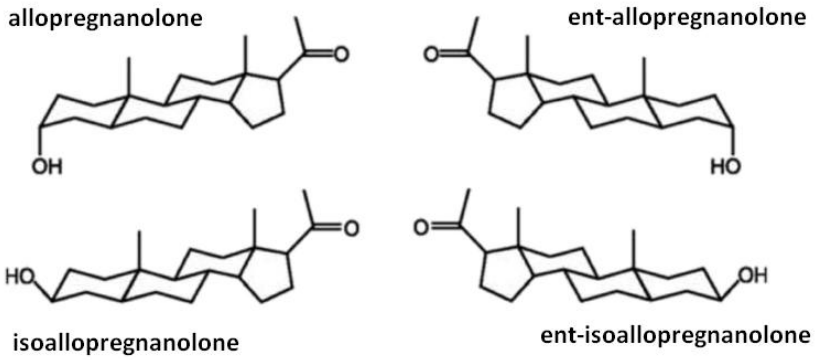

Figure 1.4: Structure of steroids, from [87]. *Ent*-allopregnanolone and *ent*-isoallopregnanolone are enantiomers, i.e., mirror image isomers, of allopregnanolone and isoallopregnanolone respectively.

In this work, we examined the interactions of two pairs of enantiomers (Figure 1.4) with lipid bilayers with supported lipid bilayers by means of atomic force microscopy. One of the pairs, allopregnanolone (Allo) and *ent*-allopregnanolone (*ent*-Allo), shows a high degree of enantioselectivity in anesthetic effects (300% difference in anesthetic potency and 500% difference in effects on $GABA_A$ receptor has been reported, the higher effect produced by natural Allo); the other pair, isoallopregnanolone (isoAllo) and ent-isoallopregnanolone (*ent*-isoAllo), displays minimal enantioselectivity [85].

1.2.2 State of the art

Enantiomers of a molecule can be distinguished from each other by the direction in which they rotate linearly polarized light. Additionally, they can usually be distinguished by their interactions with a different optically active molecule provided that the enantiomers cannot interact with this optically active molecule in an identical manner. For example, as shown in Figure 1.5 for the enantiomers of ligand X with a generic receptor ABCD, one enantiomer has four favorable interactions with the receptor, whereas the other enantiomer has only two favorable interactions with the receptor. Hence, the enantiomers are distinguishable from each other by their differential interactions with the receptor. In molecular terms, these interactions generally consist of hydrogen bonds, dipole-dipole interactions, π-bond interactions, ion-pair interactions, hydrophobic interactions and steric factors. Geometrical arguments establish that a minimum of four interaction constraints are needed for enantiomer discrimination by another optically active molecule [86].

Enantioselectivity expectations for steroid-protein and steroid-lipid interactions are summarized in Table 1.1. Because macromolecules like enzymes, receptors, specific transporters and antibodies that interact with steroids have architecturally well-defined binding sites that are sterically

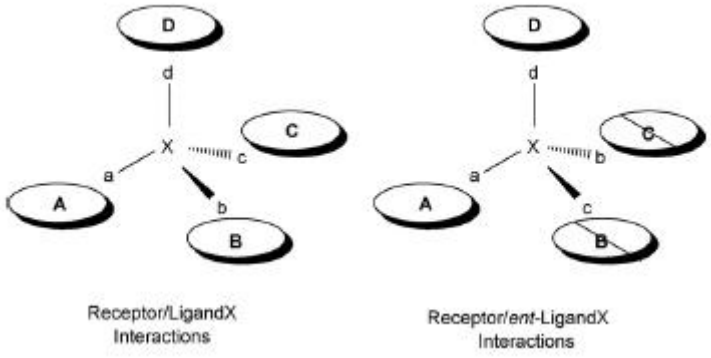

Figure 1.5: Receptor discrimination between enantiomers. Molecules X and ent-X are an enantiomer pair containing structural elements a, b, c and d which can interact with areas A, B, C and D on receptor ABCD. The enantiomer on the left has four favorable interactions (a, A; b, B; c, C; d, D) with the receptor whereas the enantiomer on the right has two favorable interactions (a, A; d, D) and two unfavorable interactions (b, C; c, B; indicated by diagonal line through the interaction sites) thus allowing for enantiomer discrimination by the receptor. From [87].

None to low	Moderate to high	Unknown
Lipid packing in monolayer and bilayer membranes	Binding to nuclear receptors	Membrane proteins
Membrane perturbation effects on receptor function	Bindind to specific transporters	

Table 1.1: Expected outcomes for steroid enantioselectivity studies [87].

and electronically complimentary to those of the steroids they bind, it is generally expected that their interactions with steroids will be enantioselective. By contrast, lipid membrane bilayers in the liquid state, although they are composed of optically active lipids, do not maintain a defined architecture because of rapid movement of the lipids. Hence, enantioselective sterol-lipid interactions for a membrane bilayer in the liquid state would not be expected. In Table 1.1, membrane proteins are placed in a column where an expectation for enantioselectivity is not given since either (or both) outcome(s), depending on whether steroid modulation is caused by direct binding to the protein and/or by membrane perturbation, can be expected. A finding of steroid enantioselectivity strongly suggests that a steroid binding site exists on the membrane protein. The failure to observe steroid enantioselectivity either means that steroid effects are mediated by membrane perturbation or that the receptor cannot discriminate between steroid enantiomers. In such a case, additional information from other types of studies (e.g., sitedirected mutagenesis, protein structural data) would be needed to distinguish between the two types of steroid modulation.

The reason that undertook the preparation of entsteroids was to provide evidence for the existence of anesthetic steroid binding sites on $GABA_A$ receptors. In 1996, it was reported that the actions of $3\alpha5\alpha$P (pregnenolone) were enantioselective [10]. Whereas $3\alpha5\alpha$P is a potent positive allosteroic modulator of GABAA receptors, *ent*-$3\alpha5\alpha$P is not. Until 2006, when site-directed mutagenesis studies provided direct support for the existence of these sites [17], the enantioselective actions of $3\alpha5\alpha$P and other steroid analogues [88] were the strongest evidence that these sites existed.

Apart from providing evidence for the existance of anesthetic steroid binding sites on $GABA_A$ receptors, steroids enantioselectivity studies have proven to be very fruitful; surprisingly, not all *ent*-steroids are less effective modulators of protein function than their natural counterparts. In cases where *ent*-steroids have actions equal to or greater than their natural counterparts, there may be opportunities to develop *ent*-steroids as drugs. Possible advantages of *ent*-steroid drugs would include a potential lack of agonist activity at nuclear receptors and reduced interference with the modification of endogenous steroids by steroid transforming enzymes. However, even if *ent*-steroid drugs are not forthcoming, the utility of *ent*-steroids as tools to address the direct and indirect effects of steroids on membrane protein function now seems established.

Issues concerning the enantiospecificity of lipid interactions are also connected to the questions about the mechanisms of general anesthetics. One unifying property of many anesthetics is that their potency is proportional to the olive oil/water partition coefficient. This is the so-called Meyer-Overton rule [89]. This simple correlation is enticing, and some still suggest that actions on these proteins are mediated by lipid membranes or by a simple physical mechanism such as a change in the hydration of lipids and proteins [90]. The lipid environments of a protein affect its functions and its mode of action [91], and, hypothetically, anesthetics could modulate these environments.The suggested mechanisms of lipid-mediated action include the effects of anesthetics on dipole potential and spontaneous curvature [92], or on the lateral pressure profile [12]. Indeed, while prevailing anesthetic hypothesis favors direct binding to proteins, many proponents of lipid mediated action exist. However, no optically active anesthetic has been shown to have enantiospecific interactions with membrane lipids [93, 94]. A caveat is that the effects on many properties suggested to be important for the hypotheses of lipid-mediated anesthesia were not studied and only a few phospholipid compositions were used.

1.3 Neurosteroids and nerve cells

1.3.1 Motivations

"Neurosteroids: of the nervous system, by the nervous system, for the nervous system" [95] is a maxim of Etienne-Emile Baulieu that has stood the test of time and scientific inquiry. That the brain is a steroidogenic

organ is well accepted, and the enzymes required for neurosteroid synthesis have been identified and localized to specific populations of glia and neurons within both the central and peripheral nervous systems. The wide range of functions of this broad class of molecules spans from the organizational to the activational.

Here we focused on specific neurosteroids such as allopregnanolone (Allo) and dehydroepiandrosterone (DHEA). In particular, it has been found that Allo promotes neurogenesis and the associated cognitive function, reduces pathology related to Alzheimer's disease and promotes regeneration of white matter. The regenerative nature of Allo action has led to a focus on the potential role of this molecule in prevention, delay and treatment of neurodegenerative diseases such as Alzheimer's disease [96]. In the case of DHEA, a coincidence between the natural decline of DHEA levels with age and the onset of diseases associated with aging process have been reported [97, 98], striking the attention on how this steroid can act at the neurological level.

In the framework of this thesis we are interested in testing the effects, if any, of Allo and DHEA on the mechanical properties of nerve cells, as well as morphological changes due to a possible reorganization of the cytoskeleton, as it happens in the case of sex steroids [99]. The present real-time AFM approach for monitoring changes in cell structure, surface roughness and stifness is of clear pharmacological interest, since a clinical trial for has Allo already started in the US.

1.3.2 State of the art

For decades, research has focused on the regulation of neuronal growth and regeneration in development and after injury or disease by chemical signals such as chemical guidance cues and growth factors, as well as on its genetic control [100, 101]. However, the importance of mechanical factors in neuronal development and pathology is increasingly recognized . Recent technological advances have enabled measurements of mechanical tissue and cell properties, forces actively exerted by CNS cells, the external application of forces in the piconewton range, and the observation of cellular and subcellular responses to mechanical stimuli. To measure mechanical material properties, usually a mechanical stress is applied to the sample, and the resulting strain (deformation) is measured. For simple elastic materials, the ratio of stress to strain determines a modulus, which defines the material's stiffness. Most biological materials, such as cells and tissues, are viscoelastic, that is, their response to a mechanical stress (or strain) is partly elastic and partly viscous and depends on the timescale at which the stress is applied. The viscous or dissipative properties of tissues are generally measured by dynamic tests such as oscillatory or stress-relaxation measurements.

Several measurement techniques have been developed to study cell mechanics [102] such as micropipette aspiration [103, 104], magnetic tweezers [105], optical tweezers [106] and nanoindentation based on AFM [107, 108, 109]. Among all these techniques, AFM takes advantage in providing high-

resolution 3D images of cellular topography at the molecular scale, as well as preforming real-time and quantitative elasticity measurement of live cells in physiological-like conditions [110, 111, 112, 113, 114].

The interaction of the cell with an extracellular environment is an integrated process involving a number of intracellular controllers orchestrating cytoskeletal proteins and their action on the cell membrane and anchorage proteins. The mechanical properties of cells (such as elasticity and surface roughness) but also cell morphology and the overall organization at the tissue level are directly linked to the dynamics of the cytoskeleton which can be regulated by external cues or exogenous molecules like, for example, drugs which are able to depolymerize the cytoskeleton and also sex steroids [99]. Actin filaments are one of the major components of cytoskeleton [115] and they mainly spread out in cellular cortex [116]. As the main structural framework, actin filaments closely interact with receptors in cytomembrane, and maintain the cellular integrity by carrying tensile and compressive forces [117]. Actin microfilaments are also the main constituent of dendritic spines. Dendrites are sites where neurons receive, process and integrate inputs from their presynaptic partners. Both the shape of dendritic trees and the density of their spines undergo significant changes during the development and life of a neuron. These structures are instrumental for the development of neuronal circuits under the regulation of several extracellular stimuli [118]. Sex hormones like oestrogen are involved in the formation of dendritic spines during the development and in their plasticity at mature synapses, controlling actin filaments [119, 120]. Moreover, they control brain plasticity, particularly through neuronal/glial remodelling, which is critical for memory, learning and cognition [121, 122, 123, 124]. At the basis of brain plasticity is the ability of neurones and glial cells to remodel their mutual connections, which requires major changes in cell morphology [125, 126]. These morphological modifications depend on the generation of dynamic structural changes of the actin cytoskeleton, as well as on the development of protusive membrane structures, such as lamellipodia and filopodia, that are involved in the generation of cell-cell interconnections. Clinical studies also suggest that lack of oestrogens, such as in women after menopause, may be related to the progression of brain degenerative diseases, such as Alzheimer's disease or Parkinson's disease [127, 128, 129].

The dynamic mechanical response of neurons cytoskeleton during the neurogenerative process is of particular interest and nowadays it is still not fully revealed. Neurogenic mechanisms in brain are novel therapeutic targets to sustain neurological function and to prevent, delay or treat neurodegenerative diseases [96]. More than a decade of research has accumulated since adult mammalian neurogenesis was detected in human brain [130] and has been confirmed and extensively studied in preclinical animal models. The challenge faced by researchers developing molecular therapeutics to promote self-renewal in the nervous system is to activate regenerative and repair pathways often in the context of progressive degeneration. Neurosteroids regulate both regeneration and repair systems in the brain, and

among this class of molecules, allopregnanolone has been broadly investigated for its role to promote regeneration in both the central and peripheral nervous systems. In the brain, allopregnanolone induced generation and survival of new neurons in the hippocampus of both aged mice and mice with Alzheimer's disease, accompanied by restoration of associative learning and memory function [96].

1.4 Physical approaches for regenerative medicine

1.4.1 Motivations

Fibrin is a natural biopolymer that is very appealing to tissue engineers and stem cell differentiation because it is biocompatible, bioresorbable and essential in normal wound healing. Fibrin/keratinocytes structures are currently studied for corneal epithelial stem cell therapy and transplantation. In this work we want to establish if there is a correlation between the rheological properties of different fibrin substrates and the behavior of the on-growing keratinocytes.

It is known that mesenchymal stem cells (MSCs) specify lineage and commit to phenotypes with extreme sensitivity to tissue level elasticity [131]. By modulating the mechanical and chemical properties of a fibrin-based matrix, MSCs have been differentiated into osteoblasts and mouse embryonic stem cells have been coaxed down neural and astroglial lineages [132]. To study if such a correlation between the property of the substrate and the on-growing stem cells is present also in the case of fibrin+keratinocytes structures, we chose four different fibrin substrate with varying fibrinogen concentration in order to obtain different mechanical properties.

The influence of the fibrinogen concentration in fibrin's mechanical properties has been investigated but researchers have produced different values for this influence and also for the Young's modulus; unfortunately, the testing protocols, if known, are often very different and unclear [133]. Moreover, since many of the viscoelastic properties of fibrin and other biopolymers gels, such as strain hardening, are radically different from those of common rubber-like materials, continued study of such materials is likely to provide data valuable to testing theories of polymer dynamics as well as understanding basic physiology and disease [134]. The viscoelastic properties of fibrin is a subject that requires interaction between scientists and clinicians and still nowadays there is not a complete understanding of how the physical features of fibrin can affect its biological and clinical role [135]. At the same, a model which can properly describe the complete viscoelastic behavior of fibrin gel is still lacking.

All these unresolved points lead us to perform a complete viscoelastic characterization of different fibrin samples in order to produce new data and to check the validity of the so called poroelastic model, apart from testing if there is a relation between the stiffness of the substrate and the features of the overlying stem cells. As already stated, the fibrin/keratinocytes

structures we studied are of great interest for regenerative medicine and in particular for corneal transplantation. The success for transplantation is guaranteed if the percentage of holoclones (the stem cell which has the higher growth potential and that allows a continuous renovation of the cultivated skin) is preserved and maintained around 4-5%. Another reason for our study was to find out if a specific choice of the mechanical properties of the fibrin substrate could also lead to an improvement in the percentage of the covering holoclones. All these studies were performed in collaboration with Centro di Medicina Rigenerativa (Prof. Graziella Pellegrini) which kindly provided us the samples and carried out the parallel biological and clinical characterization.

1.4.2 State of the art

Owing to the rapid progress in biomedical science and the highly anticipated therapeutic potentials, stem cell-related research has boomed since the beginning of the new millennium. However, in contrast to enormous basic research papers that have been published, clinical applications of stem cells, except hematopoietic stem cell transplantation, are still in infancy. Nevertheless, during the last decade there has been a remarkable success in corneal epithelial stem cell therapy, which merits special attention to what has been found regarding corneal epithelial biology, and what has been reported regarding the therapeutic modalities [136].

The corneal epithelial stem cells are located in the basal layer of limbus (therefore are called limbal stem cells LSCs), and are pivotal for the maintenance of corneal transparency and avascularity. In event of LSC deficiency that is caused by burns or autoimmune diseases, conjunctival epithelial cell invasion is accompanied by pannas ingrowth and persistent inflammation. Transplantation of autologous or allogeneic healthy limbal tissue restores corneal epithelium and therefore improves vision.

The earliest example of cell therapy using cultured keratinocyte stem cells dated back to the 1980s, when it was first demonstrated that human epidermal keratinocytes could be grown in vitro and transplanted back to burn patients to reconstruct a new skin [137]. The relatively easy access to the cornea, the homogeneity of the cells forming the corneal epithelium, and the improvement of cell culture protocols are factor contributing to considerable success in corneal epithelium restoration [138]. In 1997, Pellegrini et al. were the first to report the use of cultivated corneal epithelium (Figure 1.6) to reconstruct corneal surface damaged by severe alkaline burn in two patients [139].

Conventional biomaterials used in tissue engineering like polyglycolic acid (PGA) or polylactic and glycolic acid (PLGA) are not suitable for cultivating keratinocytes because they are neither biodegradable nor soft. In contrast to the tremendous success of amniotic membrane (AM) as a substrate, only few other biomaterials have been tried clinically. Fibrin gel was first used as a biodegradable scaffold for cultivating chondrocytes [140] or

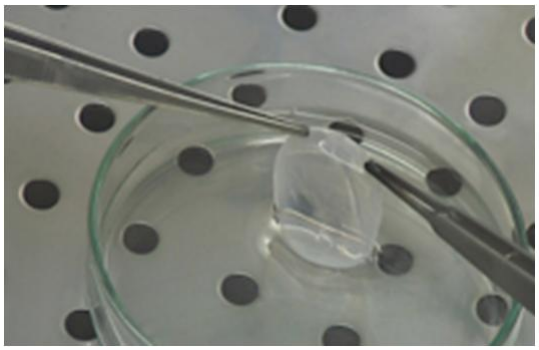

Figure 1.6: A cultured sheet of corneal epithelium, from the website of Centro di Medicina Rigenerativa, *www.cmr.unimore.it*.

myofibroblasts [141]. In 1994, Kaiser et al. [142] reported three patients with deep partial and full skin thickness burns treated with cultured autologous keratinocytes suspended in fibrin glue. In two of these patients the keratinocyte-fibrin matrix was overgrafted with allogeneic, glycerine-preserved split thickness cadaver skin. The non-confluent cells developed into a continuous epithelial layer within 4 days, and histological examination showed a stratified neoepidermis. Clinically the new skin had satisfactory stability and mechanical quality. The fibrin glue matrix seems to give sufficient adherence stability to keratinocytes that are grafted in an actively proliferating state. Later Pellegrini et al. [143] showed that the relative percentage of holoclones (keratinocyte stem cells) is maintained when epidermal keratinocytes are cultivated on fibrin, and the clonogenic ability, growth rate, and long-term proliferative potential of epidermal keratinocytes are not affected. When fibrin-cultured autografts bearing stem cells are applied on massive full-thickness burns, the "take" of keratinocytes is high, reproducible, and permanent, suggesting that fibrin is a suitable substrate for keratinocyte cultivation and transplantation.

Chapter 2

Investigated biological systems

2.1 Biological membranes

The biological membrane is one of the most important cell structure. It represents an envelope of the cell with unique barrier function, that provide directional transport of species into the cell and waste and toxic compounds out of the cell. In addition, the low permeability of the membrane for charged particles, e.g. ions, and the presence of active transporters allow to maintain non-equilibrium ion distribution between extra cellular and cytoplasmic side of the cell, which is crucial for cell function. Destruction of the membrane results in establishment of equilibrium and cell death. The membrane with supported protein net-glycocalix and the actin cytoskeleton are responsible for the cell shape and, owing to the viscoelasticity, also for reversible changes of this shape during cell function.

Biomembranes provide, however, not only structural and barrier functions. They contain integral and peripheral proteins, that are responsible for communication of the cell with surrounding environment, i.e. they have receptor function and are responsible also for transfer of the signals into the cell by means of sophisticated signaling pathways. In a membrane also several catalytical processes are concentrated, for example the energy transduction connected with synthesis of energetically reach molecule adenosine thriphosphate (ATP). From the physical point of view the biomembrane represent an anisotropic inhomogeneous structure with properties typical of liquid crystals of smectic type [144].

The bimolecular structure of the cell membrane was first postulated in 1925 by Gorter and Grendel [145]. They found that the surface area of lipids extracted from red blood cells was double the surface area of the cell itself. They concluded that cell membranes are made of two lipid layers organized in the form of a bilayer. Their model didn't consider the presence of proteins, which were later included by Danielli and Davson in 1935 [146]. For a long period, the most accepted model of membrane structure originated from the so called fluid mosaic model, proposed by Singer and Nicolson in 1972 [147]. In their model, the lipid bilayer is considered as a homogeneous fluid in which globular protein molecules diffuse in two dimensions. Nowadays,

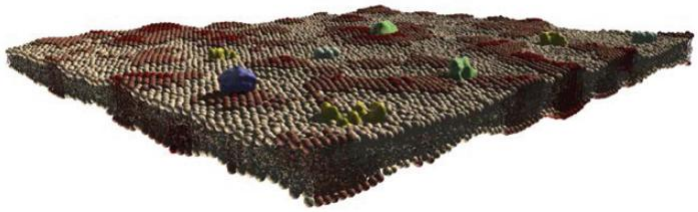

Figure 2.1: Modern view of biological membranes. Membrane proteins and lipids of different species and states are distributed inhomogeneously in the membrane plane. Picture taken from [148].

biomembranes are believed to be heterogeneous structures where lipids can exist in different states and form domains, and interact dynamically with the proteins (Figure 2.1) [5, 71].

Due to rather complicated structure, anisotropy and inhomogeneity, the study of the physical and chemical properties of the biomembranes is difficult. Therefore several models of biomembranes have been developed, including micelles, monolayers, liposomes and also solid supported lipid films. These structures allow to vary in large scale the lipid composition and in some cases allow also to easily incorporate integral or peripheral proteins. Thus, the model membranes can be constructed in a way that try to mimic the structure and properties of biomembranes. Throughout this thesis, pure lipid bilayers will be considered. Being the major constituent of biomembranes, any result concerning the lipid double layer, has an immediate biological relevance.

2.1.1 Phospholipids

Lipids are the major constituent of biological membranes. They can be divided in three main classes: glycolipids, phospholipids and sterols. Phospholipids are the most abundant class in biomembranes [144]. Phospholipid molecules are made of three parts: a hydrophilic head group and a hydrophobic hydrocarbon tail which are connected by a backbone, most commonly made of glycerol (Figure 2.2). Being constituted by a polar hydrophilic part and a non-polar hydrophobic tail, phospholipids are amphiphilic molecules. The name phospholipid is due to the presence of a negatively charged phosphate group (PO_4) in the head group. Differences in head group and tail result in the different species of phospholids.

Head groups may differ in size, polarity and charge, depending on the organic compound that is bound to the phosphate group. The most common are choline, ethanolamine (both positevely charged), serine and glycerol (both uncharged). The resulting head groups are called phosphatidylcholine (PC), phosphatydilethanolamine (PE), phosphatidylserine (PS) and phosphatidylglycerol (PG). PC and PE are zwitterionic, while PS and PG are negatively charged. There is no evidence of positively charged headgroups in biological membranes [149]. The relative abundance of different head

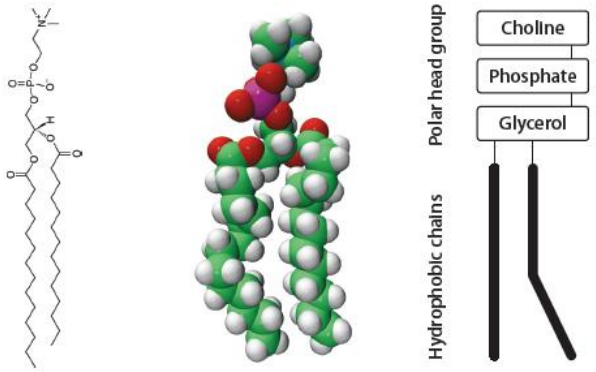

Figure 2.2: Chemical structure and schematic representation of a molecule of dimyristoylphosphatidylcholine (DMPC), showing the hydrophilic head group and the hydrophobic tail. The picture on the right is adapted from [144]. The left and center are taken from the website of Avanti Polar www.avantilipids.com

groups in biomembranes can influence their phase behaviour as well as electrical properties or their interaction with proteins or drugs, being the main binding site for them at the lipid/water interface. Hydrophobic tails are basically hydrocarbon chains which can differ in number, length and saturation. A phospholipid molecule can have between one and four chains attached to the glycerol backbone, two being the most common case [150]. The length of the chains is determined by the number of carbons which can oscillate between 12 and 24 depending on the particular fatty acid. Saturation level is related to the number of double bonds between the carbon atoms in the chain, and can greatly affect the hydrocarbon chain mobility. The chemical structures of the lipids employed in this work are reported in Figure 2.3.

2.1.2 Lipid bilayers

Lipid bilayers are self assembling structures formed by phospholipids in an aqueous environment [144]. This is not the only configuration that they assume when placed in water. Lipid polymorphism is a well documented phenomenon [151, 152] and different structures can form depending on the packing constraints for the lipid molecules and their concentration (Figure 2.4). The common feature is that they aggregate exposing their polar heads to the water, thus shielding the hydrophobic tails which strongly repel water. This corresponds to the most energetically and entropically favoured configuration [149]. The ability to self assembly is the result of a balance between attractive forces that minimize the hydrophobic effect and repulsive (steric or electrostatic) forces between the molecules [150].

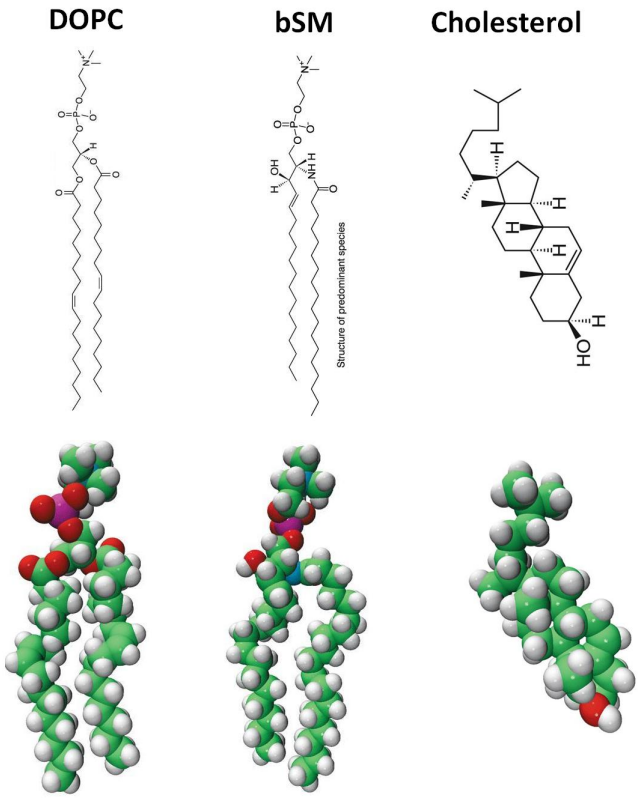

Figure 2.3: Chemical structure and schematic representation of the lipids mainly used within this work: 1,2-dioleoyl-sn-glycero-3-phosphocholine (DOPC), sphingomyelin (Brain, Porcine) (bSM) and cholesterol. Pictures are taken from the website of Avanti Polar www.avantilipids.com

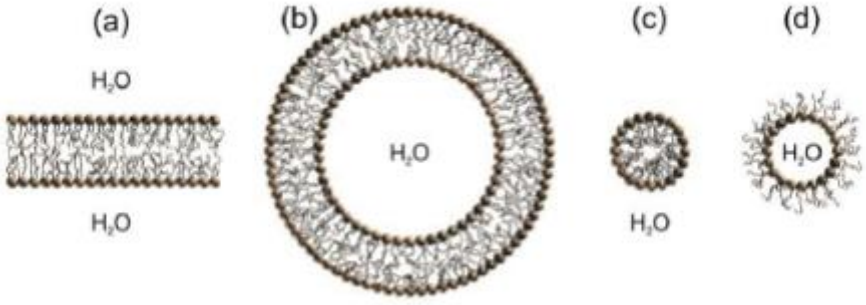

Figure 2.4: Polymorphism of lipids in aqueous environment. (a) bilayer; (b) vescicle; (c) micelle; (d) inverse micelle. Pictures are taken from [148].

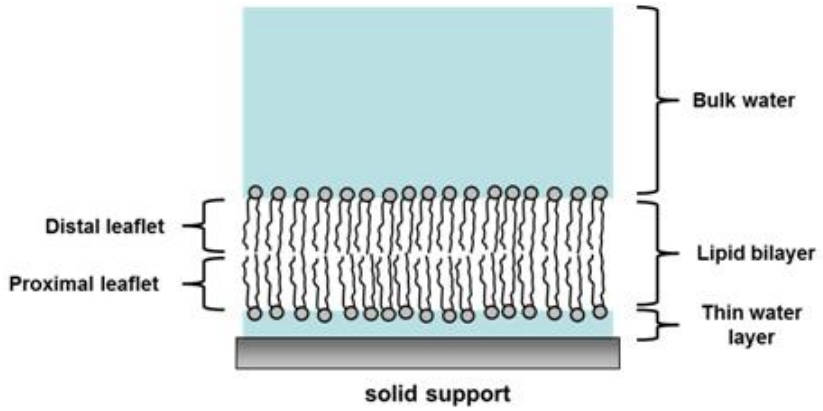

Figure 2.5: Scheme of a supported lipid bilayer. The presence of a thin water layer between the bilayer and the substrate is highlighted together with the separation of the distal and proximal leaflets. From [161].

2.1.3 Supported lipid bilayers

Supported lipid bilayer (SLB) consists of a lipid bilayer on a rigid and typically hydrophilic substrate such as glass, silicon oxide or mica. It was initially developed by McConnell's group to study the interaction of cells with lipid bilayers [154, 155]. SLBs can be assembled by two main different strategies, each presenting specific advantages: the Langmuir Blodgett/Schaefer approach [156] and the vesicle fusion technique [157].

The first technique is based on two consecutive transfers to a solid substrate of lipid monolayers assembled at the liquid/air interface in a Langmuir trough. The appealing feature of this approach is connected with the possibility of forming lipid bilayers characterized by a transbilayer lipid asymmetry [158], reproducing the actual situation found in biological membranes, even if the retention of the initial composition asymmetry between the two leaflets has been questioned [159].

The vesicle fusion technique allows forming supported lipid bilayers from unilamellar vesicles in solution. Upon contact with surfaces, under specific conditions, unilamellar vesicles rupture, forming a planar bilayer. The implementation of the vesicle fusion technique is substantially easier than the technique based on Langmuir trough. In both preparation strategies, the presence of a thin water layer between the bilayer leaflet nearer to the substrate (proximal leaflet) and the substrate itself enables lipid diffusion [160]. Figure 2.5 shows a scheme of a supported lipid bilayer.

In general, lipid bilayers display a reversible phase transition between a solid ordered (S_o) and a liquid disordered (L_d) phase when the temperature, or other parameters, change (e.g. pressure, pH). The transition is accompanied by changes in lipid chains (ordered or disordered) and lattice order (solid or liquid). The change in the lipid chain order is reflected in a variation of the membrane thickness which makes the transition easily observable by AFM topographic images.

2.1.4 Vescicles

A vesicle is a lipid bilayer rolled up into a spherical shell, enclosing a small amount of water and separating it from the water outside the vesicle. Because of this fundamental similarity to the cell membrane, vesicles have been used extensively to study the properties of lipid bilayers. Another reason vesicles have been used so frequently is that they are relatively easy to make. If a sample of dehydrated lipid is exposed to water it will spontaneously form vesicles [162]. These initial vesicles are typically multilamellar (many-walled) and are of a wide range of sizes from tens of nanometers to several micrometres [163]. Methods such as sonication or extrusion through a membrane with pores are needed to break these initial vesicles into smaller, single-walled vesicles of uniform diameter known as small or large unilamellar vesicles (SUVs, LUVs). SUVs typically have diameters between 50 and 200 nm, while LUVs may have sizes up to few micrometers [164]. Alternatively, rather than synthesizing vesicles it is possible to simply isolate them from cell cultures or tissue samples [165].

Since artificial SUVs and LUVs can be made in large quantities they are suitable for bulk material studies such as X-ray diffraction to determine lattice spacing [166] and differential scanning calorimetry to determine phase transitions [167]. Dual polarisation interferometry can measure unilamellar and multilamellar structures [168] and vesicles can also be labeled with fluorescent dyes to allow sensitive FRET-based fusion assays [169]. In spite of this fluorescent labeling it is often difficult to perform detailed imaging on SUVs simply because they are too small. To overcome this problem researchers have developed the giant unilamellar vesicles (GUVs).

GUVs are large enough (diameter of tens of micrometres) to be studied by traditional fluorescence microscopy. Many of the studies of lipid rafts in artificial lipid systems have been performed with GUVs for this reason [170]. Compared to supported bilayers, GUVs present a more "natural" environment since there is no nearby solid surface to induce defects or denature proteins. However, GUVs are relatively fragile, time consuming to make and can only be produced in limited yield compared to SUVs.

2.2 Neurosteroids

Neurosteroids are steroids synthesized within the brain and modulate neuronal excitability by rapid non-genomic actions. The term 'neurosteroids', originally coined by the French physiologist Etienne Baulieu, is now widely used to refer to steroids that are synthesized in the brain. Circulating steroid hormones serve as precursors for the synthesis of neurosteroids, which are produced locally in the hippocampus and other brain structures [95]. Neurosteroids modulate brain excitability primarily by interaction with neuronal membrane receptors and ion channels, principally $GABA_A$ receptors, a subtype of receptor for the neurotransmitter GABA that mediates the bulk of synaptic inhibition in the central nervous system

Neurosteroid	Pharmacological actions	Effect on $GABA_A$-R
Allo	Sedative-hypnotic Anxiolytic, anticonvulsant Antistress, neuroprotection	Potentiation
isoAllo	Inhibitor of Allo's effects	No direct interaction
Preg-S	Anxiogenic, proconvulsant Memory enhancing, neuroprotector	Inhibition
DHEA	Memory enhancing, neuroprotector Sexual regulator	No interaction

Table 2.1: Pharmacological profile of the neurosteroids used in this work

[8, 173, 174]. $GABA_A$ receptor function can be regulated either in a positive or negative way, depending on the chemical structure of the steroid molecule [18, 174]. Structurally, $GABA_A$ receptors are heteropentamers with five protein subunits that form the chloride ion channels [175]. The modulating effects of neurosteroids occur by binding to discrete sites on the receptor that are located within the transmembrane domains of the α- and β-subunits [17]. The binding site for neurosteroids is proposed to be distinct from that of the GABA, benzodiazepine and barbiturate sites. Exposure to neurosteroids enhances the open probability of the $GABA_A$ receptor chloride channel, so that the mean open time is increased and the mean closed time is decreased. This increases the chloride current through the channel, ultimately resulting in a reduction of neuronal excitability. Recent studies have indicated the existence of at least three neurosteroid binding sites on the $GABA_A$ receptor: one for allosteric enhancement of GABA-evoked currents by allopregnanolone, one for direct activation by allopregnanolone, and one for antagonist action of sulfated neurosteroids such as pregnenolone sulfate [173, 65]. The physiological and pharmacological profile of the neurosteroids studied in this work is listed in Tabel 2.1, while their chemical structures are shown in Figure 2.6.

2.2.1 Allopregnanolone (Allo)

Allopregnanolone (3α-OH-5α-pregnan-20-one) is a reduced metabolite of progesterone, synthesized in the gonads, adrenal cortex, and the central nervous system. In the central and peripheral nervous systems, Allo synthesis occurs primarily in glial cells - astrocytes, oligodendrocytes, and Schwann cells and in many neuronal cell types including neural progenitors [176]. Allo is a potent positive allosteric activator of the $GABA_A$ receptor: at nanomolar concentrations it enhances the action of GABA at $GABA_A$ receptor whereas, at higher concentrations, it directly activates $GABA_A$ receptor. Allo binds to two transmembrane sites of the hetero-pentameric $GABA_A$ receptor [17].

Within the mammalian brain, Allo has been shown to modulate anxiety, depression, seizure activity, sedative-hypnotic activity, and the immune system. Adding to this list, Allo promotes the neuroregenerative system

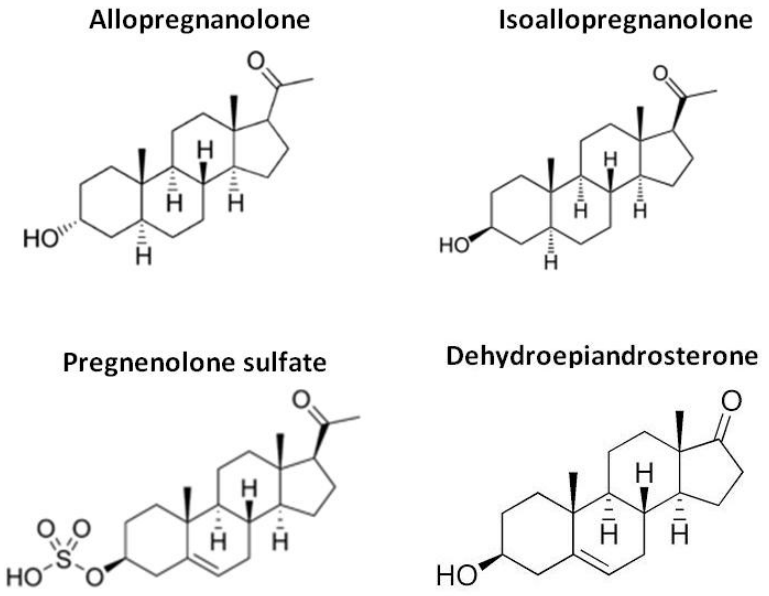

Figure 2.6: Structural formulas of the neurosteroids studied in this work.

and modifies the course of neurodegenerative disease. In preclinical analyses in normal aged and transgenic mice for Alzheimer's, Allo induced the generation and survival of new neurons in the hippocampus and subventricular zone. Allo-induced neurogenesis was accompanied by restoration of associative learning and memory function [177].

2.2.2 IsoAllopregnanolone (IsoAllo)

Isoallopregnanolone (3β-OH-5α-pregnan-20-one), is a stroid closely related to allopregnanolone. The only structural difference from its isomer allopregnanolone is the hydroxyl group in 3β- instead of 3α- position. IsoAllo is synthesized in the mammalian ovary and by its own is, as far as we know today, without hormonal or $GABA_A$ receptor effects [178]. Instead, isoAllo has often been used as a control when testing the specificity of allopregnanolone and its $GABA_A$ receptor enhancing effect, to show that the sterical configuration with the 3-hydroxy group is of major importance for the $GABA_A$ receptor stimulating effects of allopregnanolone [180]. Furthermore, no IsoAllo influence has been noted on anesthesia [179] or anxiolysis [180].

However, it has recently been shown that IsoAllo can antagonize the effect of Allo on the $GABA_A$ receptor as shown *in vitro* [14], on slices of brain tissue [181] and *in vivo* as it inhibits Allo-mediated induction of anesthesia in rats [182]. The antagonizing effect of IsoAllo on Allo seems specific as GABA, benzodiazepine or barbiturate effects are not inhibited by isoAllo [178].

2.2.3 Pregnenolone sulfate (Preg-S)

Steroid sulfates are formed by sulfonation of steroids by cytosolic sulfotransferase enzymes (SULT) [183, 184]. Pregnenolone sulfate (Preg-S) is the sulfated ester of pregnenolone and it is present in the brain at a relatively high concentration compared with many other neurosteroids [185]. It is unlikely that pregnenolone sulfate is capable of easily crossing the plasma membrane due to the hydrophilic sulfate moiety. On the other hand, for its function as source for pregnenolone and subsequent synthesis of steroid hormones like estradiol, progesterone etc., it is indispensable that the substrate (Preg-S) enters the cytosol to come into contact with the cytosolic localized sulfohydrolases. The transmembrane transport can be facilitated by a variety of transporter proteins [186].

From a pharmacological point of view, Preg-S qualified as an excitatory neuroactive steroid, because it negatively modulates the $GABA_A$ receptor, and because it positively regulates the ionotropic glutamate receptor family of ligand gated ion channels such as N-methyl-d-aspartate receptor (NMDA) and amino-3-hydroxy-5methyl-4-isoxazole propionic acid (AMPA) receptors [187, 188]; Preg-S plays a critical role in several physiological and paraphysiological processes such as sleep modulation [189, 190], emotionality, memory performance, and in age-related neuropsychiatric disorders [191].

2.2.4 Dehydroepiandrosterone (DHEA)

Dehydroepiandrosterone (DHEA) is a steroid, produced in adrenals, in neurons and in glia [97]. The physiological role of brain DHEA appears to be local, i.e. paracrine, while that produced from adrenals, which represents the almost exclusive source of circulating DHEA, is systemic. Circulating levels of DHEA decline after birth until about the age of five, then start to rise a few years before sexual maturation begins. Levels peak around the age of 20 to 30 and then decline to only 20-30% of peak levels by the age of 70 to 80 [192]. The precipitous decline of both brain and circulating DHEA with advancing age has been associated with aging-related neurodegenerative diseases [97, 98].

It is experimentally supported that DHEA protects neurons against noxious conditions [193]. DHEA exerts its multiple pro-survival effects either directly modulating at micromolar concentrations $GABA_A$), N-methyl-D-aspartate (NMDA), or sigma1 receptors, or following its conversion to estrogens and androgens. Lowered levels of DHEA have been associated with critical illness, emotional stress, and a variety of medical conditions, including rheumatic disease [194], cardiovascular disease [195], immune system disorders [196], and osteoporosis [197]. Elevated levels have been observed in connection with obesity and type II diabetes [198], female hirsutism [199] and individuals subjected to prolonged physical stress [200]. Studies are currently exploring relationships between DHEA levels and various areas of neurological function, and at least one paper has suggested that the primary effect of DHEA is in fact neurological, with secondary effects on immune

function and growth [201].

Because of the coincidence between the natural decline of DHEA levels with age and the onset of diseases associated with the aging process, a great deal of research has been directed into an examination of the roles that both hormones play in the body, and to the possibility of supplementing levels to slow or reverse the aging process. Although these studies have reported widespread effects for the hormones, a molecular mechanism of action has not yet been definitively isolated. It remains unclear whether either compound has a physiological role other than serving as a precursor molecule [202]. Recent reviews [200] point out that this lack of understanding about the mode of action of this hormon, along with problems in the design and analysis of certain studies, have led to discrepancies among the findings [97, 203].

2.3 Nerve cells

2.3.1 Basics of neurons' anatomy

The nervous system consists of neurons, or nerve cells, whose main task is transmission, processing, and storage of information, and glial cells, which are involved in a multitude of different functions, are tightly connected and complement one another.

Neurons generally consist of a cell body (or soma) and a number of cellular extensions, or processes (Figure 2.7). In immature neurons and in many in vitro assays, these processes are called neurites. In mature neurons, one of these neurites has become an axon, which is the long, dominating process that sends information from the soma to the tissue that is innervated by the neuron. The remaining neurite(s) turn into dendrites, which are shorter and highly branched processes that collect information.

Neurons extend their processes to connect to other neurons and tissues, which is facilitated by growth cones, the leading tips of neuronal processes. Once the neuronal network is connected, axons further grow passively by being stretched (referred to as towed growth). Mechanical tension along these axons arises from the mismatch in growth rates between skeleton and nervous tissue. The former keeps growing much longer than the latter, so that connected axons are under tension. Connections between neurons and other cells through which signals are transferred are called synapses [204].

2.3.2 SH-SY5Y cell line

In this work we evaulated the effect on neurosteroids on SH-SY5Y cells, a human derived cell line often used as *in vitro* model of neuronal function and differentiation. SH-SY5Y (human neuroblastoma) was cloned from a bone marrow biopsy derived line called SK-N-SH and first reported in 1973 [206]. A neuroblast-like subclone of SK-N-SH, named SH-SY, was subcloned as SH-SY5, which was subcloned a third time to produce the SH-SY5Y line,

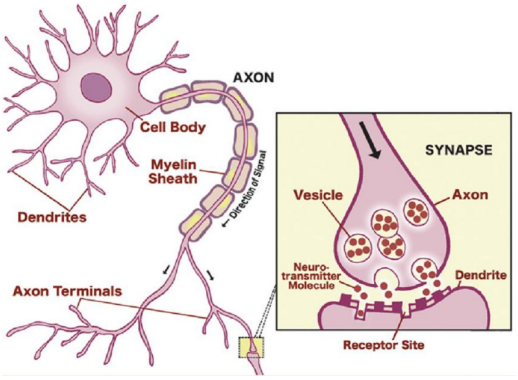

Figure 2.7: Basic anatomy of a nerve cell. Adapted from [205].

first described in 1978 [207]. The cloning process is essentially artificial selection, involving expansion of individual cells or a small group of cells that express a particular phenotype of interest, in this particular case neuron-like characteristic. The SH-SY5Y line is genetically female with two X and no Y chromosome, as expected given an origin from a four-year-old female.

The cells typically grow in tissue culture in two distinct ways. Some grow into clumps of cells which float in the media, while others form clumps which stick to the dish. SH-SY5Y cells can spontaneously interconvert between these two phenotypes in vitro although the mechanisms underlying this process are not understood. However, the cell line is appreciated to be N-type (neuronal), given its morphology and the ability to differentiate the cells into along the neuronal lineage (in contrast to the S-type SH-EP subcloned cell line, also derived from SK-N-SH) [208].

The cells both propagate via mitosis and differentiate by extending neurites to the surrounding area. The dividing cells can form clusters of cells which are reminders of their cancerous nature, but certain treatments such as retinoic acid, BDNF, or TPA can force the cells to dendrify and differentiate. Moreover, induction by retinoic acid results in inhibition of cell growth and enhanced production of noradrenaline from SH-SY5Y cells. An image of human neuroblastoma cells is presented in Figure 2.8.

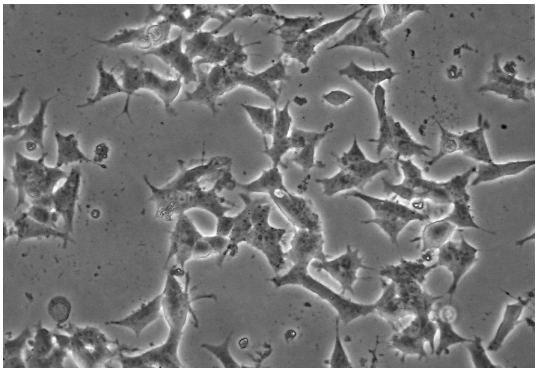

Figure 2.8: Optical microscopy image of SH-SY5Y cells [209].

2.4 Fibrin

2.4.1 Fibrin structure

Fibrin is formed by polymerization of fibrinogen monomers catalyzed by thrombin. Fibrinogen is an elongated protein, 45 nm in length, and is made up of globular domains at each end connected by α-helical coiled-coils to a globular region in the middle. During clotting, thrombin converts fibrinogen to fibrin by cleaving fibrinopeptides from the central domain, exposing knobs that can then interact with holes that are always exposed at the ends of the molecule, giving rise to a half-staggered structure called the protofibril, which has a periodicity of 22.5 nm. Cleavage of the A fibrinopeptides exposes the glycine-prolinearginine sequence, while cleavage of the B fibrinopeptides exposes the glycine-histidine-arginine sequence. When protofibrils grow sufficiently long, they assemble into fibers by lateral interactions that involve both specific, relatively weak protein bonds and interactions with chloride ions (Figure 2.9) [210, 211]. Gels can be formed by either protofibrils or fibers, to make so-called fine and coarse clots, respectively [212]. Lateral growth of fibers appears to be limited because protofibrils are twisted and the interactions in lateral aggregation are specific, so that, as the fiber diameter is increased, they must be stretched to traverse an increasing path length [213]. With this model, fiber growth ceases when the energy to stretch an added protofibril exceeds the energy of bonding.

Fibers branch to make a three-dimensional network, and most branch points are trifunctional, in other words consisting of the junction of three fibers [214]. Branching is generally the opposite of lateral aggregation, in that the conditions that favour lateral aggregation yield clots made of thick fibers with few branch points, whereas the conditions that hinder lateral aggregation yield clots with thin fibers and many branch points. Branching

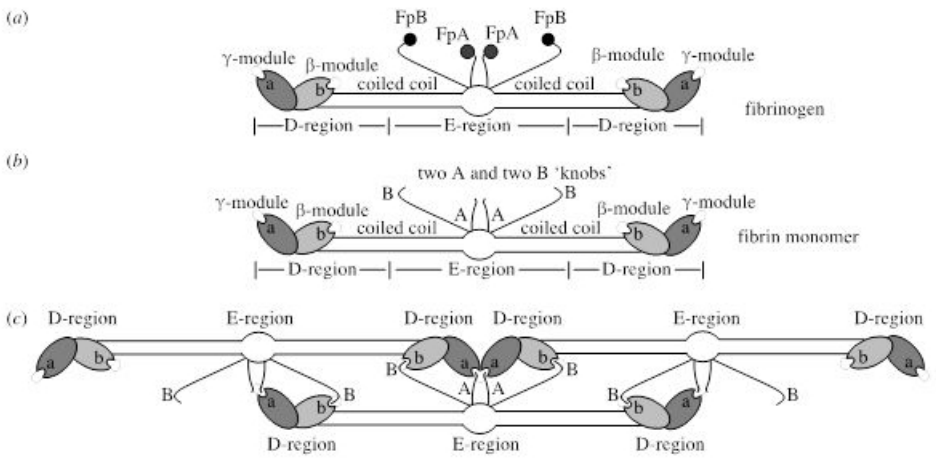

Figure 2.9: (a-c) Schematic of the structure of fibrin monomer and their assembly into protofibrils, from [210].

is essential for fibrin to make a space-filling gel. The properties of clots vary greatly depending on the conditions of polymerization [135]. The thickness of fibers, the extent of branching and the pore size of clots can vary to a very large extent, depending on a whole host of factors. For example, the thrombin concentration can have dramatic effects on clot structure, with low thrombin yielding clots with thick fibers, few branch points and large pores. Similarly, salt concentration, pH and many plasma proteins affect clot structure and properties.

2.4.2 Rheological properties of fibrin

Viscoelasticity

Elastic solids are characterized by Hooke's law, which states that the strain, or deformation, is proportional to the stress, or force applied per - unit - area, but stress is independent of the rate of strain. On the other hand, in the classical theory of hydrodynamics, viscous materials are characterized by Newton's law, which says that the stress is proportional to the rate of strain but independent of the strain itself. Viscoelastic materials, such as fibrin, like rubber, plastic, and many other polymers, have different degrees of both elastic and viscous properties [215].

Elastic properties are commonly measured by applying a stress, or force per unit area, to the polymer and determining the resulting strain, which is the stretching or distortion of the polymer normalized with respect to total length. The resulting stress-strain curve is used to determine the ratio of the stress required to produce a certain strain, which is called the *elastic modulus*, a parameter independent of the object's shape and size that is used to characterize materials [216]. A large modulus means that a large stress is necessary to produce displacement, so that object is stiff, while a small modulus means that less stress is required, so this other object is less stiff. These measurements can be made either statically (without movement) o dynamically (e.g., oscillatory motion), and different geometries can be employed [215].

Viscoelastic polymers are often characterized by two different parameters, one representing the elastic properties and the other representing the viscous properties. For example, an elastic or storage modulus may be used to characterize the stiffness of the polymer, while a loss modulus or creep compliance may be used to characterize the inelastic or irreversible component.

Fibrin can be considered a viscoelastic polymer, with both elastic and viscous properties. Its viscoelastic properties can vary greatly, depending on clot structure and biochemical properties [135]. The elastic moduli or stiffness of clots vary greatly depending on clot structure, and can be modulated by physiological conditions and fibrinogen concentration [133]. In Figure typical stress-strain curves for fibrin are reported.

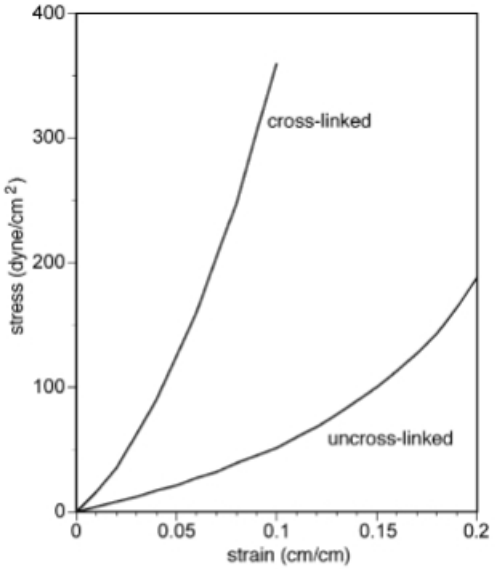

Figure 2.10: Stress-strain curves for cross-linked and uncross-linked fibrin. Elastic moduli can be calculated as the slopes of such curves. Some strain stiffening is evident for uncross-liked fibrin at higher strains. In other words, the elastic modulus increases with strain [218].

Non linear elasticity (strain stiffening)

The elongated, but still compliant, nature of the fibrin strands and the inherent branches (cross links) built into the polymerization mechanism produce protein networks with viscoelastic properties that differ in many respects from those of synthetic hydrogels. One of the most interesting rheological properties of fibrin is its nonlinear elasticity (Figure 2.11).

The elastic modulus of fibrin, measured in either shear or elongational strain, strongly increases the more the material is deformed (strained). The strain-stiffening nature of blood clots and purified fibrin gels has been experimentally evident for decades [217], but theoretical models to explain this effect have only recently been developed. Several different models can account for nonlinear elasticity of elongated fiber networks [218, 219, 220, 221, 222, 223], and which one applies depends on how flexible the filaments are, compared with the mesh size of the networks.

If the persistence length (defined as the length over which correlations in the direction of the tangent are lost [224] of the filament is similar to the mesh size of the network, as it is for fine clots, then strain stiffening emerges naturally from an entropic model that considers how the thermal fluctuations of semiflexible polymer are constrained as the end-to-end distance of the filament between cross-linking points changes when the sample is deformed [218, 221]. This entropic model, which assumes no changes in the protein structure until the filament is pulled nearly straight, accounts very well for the elasticity of networks containing fibrin protofibrils (fine clots), as shown schematically in Figure 2.11 (a).

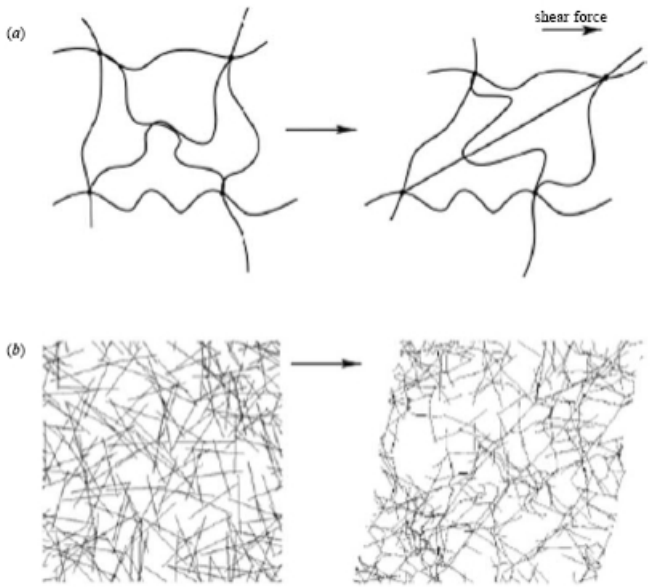

Figure 2.11: Schematics for two different mechanism of strain stiffening. (a) Semiflexible polymers linked at ends in network junction lose configurational entropy as their end-to-end distances are increased or decreased from their resting lenghts during shear deformation. Filaments with intrinsically nonlinear force elongation relationships resist more strongly when they are stretched more to the limit at which the end-to-end distance equals their contour lenght. Adapted from [218]. (b) Stiff filaments deform initially by bending at small strains and then by stretching at larger strains when their end-to-end vectors align in the shear field. In this mode, fibers with linear force-extension relationships produce strain stiffening in network owing to geometrical changes as they align in shear. Adapted from [220].

Under more physiological conditions, fibrin forms thicker bundles containing dozens or hundreds of protofibrils, which appear too straight in light micrographs to exhibit any significant thermal fluctuations. Coarse fibrin clots, as well as plasma clots, still strain stiffen, and for this case, alternative mainly enthalpic models, based on the orientation and stretching of the fibers are proposed to account for the nonlinear elasticity observed in the experiment [219, 220, 222, 223]. The basic idea of these models, shown schematically in Figure 2.11 (b), is that stiff fibers are easier to bend than to stretch, and therefore as strain increases and the filaments align more in the strain direction, a transition occurs from bending to stretching modes, which leads to increased stiffness at increased strains. This latter model is essentially enthalpic and predicts that at strains where the samples stiffen, changes in the protein structure can be expected, and indeed a change from α-helical to β-structures is observed for fibrin fibers at large deformation [225].

2.5 Keratinocyte stem cells

Epidermis, the outerpost layer of skin, consists of a stratified squamous epithelium composed of a main cell type, the keratinocyte. Owing to the pioneer work of Rheinwal and Green (1975) [226], normal human keratinocytes can be serially propagated in vitro. Cultured keratinocytes reconstituite a stratified squamous epithelium which maintains biochemical, morphological and functional characteristics of authentic epidermis.

The epidermis is a multilayered epithelium which survive through a self-renewal process. Keratinocytes forming from the epidermal basal layer are endowed with proliferative capacity [227], hence they regularly undergo mitosis, differentiation and upward migration to replace terminally differentiated cornified cells that are continuously shed into the environment. The human epidermis is thus completely renewed approximately every month. To accomplish this process and to face the emergency of wound healing, the epidermis relies on the presence of stem cells, namely cells that upon division replace their own number, generate transient amplifying cells and also give rise to cells that differentiate into one or more specialized cell types. Stem and transient amplifying cells are located both in the epidermal basal layer and in the hair matrix. The basic, essential and indispensable characteristic of a stem cell is its capacity for extensive self-maintenance with the potential for proliferative self-renewal extending for at least one lifespan of the organism. Conversely, the transient amplifying cell population, which arises from stem cells and will eventually generate terminally differentiated cells, has a high proliferative rate only for a limited period of time, represents the largest group of dividing cells and is probably of crucial importance in wound healing.

Using clonal analysis three types of keratinocytes have been identified, i.e. holoclones, meroclones and paraclones. The holoclone-forming cell is the smallest colony-founding keratinocyte, has the highest proliferative capacity and is the stem cell of the epidermis and the hair follicle. It soon became clear that the holoclone-forming keratinocyte is the stem cell of virtually all human squamous epithelia. Holoclones have all the hallmarks of stem cells, including self-renewal capacity, telomerase activity and long telomeres, and an impressive proliferative potential. A single holoclone can indeed generate the entire epidermis or the entire corneal epithelium of a human being. Holoclone-forming cells generate all the epithelial lineages of the tissue of origin, permanently restore massive epithelial defects and can be retrieved from human epidermis regenerated from cultured keratinocytes years after grafting. Finally, a defined number of genetically corrected holoclone-forming cells regenerate a normal epidermis in patients with genetic skin adhesion disorders. During its clonal evolution, the holoclone produces paraclone-forming cells, which have a very limited proliferative capability, generate aborted colonies containing only terminal cells and have the properties expected of TA cells. Meroclones have an intermediate proliferative and clonogenic potential and are a reservoir of paraclones [228].

Chapter 3

Experimental techniques

3.1 Atomic force microscope (AFM)

An AFM is essentially made of a micro/nanoscopic probe tip flying over the specimen under investigation, at a distance spanning in the nanometers range. The tip is mounted at the end of a flexible cantilever and it is scanned, in a raster fashion, in gentle touch with the sample. This relative motion is performed with sub-Angstrom accuracy by a piezoelectric actuator (usually a tube). Interacting with the sample the cantilever deflects and the tip-sample interaction can be monitored with high resolution exploiting a laser beam impinging on the back of the cantilever [229]. The beam is reflected towards a split photodetector configuring an optical lever which amplifies cantilever deflections. In almost all operating modes, a feedback circuit, connected to the cantilever deflection sensor, keeps tip-sample interaction at a fixed value controlling the tip-sample distance. The amount of feedback signal, measured at each scanning point of a 2D matrix, concurs to form a 3D reconstruction of the sample topography which is usually displayed as an image. In Figure 3.1 a scheme of an AFM is reported in a typical configuration for biological applications, where it is coupled with an optical microscope to simultaneously acquire an optical image and the surface topography [230].

3.1.1 AFM imaging modes

In describing the operating AFM modes usually we refer to the main interaction forces between the tip and the sample, coming from the Lennard-Jones interaction. Let recall that the force $F(z)$ depends on the potential $U(z)$ by the relationship

$$F(z) = -\nabla U(z) = -\frac{dU(z)}{dz} \tag{3.1}$$

Therefore, we can distinguish two different regimes, separated by z_0, the distance corresponding to a stationary point for the potential, U(z), and hence to $F(z_0) = 0$. For z values larger than z_0, the particle will experience

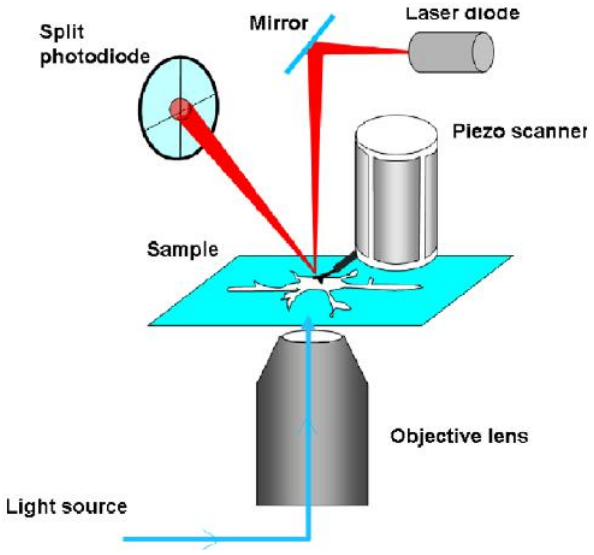

Figure 3.1: Scheme of an AFM coupled with an inverted optical microscope. Adapted from [230].

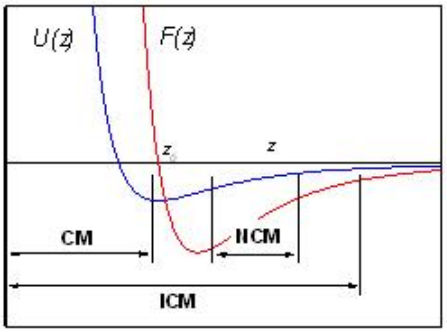

Figure 3.2: Distance dependence of Lennard-Jones potential $U(z)$ and force $F(z)$ *vs* tip-surface separation. The tip-surface separation ranges in the contact mod (CM), non-contact mode (NCM) and intermittent contact mode (ICM) are highlighted [229].

an attractive force, whereas for z values smaller that z_0, the force will be repulsive. As the force is the derivative of the potential, we can deduce that, because of the difference in the potential slope of the two regimes, the attractive forces will be considerably weaker than the repulsive ones, as shown in Figure 3.2.

Contact mode

Contact mode imaging is so called because the probe remains "in contact" with the sample all the time. Historically, the atomic force microscope was designed to exploit the strong short-range repulsive forces between a probing tip and the sample surface. The probe (tip) is brought into contact with the surface (hence the name) and repulsive forces result in the deflection of the

cantilever. In contact mode the sample surface can be scanned at constant force or at constant tip-sample distance.

In the first case the AFM feed-back loop keeps the cantilever deflection, and hence the force between the tip and the sample, constant. Before the scan starts, a setpoint, i.e. a deflection value of the lever that we want to keep constant during the imaging, is chosen. If the tip encounters a feature on the sample surface, the repulsive force varies, causing a bending of the lever. The feedback system compares the actual bending with the setpoint; if they do not coincide, the control system modulates the signal applied to the piezo so that the scanner retracts or extends in order to bring the deflection back to the setpoint. It is important to stress that, in this case, for the aim of sample topography reconstruction, the exact knowledge of the cantilever features is not necessary. In fact, the cantilever bending is measured in an indirect way, "measuring" instead the piezo displacement necessary to recover the initial position of the reflected beam over the photodetector. Therefore, topographical data are derived from the z-axis piezo voltage.

In the constant height mode the feedback system is almost switched off, so that z-height remains almost constant (in any case, low frequency signal are corrected) during the X-Y scanning, the photodetector output signal is converted in z values. This mode can be used only on samples which are relatively flat and smooth but, for surfaces to which it is applicable, it can provide images with a sharper resolution and in a shorter time compared to the constant force mode.

Non contact mode

In the non-contact mode the cantilever is never in contact with the sample, and the tip-sample forces are attractive. In this case the involved forces are much weaker than the contact mode case, and hence a more sensitive and sophisticated detection technique, instead of the bare cantilever displacement, is required. The non-contact mode is one of the two oscillating AFM modes. The cantilever is forced to oscillate through a bimorph that is placed at the base of the cantilever holder. The resonance curve of the cantilever in the free space is shown Figure 3.3 (red curve). While the tip approaches the surface, the cantilever vibration regime is affected by the presence of the interaction forces between the tip and the sample. This causes a shift in the resonance curve, whereas the oscillation frequency is locked to a working value slightly larger than the resonance frequency. When the tip approaches the sample, a reduction in the amplitude of vibration occurs (Figure 3.3, ΔA). During the image acquisition the feedback circuit attempts to restore the amplitude of vibration toward the setpoint slightly larger than the natural resonance. If the tip gets too close or too far to/from the sample the cantilever oscillation amplitude varies and, analogously to the previous case, the feedback system modulates the signal applied to the piezo-scanner so that it either retracts or extends in order to bring the cantilever oscillation amplitude back to the set point. The cantilevers used in

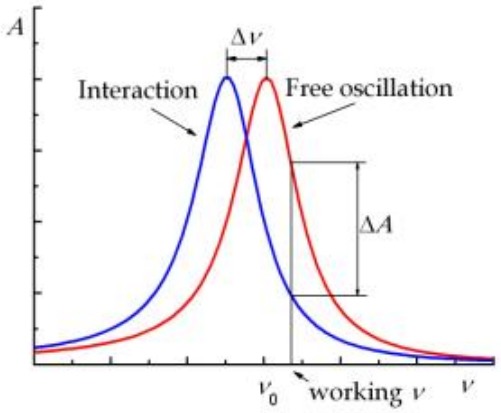

Figure 3.3: Calculated cantilever resonance curve in the free oscillation regime (red curve) and in presence of interaction (blue curve). From [229].

the non-contact mode are stiffer than those used in the contact mode to prevent the cantilever to get pulled into the sample.

Tapping mode

Intermittent, or tapping, mode is similar to non-contact mode in many ways, but the cantilever is vibrating $1 \div 10$ nm above the sample with a larger amplitude so that the tip hits the sample at the lowest point of each oscillation cycle. In this operating mode, the cantilever is excited at a frequency slightly lower than the mechanical resonance, and the topographical features are extracted using the amplitude modulation due to the forces generated by the intermittent interaction between the AFM tip and the sample. Tapping mode is possible at ambient temperature and in liquid; Tapping mode is the most used operating mode in biological applications of AFM. It is not disruptive for fragile samples since it eliminates completely friction forces between the tip and the sample that are dominant in contact mode. At the same time its resolution is better than in the non-contact mode, in which the tip is in average farer from the sample.

3.1.2 AFM spectroscopic modes

Nanoindentation involves the application of a controlled load to the surface to induce local surface deformation. Load and displacement are monitored during the loading and unloading, and mechanical properties are calculated using well-established equations mainly based on elastic contact theory. AFM can perform nanoindentations and thus measure the Young's modulus of materials on the nanometer scale. When the AFM tip is used as an indenter, a force curve can be obtained by recording the applied load on the tip with the corresponding penetration depth. The bending cantilever through which the load is applied is not usually stiff enough to indent metals or ceramic materials. For this reason, AFM nanoindentation is mainly useful to measure mechanical properties of soft matter, especially biological

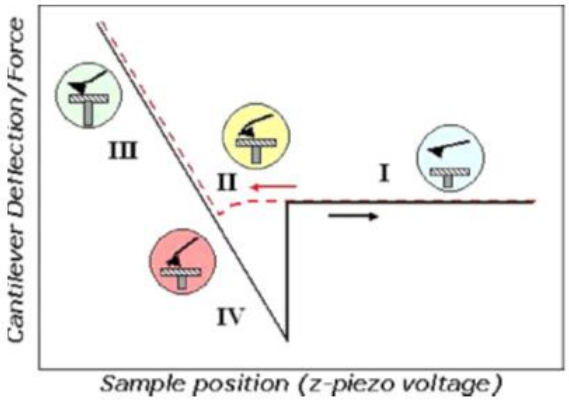

Figure 3.4: Scheme of a force curve with the different regions of the approach and withdrawal portions highlighted. The different regions are thoroughly discussed in the text. From [230].

materials [231] and polymers [232]. A typical AFM force curve consists in an approach-retract cycle between the tip and the sample during which the cantilever deflection is measured as a function of the relative motion. In Figure 3.4 a typical force curve is shown. It can be divided into several regions.

Starting from the right (region I) the AFM tip is far from the sample and no interaction is detected. Moving towards the left side of the plot (dotted curve), i.e. the tip is approaching the sample, no interaction is detected until the cantilever deflects towards the sample due to van der Waals forces (region II). These forces cause the tip to snap into contact with the sample. The 'jump to contact' point corresponds to the position where the gradient of the interaction force exceeds the cantilever spring constant. It is to be noted that at each position in the force curve the cantilever is deflected until its restoring force equals the interaction force with the sample, causing the system to be always at equilibrium. After the contact, approaching the tip further to the surface, a positive deflection of the cantilever arises (region III) due to repulsive forces. This is the contact region of the force curve, where elastic properties of the sample can be measured. Usually, the cantilever is moved towards the sample until a preset force threshold is reached. After this happens, the movement direction is inverted and the cantilever starts moving away from the sample (solid curve). Initially, the behaviour of the cantilever during withdrawal equals that described for the approach (in the absence of viscous effects), but, due to adhesion between the tip and sample, the cantilever starts to deflect negatively (region IV) until the adhesion force is overcome by the cantilever restoring force and the contact breaks. The hysteretic behaviour of curves measured in air is largely due to capillary forces arising from the thin water film wetting both probe and sample [230].

In a force-curve cycle the cantilever deflection is measured, but it can be converted to force using Hooke's law:

$$F = -kd \tag{3.2}$$

where F is the force, k is the spring constant of the cantilever and d is the cantilever deflection. Different methods of measuring the cantilever spring constant independently have been developed. Essentially they may be divided into four categories: (1) methods based on the cantilever geometrical factors [233]; (2) methods based on the measurement of a static deflection applying a known force to the cantilever [234]; (3) methods based on measuring dynamical properties with different masses on the cantilever (added mass method) [235]; (4) methods based on the thermal noise of cantilevers [236, 237]. The last method is the most widely used and it is the one employed in this work. The cantilever is treated as a simple harmonic oscillator excited by thermal noise. In this framework the noise spectrum has the form of a Lorentzian and the elastic constant is given by

$$k = {\omega_0}^2 \frac{k_B T}{\pi A} \tag{3.3}$$

where ω_0 is the resonant frequency of the cantilever, k_B the Boltzmann constant, T the temperature, A the oscillator strength [236].

Elasticity information on a biological sample can be obtained exploiting the approach part of the force curve. It is clear that, when the elastic constants of the cantilever and of the sample are comparable, once the tip is in contact with the sample, upon further approaching the sample will undergo indentation, resulting in a minor cantilever deflection for the same z-piezo movement with respect to an undeformable sample (Figure 3.5).

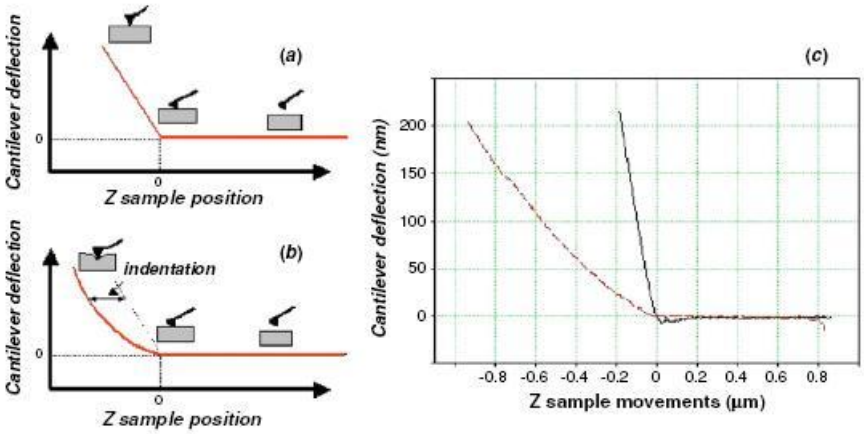

Figure 3.5: Indentation measurement by force-curve analysis. (a) Force curve on a rigid sample; (b) force curve on a soft sample. In this case the sample is indented and for the same cantilever deflection the z-piezo movement is higher than for the case of a rigid sample. (c) Comparison between two force curves performed on a living cell (dotted curve) and on the adjacent glass substrate (solid curve). The two curves have been aligned in order to have the same contact point. From [230].

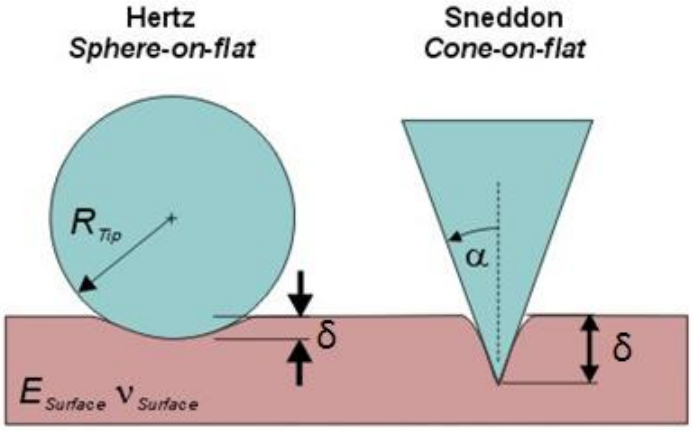

Figure 3.6: Left: the hard sphere on soft surface known as the Hertz model. Right: the rigid cone on soft surface model by Sneddon. From [243].

By measuring indentation at a given force, the local elasticity of the sample in terms of Young's modulus can be extracted, assuming a model for the tip-sample contact mechanics [238, 239, 240, 241].

The simplest data analysis occurs in the case of purely elastic deformation, where a direct fit of the force-indentation ($F - \delta$) data to the elastic indentation solution can be performed. The first model is the classic rigid sphere on flat surface, known as Hertz model. In this case, the elastic relationship is [242]:

$$F = \frac{4\sqrt{R}}{3}\frac{E}{1-\nu^2}\delta^{3/2} \tag{3.4}$$

where ν is the Poisson's ratio of the material, R is the tip radius and E is the Young's modulus of the surface.

The other model, derived by Sneddon, assumes a rigid cone indenting a soft flat surface. This model holds also in the case of a four-sided pyramidal indenter. In this case, the elastic relationship is [244]:

$$F = \frac{2}{\pi}tan\alpha\frac{E}{(1-\nu^2)}\delta^2 \tag{3.5}$$

where α is the pyramidal face angle, usually 45°. Both models do not include adhesion and visco-elasticity. The Hertz model is valid for indentations significantly smaller than the sphere radius, while for the Sneddon model the indentation has to be so large that the indenter apex can be considered infinitely sharp (Figure 3.6).

Force mapping

By collecting a set of force curves from many points on a sample, a two-dimensional map of the tip-surface interaction can be retrieved [245]. Typically, one force curve for each image pixel point is collected and the

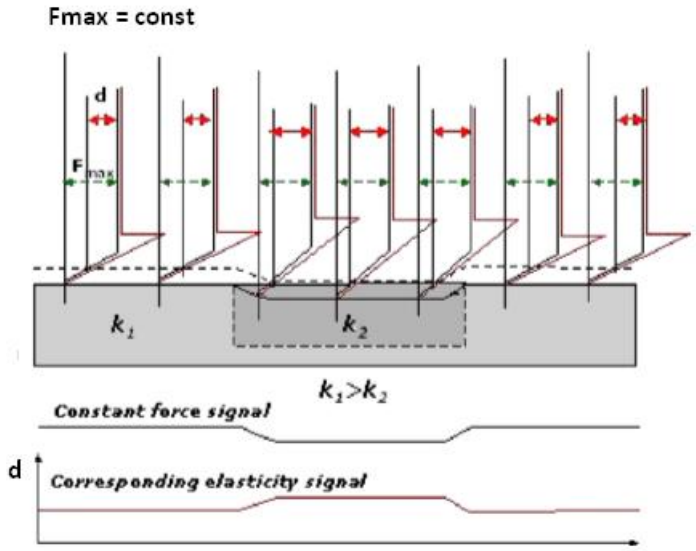

Figure 3.7: Operation scheme of the force volume technique on a sample with regions of different elasticity ($k_1 > k_2$). A single line of the image is illustrated. A set of force curves is collected reaching always the same force (deflection) threshold (indicated in the scheme as F_{max} using the no-interaction region as the zero force reference. The z-piezo extension needed to reach the threshold is different for the regions of different elasticity. The values for the z-piezo extension are exploited to obtain the usual constant force image, whereas by taking the cantilever deflection values (indicated as d in the scheme) at a constant distance from the surface (dotted line near the sample surface) the corresponding elasticity map can be reconstructed. Note that the slope of the contact region in the force curves is different for the areas of distinct elastic properties. From [230].

force curves may be analyzed both individually and collectively. The force curves as a whole form a three-dimensional *force volume* [237, 238]. In the force volume a two-dimensional matrix of force curves is acquired. Each force curve can be assigned to a defined pixel of a topographic image acquired at the same time as a result of the z-position at which a predefined force setpoint is reached. Recording all the force curves it is possible to recover a map of the cantilever deflection at a specific constant distance from the point of maximum applied force, which in the case of a rigid sample means a constant distance from the sample surface. In Figure 3.7 a representative line scan of a force volume image is depicted. From the value of the cantilever deflection at a given distance from the point of maximum force, the elasticity map of the sample can be recovered.

In the present work, the most important application of the force volume technique regards 2D mapping of the elastic properties of living cells. Different regions of a cell present generally different elastic behaviour that can be mapped with a lateral resolution down to 50-100 nm [230]. The low value for the lateral resolution on a living cell, compared to the high-

resolution capabilities of the atomic force microscope, is a consequence of the low elastic moduli of living cells (1-150 kPa) [246]. The low stiffness of living cells leads to a high indentation of the tip in the cell membrane and a large contact area which limits resolution. In other words, the usual obtained topographical image represent a convolution of the properties of the sample and the tip.

Moreover, when using AFM contact mode, the set point given by the operator is related to a certain position of the deflected beam in the photodiode a may not reflect a 'true' constant force applied to the sample; this is because the photodiode signal that corresponds to a free cantilever deflection (out of contact, zero force) may drift with time: as a consequence, while images are taken at constant deflection, they may not be taken at constant force [247].

All these evidence point out the necessity to reconstruct the so called zero loading force map, i.e. the height image at zero force. Unfortunately, determining the zero point (the point of the tip-sample contact) in the force-distance curve is not easy on soft samples because they do not show a sharp increase in the cantilever deflection. To overcome this problem, the equation describing the relation between the height of the sample, the cantilever deflection and the other sample parameters can be exploited to obtain a set of equations that can be inverted to obtain at the same time both the elastic modulus and the height offset representing the zero point [110]. To do so, a home-developed C++ software was employed (see Force Mapping section in Chapter 4 for more details).

3.1.3 Colloidal force spectroscopy

Regular AFM probes are fabricated from silicon or silicon nitride with typical radii of 10-20 and 20-30 nm, respectively. Silicon nitride probes are preferred for very stiff surfaces (the elastic modulus higher than 3 GPa). For these probes, at regular forces exerted during probing mechanical properties the diameter of the contact area usually does not exceed 1-3 nm and thus mechanical or adhesive properties can be probed with near-molecular resolution [248]. However, the use of these highly hydrophilic tips is generally feasible for relatively stiff materials (usually with the elastic modulus higher than 1 MPa) with nonhydrophilic and low-adhesive surfaces. In the case of hydrophilic, highly compliant materials (e.g., hydrogels) with sticky surfaces, regular tips are prone to contamination and easy piercing. In these cases, colloidal probes and chemically modified tips should be used.

Colloidal probes [249] are fabricated by carefully gluing microspherical particles onto the end of a tipless cantilever [250]. The microparticles are available through several commercial sources and colloidal probes themselves are commercially available as well. Microparticles with a diameter of a few micrometers from silica and borosilicate glass are most commonly used and have roughness below 1 nm for a square micrometer area, acceptable for most measurements of soft materials. Force spectroscopy performed

with such probes is usually called colloidal force spectroscopy (CFS). The colloidal probes have several advantages over conventional probes for very compliant materials. A major advantage is that the applied forces per a unit area are significantly lower than conventional probes, thus allowing for probing very compliant materials such as hydrogels with the elastic modulus well below 1 MPa and down to a fraction of kPa and even few Pas [251]. By applying less force per unit area, the total applied force can be much higher without plastically deforming the surface or damaging the probe, which provides higher resolution in force/area per a force curve by sacrificing lateral spatial resolution. The preservation and well-defined tip shape allow for very good analysis with contact mechanics models that assume spherical shape of the probe.

The process we exploited to obtain a colloidal spherical probe involves different steps and the protocol employed in this work is reported in the Materials and Methods section (Chapter 4).

3.1.4 AFM based rheology

Rheology is principally concerned with extending continuum mechanics to characterize flow of materials, that exhibits a combination of elastic, plastic and viscous behavior by properly combining elasticity and (Newtonian) fluid mechanics. A material is called *elastic* when it is capable to deform to a defined extent in response to a stress and then return to its original shape when the force is removed. During an elastic deformation, the covalent and non-covalent bonds in the atoms are not broken, but only displaced from their equilibrium distance due to the applied external force, and they recover their initial state as soon as the force is removed. On the other hand, under a large deformation regime, which means that the force is too strong or the bonds are too weak, some of the covalent and non-covalent bonds break: as a consequence, the original equilibrium state of the system can no longer be completely restored and its shape is permanently changed. This irreversible process is termed *plastic deformation*.

Viscosity is the measure of resistance of a fluid or fluid-like system to flow movement. Here, the interactions among constituent molecules are weak and the intermolecular bonds are therefore broken and formed again continuously. As a result, the consequences or 'memory' of a particular stress are limited to a short duration of time.

Soft materials which exhibit a contribution of fluid-like viscosity in addition to elasticity are callded *viscoelastic*. Their mechanical properties depend on the time scale of force application: if the force is applied for a brief duration their behavior is almost solid-like and the elastic contribution is predominant; on the other hand, if the force is applied slowly they behave like vicous fluid-like systems. Ultimate goal of rheology experiments is to quantify dynamic viscoelasticity and relate it to material structure.

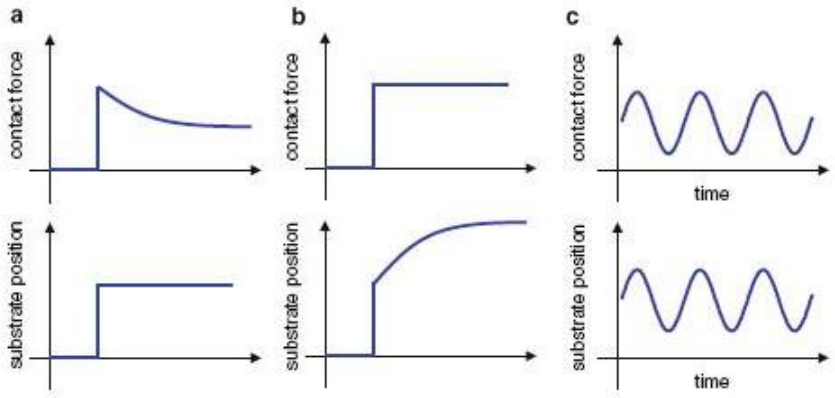

Figure 3.8: Schematics of AFM rheology measurements: (a) stress relaxation, (b) creep relaxation and (c) force modulation mode.

3.1.5 Force (creep) relaxation experiments

The use of force-time curves, instead of force-distance curves, makes it possible to measure the viscoelastic properties of biological samples [252].

When the AFM tip is brought into contact with the sample's surface for a definite time period, two type of experiments are possible (Figure 3.8). In the so-called constant height mode (Figure 3.8 (a)), the cantilever's vertical position is set constant while the cantilever's force varies with time. In the constant force mode (Figure 3.8 (b)) the vertical position of the piezoelectric changes with time while the cantilever's force is kept constant. The first case deals with *force relaxation* tests (which is the one employed in this work) while the second case resembles *creep compliance* tests.

Performing stress relaxation experiments means to control with great accuracy the position of the piezoelectric, which should be constant during the experiment. However, our set-up do not allow a feedback control on the displacement of the piezoelectric: as a consequence, the performed measurements have been rescaled after a proper calibration on a rigid sample.

Monitoring the stress-relaxation response to a prescribed displacement is a common method of determining the viscoelastic characteristics of a material. In this AFM-based study, the stress rerelaxation data were fitted with the poroelastic model, which will be described in detail in the next Paragraph.

3.1.6 Poroelastic model

In the framework of this project, the poroleastic model have been employed in order to analyze stress relaxation curves obtained on fibrin samples. This model applies to gel that aggregates a network of crosslinked polymers and a species of mobile solvent molecules. The deformation of the gel is time-dependent, resulting from following two concurrent molecular processes: the conformational change of the network, and the migration of the solvent molecules. At a macroscopic scale, the two processes result in

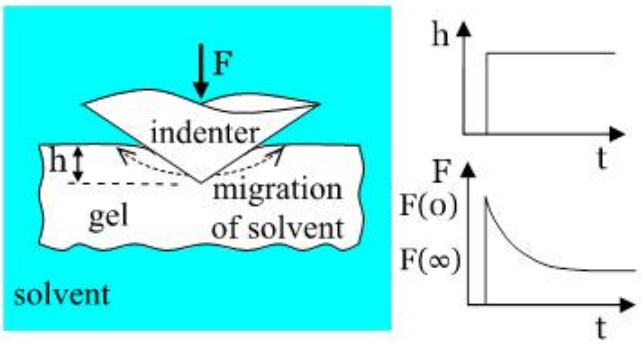

Figure 3.9: A gel submerged in a solvent. After an indenter (i.e. AFM tip) is pressed into the gel at a fixed depth, the solvent in the gel migrates, and the force on the indenter relaxes. From [253].

viscoelastic and poroelastic deformation. So long as the mesh size of the network is much smaller than the contact size of the indentation, the viscoelastic relaxation time is independent of the contact size. By contrast, the poroelastic relaxation time is quadratic in the contact size. Thus, the two types of deformation can be differentiated by indentation by using indenter of different size and different indentation values.

As illustrated in Figure 3.9, a gel is submerged in a solvent of chemical potential μ_0. After an indenter is pressed into the gel to a fixed depth h, the force on the indenter relaxes as a function of time, $F(t)$. At the instance of indentation, the solvent has no time to migrate, so that the gel behaves like an incompressible elastic solid, and the instantaneous force is the same as the force of an indenter pressed into an incompressible elastic solid, $F(0) \propto G$, being G the elastic shear modulus, which is defined as the ratio of shear stress to shear strain. After a certain amount of time, the solvent in the gel equilibrates with the external solvent, $\mu = \mu_0$ so that the gel behaves like a compressible elastic solid, and the force in equilibrium is the same as the force on an indenter pressed into a compressible elastic solid, $F(\infty) \propto G/[2(1-\nu)]$. The two limits are related as $F(0)\ /\ F(\infty) = 2(1-\nu)$. Figure 3.10 lists the formulas of $F(0)$ for indenters of several types [253].

For the gel to equilibrate, the solvent in the gel needs to migrate over a distance comparable to the size of the contact, a. At time t, the solvent migrates over the length scale $\sqrt{Dt}$. Write the function $F(t)$ in the form:

$$\frac{F(t) - F(\infty)}{F(0) - F(\infty)} = g\Big(\frac{Dt}{a^2}\Big) \tag{3.6}$$

where $\tau = Dt/a^2$ is called *normalized time*, and $g(\tau)$ is a dimensionless function specific to the type of the indenter obtained by finite element analysis. The ratio on the left-hand side measures how far the gel is away from the state of equilibrium. Equation 3.6 and relation $F(0)/F(\infty) = 2(1-\nu)$, along with the expressions for $F(0)$ and $g(\tau)$ in Figure 3.10, lead to a simple method to extract the three poroelastic constants, the shear modulus

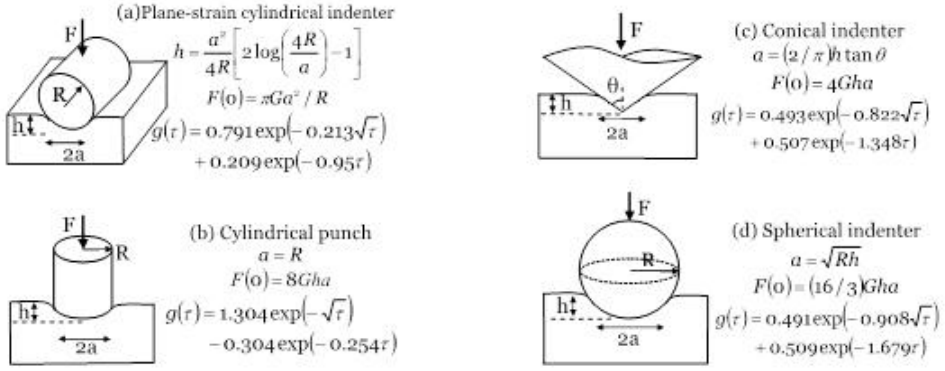

Figure 3.10: Indenters of several types pressed into a gel. From [253].

G, the Poisson's modulus ν, and the diffusivity D, from an experimentally measured relaxation curve $F(t)$. The measured value $F(0)$ determines G. The measured ratio $F(0)/F(\infty)$ determines ν. The measured curve $F(t)$, when matched to Equation 3.6, determines D. The diffusivity D is related to the permeability k by the expression

$$D = \frac{2(1-\nu)}{1-2\nu}\frac{Gk}{\eta} \tag{3.7}$$

where η is the viscosity of the solvent. Once known the permeability, the average pore size of the medium can be found by exploiting a relation derived by Carr and Hardin [254]:

$$R_p = \frac{0.5093}{k^{-1/2}} \tag{3.8}$$

In AFM stress relaxation experiments, the cantilever defection and the corresponding indentation both change during the measurement time. This situation is different from conventional stress relaxation measurements where the strain (and indentation) is kept at constant value and the stress is measured as a function of time. In experiments of soft materials like gels or cells, the change in the indentation value is typically about 1-5 % of that for the overall indentation (as reported in Figure 3.11). Therefore, it can be assumed that the indentation remains constant during relaxation experiments.

3.1.7 Indentation modulation

A convenient approach to take into account the different contributions of elastic and viscous components in the response of a system is to consider a dynamic oscillatory stress and evaluate the consequent strain. This is justified by the fact that for a purely elastic materials stress and strain occur in phase, so that the response of the second occurs simultaneously with the first; by contrast, in purely viscous systems the resoinse shows a

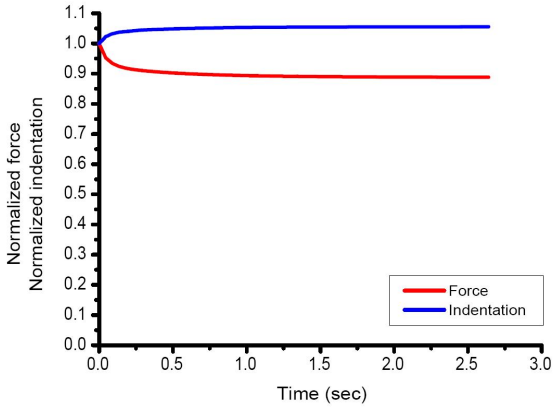

Figure 3.11: In stress relaxation experiments on fibrin the indentation can be considered constant, since a typical variation of only 1-5% is observed.

phase lag of 90°. Viscoelastic materials therefore exhibit an intermediate behavior resulting in a phase lag between 0° and 90°. As a consequence, it is possible to write the stress and the strain the system undergoes in a sinusoidal form, with a different amplitude but the same angular frequency ω and a phase shift ϕ representing the lag caused by the viscous contribution (Figure 3.12):

$$\gamma(t) = \gamma_0 sin(\omega t) \tag{3.9}$$

$$\sigma(t) = \sigma_0 sin(\omega t + \theta) \tag{3.10}$$

According to Robert Hooke's description of ideal elastic behavior of a solid, the elongation of a system is proportional to the load imposed on it. This statement results in a linear relation between stress and strain. For a normal stress

$$\sigma = E\epsilon \tag{3.11}$$

where E is called *Young's modulus* or tensile modulus. A similar equations holds for a shear stress

$$\sigma = G\gamma \tag{3.12}$$

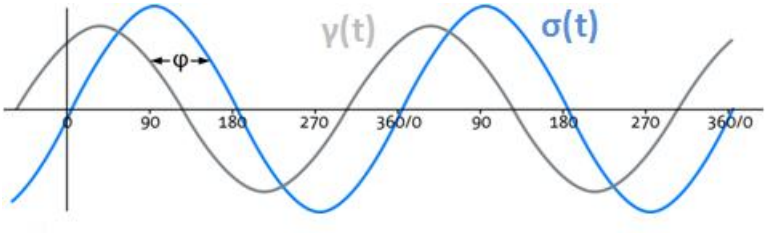

Figure 3.12: Phase shift between stress and strain sinusoidal signals.

where G is termed *shear modulus*. The domain of validity of these equations is limited to the case of small strain, otherwise plastic deformations can occur. It is possible to generalize Equation 3.12 with an appropriate redefinition of the shear modulus capable of taking into account the two mentioned sinusoidal contributions:

$$\sigma(t) = G^*(\omega)\gamma(t) \tag{3.13}$$

G^* (ω) is termed *complex shear modulus* and is defined as complex quantity dependent on frequency

$$G^*(\omega) = G'(\omega) + iG''(\omega) \tag{3.14}$$

where the real part

$$G'(\omega) = |G^*(\omega)|cos(\theta) \tag{3.15}$$

is called *storage modulus* and is related to the elastic properties, while the imaginary part

$$G''(\omega) = |G^*(\omega)|sin(\theta) \tag{3.16}$$

is termed *loss modulus* and represents the viscous contribution. When the phase lag θ takes the extreme values 0° and 90°, the purely elastic and viscous cases are respectively recovered. A further parameter can be introduced, namely the *loss tangent* η defined as:

$$\eta = tan(\theta) = \frac{G''}{G'} \tag{3.17}$$

The loss tangent provides a measure of solid-like ($\eta \ll 1$) or fluid-like ($\eta \gg 1$) behaviour of the system. For low-amplitude oscillations around an operating indentation δ_0 Equation 3.5 can be approximated by taking the first term of the Taylor expansion [256]:

$$F - F_0 \simeq \Big(\frac{3\delta_0 tan\alpha}{2}\frac{E}{1-\nu^2}\Big)(\delta - \delta_0) \tag{3.18}$$

Expressing the last equation in term of the shear modulus $G = E/2(1+\nu)$ [257] and solving it for G,

$$G = \frac{1-\nu}{3\delta_0 tan\alpha}\frac{F - F_0}{\delta - \delta_0} \tag{3.19}$$

This equation can be transformed to the frequency domain through the use of the correspondence principle [258], thus providing an expression for $|G^*(\omega)|$

$$|G^*(\omega)| = \frac{1-\nu}{3\delta_0 tan\alpha}\frac{F(\omega)}{\delta(\omega)} \tag{3.20}$$

3.1.8 Power-law rheology model

In the last section, we saw that for a viscoelastic material subject to oscillatory loading, the storage modulus and loss modulus capture the in-phase versus out-of-phase resistence to stress, respectively. For many viscoelastic materials, these moduli depend on the frequency of loading. Furthermore, the frequency dependence for each modulus may be different, such that the relative amount of in-phase versus out-of-phase deformation changes at different frequencies. Such frequency dependence is common in many biological materals, including cells.

A variety of models have been proposed to capture this frequency dependence. One such approach involves modeling in frequency dependence of the storage and loss moduli as power laws. For instance, the following relation has been demonstrated to accurely describe the stiffening of cells subjected to oscillatory loading over several orders of magnitude:

$$G^*(\omega) = G_0\left(\frac{\omega}{\Phi}\right)^{\alpha}(1+i\xi)\Gamma(1-\alpha)cos\left(\frac{\pi\alpha}{2}\right) + i\mu\omega \tag{3.21}$$

where

$$\xi = tan\left(\frac{\pi\alpha}{2}\right) \tag{3.22}$$

and

$$\Gamma(n) = (n-1)! \tag{3.23}$$

G_0 is a parameter that gives the frequency-indipendent component of the elastic response, Φ is a normalization factor, ξ is a structural damping coefficient, μ is a viscous coefficient, and α is the scaling exponent. The real part of G^* is the storage modulus G', and the imaginary part is the loss modulus G''. The coeffcients μ and ξ represent distinct viscous components; the term $i\mu\omega$ is meant to ensure that regardless of the scaling exponent α, high-frequency stimuli will result in viscous effects dominating the behavior. The ξ term is much larger than the μ term for most relevant frequency ranges, and in most cases is the primary contributor to the loss modulus. The scaling exponent determines not only ho G' and G'' change with frequency but the relative magnitudes of each modulus. If we assume that μ is small, we can see that as α approaches zero, ξ approaches zero as well, and G^* approaches G_0, which gives the elastic component of the response. However, as α approaches one, ξ increases without bound, indicating that the imaginary term will dominate and the material will exhibit strongly viscous effects.

Experiments in a variety of cell types and using various techniques for mechanical loading have demonstrated that cells exhibit a scaling exponent of around 0.2-0.3 [255, 259]. This power law dependence (Figure 3.13) is typical of a class of materials called soft glassy materials, which includes materials such as emulsions, slurries and pastes. Soft glassy materials are characterized by their possession of some degree of disorder in which the

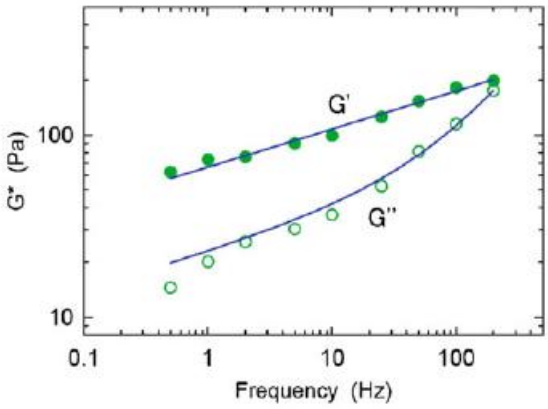

Figure 3.13: Storage modulus G' and loss modulus G'' of adherent mouse fibriblast cells. From [259].

discrete elements of which they are composed are entangled or aggregated via weak interactions.

3.2 Microaspiration Technique (MAT)

Microaspiration provides a simple and highly reproducible method to estimate the stiffness/deformability of the lipid bilayer by applying negative pressure to a liposome and measuring membrane deformability in response to well-defined pressure [260]. It was first developed by Mitchison and Swann in 1954 to characterize the elastic properties of sea-urchin eggs to provide insights into the mechanisms of cell division [261] and then to look at the mechanical properties in red blood cells [262].

In this work the microaspiration set-up is used to measure the mechanical properties of the lipid bilayer and the effects of the neurosteroids on them. The mechanics of the bilayer can be described by two important parameters: the *stretching constant* and the *bending constant*. The stretching constant describe the energetic cost to change the area of the bilayer, while the bending constant is related to the energy which is necessary to curve the bilayer surface.

By performing MAT, the applied pressure difference when a liposome is sucked by the micropipette can be converted to lateral tension in the lipid bilayer once the outer vesicle diameter and the internal diameter of the pipette are known. The conversion is made by the Laplace equation

$$\tau = \frac{\Delta P}{2}\left(\frac{r_p}{1-\frac{r_p}{R_v}}\right) \tag{3.24}$$

where τ is the lateral tension in the bilayer (in N/m), r_p is the internal diameter of the micropipette, ΔP is the pressure difference and R_v is the external vesicle radius (Figure 3.14). If the length of the bilayer projection inside the micropipette L is measured as a function of time or as a function

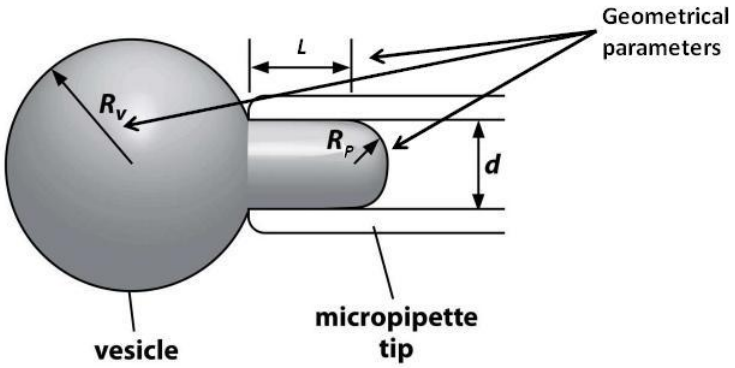

Figure 3.14: Schematic picture of a vescicle during the aspiration process. Geometrical parameters highlighted in figure are necessary to evaluate the mechanical behavior of the sample.

of the applied lateral tension to the lipid bilayer it is possible to measure the relative increase of the bilayer area α as reported in

$$\alpha = \frac{A - A_0}{A_0} = \frac{2\pi r_p}{A_0}\Delta L\Big(1 - \frac{r_p}{R_v}\Big) \tag{3.25}$$

the applied lateral tension and the relative area variation are linked by the Helfrich constitutive

$$\alpha = \frac{k_B T}{8\pi k_c} ln\tau + \frac{K_{app}}{\tau} \tag{3.26}$$

where k_B is the Boltzmann constant, k_c is the bilayer bending modulus, τ is the tension in the lipid bilayer and K_{app} is the apparent stretching constant. The K_{app} value obtained by Equation is defined as the "apparent constant" because it includes also sub-visible fluctuations of the lipid bilayer at high applied tension. At low applied tension (Figure 3.15 (a)) the first term of Equation 3.26 dominates (entropic regime) and it can be used to derive the bending constant from a plot of the natural logarithm of the lateral tension as a function of the relative deformation. However, sub-visible contributions to the projected area coming from the suppression of undulations with very small amplitudes are present also in the high-tension region (enthalpic regime, Figure 3.15 (b)). These contributions are particularly relevant for small values of the bending constant and can be taken into consideration by a procedure described in [265]. Briefly, in those cases where the entropic elasticity was evident, the apparent stretching constant was corrected for the effective one by defining a 'real' (to distinguish from the 'apparent' one, which is substantially a projection) relative area variation for each pressure step:

$$\alpha_{real} = \alpha(i) + \Delta\alpha(i) \tag{3.27}$$

being $\Delta\alpha(i)$ the correction due to fluctuations:

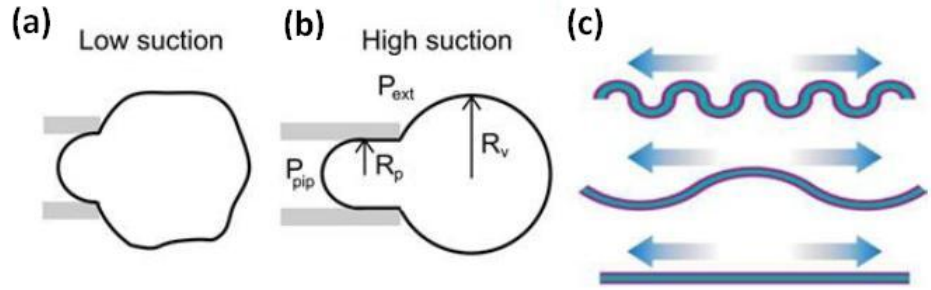

Figure 3.15: (a) At low applied tension fluctuations are clearly visibile, the entropic regime dominates and the bending constant can be calculated; (b) at high tension the enthalpic regime is approached, but sub-visible fluctuation may still be present: the stretching constant can be calculated after the correction which accounts for the flactuations; (c) representation of the stretching of a folded surface.

$$\Delta\alpha(i) = -\frac{k_B T}{8\pi k_c} ln \frac{\tau_i}{\tau_0} \tag{3.28}$$

where $\tau(i)$ is the tension relative to the i step and τ_0 is the reference value for the tension after which the enthalpic regime is supposed to start (usually higher than 1 mN/m). After that correction, a stretching constant K_s can be obtained by fitting the relation

$$\tau = K_s \alpha_{real} \tag{3.29}$$

Chapter 4

Materials and methods

4.1 Experiments on lipid bilayers

4.1.1 Experiments on supported lipid bilayers

Preparation of supported lipid bilayers

The lipids 1,2-dioleoyl-sn-glycero-3-phosphocholine (DOPC), Sphingomyelin (Brain, Porcine) (bSM) and cholesterol were purchased from Avanti Polar Lipids (Alabaster, USA) and used without further purification. Specific lipid mixtures were prepared by mixing chloroform lipid solutions in the desired molar amount. Chloroform was then evaporated under a flow of nitrogen while being heated in a water bath at $50°C$. Thereafter, the sample was kept under vacuum (10^{-2} $mbar$) for at least 2 hours in order to remove the remaining chloroform. Then lipids were rehydrated in a buffer solution (150 mM KCl, 8 mM Hepes, pH 7) to obtain a lipid concentration of 0.12/0.06 mg/ml. The sample was sonicated at room temperature for 15 min resulting in a homogenous lipid suspension. SLBs were prepared by the vesicle fusion technique [153, 154, 266]. Briefly, immediately after sonication of the lipid suspension, 70-100 μl of the suspension was deposited onto a freshly cleaved mica sheet (SPI Supplies/Structure Probe, Inc., USA) fixed on a PTFE disc attached to a metal disc. The lipid suspension was incubated for 15 min at a temperature above $40°C$ and then the sample subjected to extensive rinsing with the imaging buffer. The sample was then slowly cooled to $25°C$.

Neurosteroid injection

Allopregnanolone (Allo) and Pregnenolone Sulfate (Preg-S) were purchased from Sigma-Aldrich, iso-Allopregnanolone (isoAllo) was a kind gift from Dr A.Guidotti. Small amounts of the neurosteroids (NSs) (10^{-6} M concentration in the same buffer used for AFM imaging, diluted from a 10^{-2} M DMSO solution) were injected in the imaging chamber in order to reach the desired final concentration. After each injection, we waited for about 10-15 min in order to reach an equilibrium condition for the bilayer

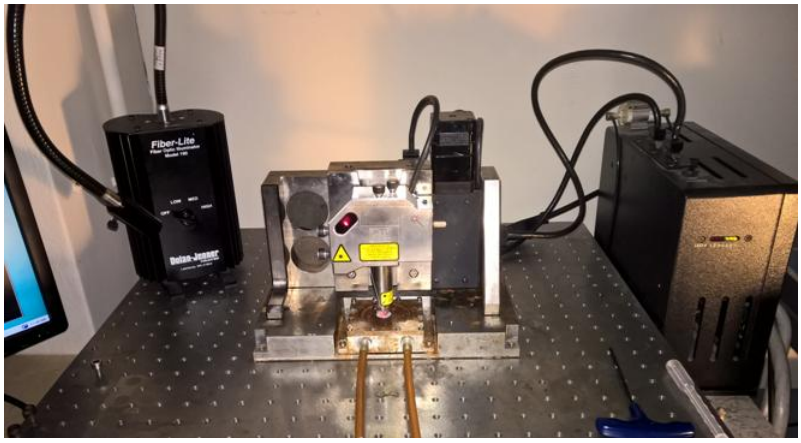

Figure 4.1: Set-up for experiments on supported lipid bilayers.

before acquiring images. It is important to stress that control experiments on lipid bilayer patches prepared in the same conditions but not exposed to NSs conserved good time stability in their properties. All the reported variations after the insertion of the exogenous molecules are therefore ascribable in large part to their effect on the bilayers.

Atomic force microscopy

Atomic Force Microscopy imaging was performed with a Bioscope I microscope equipped with a Nanoscope IIIA controller (Veeco Metrology, USA) (Figure 4.1). We used a temperature-controlled stage based on a circulating water bath on which we could mount the Bioscope head. The sample temperature was continuously monitored by a digital thermometer Fluke 16 (Fluke, Italy) equipped with a small K-thermocouple probe (Thermocoax GmbH, Germany) in direct contact with the imaging buffer. The stability of the temperature is assured within $\pm$ 0.3 °C of the specified temperature value. Triangular silicon nitride cantilevers (Bruker DNP-S) with nominal spring constant of 0.24 N/m and resonance frequency in liquid of $\simeq$ 8 kHz were used for tapping-mode imaging whereas cantilevers with a nominal spring constant of 0.06 N/m or 0.24 N/m were used for Atomic Force Spectroscopy (AFS). Typical tip radii are of about 20 nm. The elastic constants used to convert deflections into forces were determined by the thermal noise method [236, 237]: briefly, when not in contact, the free oscillation (i.e. the deflection due to thermal noise) of the cantilever is recorded with a duration of 1 sec and a resolution of 4 μs for a total of 250.000 data points. By employing a home-developed software, the power spectral density (PDS) of the thermal noise signal is calculated; accordingly, by fitting the peak corresponding to the fundamental resonant mode with Equation 3.3 it is possible to calculate the elastic constant k (Figure 4.2).

All the images presented in this work have been obtained in liquid tapping-mode AFM. However, to confirm that the information we retrieved from this technique regarding the height difference among different domains

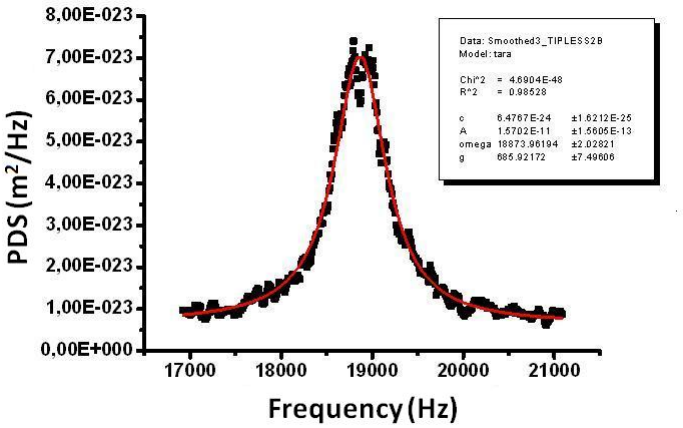

Figure 4.2: Fitting Equation 3.3 to the fundamental resonant peak allows to calculate the elatic constant k of the cantilever (thermal calibration method).

in the bilayer were not affected by imaging artifacts, we conducted comparative experiments by atomic force spectroscopy identifying the contact point of the AFM tip with the bilayer and the shared reference given by the position of the underlying mica substrate.

Figure 4.3 (a) reports a Tapping-Mode image of a lipid bilayer with liquid disordered and liquid ordered coexisting domain. The height measured from the AFM image is obtained from a line section as reported in Figure 4.3 (b). On the same sample area a Force Volume image was then obtained to detect the value of the jump-through force. Figure 4.3 (c) reports two force curves obtained on the liquid-disordered domain (red curve) and on the liquid-ordered domain (black curve). The two curves have been aligned considering the position of the underlying rigid substrate. The curves clearly show that the measured height difference in Contact Mode depends on the applied force. This behavior is a consequence of the different stiffness of the two domains highlighted by the slopes of the straight lines overlaid to the contact portion of the force curves. At the same time, it is clear that the height difference measured by Tapping-Mode AFM is very similar to the height difference that would be measured by Contact Mode AFM exploiting a stable applied force. Accordingly, the measured height differences reported in this work can be considered not too much affected by the force applied by the tip during imaging. Moreover, using Tapping-Mode AFM we can take advantage also of the phase signal which is a very sensitive signal able to detect different composition of the domains.

Images have been analyzed using the the ImageJ NIH softwares. The height difference between the domains was obtained from the distance between the maxima corresponding to the distribution of the pixel heights in each image (Figure 4.4).

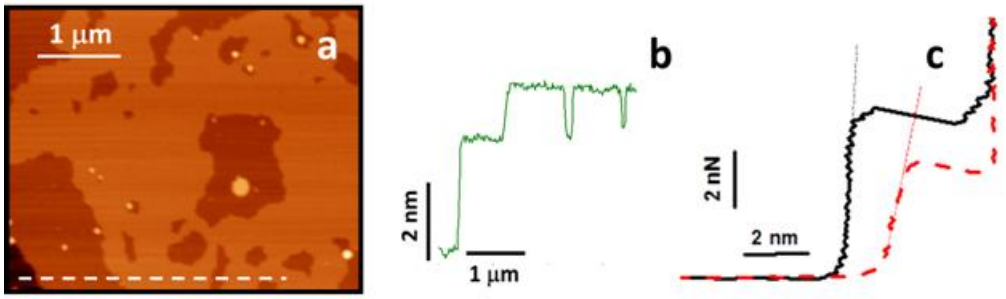

Figure 4.3: (a) Intermittent contact AFM image of a DOPC/SM/Chol lipid blayer in the region of liquid disordered and liquid ordered coexistence; (b) line section relative to the dashed white line in (a); (c) force curves measured on the liquid disordered domain (red dashed lne) and on the liquid ordered domain (black continuous line). The two force curves have been aligned to the position of the underlying substrate. The two lines highlight the slope of the contact portion of the two curves. The slopes point out different stiffness of the two regions.

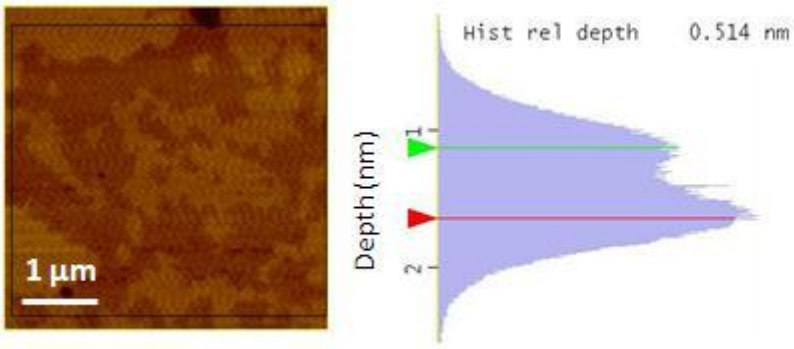

Figure 4.4: Example of the procedure used to measure the height difference between domains. The plot on the right represents the height distribution of the image on the left. The distance between the two maxima is used to obtain a value for the height difference.

Fourier Transform Infrared Spectroscopy FT-IR

To investigate the effect of Allo and isoAllo on the global lipid chain order of the bilayers we measured, as a function of temperature, the position of the maximum of the infrared absorption band of the symmetric -CH_2 stretching mode. This position ($\simeq 2850\ cm^{-1}$) is considered representative of the lipid acyl chain order and it is often exploited to investigate phase transitions in lipid bilayers. We measured the absorption spectrum of a lipid dispersion ($20\ mg/ml$) in deuterated water by transmission FT-IR (a typical example is reported in Figure 4.5). The cell was made by two CaF_2 windows separated by a 50 μm thick Teflon spacer. Before inserting the lipid dispersion in the transmission cell, the lipid dispersion was sonicated for 15 minutes. The sample temperature was controlled by circulating water from a heat bath. A previous investigation by FT-IR on a ternary lipid mixture [284] found that following the position of the maximum as a function of temperature, variations in the slope of the trend can be considered as markers for the modification of the phase state of the bilayer.

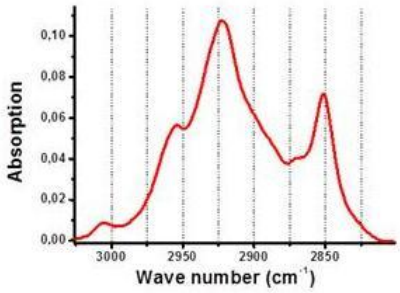

Figure 4.5: Typical IR spectrum for DOPC/bSM/chol 1:1:1 liposomes in the -CH stretching region.

4.1.2 Experiments on vescicles

Preparation of Giant Unilamellar Vescicles (GUVs)

Lipids 1,2-dioleoyl-sn-glycero-3-phosphocholine (DOPC), sphingomyelin (Brain, Porcine) (bSM) and cholesterol were purchased from Avanti Polar Lipids (Alabaster, USA) and were used without further purification. Specific lipid mixtures were prepared by mixing chloroform lipid solutions in the desired amount (the proportions used in this work are molar proportions). In this work GUVs were prepared by the usual electroformation method [172] with minor modifications. Briefly, lipid mixtures were suspended in chloroform and small drops (2-3 μL, 0.2 mg/mL total lipid) of the lipid mixture were deposited on two opposing Pt wires inside a PTFE chamber (Figure 4.6).

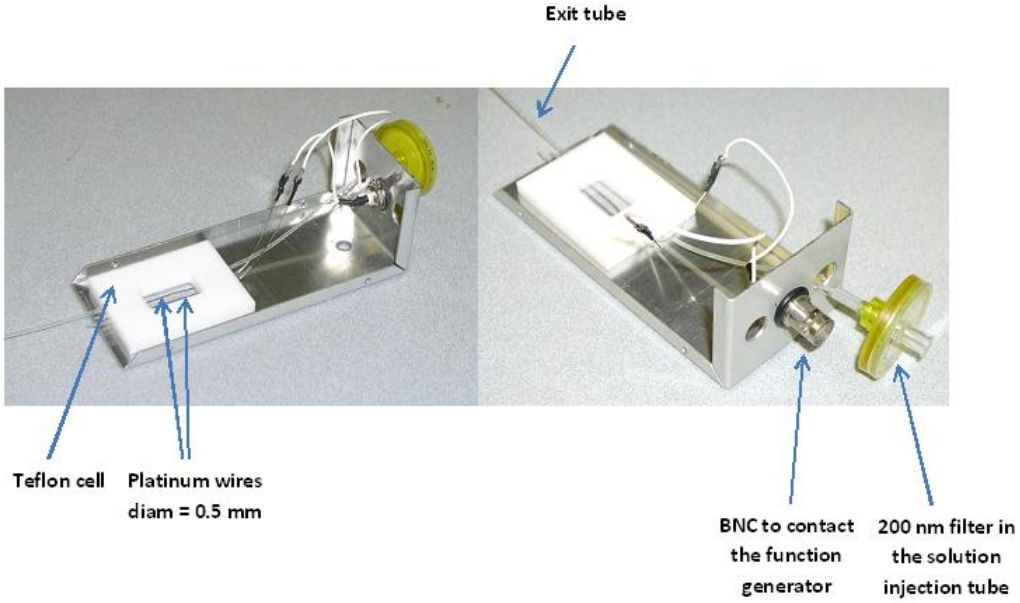

Figure 4.6: PTFE chamber used for the preparation of GUVs.

Phospholipid compositions in GUVs are expressed as mole ratios: e.g., DOPC/SM/Chol (1:1:1) denotes an equimolar ternary mixture. Chloroform was removed initially by exposing the Pt wires to a nitrogen flux and then by using a vacuum chamber (10^{-2} $mbar$) for 2 h. The two Pt wires were then connected to a wave form generator to produce a sinusoidal voltage potential difference. The PTFE chamber was then filled with a 100-200 mM sucrose solution and sealed using glass coverslips and vacuum grease. The applied electroformation protocol was as follows: (1) 10 Hz, 3.0 Vp-p for 45 min; (2) 5 Hz, 2.5 Vp-p for 20 min; and (3) 2 Hz, 1.5 Vp-p for 15-20 min. As the final step we applied a square wave of 5 Hz in order to promote vesicle detachment from the wires. After formation (Figure 4.7), GUVs were gently extracted from the PTFE chamber and resuspended in a 105-210 mM glucose solution. This procedure assures an increased contrast in Differential Interference Contrast (DIC) images acquired with an inverted optical microscope (Olympus IX70) and a conserved internal volume, at least on a short time scale (a few minutes).

Microaspiration and neurosteroid insertion

A picture of the complete set-up for micropipette aspiration is reported in Figure 4.8. Microaspiration was performed using pulled borosilicate glass capillaries to create a micropipette with an internal diameter in the order of 10-15 μm. The home-developed set-up for the prepatation of the pipettes is shown in Figure 4.9 (a). Pipettes were fire-polished (Figure 4.9 (b)) to ensure good membrane-pipette contact and pretreated with BSA (10 mg/mL) to avoid adhesion between glass and lipid bilayers. Each pipette was then connected to a pneumatic pressure transducer (Lorenz MPCU-3) to apply pressure differences between the internal side of the pipette and the exter-

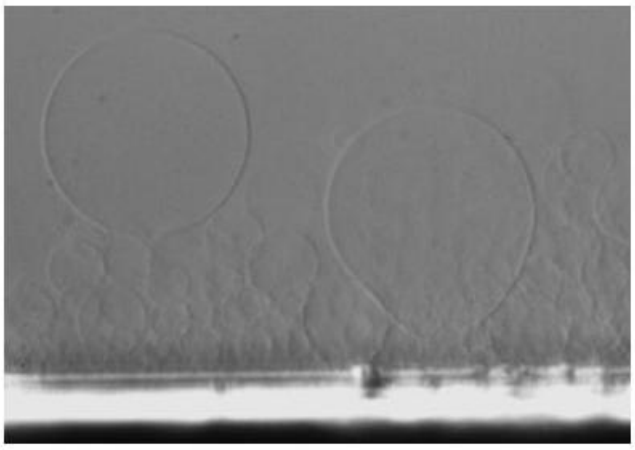

Figure 4.7: DOPC vesicles in the platinum wires electroformation chamber.

nal solution at the same height with a sensitivity of 1 mm H_2O ($\simeq 9\ Pa$). The pressure difference was applied by controlling the air pressure on top of a cylindrical tube containing the same external solution of the chamber containing the GUVs and initially kept at the right height to assure an initial negligible pressure difference. The vesicles were manipulated inside a home-made glass chamber. In response to pressure differences (between the internal pipette and the region just outside the pipette), the vesicle is aspirated into the pipette and the progressive membrane deformation (projection) can be measured as a function of the applied pressure difference or as a function of time at constant applied pressure.

When the values of the stretching constant as a function of the neurosteroids concentrations are reported, they refer to the behavior of the same vesicle. Accordingly, the first tension ramps are obtained up to a limited value of the tension (always in the region dominated by stretching deformation) in order to preserve bilayer integrity. The experimental errors were estimated on the basis of the measurement procedure for the geometrical characteristics of the liposomes. The error is mainly associated with the pixelation in the acquired digital image. We assumed for the geometrical parameters an error corresponding to one pixel ($\pm$ 1 pixel) and for the applied pressure difference an error of $\pm$ 0.5 $mm\ H_2O$. We then propagated the error in the calculation of the different parameters.

To study the kinetics of the interaction of the molecules with a lipid bilayer a fast perfusion system would be required (the measurement time should start with an already established constant concentration of the neurosteroid in the chamber). To circumvent this problem we assembled a cell with two chambers (Figure 4.10, for a close-up view of the injection system see Figure 4.11). The first chamber contains the vesicles in glucose solution while the second chamber contains the glucose solution plus a defined concentration of the neurosteroid at issue. A vesicle is grabbed by the micropipette and is then inserted inside a larger pipette filledwith the same glucose solution. All the chamber system is then moved and the vesicle

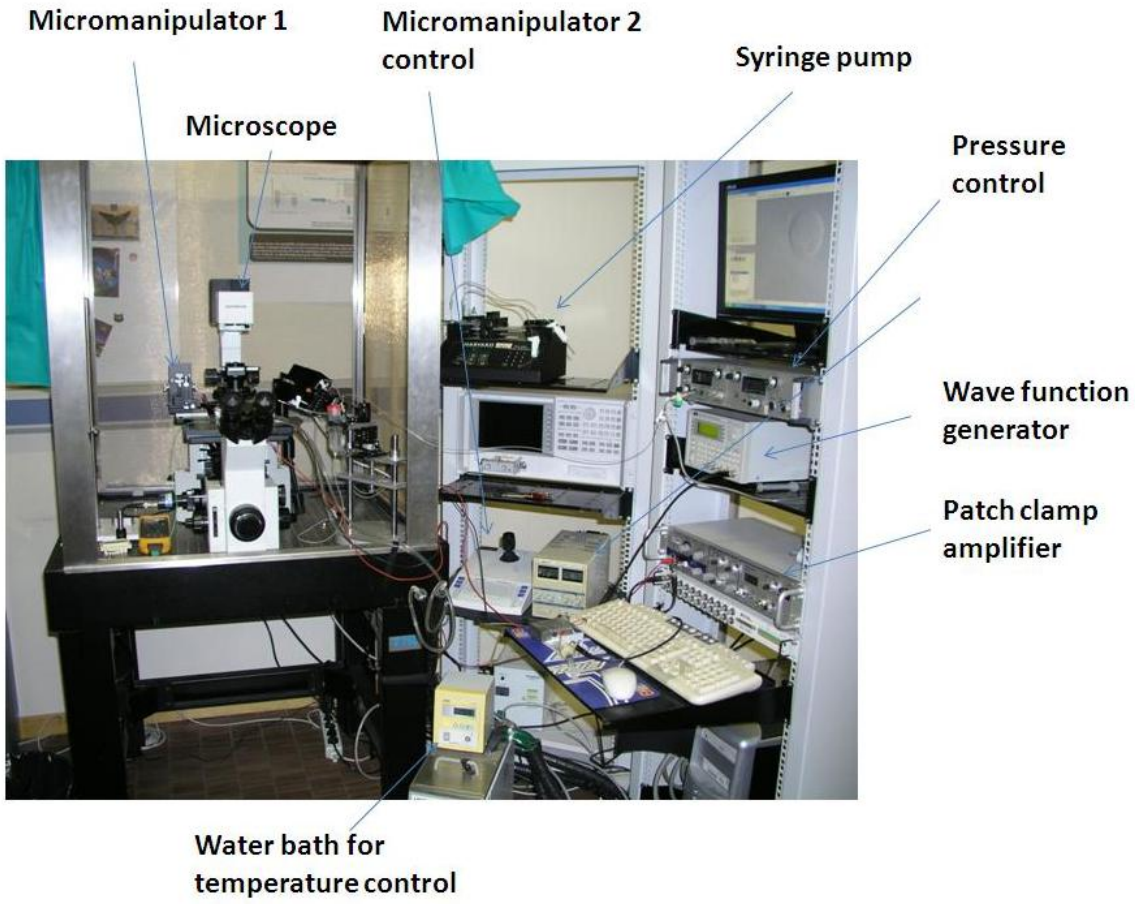

Figure 4.8: Picture of the complete set-up for micropipette aspiration.

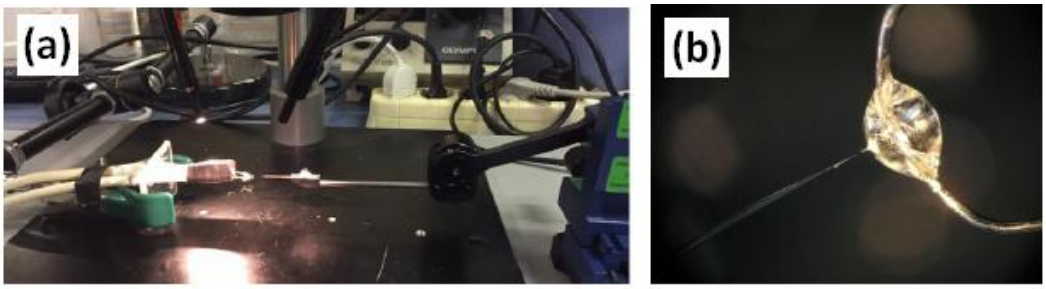

Figure 4.9: (a) Home-developed set-up for the preparation of micropipettes; (b) Micropipette fire-polishing step.

inside the big pipette is brought inside the chamber with the neurosteroid. The large pipette is then removed and this marks the start for measuring the uptake kinetics. In some cases, to study the kinetics of the release from the bilayer, at the end of the uptake step the vesicle is again included in the pipette and taken back to the first chamber. The removal of the large pipette marks the start of the desorption kinetics.

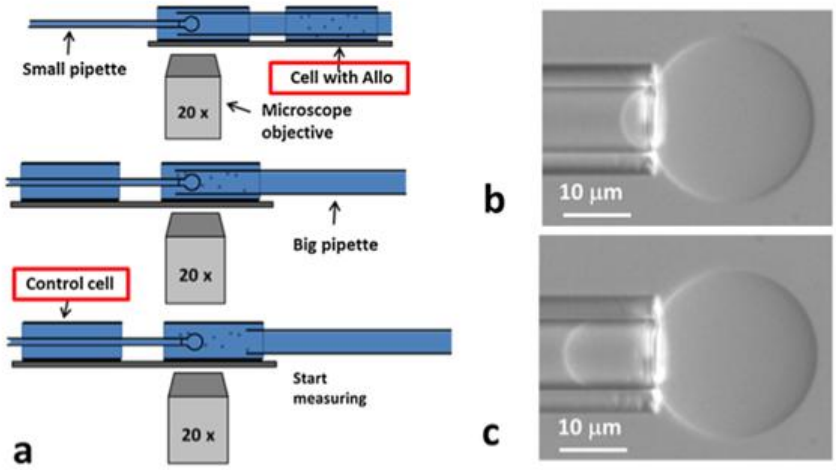

Figure 4.10: a) Scheme of the set-up used to measure the kinetics of neurosteroid uptake by the liposomes; b) Example for the case of uptake from a 100 nM Allo solution: DIC microscopy image of the initial configuration of the liposome; c) Configuration of the liposome after 10 min.

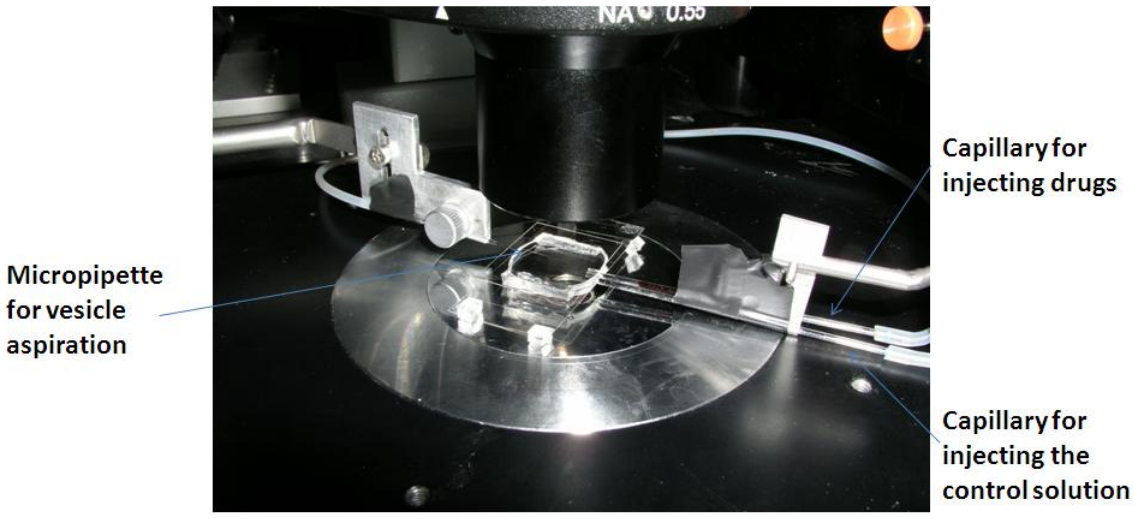

Figure 4.11: Close-up picture of the microaspiration injection system.

4.2 Experiments on nerve cells

Samples were kindly provided by Prof. Giulia Puja (Department of Life Sciences, UNIMORE).

Cell culture

Human neuroblastoma SH-SY5Y cells were maintained in culture in DMEM medium (Celbio, Milan, Italy) supplemented with 10% FCS, penicillin/streptomycin (100 U/ml pen, 100 mg/ml strep-Euroclone) at 37°C in 5% CO_2, 95% O_2 sterile atmosphere. For the experiments cells were plated on glass coverslips in 35 mm dishes.

Atomic force microscopy

Atomic Force Microscopy imaging was performed in contact mode with a Bioscope I microscope equipped with a Nanoscope IIIA controller (Veeco Metrology, USA) coupled with an inverted optical microscope (Olympus IX70). The experimental set-up is showed in Figure 4.12.

When investigating NB cells, a continuous perfusion of the imaging chamber with extracellular medium ($NaCl$ 145 mM, KCl 5 mM, $CaCl_2(H_2O)$) 1 mM, Hepes 5 mM, Glucose 5 mM, Sucrose 20 mM - pH 7.2) was performed by employing Pump Syringe Harvard PHD 2000. When switching to neurosteroid solution (Allo 100-200 nM in extracellular medium) we waited for the measurements to start until the inserted volume was at least three time the volume of the imaging chamber in order to guarantee a constant concentration. By contrast, DHEA was inserted in drops from a solution 100 μm in order to achieve the final desired concentration (200 nM - 1 μm).

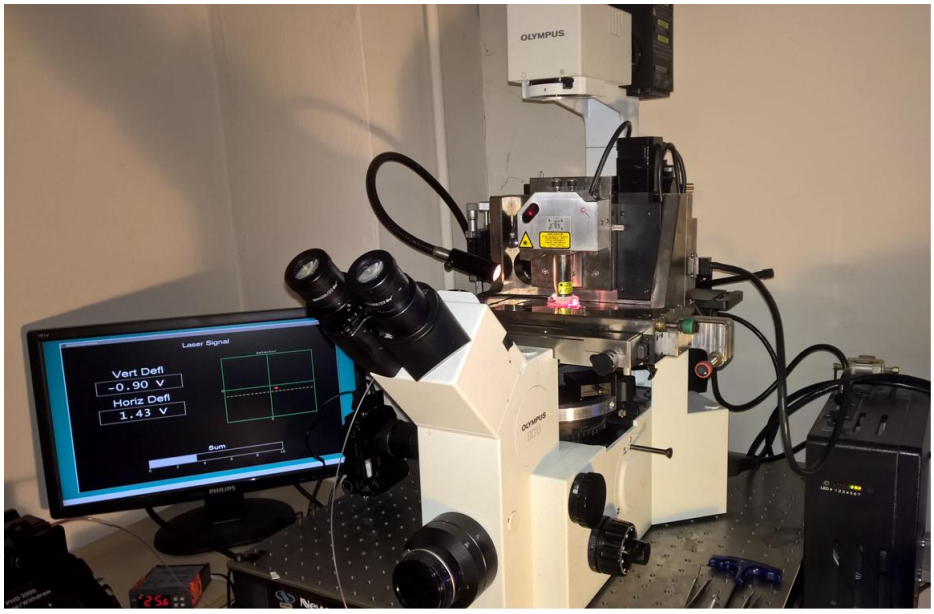

Figure 4.12: Picture of the set-up employed for experiments on cells.

The system was continuously monitored by taking several repeted force volume from the very start of the perfusion in the case of Allo. In the case of DHEA only indentation modulation technique was employed.

Force mapping

During force mapping, force curves are taken continuously while the tip is scanned laterally over the sample. Force curve were taken typically at 3.95 Hz with a 3-4 μm scan range. 256 pixels per line were taken for the entire data set of 32x32 force curves.

Force volume images were processed with a home-developed C++ software that allowed for the extraction and the analysis of the force curves. Young's modulus maps and zero-force images were obtained by exploiting the method reported in [238]. Briefly, on a soft sample, the z movement of the piezo will cause a deflection d of the cantilever and possibly an indentation δ of the sample:

$$z = d + \delta \tag{4.1}$$

By combining Equation 3.5 with the expression of the force $F = kd$, where k is the elastic constant of the cantileve, an expression for the indentation can be found:

$$\delta = \sqrt{\frac{k}{(\pi/2)(E/(1-\nu^2)tan\alpha}}\sqrt{d} \tag{4.2}$$

so

$$z = d + \sqrt{\frac{k}{(\pi/2)(E/(1-\nu^2)tan\alpha}}\sqrt{d} \tag{4.3}$$

Because in the measured data the zeros of the deflection and of the sample height are not well defined we have to rewrite Equation 4.3 more generally:

$$z - z_0 = d - d_0 + \sqrt{\frac{k}{(\pi/2)(E/(1-\nu^2)tan\alpha}}\sqrt{d - d_0} \tag{4.4}$$

where z_0 and d_0 are the offsets of the sample height and the deflection respectively. The offset of the deflection d_0 can be easily determined by calculating the mean deflection at the very beginning of the force curves (typically the first 100 nm), where the cantilever is off the surface. Determing the offset of the sample height is easy with force curves on stiff substrates but is more difficult with force curves on the soft samples because they do not show a sharp kink in the deflection.

We need to take two height values with their corresponding deflection values an enter them in Equation 4.4. These two points set up two equations that can be inverted to obtain values for the elastic modulus E and the offset z_0 of the height. In this way the Young's modulus map and the zero-force images can be reconstructed.

4.3 Experiments on fibrin/keratinocyte stem cells

Samples were kindly provided by Centro di Medicina Rigenerativa. Preparation of these sample is a patent subject matter and the complete protocol can not be reported here.

Fibrin preparation

The fibrin gels were prepared as follows: solution A was obtained by diluiting the original thrombin stock solution to a final desired concentration in $NaCl$ and $CaCl_2$. Solution B was prepard by mixing a quantity of the original fibrinogen stock solution to a saline solution. Solution A and solution B were mixed in an aluminium ring in order to obtain a 100 μm fibrin gel; different components concentration have to be used in order to prepare fibrin gels of different stiffness. Fibrin gels were left at room temperature for 10-15 min until a complete substrate polymerization was obtained and stored overnight at 4 °C.

Cell culture

3T3-J2 cells were cultured in Dulbecco's-Vogt Eagle's medium (DMEM*) containing calf serum (10 %), glutamine (4 nM) and penicillin-streptoomycin (50 IU-50 $\mu g/ml$). Human epidermal keratinocytes were cultured as described as follows. Briefly, skin biopsy samples were minced and trypsinized (0.05 % trypsin//0.01% EDTA) at 37 °C for 3 hr. Cells were collected every 30 min, plated on lethally irradiated 3T3-J2 cells and cultured in 5% CO_2 and humidified atmosphere in keratinocyte growth medium: DMEM and Ham's F12 media (2:1 mixture) containing 10% fetal calf serum, insulin (5 $\mu g/ml$, adenine (0.19 mM), hydrocortisone (0.4 $\mu g/ml$), cholera toxin (0.1 nM), triiodothyronine (2 nM), epidermal growth factor (10 ng/ml), glutamine (4 mM), and penicillin-streptomycin (50 IU-50 $\mu g/ml$). Subconfluent primary cultures were serially propagated either on plastic or on fibrin (prepared as above). Keratinocytes were cultivated in the presence of lethally irradiated 3T3-J2 cells (which provide adhesion and nutrients) and in keratinocyte growth medium, both on plastic and on fibrin. Fibrin-cultured samples were gently removed from the growing plates with the aid of two forceps and placed in a sterile aluminium ring (Figure 4.13).

Atomic force microscopy

Atomic Force Microscopy imaging was performed in contact mode with a Bioscope I microscope equipped with a Nanoscope IIIA controller (Veeco Metrology, USA).

When investigating fibrin samples, we used a temperature-controlled stage based on a circulating water bath on which we could mount the Bioscope head. The sample temperature was continuously monitored by

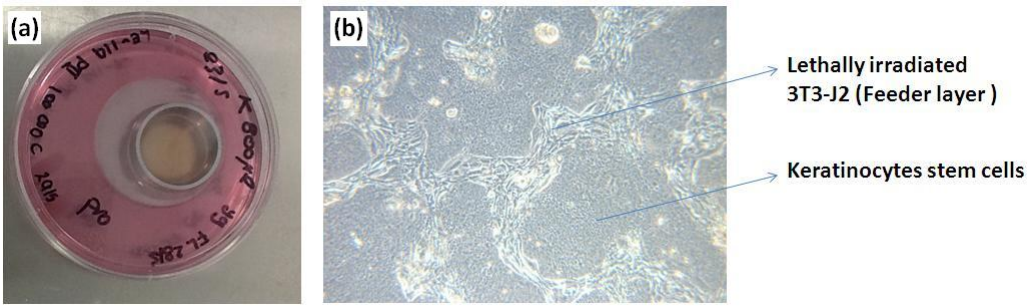

Figure 4.13: (a) Picture of the sample fibrin+keratinocyte stem cells placed in the aluminium ring; (b) Optical microscopy image of the surface of the sample where feeder layer cells and keratincyte stem cells can be identified.

a digital thermometer Fluke 16 (Fluke, Italy) equipped with a small K-thermocouple probe (Thermocoax GmbH, Germany) in direct contact with the imaging buffer. The stability of the temperature is assured within ± 0.3 °C of the specified temperature value.

When studying fibrin+keratinocyes samples, the Bioscope head above an x-y manually adjustable stage was mounted on an inverted optical microscope (Olympus IX70) in order to place the cantilever on the desired cell and to monitor possible overall morphological changes. However, this set-up did not allow us to control the temperature and experiments were carried on at room temperature ($\simeq 26°C$).

Cantilevers with a nominal spring constant of 0.06 N/m or 0.24 N/m were used for AFM cell imaging (always in contact mode for keratinocytes cells) and force spectroscopy (AFS). In the case of bare fibrin sample also colloidal probe were tested in order to perform AFM colloidal force spectroscopy (CFS).

In any case, the elastic constants used to convert deflections into forces were determined by the thermal noise method [236, 237].

Colloidal force spectroscopy (CSF)

When investigating bare fibrin samples the following protocol have been employed in order to attach silica microspheres (radius 5 μm on the end of a tipless cantilever in order to perform colloidal force spectroscopy 4.14:

1) Spread a drop of an aqueous solution containing silica microspheres onto one half of a glass coverslip. On the other half of the same side of the coverslip, put a small drop of an ultraviolet curing glue.

2) Insert a tipless AFM probe into a clip with the cantilever facing downward. Fix the clip to the arm of a 3-D micromanipulator.

3) While monitoring through an optical microscopce position the tipless cantilever so that it is close to the edge of the glue drop (Figure 4.14 (a)), lower the cantilever to press gently against the glass slide, push the cantilever into the glue (note that only the foremost tip of the cantilever needs to touch the glue), then translate out for several microns across the slide

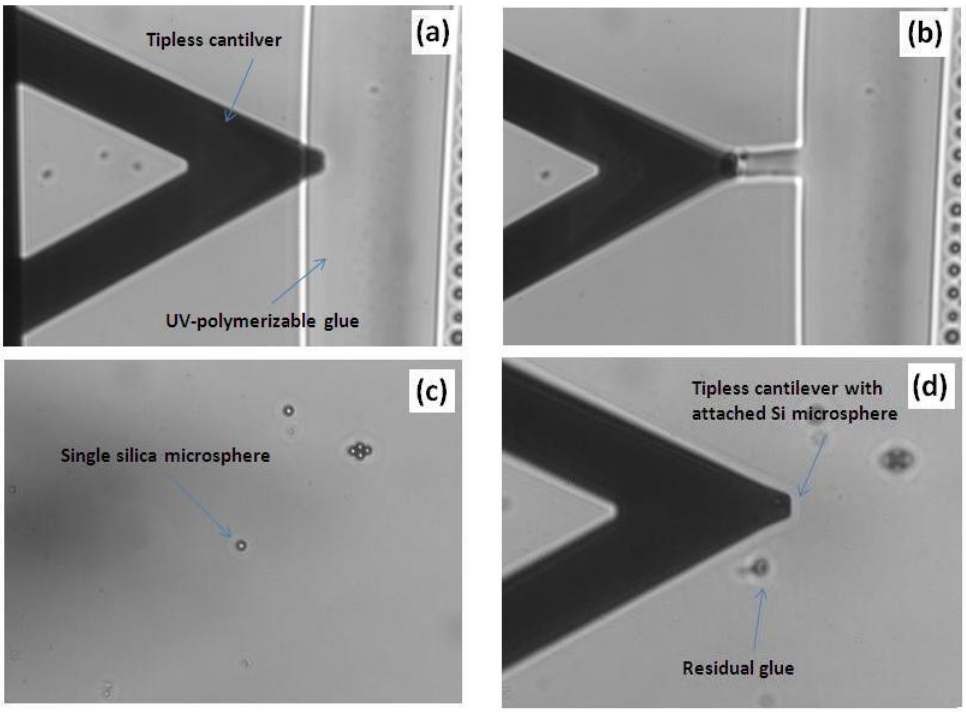

Figure 4.14: Protocol for the preparation of cantilever with attached silica microsphere in order to perform colloidal force spectrocopy. Passages (a-d) are illustrated throughout the text. Images are 20X optical microscopy pictures.

surface so that excess glue is dragged across the surface (Figure 4.14 (b)) with the results that only a very small amount of glue remains on the tip of the cantilever.

4) Lift the probe and move it to locate spheres on the same glass slide, identify a single microsphere (Figure 4.14 (c)) and position the end of the cantilever on the top of the sphere, lower vertically and allow the cantilever's tip to touch the sphere and then quickly lift up (Figure 4.14 (d)). Note that when a sphere fails to be glued to the cantilever, one should leave this sphere and try another one, since the just-touched sphere may roll along the glass slid and very probabaly get coated with glue if it is touched repeatedly with the cantilever.

5) Release the cantilever from the clip and pass it under UV rays to allow the fixing and the curing of the glue. The cantilever with the attached silica microsphere is shown in Figure 4.15.

Indentation modulation experiments

To perform indentation modulation it is necessary to superimpose a sinusoidal voltage signal to the z-piezo input provided by the AFM Controller and to measure the amplitude and phase shift of the consequent oscillatory motion of the cantilever, namely the output signal provided by the laser

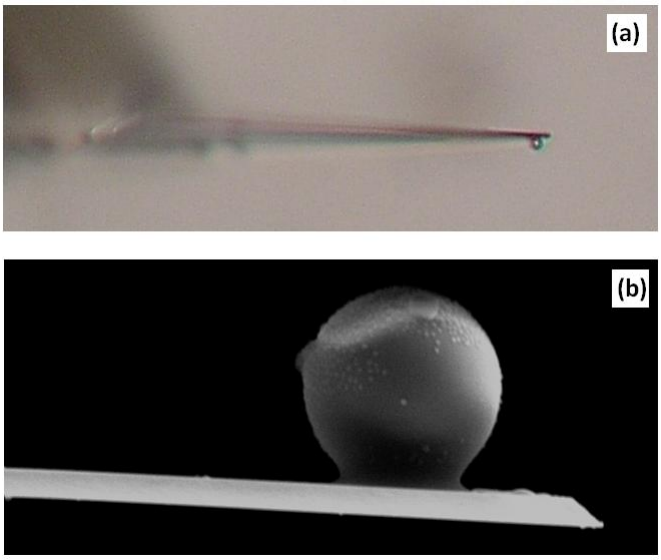

Figure 4.15: (a) Optical microscopy image of the cantilever with the attached silica microsphere; (b) Scanning electron microscopy (SEM) image of the same cantilever as in (a) (courtesy of Claudia Menozzi).

beam detector. To do this, a lock-in amplifier (S5210, Signal Recovery) was employed.

The lock-in amplifier could provide, with its internal oscillator, a sinusoidal signal with frequency ranging from 0.5 Hz to thousands of Hz, but the data acquisition had to face the problem of the time constant of the instrument. Indeed, the time constant to be chosen for the measurement of the oscillatory output had to be at least ten times bigger than the inverse of the frequency involved, and to obtain reliable data (amplitude and phase shift with respect to the signal input), 3-4 times the time constant set had to be waited. This is the reason why the lowest frequency that could be set on the lock-in amplifier was 20/50 Hz; the upper limit was set to 350/450 Hz because higher frequencies could lead to unreliable resonant behavior of the cantilever.

Since we worked without a feedback control system on the piezo, a calibration of the system on a rigid support (typically mica) is required. In particular, the results of indentation modulation on mica serve either to rescale the values obtained for the other investigated systems, i.e. amplitudes and phase shifts on mica must be subtracted from the measuraments on other samples, or to define the range of reliability of the technique (on a rigid sample, in ideal conditions, the amplitudes and phases in input and output should be equal, but practical and operative deviations due to instrumental chatacteristics can be present).

Moreover, apart from the calibration problem, working without a feedback control on the piezo means that the contact between the tip and the sample could not be held for more than few seconds in order to avoid the risk of drift. That is why a compromise for the period of contact was found

in 7 seconds, during with the oscillatory modulation was superimpose to the z-piezo, and 7 seconds of break, with the tip lifted up, to allow complete relaxation. The force-distance approach required one second, consequently a complete cycle of measurement (approach, modulation and data acquisition, retract and break) lasted 15 seconds.

Before performing the indentation modulation with the lock-in amplificator, a relevant issue had to be sorted out. Since the voltage input to the z-piezo commanded by the Controller had a magnitude of hundreds volts, the superposition of a tiny signal was not straightforward, as it required a summing amplifier capable of dealing with such high voltages. The electronic component employed was an isolation amplifier (ISO124, Burr Brown). Capable of transmitting a signal across a differential capacitive barrier in a digital way, it was used to take the high voltage input from the Controller as an offset, sum it to the oscillatory modulation and transmit the total signal to the microscope. With a power supply realized with standard batteries, the component was placed in a box with two switches and connected to the other devices through the input-output board with standard BNC cables.

The series of frequencies employed in this work were (50, 80, 100, 130, 150, 200, 230, 280, 320, 360) Hz and (20, 50, 100, 150, 200, 250, 300, 350, 400, 450) Hz. The voltage amplitude of the sinusoidal signal added to the z-piezo was 1.2 V RMS, which allowed sufficiently deep indentation but, on the other hand, was not strong enough to cause plastic deformations. As previously mentioned, prior to investigate the samples a calibration on a rigid surface had to be carried out. Figure 4.18 (a) reports the cantilever response (red line) to the z-piezo oscillation (black line). Since relative to a rigid substrate the two signals are in phase and once multiplied for the respective sensitivities (of the z-piezo, which was 26 nm/V, and of the photodetector, which could be calculated from the force-distance curve on mica) it is found that they are almost equal also in the amplitude, as expected. However, over the whole frequency range phase shifts are observed due to the experimental apparatus involved and therefore they have to be subtracted from the data acquired on the samples.

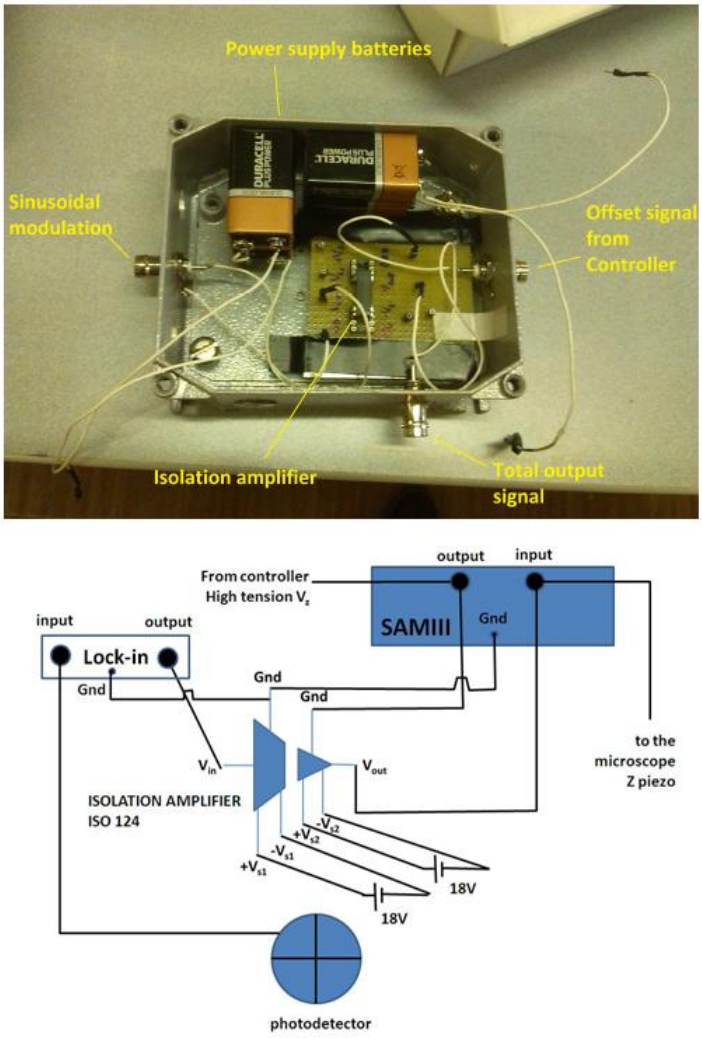

Figure 4.16: On the upper side, the box with the isolation amplifier. On the lower side, the scheme of the connections with the lock-in amplifier.

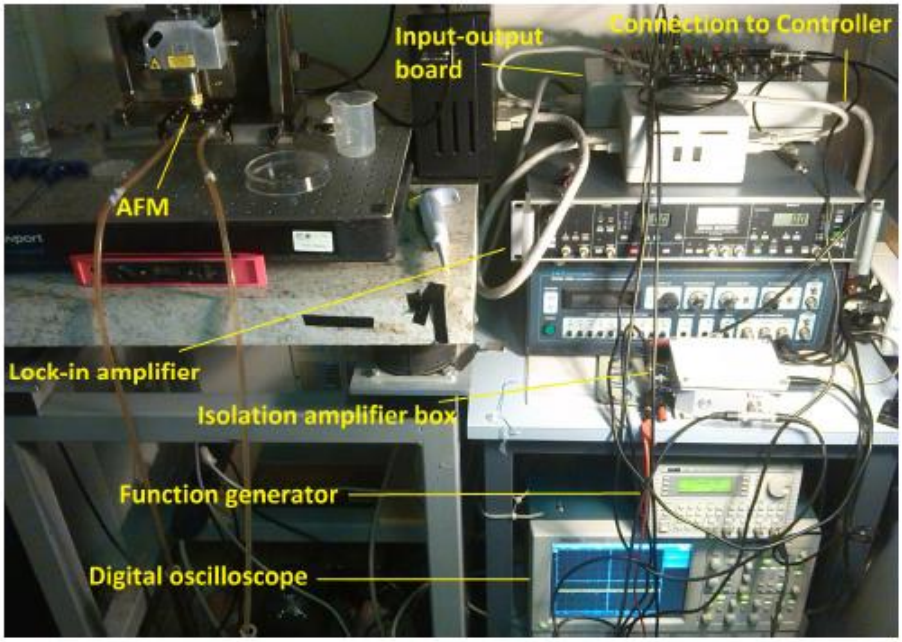

Figure 4.17: The complete experimental apparatus for indentation modulation experiments.

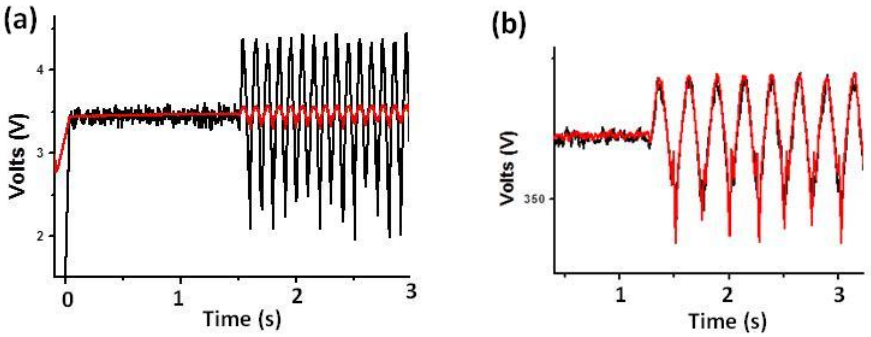

Figure 4.18: Calibration on mica substrate; (a) Cantilever response (red line) to the 1V RMS z-piezo 10 Hz oscillation. The two signals have the same amplitude (b) once corrected for the sensitivities.

Chapter 5

Effects of neurosteroids on model lipid membranes

In order to evaluate the effects of neurosteroids on model lipid bilayer, we decided to work with a ternary mixture containing a natural brain sphingomyelin extract. We concentrated on a DOPC/bSM/chol mixture with different lipid proportion to resemble mammalian plasma membrane of nerve cells. bSM is a mixture per se, even if it is mainly composed ($\simeq 50\%$) by a 18:0 fatty acid chain. Accordingly, the mixture will be considered as a "pseudo-ternary lipid mixture". This lipid combination is considered a very representative case for the studies of phase behavior of ternary lipid bilayers [268]. One of its main characteristics is related to the fact that the typically used 1:1:1 molar mixture is, at room temperature, very near to a critical point. In fact, the presence of critical points in the thermodynamics of biological membranes is nowadays considered one of the possible explanations for the existence of small and dynamic domains usually called "lipid rafts" [73]. Typically, the phase diagrams for these ternary lipid mixtures are represented in terms of the Gibbs triangle resulting from slices at a defined temperature of the overall isobaric mixture behavior. Their determination relies on the use of microscopy techniques such as Fluorescence Microscopy [269] or AFM [270], or on spectroscopic techniques such as NMR or FRET [271, 272]. It is important to stress that, in the context of the lipid raft hypothesis, the raft domains somehow recapitulate the behavior of liquid-ordered domains in lipid bilayer model systems. A scheme of the phase diagram for the DOPC/bSM/chol mixture, at a temperature of $25°C$, is reported in Figure 5.1. The scheme is taken from a work by Petruzielo et al. [271].

In the phase diagram for the ternary lipid mixture DOPC/bSM/chol two regions of phase coexistence are highlighted: the Liquid Disordered/Liquid Ordered phase coexistence region ($L_d + L_o$) and the triangular three phase region in which also a Solid Ordered phase is present ($L_d + L_o + S_o$). The liquid-liquid phase separation occurrence depends strongly on the type of lipids and it is typically found for the interaction of cholesterol with sphingomyelin. This interaction can produce the appearance of domains in which

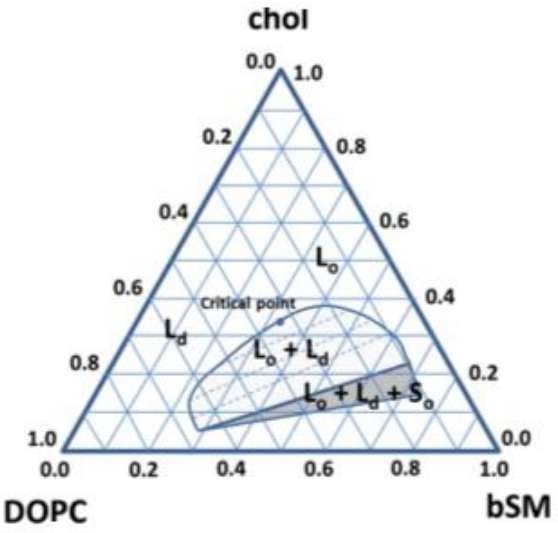

Figure 5.1: Phase diagram for the ternary lipid mixture DOPC/bSM/chol based on Ref. [271]. Two regions of phase coexistence are highlighted: the Liquid Disordered/Liquid Ordered phase coexistence region (L_d + L_o) and the triangular three phase coexistence region in which also a Solid Ordered phase is present (L_d + L_o + S_o). The phase diagram represents a slice at about 25°C of the co mplete phase diagram. The straight dashed lines inside the liquid-liquid phase coexistence regions represent schematically the tie-lines.

the lipid acyl chains are tightly packed while preserving high lateral mobility that is typical of a liquid phase (L_o phase). On the other hand, the L_d phase is similar to the well-known phase obtained at high temperature also in the case of lipid bilayers composed by only one type of lipid. Due to the different structures of the bilayer in the two phases, with an enrichment of sphingomyelin and cholesterol in the liquid ordered one, the different phases will provide a different thickness to the bilayer. Thickness difference is the observable that allows AFM to infer the presence of different phases. For the lipid composition 1:1:1, the bilayer, at 25°C, should be in the liquid-liquid coexistence region. In Figure 5.2 images from epifluorescence microscopy on GUVs are shown while Figure 5.3 reports a typical AFM image of the SLBs obtained for this composition. In both cases the presence of a phase separation is quite evident for the lipid bilayer. Moreover it is interesting to note that in the case of SLBs some regions of the bilayer are in the phase coexistence state, with domains having a height difference of about 1 nm, whereas other large bilayer regions show a homogeneous structure. One possible explanation for this behavior could be the different lipid composition of the bilayer patches resulting from intrinsic inhomogeneity in composition of the vesicles which gave rise to them [273]. However, we always found that the homogeneous phase is related to the larger patches on the substrate, whereas smaller patches are always found in the phase coexistence state. Figure 5.3 b) shows the interesting analysis of the domain heights.

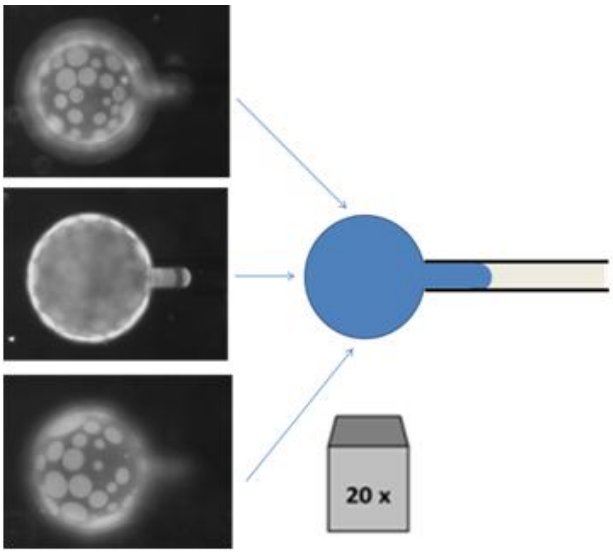

Figure 5.2: Fluorescence images of a DOPC/bSM/chol 1:1:1 (plus 1% of a fluorescently labeled lipid, Texas Red-DHPE) vescicle grabbed by a micropipette at 24°C. The three images show the upper, equatorial and lower regions of the vescicle. The circular brighter domains represent regions of the liquid disorder phase, where the fluorescent marker is able to bind, whereas the darker regions represent liquid ordered phase. These images show that these GUVs are in the phase separation condition. From [274].

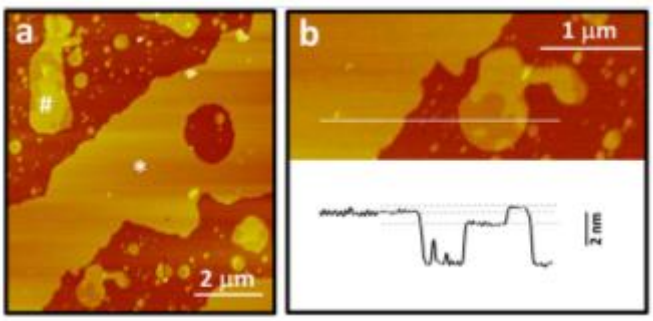

Figure 5.3: AFM images of a DOPC/bSM/chol 1:1:1 supported lipid bilayer at 25°C. a) The image shows homogeneous lipid bilayer patches (*) and smaller lipid bilayers in phase coexistence state; b) Height difference between the homogeneous bilayer and the domains in a patch with phase coexistence. The height of the homogeneous bilayer is intermediate between the two domains in the small patch. The line section refers to the white line on the image. From [275].

The homogeneous bilayer has a height which is intermediate between those of the L_d and L_o domains in the small adjacent patch. This is exactly the behavior which is expected for a transition between a phase separated region and a nearby homogeneous phase. We suggest that the homogeneous patches are related to an increased lateral pressure that shifts the bilayer from a phase coexistence region to a homogenous region favoring the more condensed phase.

5.1 Allopregnanolone (Allo)

5.1.1 Experimental results and discussion

After bilayer formation, we perfuse the AFM imaging chamber with increasing Allo concentrations. We typically use concentration steps in the order of 50-100 nM. Figure 5.4 shows what happens to the bilayer after Allo perfusion. The immediate effect is represented by a strong increase of the lateral area occupied by the lipid bilayer.

This behavior is consistent with what was found in the case of GUVs of the same lipid composition exposed to a solution containing Allo and studied by the Micropipette Aspiration Technique in which Allo uptake induces a global area increase of the bilayer (Figure 5.5). Even if the two model systems, GUVs and SLBs, have different characteristics, in some cases they can be prepared so to provide similar results dealing with their phase organization, as shown in a recent report [276]. Moreover it has been reported that a SLB undergoes the same relative area variation of an unsupported lipid bilayer when it crosses its main phase transition temperature [277].

The average value for the time constant of Allo uptake by the lipid bilayer is (55 ± 25) s. The overall time constant that we measured could also include phenomena different from simple molecule uptake, such as transfer of the molecules from one leaflet to the other and transfer inside the GUV. The obtained value is consistent with the slow activation kinetics observed for Allo on the $GABA_A$ receptors and with the accumulation of fluores-

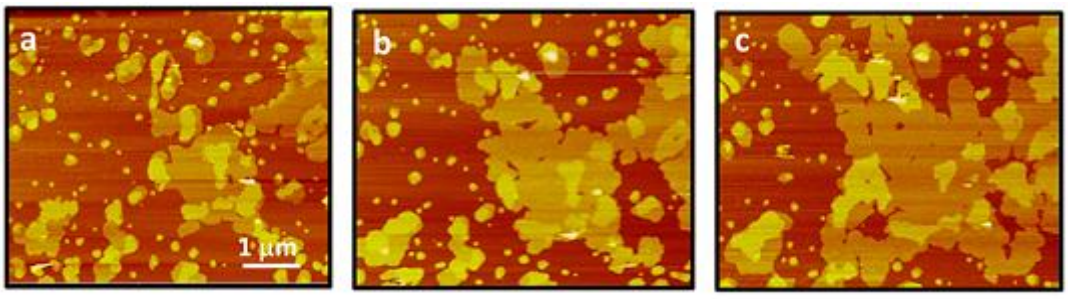

Figure 5.4: Effect of Allo on the lipid bilayer. a) Lipid bilayer patches composed by the lipid mixture DOPC/bSM/chol 1:1:1 in the absence of Allo; b) The same sample area as in a) after the injection of 50 nM Allo; c) The same sample area after the injection of 100 nM Allo [275].

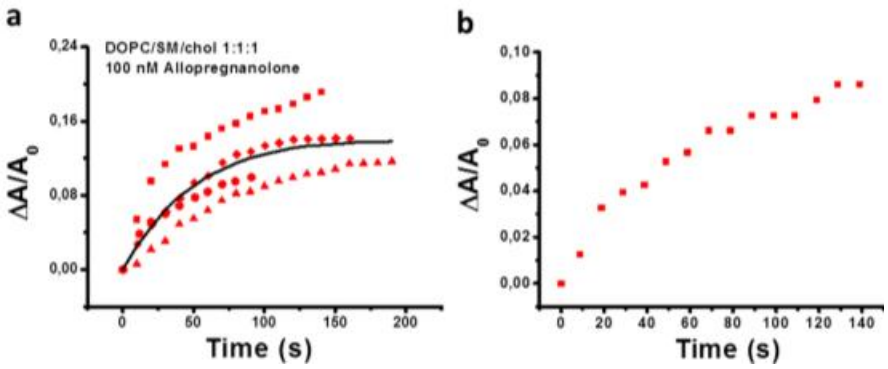

Figure 5.5: Representative relative area variation for DOPC/bSM/chol 1:1:1. a) GUVs are moved froma a chamber without to a chamber with 100 nM Allo concentration. The different scattered traces correspond to different experiments, whereas the continuous line represents the average behavior resulting from 7 experiments; b) a liposome grabbed by a micropipette is exposed to a 100 muM/s flux of a solution containing 100 nM Allo and placed directly in front of the GUV. From [274].

cently labeled neurosteroids in the plasma membrane [69]. It is evident that the range of measured time constant values is very broad for a given Allo concentration. This result could be related to vesicles with slightly different lipid compositions as it is typically found for GUVs produced by electroformation and including lipid mixtures.

We also measured the desorption process of Allo from lipid bilayers (Figure 5.6 a)) and we found that it occurred typically with a time constant similar to that of the uptake process, even if the desorption process was better described using more than one characteristic time as it has been found for the fluorescence decay of fluorescently labeled neurosteroids [278]. In some cases the desorption process was slower than the corresponding uptake one and the liposome area did not go back to the original area value. The latter behavior could be related to (i) a small residual amount of the neurosteroid inside the lipid bilayer or (ii) to an induced volume variation of the vesicle besides its area variation. Exploiting electrophysiological studies, the fact that the plasma membrane could act as a neurosteroid reservoir has already been proposed, explaining in this way the long tail of potentiation effects when the aqueous solution is extensively washed [278]. In some cases (about 20% out of a total of 20 experiments), immediately after the exposure of the vesicle to Allo solution, we observed an initial decrease of the bilayer projection inside the micropipette followed by the usual increase (Figure 5.6 b)). The projection retraction could also be due to a volume increase of the vesicle induced by the formation of pores leading to a water-associated glucose flux inside the vesicle. However, we excluded this possibility because it is unlikely that, once formed, pores are closed by an increase of the same molecules that created them. The variability in the results obtained prompted us to study the effect of Allo uptake by a lipid bilayer

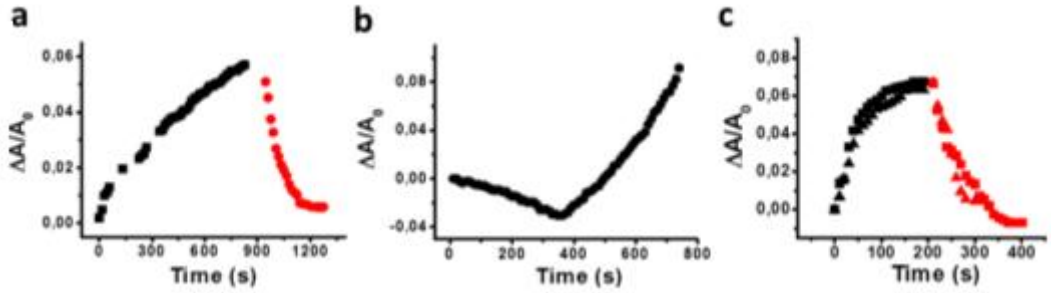

Figure 5.6: Example of different behaviors for DOPC/bSM/chol 1:1:1 and DOPC GUVs. a) Kinetics of Allo uptake (followed by desorption) from a 100 nM solution in the case of a DOPC/bSM/chol 1:1:1 vesicle. The desorption was studied by taking back the vesicle in the original solution without Allo. b) Example of a case in which the DOPC/bSM/chol 1:1:1 vesicle, immediately after having been exposed to an Allo solution, undergoes an area decrease followed by the usual increase. This behavior was observed in about 20% of the 20 experiments that we performed. c) Example of the uptake and desorption processes for DOPC vesicles exposed to a 100 nM Allo concentration. In this case, the DOPC vesicle is in a uniform phase (L_d). From [274].

which does not include cholesterol and which is in a homogeneous phase at room temperature. Hence, we chose to work with DOPC vesicles which have a phase transition from the L_d to S_o phase at -5°C. Exposing DOPC vesicles to a 100 nM Allo solution produced the kinetics patterns shown in Figure 5.6 c), where we also measured the desorption process. In the case of DOPC vesicles we never observed a retraction of the projection inside the micropipette. Moreover, the relative area variations are very similar in different measurements. In light of these evidences, we think that the variable results obtained in the case of DOPC/bSM/chol vesicles are mainly due to the presence of different phases in the bilayer because of the specific lipid mixture and to the possible different distribution of the bilayer between the two phases.

Besides area increase, Allo induces also a reorganization of the lipid domains. It is important to point out that, in the absence of Allo, under similar imaging conditions, the domains are rather immobile. The reorganization is characterized by a relative size increase of the regions in the L_d phase. It is to be stressed that the lipid mixture at issue is very near to a critical point for this temperature and, accordingly, the relative distribution between the different phases is near 50% for each phase. An average estimation for the change in the relative presence of the domains shows that the L_d phase relative increase is (10 ± 4)% after reaching 300 nM Allo concentration. Table 5.1 summarizes the results showing the relative proportions of the different phases and the total area variation.

Figure 5.7 shows the analysis of the height difference between the domains when the NS is added to the lipid bilayer. The presence of Allo leads

		Initial	300 nM	Average area variation
Allo	L_o	$(43 \pm 5)\%$	$(33 \pm 4)\%$	$+(24 \pm 5)\%$
	L_d	$(52 \pm 5)\%$	$(67 \pm 4)\%$	

Table 5.1: Effect of Allo on the relative proportion of L_o and L_d domains. The Table reports the average initial situation and the average situation at 300 nM Allo considering 12 lipid bilayer patches. The last colums represents the average variation of the total area of the membrane patches calculated on a set of 12 patches.

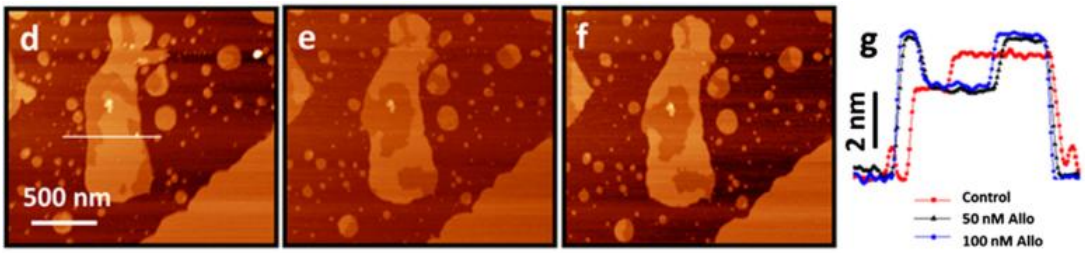

Figure 5.7: Effect of Allo on the lipid bilayer. d-f) Sequence of images at high magnification representing a phase coexistance state: d) control (no Allo); e) 50 nM Allo; f) 100 nM Allo; g) cross sections corresponding to the image sequence d-f) (white line in d). From [275].

to an increase of the height difference between the domains. This behavior is consistent with an increased composition difference for the domains and would correspond to a shift in the phase diagram of Figure 5.1 towards a region of decreased cholesterol amount on the basis of the reported positive slope of the tie-lines in the two-liquid phase coexistence region [271]. Moreover, the height difference variation results by a variation of both the L_o and the L_d phases with respect to the mica substrate. In fact, the L_o phase thickness increases after the introduction of Allo while the L_d phase slightly decreases. This behavior once again supports the idea that Allo induces a global transformation in the lipid bilayer. Considering these observations, the effect of Allo on this lipid bilayer is equivalent to decreasing the cholesterol content or reducing the interaction between cholesterol and bSM. In this context, it is interesting to note that the effect of Allo on the $GABA_A$ receptor has been found related to the amount of cholesterol in cells [279, 280]. In particular, it has been demonstrated that the effect of steroidal GABA potentiators was reduced by increasing cholesterol amount in cells. At the same time the amount of cholesterol in cells is also able to modulate the GABA potency, with a reduction of the agonist potency after cholesterol depletion [281]. The results we obtained in our study suggest that NS could compete with cholesterol inside the bilayer and could alter its effect and its interaction with high melting temperature lipids.

As stated above, the hypothesis of the presence of a critical point in a biological membrane is nowadays considered very appealing because it could

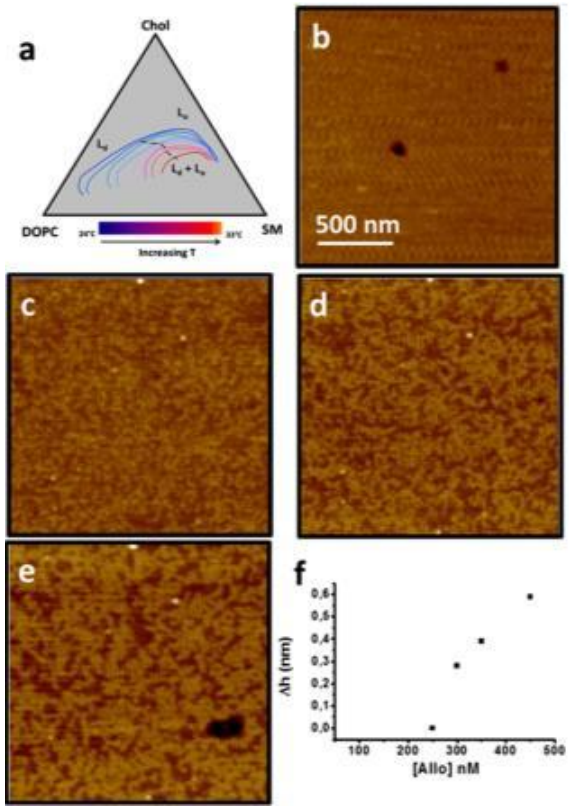

Figure 5.8: Effect of Allo on the miscibility border of the DOPC/bSM/chol 1:1:1 bilayer. a) Schematic representation of the phase diagram as a function of temperature [271]. The continuous lines represent the upper border of the miscibility region for different temperatures, whereas the dashed line shows the movements of the critical points as a result of temperature varation. As the temperature increases, the miscibility border shifts to lower regions of the Gibbs triangle. b) DOPC/bSM/chol bilayer at $27°C$ in a homogeneous phase. c-e) the same bilayer as in b) after the addition of c) 250 nM Allo, d) 350 nM Allo and e) 450 nM Allo. f) Height difference between the phases formed after Allo addition in function of its concentration. From [275].

explain peculiar behaviors of these thermodynamic systems such as the existence of small and fluctuating domains [73]. From a biological point of view it is probable that a single critical point might represent a too specific situation to have functional relevance, but it must be stressed that multidimensional order parameters and several critical points might be present in these models [81]. Therefore we decided to study the behavior of the lipid mixture at issue around its critical point. Here we increased the temperature of the AFM imaging chamber until we completely removed the phase coexistence. We did not measure the parameters which are strictly required to ascertain the real critical position of the lipid bilayer because we were mainly interested in the miscibility transition temperature. After getting a homogeneous bilayer, as shown in Figure 5.8 b), we added Allo to the lipid bilayer. The progressive addition of the NS leads to the reappearance of

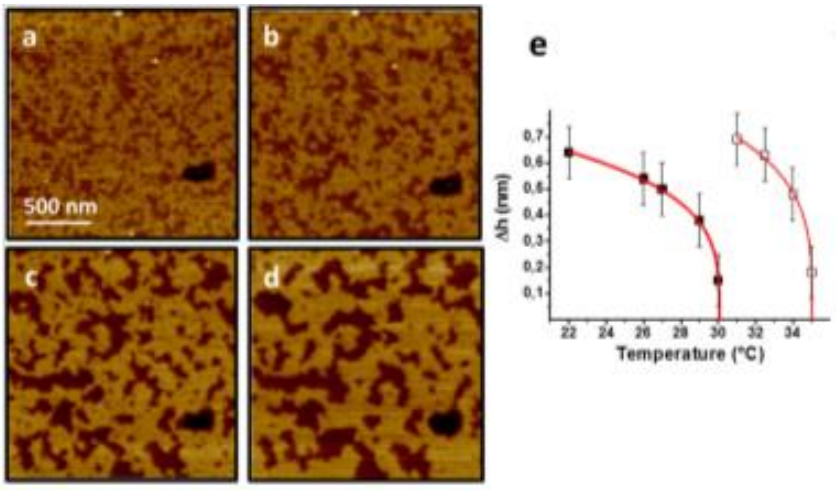

Figure 5.9: Effect of the temperature in the presence of 450 nM Allo: a) $27°C$; b) $25.8°C$; c) $24.5°C$; d) $23.3°C$; e) Height difference between the L_o and L_d domains in the case of a pure DOPC/bSM/chol 1:1:1 supported lipid bilayer (filled squares) and in the case of the same bilayer exposed to a 400 nM Allo solution (open squares). The data have been fitted with the function $|T - T_c|^\beta$. The obtained values for β are 0.28 for a pure lipid bilayer and 0.26 for a bilayer in the presence of Allo.

very small domains, as shown in Figure 5.8 c) that corresponds to 250 nM Allo concentration. Upon further increase in the concentration of the exogenous molecule, the different domains in the bilayer progressively increase their height difference, according to an increasing composition difference between the domains (Figure 5.8 d-e). A plot of the height difference between the two different phases as a function of Allo concentration is reported in Figure 5.8 f). If, at a constant Allo concentration (in this case 450 nM), we decrease the temperature, we again observe an increase in the height difference (Figure 5.9 a-d)). This behavior suggests that Allo addition is equivalent to what would happen by decreasing the temperature for the lipid bilayer (like in the freezing point depression case). It is interesting to note that the application of the NS to a lipid bilayer initially near to a critical point maintains a situation compatible with the neighborhood to a similar point, as manifested by the formation of small and fluctuating domains. This behavior is also confirmed by the fact that, after the insertion of Allo, the relative fraction of the two phases is again near to 50%.

Figure 5.9 e) reports the height difference between domains for a pure lipid bilayer and a lipid bilayer exposed to 400 nM Allo concentration as a function of the temperature. For the pure lipid bilayer, the height difference approaches zero for a temperature of $30°C$ as expected for a critical point at such temperature. The height difference can be represented by the function $|T - T_c|^\beta$ with a value for β of 0.28. The expected value for a critical point in a 2D Ising system should be 0.125 whereas it should be 0.325 for a 3D Ising system. A value corresponding to a 2D Ising system has

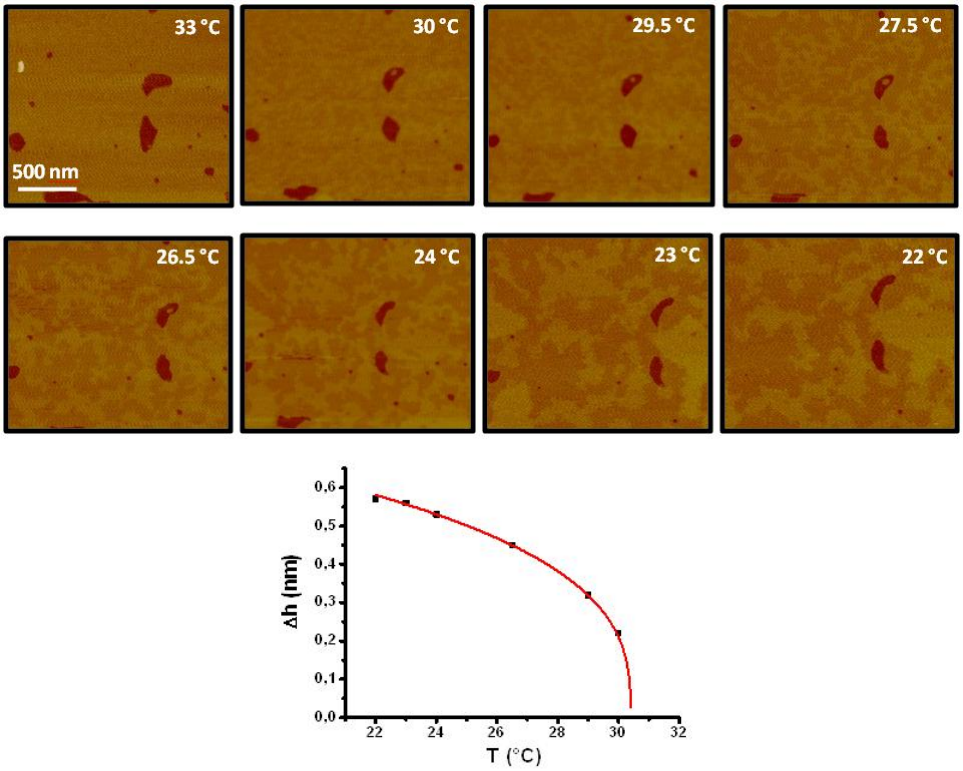

Figure 5.10: Example of the height difference between domain as a function of temperature for a DOPC/bSM/chol 1:1:1 supported lipid bilayer in the presence of 400 nM Allo concentration. The height difference values can be fitted with the function $|T - T_c|^{\beta}$ with a feature for β equal to 0.34. This value is compatible with a 3D Ising case. However, it is to be stressed that the fit has been obtained with a small number of data points and, especially, with points which are not very near to the supposed critical point. From [275].

been obtained in the case of critical behavior in GUVs [282], whereas a value compatible with a 3D Ising system has been obtained on multilamellar systems [283]. A previous investigation on supported lipid bilayers obtained a value compatible with the 3D Ising case [270]. Here we obtained a figure that is not compatible with either of the two models. This could be due to many reasons, including the fact that the specific case of supported lipid bilayers could be a system subjected to constraints due to the presence of the substrate. Other reasons could be related to the fact that our system is not exactly near to a critical point and the predicted values are rigorously valid only for a system approaching very nearly the critical point. It is also important to stress that our fits rely on a very small number of data points and data nearer to the critical point could largely affect the fit. It is however interesting to note that in some cases we observed a behavior which can be described by a feature for β of 0.33, probably connected with a bilayer very near to a critical condition. An example is shown in Figure 5.10.

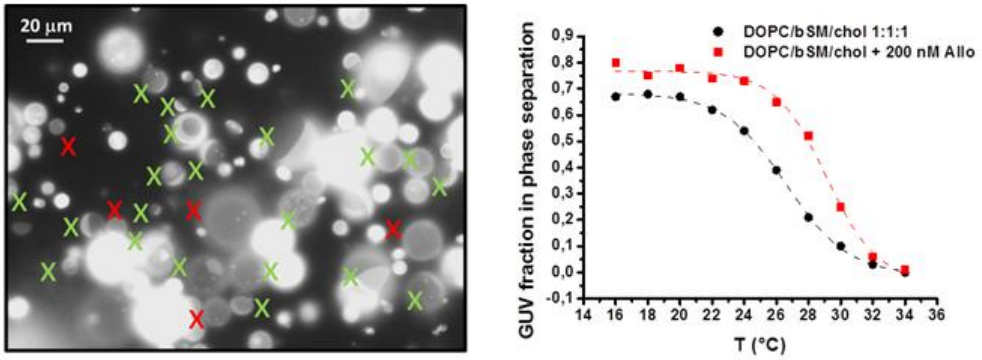

Figure 5.11: Example of an epifluorescence image exploited to count the vesicles in the phase separation region. A red X marks the vesicles in a uniform phase, a green X marks the vesicles in phase separation. b) Plot of the fraction of GUVs in the phase separation region as a function of temperature in the absence and in the presence of 200 nM Allopregnanolone. It is evident that the presence of Allo shifts the phase separation transition to higher temperatures. From [275].

Figure 5.9 e) shows also the behavior of a lipid bilayer exposed to 400 nM Allo concentration as a function of temperature. It is evident that the critical temperature of the bilayer increased by almost $5°C$. In that condition, the value obtained for β is 0.26, which is very similar to that obtained for a pure bilayer. These results clearly show that Allo has an effect on the miscibility transition temperature for this "pseudo-ternary mixture". To provide further support to this statement, we studied by epifluorescence microscopy on GUVs the effect of Allo concerning the miscibility temperature. The results are reported in Figure 5.11. By measuring the fraction of vesicles in the phase separation region as a function of temperature in the absence and in the presence of Allo, we were able to support the effect we observed by AFM.

In order to get an idea of the effect of the NSs on the global acyl chain order in the bilayer we followed by transmission FT-IR spectroscopy the position of the absorption maximum due to the symmetric -CH_2 stretching mode as a function of temperature and in the presence of Allo. This absorption mode ($\simeq 2850\ cm^{-1}$) is in fact considered representative of the acyl chain order in the bilayer, moving to higher wavenumbers if the disorder increases [284]. A typical IR absorption spectrum for this lipid mixture is reported in Figure 5.12 a). Figure 5.12 b) shows the trend of the symmetric CH_2 stretching mode as a function of temperature for the pure lipid dispersion and the lipid dispersion plus 200 nM Allo. Remarkably, the variations in the slope that we observed for the pure lipid mixture agree well with the boundaries of the two-liquids phase separation region for the lipid mixture we are considering [285]. Figure 5.12 b) clearly shows that the addition of Allo, considering a constant temperature, induces an increase of the lipid acyl chain disorder, in accordance with AFM experiments where we see an

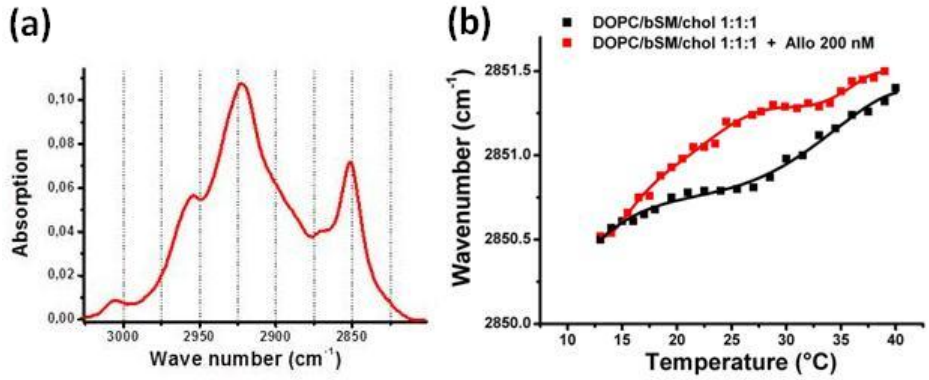

Figure 5.12: a) IR absorption spectrum for DOPC/bSM/chol 1:1:1 liposomes in the -CH stretching region. b) temperature dependence of the symmetric -CH_2 stretching frequency in the IR spectra for DOPC/bSM/chol 1:1:1 lipid mixture (black squares), DOPC/bSM/chol 1:1:1 + 200 nM Allo (red squares). The continuous lines are guides for the eye. Modified from [275].

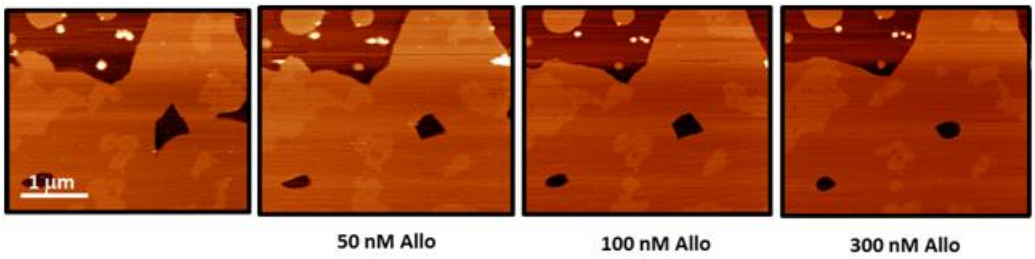

Figure 5.13: Effect of Allo on a DOPC/bSM/chol 25:55:20 supported lipid bilayer: the same overall behavior is observed for different mixtures.

overall increase in the L_d area.

We also investigated the behavior for a lipid mixture that is not expected to reside near to the line of critical points, in order to see if the behavior observed after the addition of Allo depended on the position of the bilayer in the phase diagram. The images presented in Figure 5.13 show that the same overall behavior is observed for the different considered mixtures.

The case of a lipid mixture composed by DOPC/bSM/chol in the molar proportions 42:33:25 is of particular interest. At 25°C the bilayer presents a phase coexistence region which can be removed by increasing the temperature up to 30 °C (Figure 5.14 a)). In this case we did not observe the appearance of small domains at variance with the previous case. Once the bilayer was in the homogeneous phase we inserted Allo. Figure 5.14 b) shows the behavior of the bilayer after the insertion of the NS. It is clear that the NS took the bilayer back to the phase coexistence region with the formation of larger domains. The progressive addition of Allo leads also to the appearance of putatively solid domains, as it can be seen from Figure 5.14 c, d) which corresponds to 400 nM Allo. Indeed, the L_o domain on the

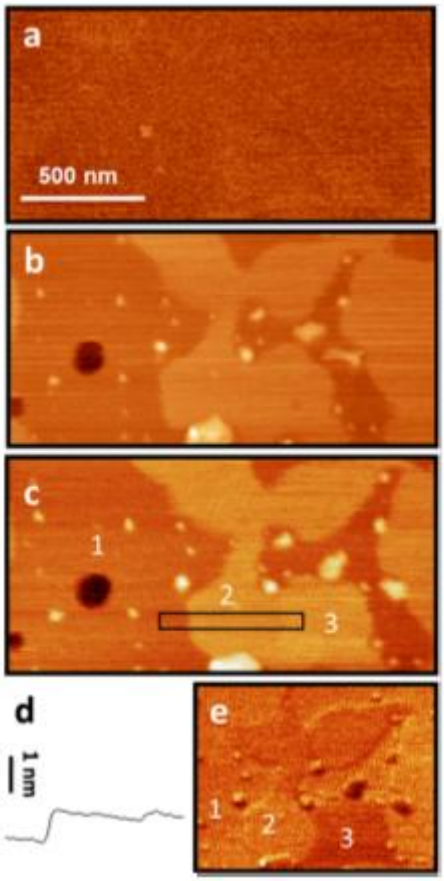

Figure 5.14: Effect of Allo on a DOPC/bSM/chol 42:33:25 supported lipid bilayer. a) AFM image of a lipid bilayer in the absence of Allo at $30°C$; b) The same lipid bilayer as in a) with 200 nM Allo; c) with 400 nM Allo. The higher domain of the bilayer in the bottom part of the picture (see white line) shows two height levels as shown in d). The higher level domain could be interpreted as a region in the solid ordered phase. Accordingly, the numbers refers to the different domains: 1) L_d, 2) L_o, 3) S_o; d) Average line section of the region highlighted in c); e) Phase signal image of the same region as in c). The numbering has the same meaning as in c). The contrast on domain 3 could be related to the presence of a solid ordered phase. From [275].

right and lower portion of Figure 5.14 c shows the presence of a region with a slightly larger thickness. The identification of S_o regions by AFM in ternary lipid mixtures can be elusive due to the very small height difference with respect to L_o domains. Figure 5.14 d) shows an averaged line section of the domain in Figure 5.14 c) whereas Figure 5.14 e) shows the image acquired by the phase signal of tapping-mode AFM on the same region of Figure 5.14 c). The phase signal produces a visible contrast when the tip of the AFM is interacting with regions of different mechanical properties [230, 286]. The variation of the phase contrast on the higher domain in Figure 5.14 e) could correspond to the presence of a S_o region that is mechanically more rigid than the L_o phase.

5.1.2 Mechanical characterization and force spectroscopy

It is well known that, to a greater or a lesser extent, the interaction of exogenous molecules with the lipid bilayer can affect its mechanical properties [287, 288, 289, 290]. The MAT provides access to the measurement of both the bending constant and the stretching constant of a lipid bilayer [291, 292, 293, 294].

A typical plot of the tension as a function of relative area deformation for a DOPC/bSM/chol 1:1:1 vesicle is reported in Figure 5.15 together with the variation of the mechanical properties of the same vesicle in the presence of different Allo concentrations. In this case, the initial K_{app} is on the order of 490 mN/m. The effect of bending fluctuations on the relative area fluctuations is typically negligible in lipid mixtures including cholesterol [295, 296]. Usually, when the contribution of thermal undulations is important, they remain present also in the high tension region which is used to measure the apparent stretching constant. To this aim, a procedure to remove the contribution from undulation suppression at high applied tension has been developed [297].

After exposing the same GUV to a 100 nM Allo solution, we again measured its mechanical properties. The plot in Figure 5.15 a) shows that the mechanical properties of the bilayer have been strongly modified by Allo uptake. The value of K_{app} is nowequal to 220 mN/m but the presence of a contribution from the bending stiffness of the bilayer for low applied tensions (bending constant K_b =0.6 $\times$ 10^{-19} J for Allo 100 nM) is now evident. This evidence prompted us to calculate the effective stretching constant in the presence of Allo. The obtained value is 340 mN/m,which is still lower than the value in the absence of Allo, meaning that the system becomes more deformable due to the presence of the neurosteroid. We then doubled the Allo concentration (200 nM) and we measured the mechanical parameters also in this case. Figure 5.15 a) shows that in the 200 nM case the bending constant and the stretching constant are not significantly altered with respect to the 100 nM case. Measurements on other vesicles confirmed that the effect of Allo on the mechanical properties saturates at an Allo concentration of about 100/150 nM. Considering all the experiments that

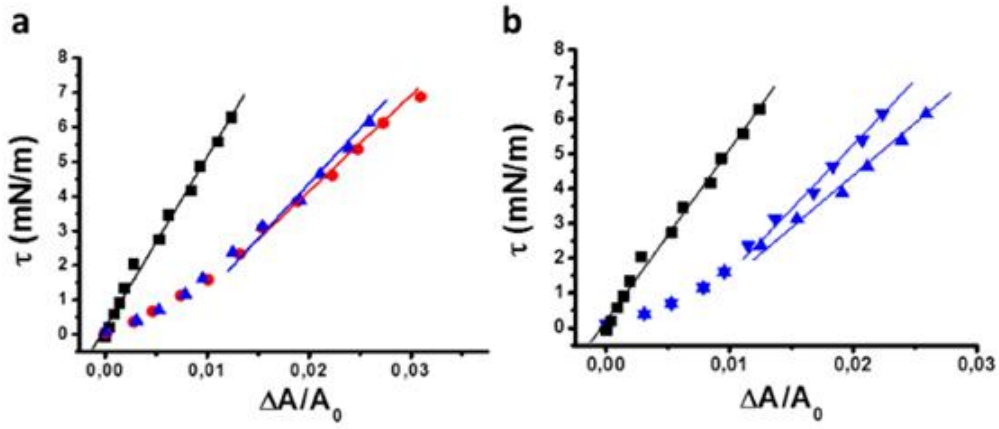

Figure 5.15: Effect of Allo on the mechanical properties of GUVs. a) The black squares report the behavior of a DOPC/bSM/chol 1:1:1 vescicle as the applied tension is increased. The black line is the linear fit to obtain the apparent stretching constant. The red circles correspond to the mechanical characterization in a 100 nM Allo solution whereas the blue triangles to the case of 200 nM Allo solution. b) The black squares represent the same data as in a). The stars are related to the portion of the plot used to measure the bending constant of the bilayer (low tension region) and are the same points as in a) for the 200 nM Allo concentration case. The up-pointing triangles represent the same data as in a) for the high tension region. The down-pointing blue triangles represent the values of the high tension region after subtraction of the contributions coming from the bilayer bending modulus. The apparent stretching constant of 490 mN/m changes to a value of 340 mN/m. From [274].

we performed (n = 5), the stretching constant for 1:1:1 DOPC/bSM/chol GUVs changes from 390 ± 100 mN/m to a value of 250 ± 100 mN/m when exposed to 200 nM Allo.

To better understand the variation of the mechanical properties, we studied the effect of Allo at the same concentrations on a pure DOPC GUV. In this case we found that K_{app} was practically unaffected by the uptake of Allo. The mechanical property variations which are reported in the literature when exogenous molecules interact with lipid bilayers similar to DOPC are typically obtained for much higher concentrations than the ones used in our work [289]. Considering the comparison between DOPC and DOPC/bSM/chol GUVs, we can speculate that the variation in the stretching constant for the latter type of GUVs could be due to the variation of the relative proportion of L_d and L_o domains, as suggested by our AFM investigation (see previous Paragraph). Indeed, it has been demonstrated that the L_o phase has different mechanical properties compared to the L_d phase, being the L_o phase stiffer than the L_d [298]. If the relative proportion of the two phases changes, the overall mechanical properties of the vesicles should also vary. In this sense, our AFM investigation on this model system established that Allo favors a relative increase of the L_d phase, which is the

more compliant and softer phase. Other possible explanations for the effect of Allo on the mechanical properties of DOPC/bSM/chol GUVs could be related to the effect of the molecule on the order inside the lipid bilayer. Again, our FTIR characterization showed that the addition of Allo promotes an increase in the disorder of the bilayer, which is intrinsically related to a decrease in the mechanical response of the system. It is also important to consider that, even in the case of DOPC/bSM/chol 1:1:1 GUVs, in some rare cases, the addition of Allo did not change the lipid bilayer mechanical properties. This behavior could be rationalized by considering cases in which the vesicle is in the homogeneous phase and the small quantity of Allo is not able to significantly affect the phase state and, consequently, the mechanical parameters. Further interpretations for the decreased mechanical properties as Allo interacts with the bilayer, could be provided by MD simulations that, for example, unravel important details such as the specific interactions of Allo or in general of exogenous molecules with the lipids [299].

Another possible way to further testing the mechanical properties of lipid bilayers is to perform AFM force spectroscopy (AFM-FS) [300]. By means of AFM-FS, it has been well estabilished that the vertical force applied by the AFM tip to supported lipid bilayers (SLBs) is a direct measurement of the lateral interactions between lipid molecules [301]. The penetration of the AFM tip through the bilayer is characterized by a discontinuity in the approaching force-distance curve, which happens at a force that has been interpreted as the maximum force the bilayer is able to stand before breaking, the so-called $breakthrough force$, F_b. According to previous studies, subtle variations in the chemical structure of the phospholipid molecules [302] as well as in the physicochemical environment [303, 304, 305] induce variations in the F_b value, which can therefore be considered as the fingerprint of the mechanical stability of a specific lipid membrane in a given environment. As F_b is characteristic of the chemical structure and molecular organization of a particular bilayer at specific environmental conditions, in multicomponent systems the F_b value can be directly associated to the composition of phase-segregated domains. From this perspective, force spectroscopy contributes to clarify the nature of each phase observed in AFM topographical images and can provide indications about the specific effect of an exogenous molecule on each phase of the bilayer [306] (see Figure 5.16).

By identifying the breakthrough force for each pixel of a force volume image - and this can be done by using a simple home-developed software - it is possible to build up an histogram where the breakthrough-force distribution related to each domain is clarly detectable. It is important to stress the fact that the AFM tip punch-through is an event of stochastic nature which is strictly related to flacuations, so the breakthrough-force which is typically reported is actually the most probable value of a distribution which can be approximated by a gaussian distribution. By following the changes in the value of the breakthrough-force associated to physical or chemical variations in the enviromental parameters, i.e. temperature or addition of exogenous

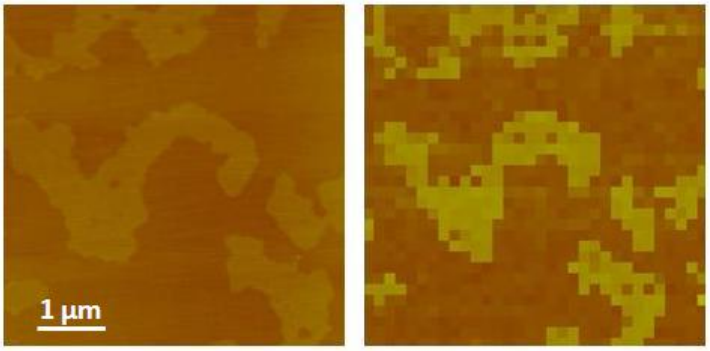

Figure 5.16: Example of correspondance between the topographical image and the force volume image. The different value of the breakthrough allow to identify and discriminate the two different phases (L_o brighter, L_d darker).

molecules, like, in our case, neurosteroids. These kind of measurements can provide valuable information about changes in structural and physical properties of bilayer while in phase sepraration or transition [307]; in particular our main objective was to understand if a general trend in the force distributions is observed after the addition of the neursteroid, in particular wheter only one or both the breakthrough values for the liquid phases were affected by the presence of the inserted molecule.

As a first step we decided to perform temperature-controlled AFM-FS on a mixture of diphyPC:DPPC:chol 1:1:1; we decided to perform force spectroscopy on this kind of mixture because it presents domains which are more stable in comparison to the usual DOPC:bSM:chol one and its phase behavior has been largely investigated in the literature [308]. Figure 5.17 shows the main results of this kind of characterization: it is evident that the difference between the breakthrough force related to the L_o phase and the one related to the L_d phase as a function of temperature (Figure 5.17 (a)) has the same behavior as the height difference between the two domains which has been found to be largely independent of the exact force value when the analysis is performed around the minimum force condition (Figure 5.17 (b)). This is a quite interesting result, since the two trends originate from two distint measurements, the first coming from a mechanical characterization (i.e. force volume image), while the second being from the usual topographical scanning. According to these findings we can state that the mechanical characterization of the bilayer is truly indicative of the thermodynamical state of phase of the systems. Furthermore, Figure 5.18 (a) shows the separated breakthrough force values for the two liquid phases. Interestingly, we can notice that only the F_b value of the liquid ordered phase seems affected by the temperture variation, while the F_b value of the L_d phase remains quite contstant. This result is in agreement with the NMR results in [308], where the behavior of the DPPC methyl quadrupole splitting as a function of temperature is reported (Figure 5.18 (b)). This finding once again states that the breakthrough-force value can be exploited as an indication of the lipid bilayer order.

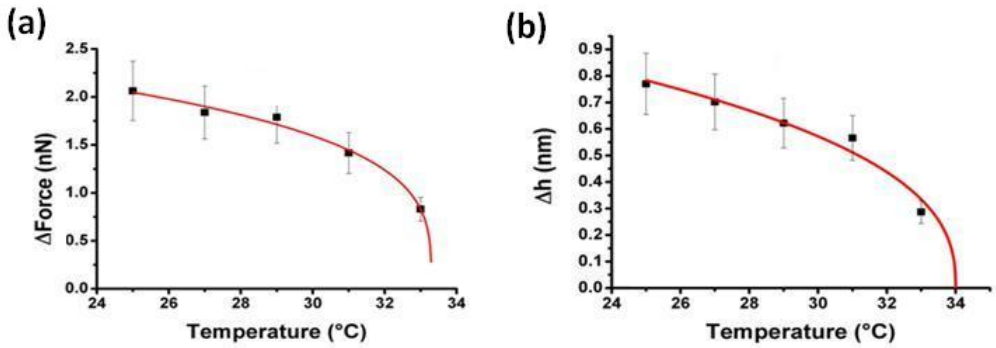

Figure 5.17: (a) Difference between the breaktrough forces relative to the L_o and the L_d phase in function of temperature: data are from force spectroscopy. (b) Difference between the height relative to the L_o domains and the height relative to the L_d domain: data are from topographical imaging. Red curves are guide for the eye. Since the two trends correlates it is possible to state that FS characterization is really indicative of the thermodynamical state of the bilayer.

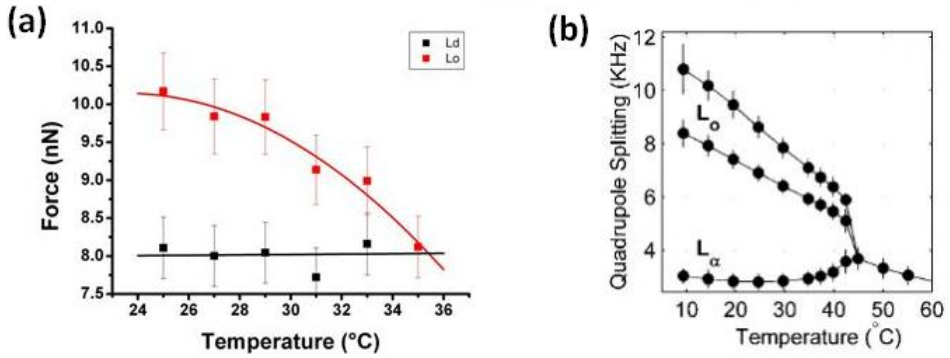

Figure 5.18: (a) The breakthrough-force values for the two liquid phases are reported as functions of temperature: the F_b value of the liquid ordered phase seems affected by temperture variations, while the F_b value of the L_d phase remains quite contstant; this evidence is in agreement with NMR results, where the behavior of the DPPC methyl quadrupole splitting as a function of temperature is reported. Image (b) is taken from [308].

Relying on these promising results, we tried to see what is the effect of Allo addition on the relative positions of the F_b peaks. We prepared a DOPC/bSM/chol 1:1:1 bilayer and increased the temperature until the domains disappeared, in order to achieve the condition of uniform phase. Then, Allo was inserted by steps of 300 nM. Again we see that Allo promotes phase separation because the initial distribution of breakthrough forces relative to the uniform phases splits into two distributions, according to the formation of the two separated liquid phases. By increasing Allo concentration, the positions of the two peaks shifts towards higher values of forces, meaning higher stability and increased order (Figure 5.19 (a)).

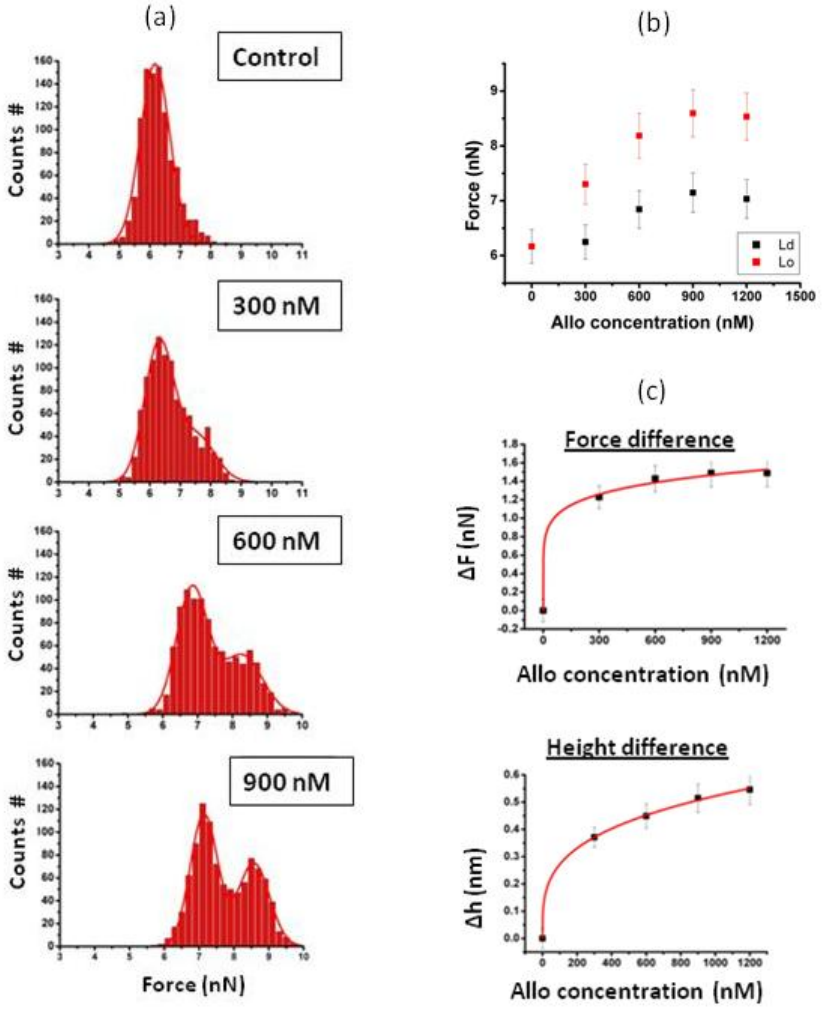

Figure 5.19: (a) Allo promotes phase separation: the single distribution relative to the initial uniform phase splits into a double distribution after the addition of Allo, indicating the formation of two different domains; Allo affects both the L_o and the L_d phase, since we observe a shift in both the position of the two peaks (b); again the difference in the F_b force relative to the two peaks correlates with the topographical height difference between the two domains (c).

This result is in contrast with what was found by FTIR measurements, where an increased Allo concentration meant an increased disorder (Figure 5.12). However, we are talking about two different measurement techniques: in particular FTIR is sensitive to the lipid chain, while atomic force spectroscopy - due to its indentation features - is responsive also to the water-lipid interface. So, increased order or disorder may be relative to what the involved technique is truly probing.

Moreover, we can state that Allo affects the behavior of both the L_o and L_d phases because we observe a shift in the position of both peaks (Figure

5.19 (a) and (b)). Moreover, by plotting the force difference between the two peaks vs Allo concentration we observe a correlation with the behavior of the topographical height difference between the domains (Figure 5.19 (c)).

5.2 IsoAllopregnanolone

In this work we considered also the effect of isoAllopregnanolone, a 3β isoform of Allo differing only for the spatial orientation of an OH group, on a lipid bilayer of the same composition. It is important to stress that isoAllo is not a mirror image of Allo, and it is reasonable to expect a different interaction with a lipid bilayer [15, 16]. However, given that the functional effect of isoAllo is that of inhibiting the activity of Allo in a non-competitive way [14], it is interesting to study if the two molecules have also different and somehow opposite effects on the lipid bilayer.

Figure 5.20 shows the effects of the perfusion of isoAllo on a DOPC/bSM /chol 1:1:1 supported bilayer. It is evident that in this case the insertion of this NS in the bilayer induces a decrease of the overall lipid bilayer area. Moreover, an analysis of the relative proportion of the two phases shows that the addition of isoAllo induces an increase of the L_o fraction over the L_d one. The variation of the L_o fraction for a 300 nM isoAllo concentration is $(2 \pm 1)\%$. Table 5.2 reports the effects of isoAllo addition on the relative L_o to L_d proportion and on the average area variation of the here considered ternary lipid mixture.

Interestingly, the interaction of GABAergic phenols on lipid bilayers has been recently studied by NMR [309] and it has been found that these molecules strongly interact with the lipid bilayer partitioning near to the polar group and the first part of the acyl chains. At the same time, these molecules favor a tighter packing of the lipid bilayer. It could be that the insertion of isoAllo in the DOPC/bSM/chol mixture induces a decreased repulsive force between the lipids involved in the L_o phase and a decrease of the overall membrane area. Considering the results obtained in the present study, we could speculate that the antagonistic effect of isoAllo on Allo could also be related to an opposite effect on the lipid bilayer.

We also investigated the effect of isoAllo when the lipid bilayer is just

		Initial	300 nM	Average area variation
isoAllo	L_o	$(50 \pm 3)\%$	$(52 \pm 3)\%$	-$(14 \pm 3)\%$
	L_d	$(50 \pm 3)\%$	$(48 \pm 3)\%$	

Table 5.2: Effect of isoAllo on the relative proportion of L_o and L_d domains. The Table reports the average initial situation and the average situation at 300 nM Allo considering 12 lipid bilayer patches. The last colums represents the average variation of the total area of the membrane patches calculated on a set of 12 patches.

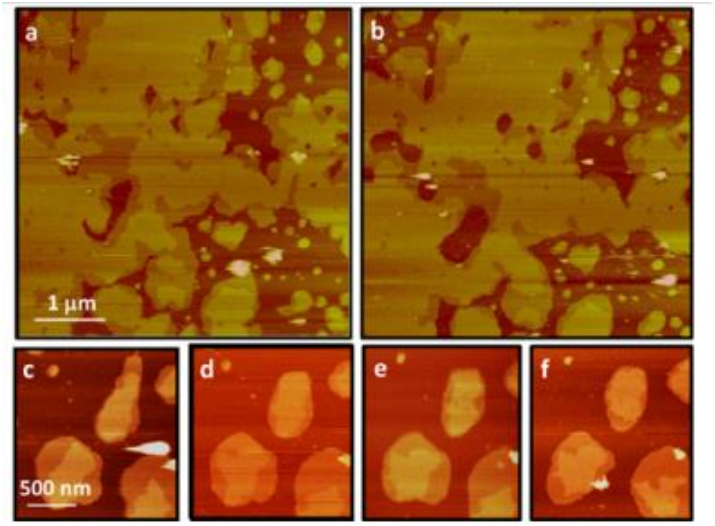

Figure 5.20: Effect of isoAllo on DOPC:bSM:chol 1:1:1 supported bilayer; (a-b) overall view of bilayer patches before (a) and after 300 nM isoAllo in the imaging chamber; (c-f) sequence of images of lipid bilayer patches in the phase coexistance region as the concentration of isoAllo is increased: (c) no isoAllo; (d) 50 nM; (e) 100 nM; (f) 300 nM. From [275].

outside the phase coexistence region. In this case we found that, up to 400 nM isoAllo concentration, no effect was evident from AFM images. This is at variance with what happens in the case of Allo which stabilizes the phase separation of the bilayer. In the case of isoAllo it could be that the addition of the exogenous molecule shifts the system to the homogeneous phase.

The observed decrease in the overall area of lipid bilayer patches and the induced increase of the liquid ordered fraction of the bilayer are consistent with what has been found also by MAT investigation. Figure 5.21 shows that liposomes in the presence of 100 nM isoAllo undergo a lipid area reduction. The decay time constant for the lipid area has a feature of about (120 $\pm$ 40) s, suggesting a slower kinetics with respect to the case of Allo uptake. Moreover, the absolute value of the relative area variation is smaller in the case of isoAllo. If we compare the effect of isoAllo on SLBs and GUVs on the overall bilayer area we find that in the case of GUVs remarkable smaller area variations are observed ($\simeq$ -3% for GUVs and $\simeq$ -14% for SLBs). This is probably due to the fact that GUVs are subjected to a lateral tension that tend to expand the vescicle and this effect can counterbalance the overall shrinking caused by isoAllo. Moreover, it should be kept in mind that SLBs and GUVs are different model system and in the case of SLBs the presence of the substate can affect the lateral mobility of the lipids.

The stretching constant of the DOPC/bSM/chol vesicle exposed to an isoAllo solution of varying concentration does not change significantly (Figure 5.21 (b)) up to 400 nM. A possible interpretation for the lack of concentration dependence of the mechanical properties in the case of isoAllo

could be related to a smaller partition coefficient with respect to Allo or to the fact that the area increase by isoAllo uptake could be compensated for an increase of the order in the bilayer, even if, at the level of lipid chains order, no particular effect was observed with FT-IR measurements (Figure 5.22). Also in this case, MD simulations could provide useful insight into this behavior [300].

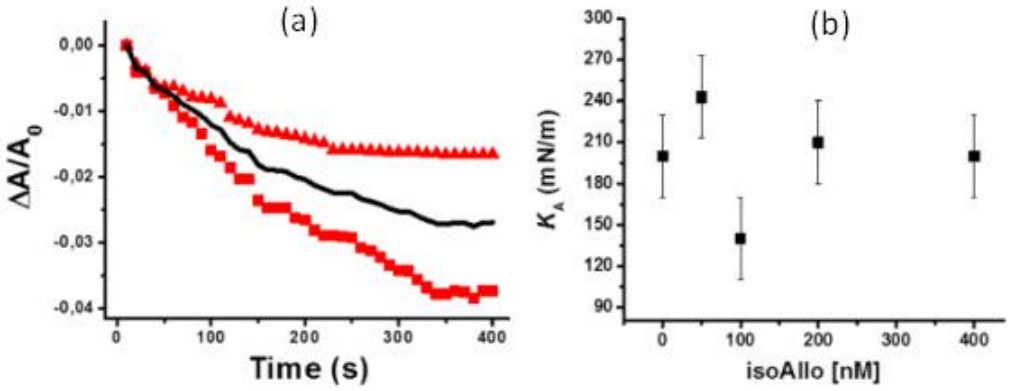

Figure 5.21: (a) The scattered points represent two traced for the relative area variation of a DOPC/bSM/chol 1:1:1 liposome exposed to a 100 nM isoAllo solution. The continuous line represents the average behavior. (b) Stetching constant values for a DOPC/bSM/chol 1:1:1 vescicle as a function of the isoAllo concentration to which it is exposed. From [274].

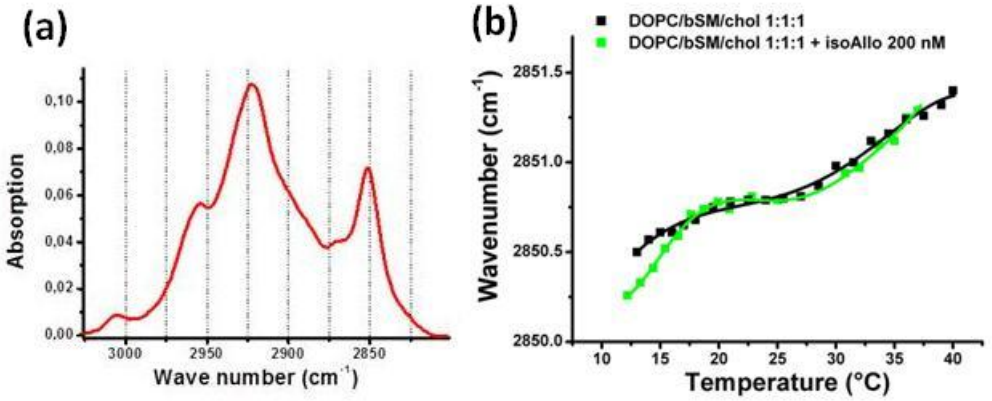

Figure 5.22: a) IR absorption spectrum for DOPC/bSM/chol 1:1:1 liposomes in the -CH stretching region. b) temperature dependence of the symmetric -CH_2 stretching frequency in the IR spectra for DOPC/bSM/chol 1:1:1 lipid mixture (black squares) and DOPC/bSM/chol 1:1:1 + 200 nM isoAllo (green squares). The continuous lines are guides for the eye. Modified from [275].

5.3 Pregnenolone sulfate (Preg-S)

Potentiating sterois of the $GABA_A$ receptor, like Allo, are uncharged and highly lipophilic molecules. By contrast, the most GABA-antagonist steroids display a charged sulfated group that keeps this class of neurosteroid from passing directly through the plasma membrane, but that in the same time can interact with the membrane causing a modulation of the membrane receptors. In order to test the effects of a charged neurosteroid on the model lipid membrane DOPC/bSM/chol 1:1:1 we decided to study pregnenolone sulfate (Preg-S) (manuscript in preparation).

We selected a single vesicle and performed the MAT mechanical characterization up to a lateral tension in the order of 4-5 mN/m to avoid the lysis event of the liposome. This step represents the control situation in which the mechanical properties are measured in the absence of the neurosteroid interaction. We next decreased the lateral tension to the initial value assuring a stable position for the vesicle in contact with the micropipette. The chamber was then filled with a specific amount of pregnenolone sulfate (Preg-S) in order to obtain the desired final neurosteroid concentration.

Figure 5.23 reports the comparison of the mechanical characterizations of a DOPC/bSM/chol 1:1:1 GUV in the absence and in the presence of 200 nM, 1 μM and 10 μM Preg-S. The striking evidence from the mechanical characterizations on the same vesicle is related to a strong increase of the lipid bilayer bending constant after exposing the bilayer to the Preg-S solution. Considering an analysis over 10 vesicles, we obtained a control value for the bending constant of $(12 \pm 5)\ k_BT$ and a value of $(45 \pm 10)\ k_BT$ after exposing the lipid bilayer to a 10 μM Preg-S solution. The features we obtained for the bending constant in the case of the lipid bilayer not exposed to the neurosteroids are lower than the values obtained by other techniques such as fluctuation analysis [310].

Using MAT, a certain amount of glucose and sucrose must be present in the solution in order to improve the visibility of the bilayer by Differential Interference Contrast (DIC) microscopy and to assure stability to the vesicles. It has been demonstrated that the bending constant for lipid bilayer is strongly affected by the presence of sugar in the solution, decreasing upon an increase of sugar concentration [311, 312]. It has to be considered that there could be also a contribution from gravity force when the GUV internal concentration of sucrose is higher than 100-200 mM [313]. To confirm the effect of sugar concentration on the measured mechanical properties of lipid bilayers, we performed an analysis on the same vesicles at higher glucose concentration (200 mM) obtaining, for the control experiment, a feature for the bending constant of $(7 \pm 3)\ k_BT$; again, this value doubled after the exposition to 10 μM Preg-S (Figure 5.24). Being mainly interested in the variation of this parameter as the vesicles are exposed to increasing concentrations of Pgn-S, we decided to work with a 110 mM glucose concentration.

Table 5.3 reports the results obtained for the different Preg-S concen-

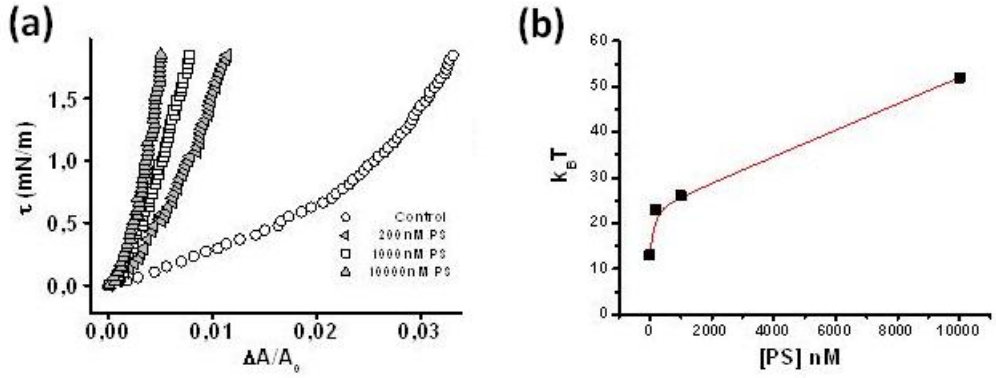

Figure 5.23: (a) Mechanical characterization of a DOPC/bSM/chol GUV in 110 mM glucose solution. The open circles represent the control experiment in the ansence of Preg-S; left-pointing triangles respresent the case of the same vesicle exposed to 200 nM Preg-S, the open-squares refer to 1 μM Preg-S and the up-pointing triangles to 10 μM Preg-S; (b) Variation of the bending constant for the vesicle as a function of Pgn-S concentration. The continuous line is a guide to the eye.

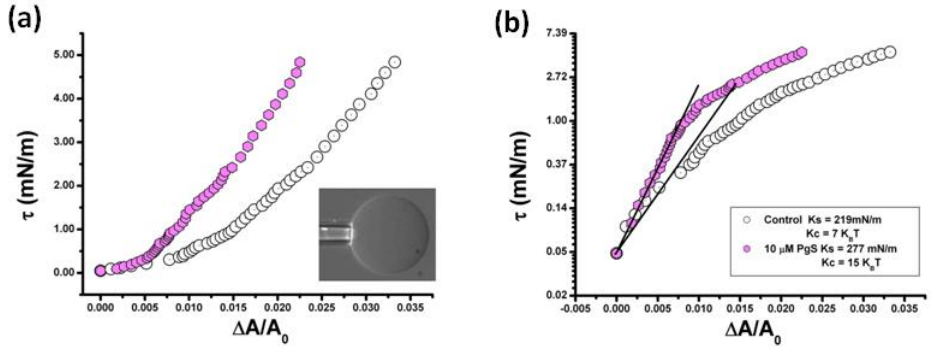

Figure 5.24: Same experiment as in Figure 5.23 but performed in 200 mM glucose instead of 110 mM: higher glucose concentration means a smaller value of the bending constant. (a) Mechanical characterization of a DOPC/bSM/chol 1:1:1 bilayer in the absence (white cirles) and in presence (purple circles) of 10 μM Preg-S; (b) same plot as in (a) but in the semi-log representation to clearly identify the region dominated by the entropic behavior (low tension region), from which it is possible to estimate the lipid bilayer bending constant (here K_c).

trations. Due to the strong scattering of the data from different GUVs exposed to the same environment (the scattering might be due to different GUV compositions related to the lipid mixture) we decided to analyze all the experiments on the basis of the relative variation in the bending constant as a function of Preg-S concentration. To perform this analysis, the values of the measured bending constant were normalized to that of pure lipid case (control experiment).

GUV	Normalized control	200 nM	1 μM	10 μM
DOPC/bSM/chol 1:1:1	1	1.6 ± 0.4	1.9 ± 0.3	3.9 ± 0.6

Table 5.3: Effect of Preg-S on the bending constant of lipid bilayers. The values for the control bilayer have been normalized and the values in the presence of Preg-S varying concentration are reported with respect to the normalized value.

We also measured the stretching constant of the lipid bilayers as a function of the amount of Preg-S to which he GUVs are exposed. The stretching constant, which is measured at high tension ($> 1\ mN/m$), might be affected by the contribution of the bending constant. To compare the stretching constants after the removal of the bending deformation contribution, we used the procedure reported in [265]. After the removal of the bending contribution, the stretching constant seems little affected by the presence of Preg-S. The stretching constant for the pure lipid system is (320 ±50) mN/m, while the corresponding value for the GUVs exposed to 10 μM Preg-S is (310 ± 50) mN/m.

Summarizing the above results, dealing with the effect of Preg-S on the lipid bilayer mechanical properties, it appears that the neurosteroid strongly affects the bending constant of lipid bilayer with a negligible effect on the stretching one. This behavior is different with respect to the case of allopregnanolone [274]. In fact, in the case of allopregnanolone, its interaction with the lipid bilayer induced a strong decrease of the mechanical parameters, as it is expected when an inclusion is present inside the bilayer [313]. Pregnenolone sulfate is characterized by a negatively charged group which can strongly affect its interaction with the lipid bilayers. It has been reported, by using fluorescently tagged Preg-S, that this sulfated neurosteroid is not able to cross the cell membrane [314]. Its interaction with the cell membrane is therefore mainly restricted to the outer leaflet of the lipid bilayer, with the charged group probably positioned at the lipid/water interface. The cell internalization in biological situations is probably obtained by active transporters.

In order to better understand the adsorption of Preg-S at lipid bilayers we studied the kinetics of the interaction by transferring a GUV by micromanipulation from a chamber not containing Preg-S to a chamber with a 10 μM Preg-S solution. This experiment allows measuring the relative area variation of the GUV, obtaining information on the molecular adsorption phenomenon. Figure 5.25 shows the relative area variation with time of a DOPC/bSM/chol 1:1:1 GUV when it is exposed to a 10 μM Preg-S solution. For comparison, in the same plot, a similar measurement, obtained by exposing a similar GUV to a 100 nM allopregnanolone solution, is reported. It is evident that the presence of Preg-S in solution has a negligible effect on the area variation of the GUV as opposed to the case of allopregnanolone where the exposure to a 100 nM solution induces a relative area increase of

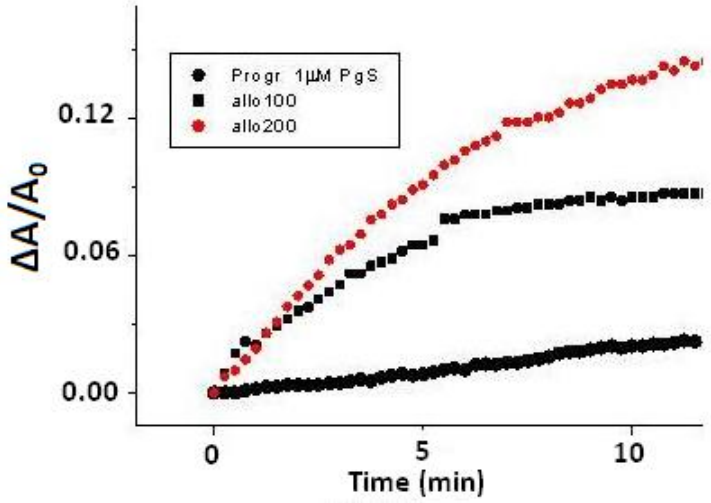

Figure 5.25: Kinetics of Preg-S interaction with lipid bilayers. The circles (black) circles show the relative area variation of a DOPC/bSM/chol 1:1:1 GUV when it is exposed to a 1 μM Preg-S concentration. The interaction kinetics (at much lower concentration, i.e. 100 and 200 nM) of allopregnanolone (a not charged neurosteroid) with GUVs with the same lipid composition are reported for comparison.

about 12-15%. The little increase of the area in the case of Preg-S could be accounted for just by the osmotic pressure variation produced by the water evaporation during the experiment [315]. Another possibility could be that the increase of the area induced by the adsorption of Preg-S is compensated for by the phase variation of the bilayer which favors a more compact bilayer.

In order to establish the possibility of an effect of Preg-S on the phase state of the bilayer we assembled Supported Lipid Bilayer of DOPC/bSM/chol 1:1:1 on a mica substrate and we studied the variation of the proportion of L_o and L_d domains when the bilayer is exposed to Preg-S. Figure 5.26 shows a sequence of AFM images on the same lipid bilayer area for increasing Preg-S concentrations.

Considering the lipid mixture we are using and the imaging temperature (20 $°C$), the higher and brighter domains can be associated with L_o domains, whereas the regions surrounding the brighter domains can be associated with the L_d domains. By injecting Preg-S in the imaging chamber it is evident that there is a very small overall increase of the area occupied by the lipid bilayer on the mica surface (the area occupied by holes in the SLB slightly decreases) while there is an increase of the fraction of the bilayer in the L_o phase. We don't have a clear understanding about the mechanism inducing an increase of the L_o fraction. It can be interpreted as an effect similar to an increase of the cholesterol concentration in the bilayer. However, a molecular dynamics investigation of the interaction of Preg-S with the lipid bilayer could help understanding the distribution of the neurosteroid in the lipid bilayer and its effect on the phase distribution.

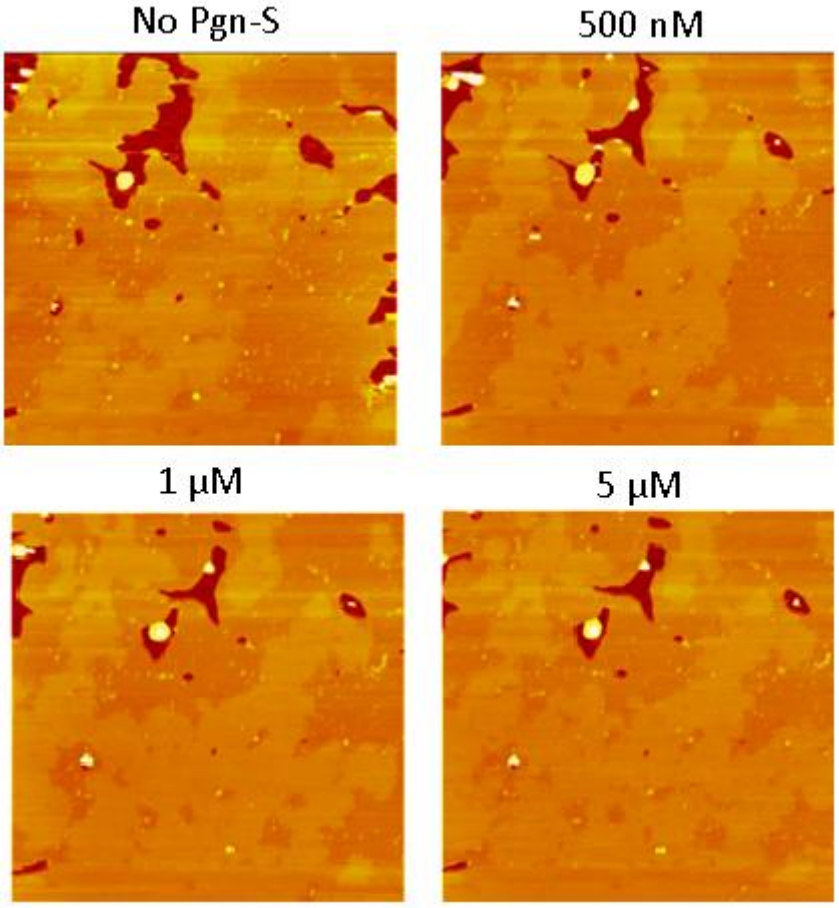

Figure 5.26: Effect of Preg-S on a SLB composed by DOPC/bSM/chol 1:1:1. The sequence of images have been obtained on the same bilayer area for increasing Preg-S concentrations. The darker regions represent holes in the lipid bilayer where the underlying mica support is exposed. The brighter domains are associated to L_o domains surrounded by L_d domains.

It has been demonstrated that some anesthetics act on the lipid bilayer by altering the proportion between L_o and L_d or the mixing temperature marking the transition from a uniform phase to phase separation and this mechanism has been considered relevant to the activity of specific membrane proteins like, for example, the $GABA_A$ receptor [74, 316].

The rationale behind this mechanism could be that a variation in the amount and stability of the liquid ordered phase, typically associated with the formation of lipid rafts in biological cell membranes, is relevant for the clustering of molecular partners and for activation of specific biochemical pathways. In this context, a recent coarse-grain molecular simulation studied the interaction of hydrophobic (both aliphatic and aromatic) compounds on the stabilization of phase separation in a ternary lipid mixture including a unsaturated lipid, a saturated lipid and cholesterol [300]. It has been found that aromatic molecules induce a stabilization of phase separation (meaning that they induce a stronger difference between the two involved

phases). This result agrees with what we found in the case of allopregnanolone [275]. From simulations, it appears that there are some molecules which are able to stabilize phase separation and other molecules, acting like linactants [317], which destabilize phase separation. In case of molecules favoring phase separation, they mainly partition in the liquid disordered phase and they are able to shift cholesterol from the L_d to the L_o phase, producing an increase of cholesterol concentration in the L_o phase. This cholesterol transfer increases the difference between the two domains.

Here we found that the insertion of Preg-S does not affect too much the height difference between the two phases, meaning that the sulfated neurosteroid is not able to change in a relevant way the order difference between the L_o and theL_d domains, probably as a consequence of the fact that its interaction is mainly confined to the lipid bilayer/water interface.

To better investigate the variation of the difference between the domains induced by exposing the bilayer to Preg-S molecules, we exploited the Force Spectroscopy technique to measure the most probable force value for the jump through event in the case of the pure lipid system and for the lipid system in the presence of Preg-S [286].

Figure 5.27 shows the most probable values for the two phases of the pure lipid bilayers and how the two values change when the bilayer is exposed to increasing Preg-S concentrations. It appears that Preg-S doesn't affect too much the most probable jump-through force values. There is just a small increase in the separation between the values on the L_d and L_o domains. The small effect could be interpreted as a very limited entry of Preg-S inside the lipid bilayer, accordingly to what has been obtained studying the interaction kinetics by microaspiration.

The depotentiating effect on the $GABA_A$ receptor current by sulfated neurosteroids shows a very limited enantioselectivity [60]. This behavior points to a probable relevant effect on the channel mediated by the lipid bilayer. At the same time, it has been demonstrated that Preg-S is not able to cross the lipid bilayer [314] and it affects the membrane capacitance without translocating inside the bilayer across transmembrane voltage [24]. In fact, the capacitance variation exhibited no voltage-dependence as expected for the movement of charged lipophilic molecules moving through the membrane electric field. Here we showed that the main effect of pregnenolone sulfate is that on the bending constant of the lipid bilayer. The overall area of GUVs did not change significantly upon being exposed to a neurosteroid solution, implying a limited insertion of the molecules in the lipid bilayer. The bending constant of lipid bilayer is a very important mechanical parameter which can be relevant for the activity of membrane proteins [318, 319]. Accordingly, the variation of this membrane parameter could represent another way by which the neurosteroid could produce its effects on the membrane proteins apart from a specific recognition event. The physical mechanism by which Preg-S could affect the bilayer bending constant is probably related to its electric charge. In fact, the lipid bilayer bending constant might have an energetic contribution coming from the elec-

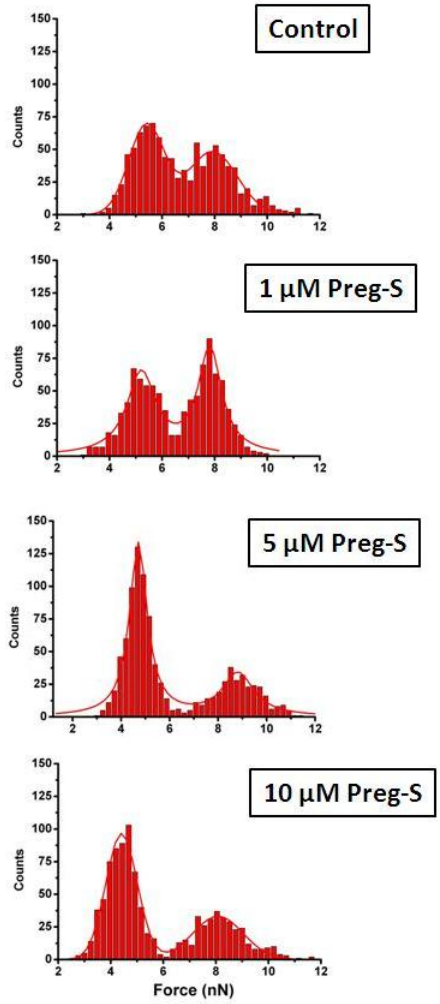

Figure 5.27: Atomic force spectroscopy study of a DOPC/bSM/chol bilayer exposed to increasing Preg-S concentration.

tric charge of the lipid/water interface [320]. This contribution is obtained by considering the diffuse double layer which is created in the water phase by the presence of an electrically charged interface and it is described by the Gouy-Chapman theory [322, 323, 324]. The effect of charged interfaces on the mechanical properties of lipid bilayers has been the object of theoretical investigations and it has been also experimentally verified [325, 326]. In our case, once the Preg-S molecules are incorporated in the lipid bilayer they might expose the electric charge to the water phase thus increasing the bending constant due to the coulombian repulsion between the negative charges. The increased value of the bending constant could remove part of the membrane undulation producing an increase of the projected lipid bilayer area as sketched in Figure 5.28.

One could argue that a similar increase in the projected area should be clearly visible in experiments where a GUV grabbed by a micropipette is exposed to a solution containing Preg-S molecules. However, typical transfer

experiments in which a GUV is transported from a chamber without Preg-S to a chamber with the neurosteroid should be performed by applying a stable aspirating pressure to the GUV in order to assure enough stability to the system during the micromanipulation. In this case, the GUV could be transferred to the chamber in a situation where the undulation fluctuations have been already removed by the applied tension, resulting in a negligible effect by Preg-S on the overall area variation.

From the results we obtained with Preg-S we can state that the amount of neurosteroid which is adsorbed to the lipid bilayer is very small. Its interaction with the lipid bilayer is probably confined to the external leaflet of the bilayer. In vivo, the transfer of Preg-S inside the cell occurs by an active transport. The main effect of Preg-S on the lipid bilayer is a variation of the bending constant probably due to a variation of the electric surface charge of the bilayer. This parameter of the lipid bilayer is however very relevant for the activity of membrane proteins [319].

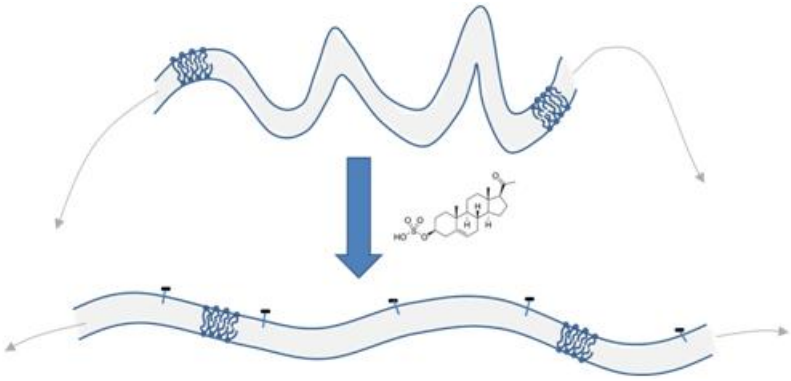

Figure 5.28: Scheme of the effect of Preg-S on the bending constant of lipid bilayers. In a) a lipid bilayer endowed with high undulation fluctuations is represented. This configuration results from a bending constant of the lipid bilayer comparable with thermal energy. After exposing the lipid bilayer to Preg-S, the charged molecules incorporated at the bilayer/water interface produce an increase of the bending constant removing the largest fluctuations.

Chapter 6

Effects of neurosteroids' enantiomers on model lipid bilayer

Because enantiomers have mirror image shapes and receptor have well-defined and structurally mantained binding pokets, receptors can discriminate between ligands of different shapes. By contrast, the lipid membrane is a dynamic environment that does not mantain structurally well-defined binding sites for steroids. Hence, in the membrane, the effects of *ent*-steroids will be essentially equivalent, since both enantiomers display the same phyiochemical properties. However, the lack of enantiospecific interactions between *ent*-steroids and the lipid membrane is by no means obvious a priori, as phospholipids and cholesterol are chiral molecules known to display enantiospecific interactions. Therefore, the direct receptor binding and indirect membrane perturbation effects of the steroid on receptor funtion could potentially be distinguished by differences in the magnitude of enantioselectivity observed for each mechanism of modulation.

Here we tested the effect of *ent*-Allo and *ent*-IsoAllo on a DOPC/bSM/chol 1:1:1 mixture which resemble plasma membrane of mammalian nerve cells. As usual, we decided to start from a condition where the domains relative to the liquid ordered and liquid disordered phase were clearly detectable, in order to see what is the effect of the two enantiomers on phase separation.

6.1 *Ent*-Allopregnanolone

Figure 6.1 report a sequence in which *ent*-Allo was added in steps of 50-100 nM. Analyzing the relative changes in the fraction of L_o/L_d area and in the overall area of patches 1-2-3 marked in Figure 6.1 (a) we can state that with 300 nM ent-Allo the L_o fraction decrease by about 2-3% while the overall lipid area increases by about 10%. With Allo we had an average area increase of 24% and a decrease of the L_o fraction of about 10%, so we can say that Allo and ent-Allo affect the lipid bilayer in the same way (expansion of the bilayer and decrease of the liquid ordered phase), *ent*-Allo

having a quite weaker effect.

Figure 6.2 shows another sequence of *ent*-Allo addition on a uniform bilayer (pictures are frames of a movie) and still we can observe a global decrease of the L_o phase, even though some single L_o domains, if taken individually, do expand: this behavior could be due to a non-uniform distribution of cholesterol inside the bilayer.

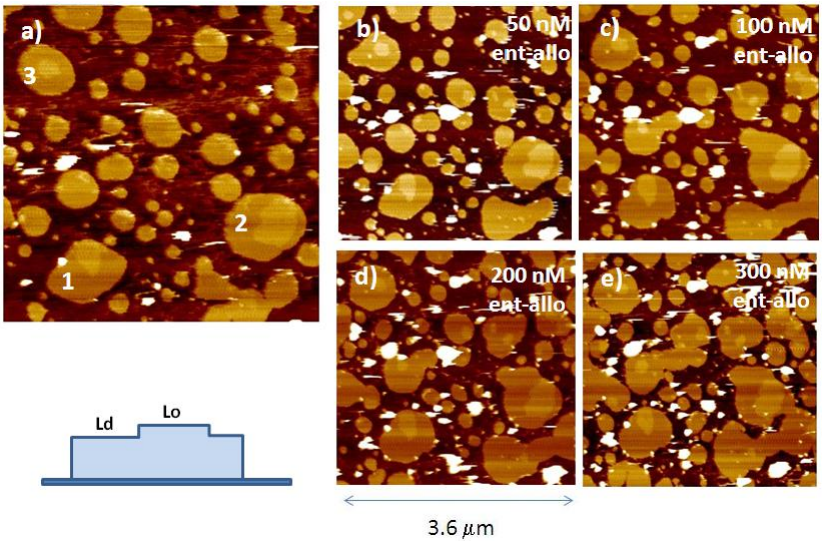

Figure 6.1: Effect of ent-Allo on DOPC:SM:chol 1:1:1 supported bilayer; overall view of bilayer patcher before (a) and after the addition of (b) 50 nM; (c) 100 nM; (d) 200 nM; (e) 300 nM *ent*-Allo.

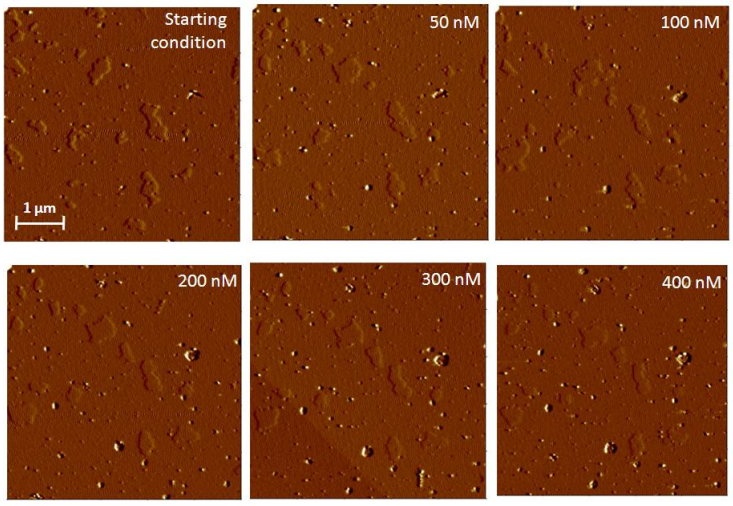

Figure 6.2: Effect of *ent*-Allo on a uniform DOPC:SM:chol 1:1:1 supported bilayer; globally, there is a reduction of the liquid ordered phase, even if some liquid ordered domains do expand: probably this is due to a non-uniform distribution of cholesterol inside the bilayer. Pictures are frames of a movie.

6.2 *Ent*-isoAllopregnanolone

Figure 6.3 report a sequence in which *ent*-isoAllo was added on quite uniform DOPC/bSM/chol 1:1:1 supported bilayers. The effect we can observe is an overall compacting of the bilayer, which is highlighted by the formation and the broadening of the holes; at the same time there is a general decrease in the liquid ordered area fraction of about 3%. These results are in agreement with what we obtain when we add isoAllo on the same lipid mixture (Figure 6.4): again, we notice a compaction of the bilayer with an increase in the area occupied by the holes, and a decrease of about 4% in the liquid ordered area. Moreover, the addition of isoAllo and *ent*-isoAllo produce a very similar trend in the variation of the domain height difference *vs* increasing neurosteroids' concentrations (Figure 6.5), affecting the thickness of both the liquid phases. Building on these achievements, we can state that the two enantiomers, isoAllo and *ent*-isoAllo, affect the lipid bilayer state of phase in the same manner.

However, the fact that isoAllo causes a reduction in the liquid ordered area is in contrast with what we previously obtained with the addition of

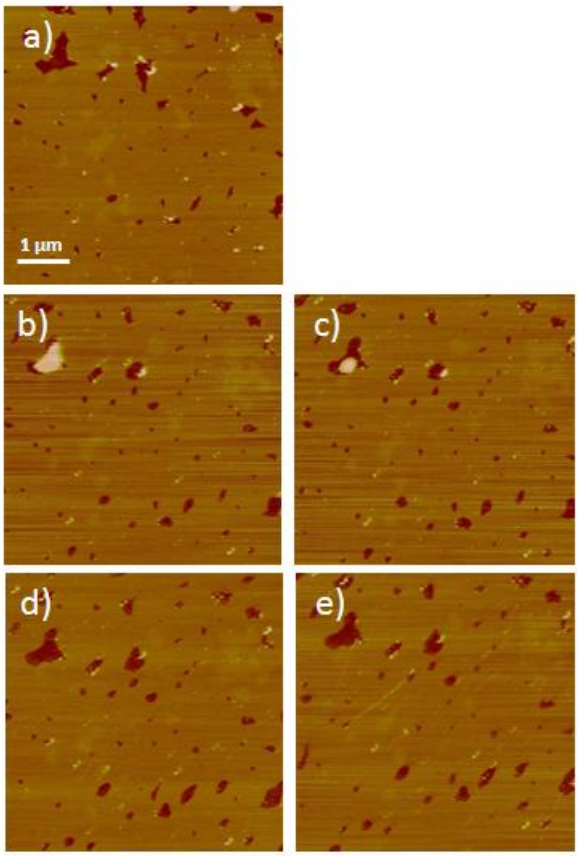

Figure 6.3: Effect of *ent*-isoAllo on DOPC:SM:chol 1:1:1 supported bilayer; overall view of the bilayer before (a) and after the addition of (b) 100 nM; (c) 200 nM; (d) 300 nM; (e) 400 nM *ent*-isoAllo.

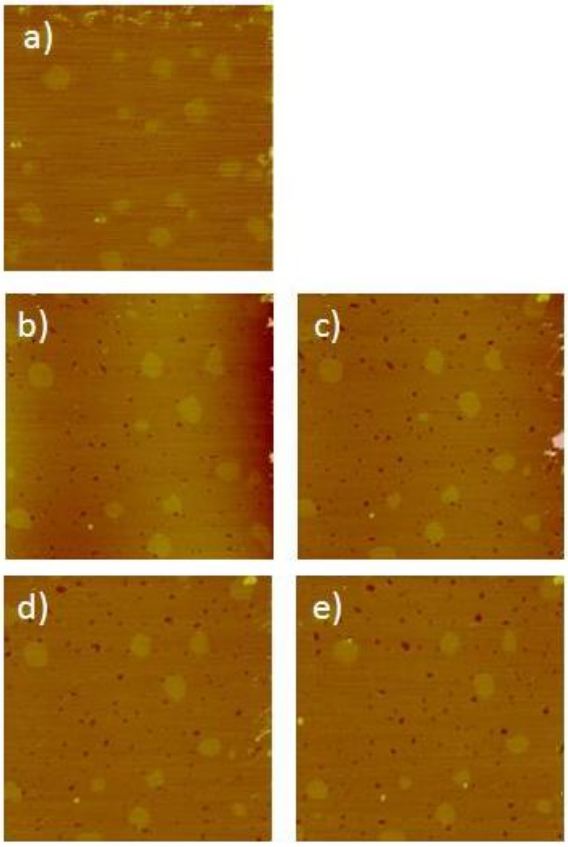

Figure 6.4: Effect of isoAllo on the same lipid mixture tested in the experiment of *ent*-isoAllo (Figure); overall view of the bilayer before (a) and after the addition of (b) 100 nM; (c) 200 nM; (d) 300 nM; (e) 400 nM isoAllo.

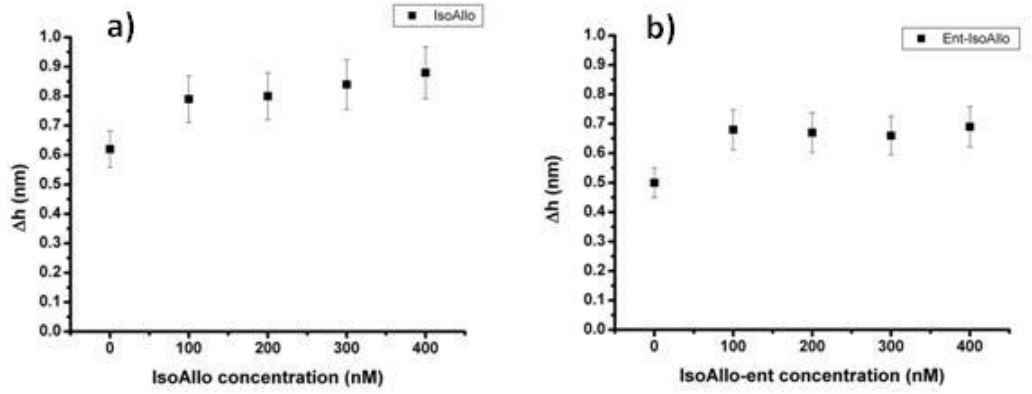

Figure 6.5: Effect of isoAllo and *ent*-isoAllo on the height difference between the L_o and the L_d domains of a DOPC/bSM/chol 1:1:1 supported bilayer. The two behaviors correlates: in both cases the inserted neurosteroids determines an increase in the height difference, meaning that the domains become more different in terms of composition.

isoAllo on the same nominal lipid mixture (Paragraph 4.2), when we observed a promoted increase in the L_o phase. These opposite results can be explained in light of a probable variation in the lipid composition of the mixtures used for different experiments, being the behavior in the ternary phase diagram very sensitive to changes in concentrations, especially for what may concern the amount of cholesterol. Little deviations in the lipid composition mixture can bring to different results: here we want to stress that, irrespective of the absolute effect given by the presence of the neurosteroid, the two enantiomers cause the same effects on the investigated properties (L_o to L_d relative area variation and height difference between the two phases), essentially meaning that lipid bilayers does not diplay enantioselectivity for such a pair of molecules, even if a small effect is found, like in previous investigations [327].

Chapter 7

Effects of neurosteroids on nerve cells

Aim of this Chapter is to evaluate the effects of neurosteroids of pharmacological interest, allopregnanolone (Allo) and dehydroepiandrosterone (DHEA), on the reorganization of the cytoskeleton and on the mechanical properties of nerve cells.

7.1 The neuronal cytoskeleton

Neurons possess a distinct cytoskeleton. The cytoskeleton (CSK) is an interconnected structure of various cross-linked and interlinked filamentous biopolymers that extends from the nucleus to the cell surface. The mechanical forces of the cytoskeleton are associated with many biological functions of cells such as its growth, differentiation, and apoptosis, (programmed cell death) which cause the changes in cell shape [328]. Numerous evidences have shown that CSK plays a vital role in transmitting mechanical stresses from the cell surface to the nucleus across the cytoplasm [329, 330, 331, 332].

The cytoskeletal network is composed of three types of filaments : actin filaments, microtubules and intermediate filaments [333] as shown in Figure **??**. The actin filaments (diameter of 6-8 nm) are woven into network with little extensible cross-linked filaments [328]. These filaments are in tension due to the cell contractile apparatus and also passively by the cell distension through its adhesive substrate or by the swelling pressure of liquid cytoplasm [334]. An actin filament is assembled by numerous actin monomers via noncovalent interactions. The polymerization and depolymerization of actin monomers (G-actin) into actin polymers (F-actin) generates mechanical forces that are important for many cellular processes, such as generating cell membrane propulsion and protrusion counteracting plasma membrane tension and deformation changes during endo- and exocytosis, and acting as molecular tension sensors to regulate numerous aspects of intracellular homeostasis.

Microtubules are tubular biopolymers (outer and inner diameter of 24 and 12 nm, respectively) [334] and are in compression to resist the contrac-

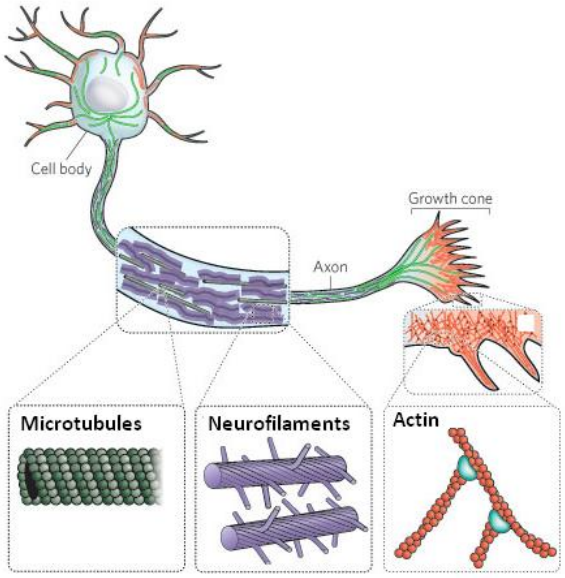

Figure 7.1: Cytoskeletal elements of a nerve cell. Adapted from [335].

tion from interconnected actin network [336]. Microtubules generate forces in cells through the polymerization of α-β tubulin dimers or by catastrophic depolymerization events that result from dynamic microtubule instability [337]. In addition, microtubules can store elastic energy from frequent bending and can experience breaking, which has been proposed to mediate mechanochemical signalling in cells [338]. Microtubules generate pushing forces or pulling forces, thereby providing structural support to membranes and proteins or transporting molecular cargo. Besides their classical cargo transport and structural support actions, microtubules have recently been shown to have previously unrealized functions in neurons in the regulation of dendritic spine morphology and synaptic plasticity; moreover, forces generated by microtubule dynamics are crucial to the axons guidance and lengthening. Microtubules are stabilized by cross-linking proteins such as microtubule-associated protein 1 (MAP1) (in axons and dendrites), MAP2 (in dendrites),and Tau (in axons). It is the cytoskeleton together with its associated proteins that causes neuronal processes to be under tension [339, 340].

Intermediate filaments (diameter of 10 nm) that are believed to be in tension contribute significantly to cell stiffness only at large strains ($>$ 20 %) [341]. Neurofilaments, the most representative type of intermediate filaments in neurons, can dynamically interact with microtubules and other cytoskeletal elements, forming a physically interlinked filamentous network. Several observations indicate that neurofilaments can modulate mechanical forces in axons. Structurally, neurofilaments are long filamentous fibres that have side-arms giving rise to a 'whisker-like' or bottle-brush appearance. The side-arms of neurofilaments are thought to provide structural support in axons and thereby to protect them from compression loads [342].

7.2 Neurosteroids' effects on cytoskeleton

Neurosteroids are thought to exert their effects through binding to nuclear receptors in neurons, which triggers the regulation of gene transcription, and through binding at the membrane level to neurotransmitter receptors, like $GABA_A$ or NMDA receptors. Neverthless, despite continuous research, no specific DHEA receptors have been identified in the central nervous system [343]. For this reason, it is thought [344] that DHEA can operate through a novel model of action, i.e. a direct regulation at the cytoskeleton level.

The hypothesis that DHEA interacts directly with cytoskeleton components is supported by several and sometimes conflicting observations, but in any case a direct change in the morphological features of the cytoskeleton is reported. Using fluorescence microscopy, in [345] it was found that the addition of DHEA lead to profound and characteristic changes in the morphology of microtubules and actin microfilaments in SH-SY5Y cells, an established in vitro model for neurons. These effects were also characteristic for the differentiation state of the cells because the metabolism of steroid hormones changes with differentiation. Analyzing the effect of steroid hormones on microtubules it was found, for example, that physiological concentrations of DHEA lead to numerous filopodia and induced stress fibers. The observed effects occured within minutes and could not be prevented by inhibitors of protein biosynthesis, indicating their non-genomic nature.

Almost all of the SH-SY5Y cells exhibited thin cortical and central stress fibers and small focal adhesion contacts. Some of these cells had short processes and/or a few filopodia. In [346] it is shown that 30 min incubation with 30 nM DHEA increased stress fiber assembly and the formation of focal adhesion contacts in SH-SY5Y cells. Both effects were mimicked by DHEA-Bodipy.

Moreover, in primary cultures of mouse embryonic neocortical neurons, it was found that DHEA incresed the length of neurites containing the axonal marker Tau-1 [347] and in [348] it is reported that DHEA tightly binds to MAP2C, a microtubule-associated proteins characterized by their ability to promote tubulin polymerization and to stabilize microtubules.

If the results reported up to this point seem to indicate a promoted stabilization of the cytoskeleton due to the presence of DHEA, data presented in [349] are against these evidences. Here a different cell line was investigated, PC12 cells, and in this case DHEA have been found to stimulate actin depolymerization, as measured by the ratio of G-monomeric to total cellular actin, an established marker of actin cytoskeleton dynamics; in addition, submembrane actin filaments, a fast-response cellular system regulating trafficking of catecholamine vesicles, disassembly. An actin meshwork inhibits catecholamine secretory vesicles from reaching exocytosis sites. By decreasing this actin meshwork, DHEA increase the ability of catecholamines to be secreted from secretory vesicles.

The same effect is reported for Allo, whose effect on catecholamine se-

crection is preceded by an acute increase of monomeric G-actin, suggesting a rapid stimulatory effect on actin depolymerization and the subsequent destabilization of actin filaments. Data on steroid actin filament destabilization were further confirmed by confocal laser microscopy, showing a steroid-mediated decrease in rhodamine-stained actin, confined to the subplasmalemmal area [349].

Also in [350] the effect of Allo in the cytoskeletal organization is reported. In this case, Schwann cells were employed and after Allo treatment, a dynamic rearrengment of the cortical actin cytoskeleton was observed; in particular, actin accumulated at the leading edge of cells and in filopodia, whose number and lenght was significantly increased by the tratment. Moreover, by adding cytochalasin D (an actin depolymeryzing drug), the Allo effect was completely counteracted.

7.3 Effect of Allo on neuroblastoma cells

In Chapter 5 we evaluated the effect of allopregnanolone (Allo) on model lipid bilayers in order to understand how the insertion of this neurosteroid of pharmacological interest affects the mechanical and thermodynamical properties of lipid membranes. Since several studies proved the potential role of this molecule in the prevention, delay and treatment of neurodegenerative diseases such as Alzheimer's, we decided to study the effect of allo on model lipid membranes whose composition resembled that one of mammalian neurons. If in that case our interest was mainly devoted to a strict chemical-physical characterization - in terms of phase diagram properties - of a model system, here our main focus is to elucidate the role of this molecule in affecting the mechanical/thermodynamical properties of the real biological target, i.e. nerve cells. In collaboration with Prof. Giulia Puja (Department of Life Sciences, UNIMORE) we decided to concentrate our attention on the well-known human-derived cell line SH-SY5Y (in the following: NB, neuroblastoma cells).

Figure 7.2 shows some optical microscopy images of living NB cells. In particular, in Figure 7.2 (d) the experimental working condition is represented, with the AFM cantilever positioned on a well-defined NB cell, even if it is usually difficult to say whether the cell under investigation is single or not. In most cases the cells we studied were agglomerated in clusters.

Figure shows some typical AFM topographical images of living NB cells; the cytoskeletal organization of these cells is quite evident. The neuronal axon is a long membrane-bounded extension, in which neurofilaments (a class of intermediate filaments in neurons) form a structural matrix that embeds microtubules, which transport materials from the cell body to the axon terminals at the synapses. Dendrite spines are branched projections formed out of actin microfilaments where neurons receive, process and integrate inputs from their presynaptic partners in order to propagate the electrochemical stimulation.

Recent evidence [352] indicates that cell morphology and tissue organ-

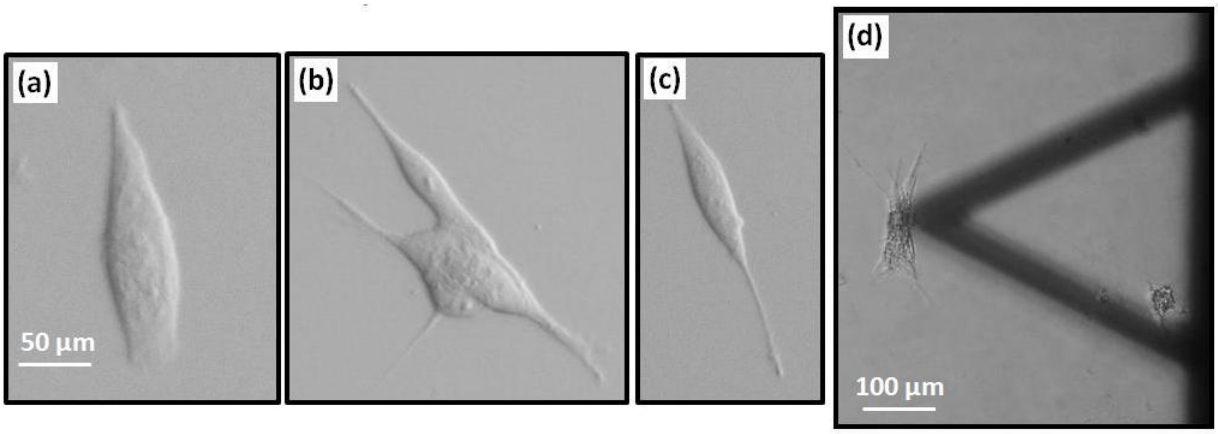

Figure 7.2: (a), (b), (c) Representative optical microscopy images (in differential interference contrast) of NB cells. The long, slender projections in (b) and (c) can interpreted as axons; (d) usual experimental working condition where the AFM cantilever is placed on a single NB cell.

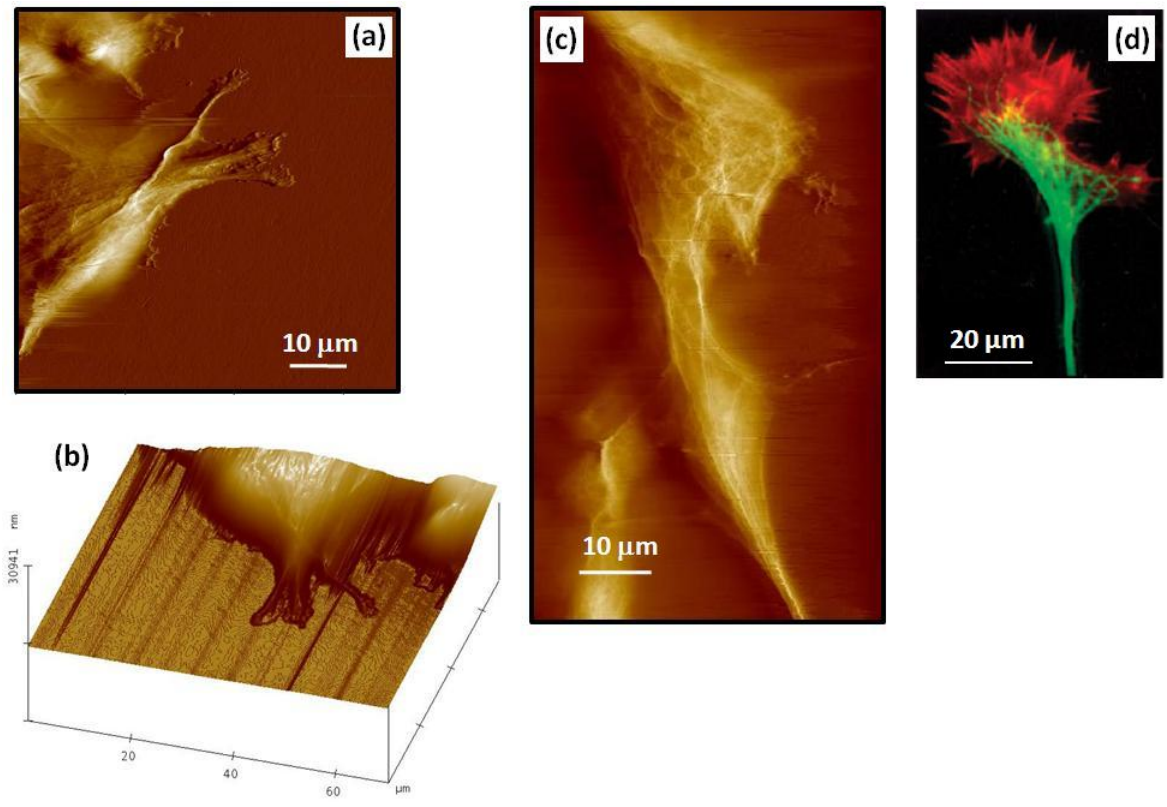

Figure 7.3: Representative AFM topographical images of NB cells (a) and (c) where the organization of the cytoskeleton and the dendritic spines are particularly evident; (b) is a 3D recontruction of image (a); (d) is a fluorescent image of a neuron where microtuboles (green) and actin-filaments network are highlighted (adapted from [335].

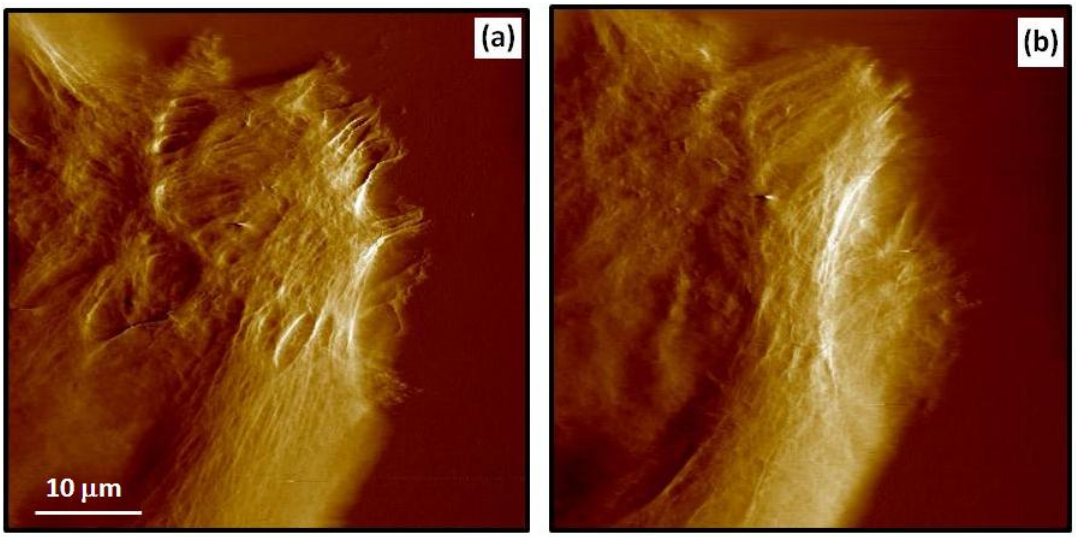

Figure 7.4: AFM force error images of a cluster of living NB cells before (a) and after (b) 1 hour perfusion of 100 nM Allo.

isation is obtained through the regulation of the actin cytoskeleton. Actin filaments closely interact with receptors in the cytomembrane and mantain the cellular integrity by carrying tensile and compressive forces [117]. Therefore, the mechanical properties of cells (such as elasticity and surface roughness) are directly linked to the dynamics of actin filaments.

To study the morphological changes, if any, of NB cells under the effect of Allo, AFM images of normal NBs and treated cells were obtained and compared, respectively. In Figure 7.4 (a) the AFM force error image of a normal living NB cluster of cells is reported, while 7.4 (b) shows the same cluster after 1 hour of 100 nM Allo perfusion. No evident changes can be observed, apart from a slight general loss of definition in the image. Before the treatment, the cells were arranged in a relatively rough, highly organized network, where fine filamentous structures associable to actin filaments were clearly visible. As compared with the normal neuronal cells, the cytoskeletal structures of treated cells appear smoother and less differentiated; also the organization of the dendritic spines looks less defined. These evidences are not so straightforward, but point in the direction of a global reorganization of cytoskeletal structures probably associated to an actin depolymerization due to the presence of Allo, as also suggested in [349, 350]. However, by performing a real-time characterization of the mechanical properties during Allo perfusion, no notable variation can be observed up to 1 hour of treatment (Figure 7.5), apart from a very slight softening of the cells and a very faint increase in the overall height.

The concentration of 100 nM was estabilished since an effect of Allo on pure model lipid membrane was observed already at 50 nM (see Paragraph 5.1.1). Since no evident results were observed at this concentration, if we neglet the apparent slight changes in the organization of the cytoskeleton, we decided to perfuse the cells with Allo 200 nM. Results on a well-defined

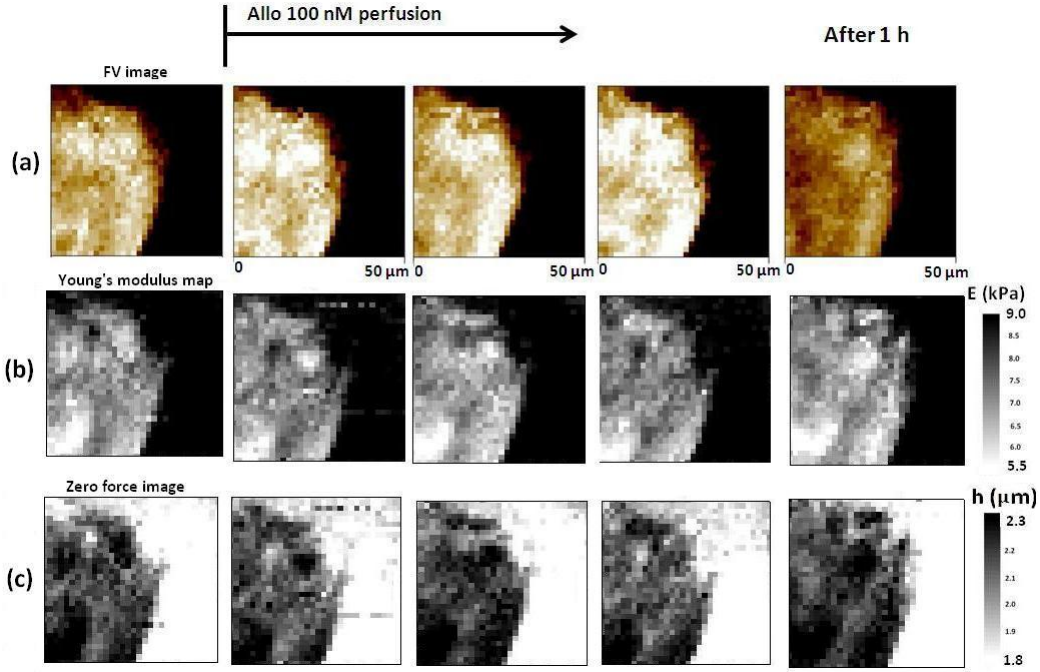

Figure 7.5: Mechanical charaterization of NB cells of Figure 7.4. (a) Sequence of force volume images reported in (b) as Young's modulus map and in (c) as zero-force image. The Young's modulus map shows the mechanical properties of the system reported as a Young's modulus value for each pixel, while in the zero-force image the real topography of the sample is reconstructed. It is necessary to furnish the Young's modulus map and the zero-force images because force volume images are not truly indicative of the behavior of the system: the same deflection threshold must be guaranteed for each force curve but in many cases this condition is not satisfied.

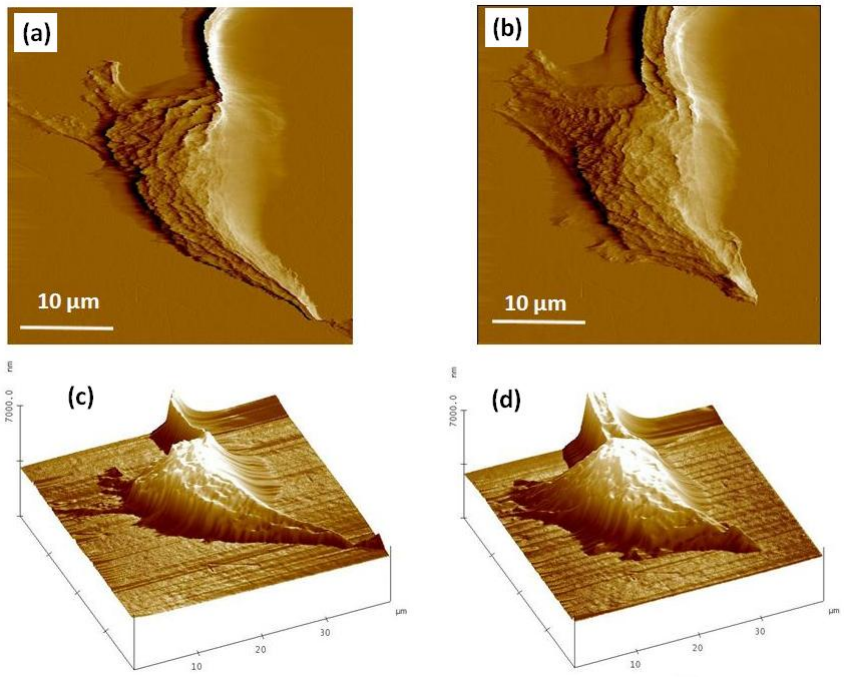

Figure 7.6: AFM topographical image of a living single well-defined NB cell before (a) and after (b) 200 nM Allo perfusion; (c) and (d) are 3D reconstructed images repectively of (a) and (b). An overall increase in the height of the cell and some modifications in the organization of the cytoskeleton can be observed.

single NB cell are shown in Figure 7.6; after the 200 nM treatment we see again an increase in the height of the cell, as an overall blowing, and a slight smoothing in the cytoskeletal organization. Also some modifications in the dendritic structures are detectable.

Figure 7.7 reports another topographical charaterization of the effect of Allo 200 nM on the terminal part of a NB cell cluster. In this case the most remarkable observations can be done once Allo was perfused and than subsequently removed by a back-perfusion to the original extracellular solution (Figure 7.7 (c)). In this last image the cytoskeleton appears very destructurated and the original actin-like filament network appears smoothed and less defined. However it is hard to say if these modification are attributable to a time-dependent action of the neurosteroid of the cells or to the back-perfusion to the original solution where probable osmotic effect may be present. Anyway, the mechanical charaterization during the perfusion of Allo 200 nM of another region of this cluster is reported in Figure 7.8. Another time there is not a well-defined evidence of a clear effect due to the presence of Allo: a very small softening of the sample can be observed, in addition to a slight increase in the height, but these are very tiny effect that for the moment can not be ascribed to a specific effect of the neurosteroid.

A slight softening of NB cells under the effect of Allo can be gathered

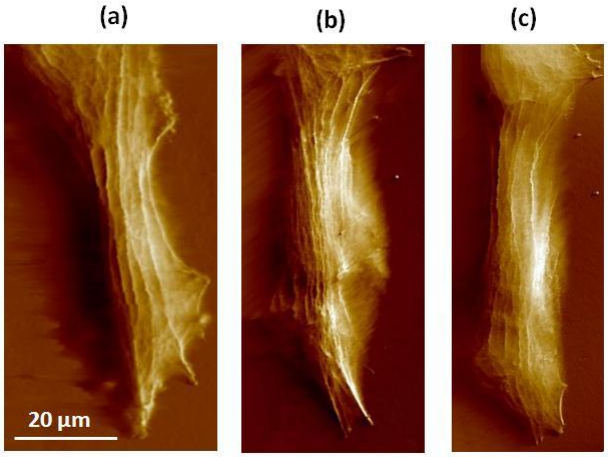

Figure 7.7: AFM topographical images of a cluster of living NB cells before (a) and after (b) 1 hour perfusion of 200 nM Allo. In (c) the same cells are reported after 1 hour of back-perfusion to the original solution.

also from data acquired by indentation modulation technique. Figure 7.9 reports a complete mechanical characterization of a NB cell as a function of Allo concentration (100-200 nM) in terms of complex shear modulus G^*. When studied separately, the storage modulus G' and the loss modulus G'' do not show any relevant change as a function of Allo concentration (sequence in Figure 7.9 (a)); however, when data are reported as complex shear modulus $|G|$ as a function of frequency, a general shift to lower values is detectable as Allo concentration increase (Figure 7.9 (b)); this means a general softening of the cell under investigation. This behavior is confirmed by Figure 7.9 (c), where the effect of Allo on the force curves is reported. Notably, the β exponents that describe the scaling of G' as a function of frequency are in agreement with typical values reported in the literature [255], meaning a mechanical behavior compatible with so-called soft-glassy materials.

7.4 Effect of DHEA on neuroblastoma cells

Besides the characterization of NB cells in the presence of Allo, we performed a similar AFM characterization of NB cells treated with dehydroepiandrosterone (DHEA). In this case we did not performe a perfusion procedure to exchange the extracellular medium, but we directly inserted the neurosteroid in solution in order to achieve the desidered concentration. Moreover, it must be stressed that this is a preliminar study and only data for mechanical analysis can be reported here.

Figure 7.10 reports the results from an indentation modulation experimet carried on the same living NB cell at different DHEA concentration. As DHEA concentration increases, a general stiffening (i.e. higher $|G|$) of the cell is observed and this effect is detectable already at low concentration

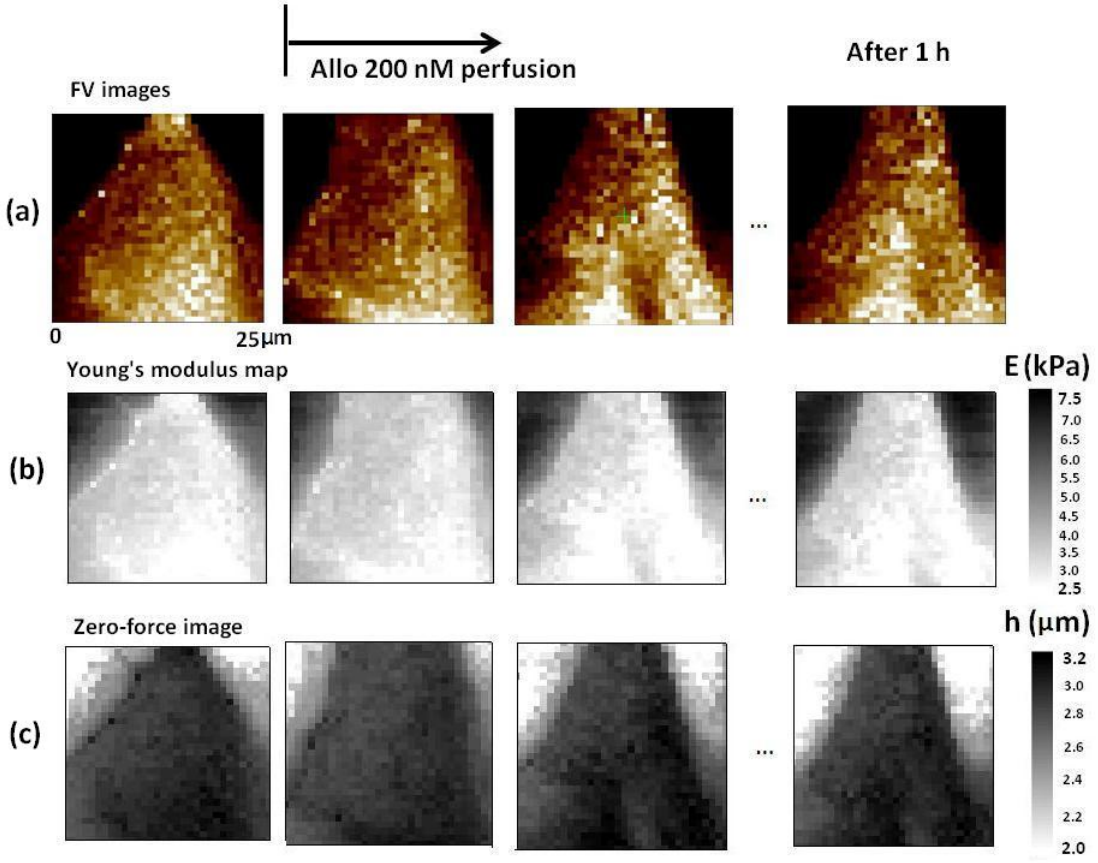

Figure 7.8: Mechanical characterization of a NB cell cluster treated with Allo 200 nM; (a) Sequence of force volume images; (b) Sequence of Young's modulus map; (c) Sequence of zero-force images. These sequences represent the real-time 1 hour perfusion of Allo 200 nM. No appreciable changes can be reported during the perfusion: only after 1 hour the sample appear a little bit softer and higher, but this variation are not indicative of a streightforward effect of the tested neurosteroid.

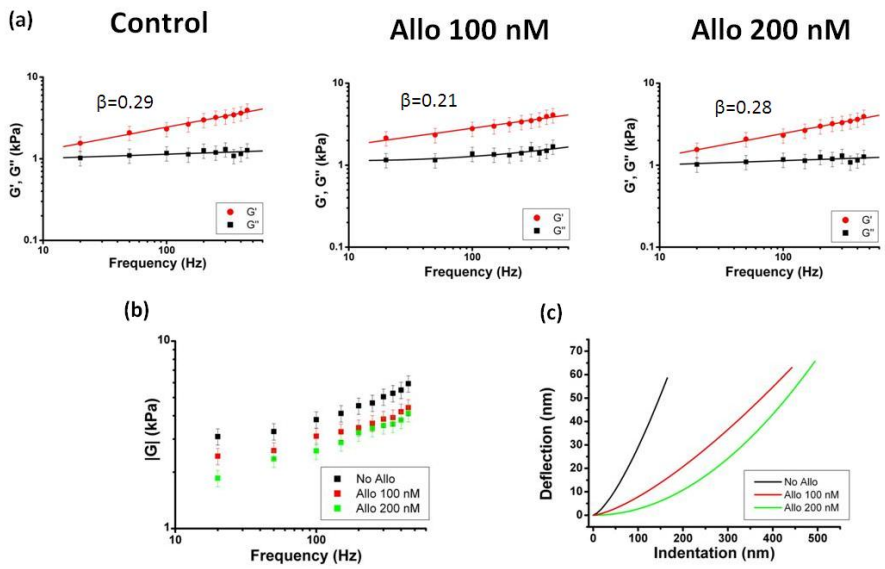

Figure 7.9: Indentation modulation analysis of NB cells treated with Allo 100 nM and Allo 200 nM; in (a) a sequence of plots reporting the behavior of the storage modulus G' and the loss modulus G" *vs* frequency as a function of Allo concentration (100-200 nM) is reported; (c) shows the effect of Allo on the force curves; (d) reports the trends of the complex shear modulus |G| in function of frequency for the investigated Allo concentration.

(200 nM). The overall behavior of $|G|$ as a function of frequency for different DHEA concetrations (200 nM and 1 μm) is reported in Figure 7.11 where the results of indentation modulation on another living NB cell are presented.

These experiments highlight that DHEA seems to enhance either the elastic and the viscous components, since a remarkable increase in the absolute values of both G' and G'' is observed with increasing DHEA concentration at variance with the results obtained with Allo, where only small softening effects were detectable. In other words, DHEA seems more effective in changing the mechanical properties of NB cells with respect to Allo and in this case a topographical characterization would be very helpful in order to understand how this steroid affects the reorganization of the cytoskeleton. In particular, the observed stiffening could be related to an increase in the stress fibers, as reported in [346], where the same cell line was studied under the effect of DHEA.

Fast responses, as observed in the case of DHEA, where mechanical variations were observed immediately after steroid insertion, are indicative of a nongenomic nature of the physiological processes modulated by this steroid. Responses that follow nongenomic pathways are not rare [351], but we must stress that the effects of steroids are typically mediated by the modulation of gene expression and are known to occur within a time lag of hours or even days, as may happen in the case of Allo, where appreciable effects were not detected within one hour.

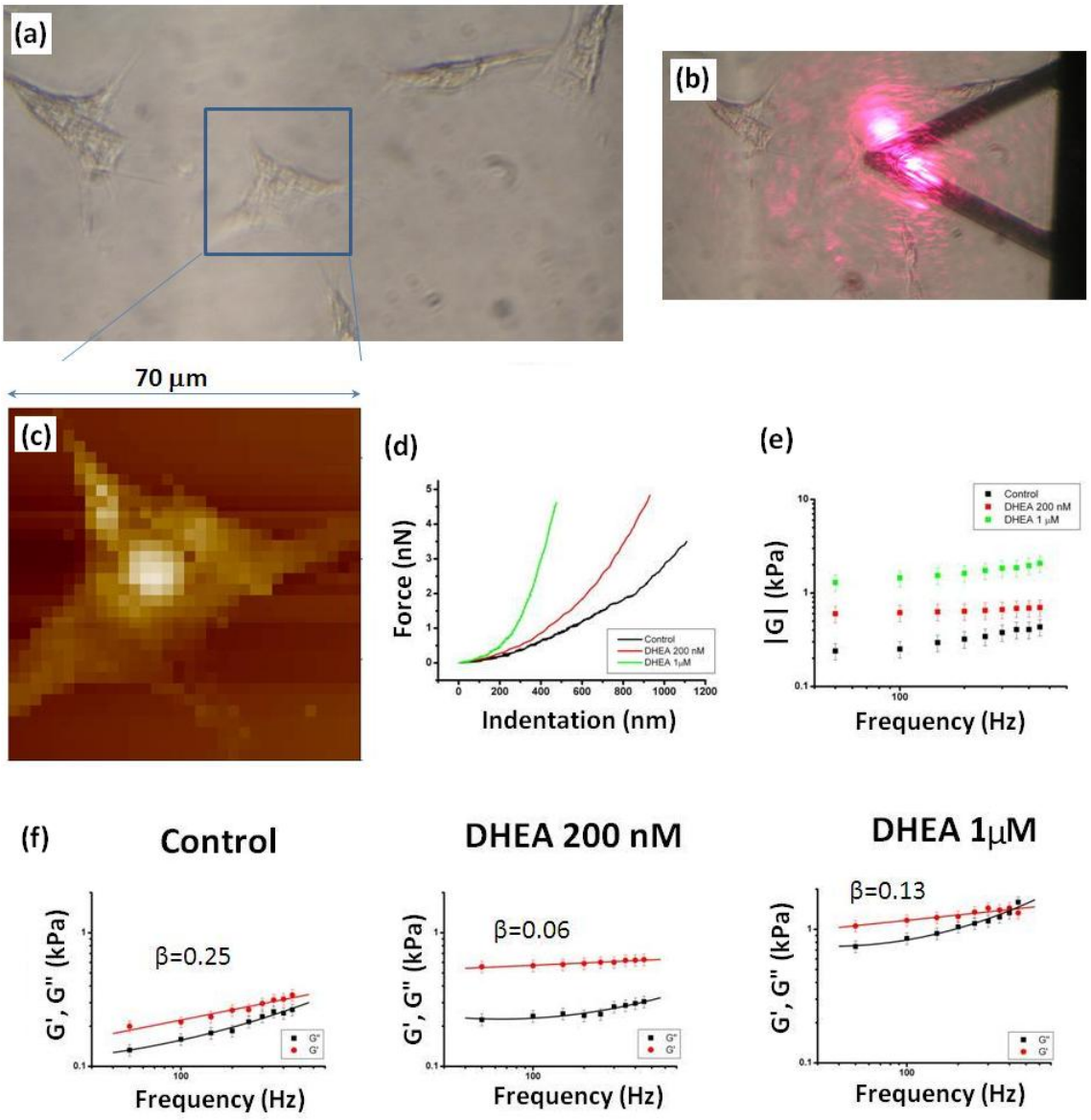

Figure 7.10: (a) Optical microscopy image where a living single well-defined NB cell is identified by the blue square; (b) Optical microscopy image that shows the AFM cantilever placed on the NB cell of interest; (c) Force volume relative to the control situation; (d) Behavior of the force curves as DHEA concentration increases: the force curves are relative to the center region of the investigated cell; (e) Plot of the shear modulus $|G|$ as a function of frequency for different DHEA concentrations; (f) Sequence where the trends of the storage modulus G' and the loss modulus G'' are reported as a function of frequency for the indicated DHEA concentrations. β scaling exponent are in agreement with soft-glassy materials.

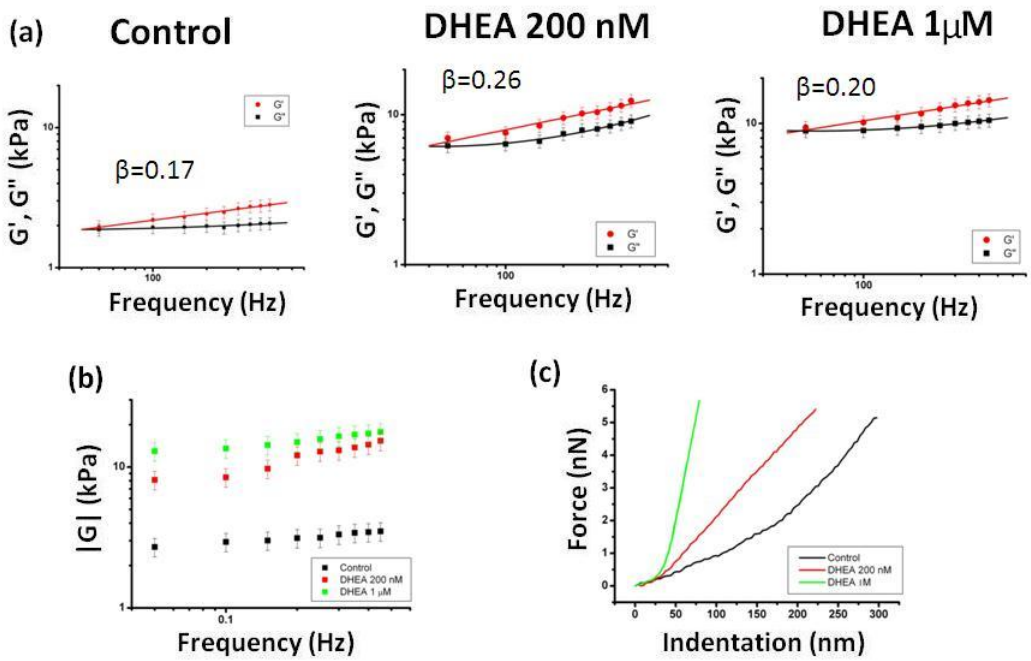

Figure 7.11: (a) Sequence that shows the behavior of the storage modulus G' and the loss modulus G'' as functions of frequency for different DHEA concentrations; β scaling exponent is in agreement with the behavior of soft-glassy materials (b) Plot of the shear modulus $|G|$ as a function of frequency for different DHEA concentrations; (c) Force curves reported for different DHEA concentration.

Chapter 8

Physical approaches for regenerative medicine

Fibrin/keratinocytes structures are currently used for epithelial stem cell therapy and corneas transplantation. As already pointed out in the introductory Chapter, the mechanical/rheological properties of the scaffold on which stem cells grow are of pivotal importance to guarantee a satisfactory percentage of preserved holoclones ($\simeq$ 4-5 % for corneas transplantation), i.e. to allow a continuos renewal of the cultivated tissue. A main target of regenerative medicine is to undestrand whether by properly tuning the mechanichal characteristic of the substrate the percentage of preserved holoclones could improve. Moreover, in many cases, a direct connection between the mechanical properties of the on-growing keratinocytes and the stiffness of the underlying scaffold can be estabilished. Elucidating if it also the case for keratinocytes on a fibrin scaffold would be very interesting and appealing, too.

8.1 Characterization of fibrin samples

In this work we investigated four different fibrin substrates, namely - K1/2, KSTD, T and K2X - with varying crosslinker concentration [1] in order to study samples of different stiffness. From the force curves reported in Figure 8.1 we can point out a strict relationship between the components concentration (in particular fibrinogen concentration, which is doubled in each sample, from the less concentrated one K1/2 to the most concentrated one K2X) and the stiffness of the sample, i.e. the more fibinogen the stiffer. For each kind of sample two curves are reported, both of them being the average of at least five different measurements: the one (continuous line) coming from a pyramidal-indentation experiment, the other (dotted line) coming from a colloidal force spectroscopy experiment. Our data suggest very consistent results since the force curves presented in Figure 8.1 are relative to experiments where different sample of the same kind where tested

[1] The precise composition of the fibrin samples can not be reported here, since a patent is still expected from Centro di Medicina Rigenerativa, that kindly furnished the samples.

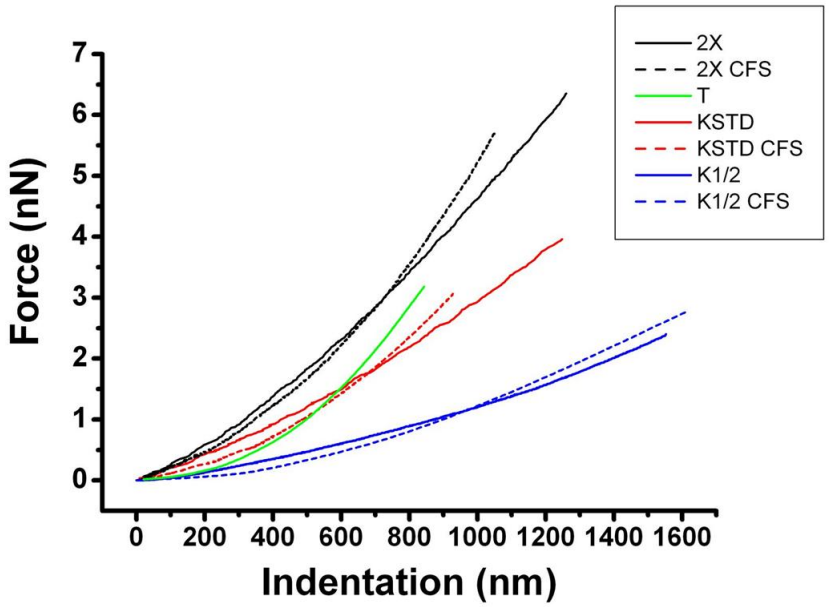

Figure 8.1: Force curves for the four investigated fibrin samples. Continuous lines come from pyramidal-indenter experiments, dotted lines come from colloidal-indenter experiments. All curves are the average of at least five measurements.

with also different tip geometry. Here we want to stress the reproducibility of the obtained results, basically meaning high stability in the sample preparation and quite uniform mechanical properties throughout the samples.

By accurately observing the reported force curve one should note the change in the slope of the force curves for large values of indentation, which is particularly evident for fibrin T and K2X and it is better reported for colloidal-probe indenter experiment (dotted lines); this is the signature of the so called strain-stiffening phenomen (non linearity for large deformations). Strain-stiffening, added to evident changes in the stiffness with temperature (Figure 8.2) and to dissipative features (relaxation of the indenter force *vs* time, Figure 8.3), lead to the conclusion that these samples must be characterized in the framework of their complete viscoelastic properties: providing only one parameter, i.e. the Young's modulus, it is not sufficient to give a complete description of the mechanics of these systems.

To circumvent these problems we decided to exploit the features of the poroelastic model, by performing a calculation of an effective Young's modulus, namely E_∞, which is free from every dissipative contribution; this value is representative of an equilibrium situation, once the dissipative features, here described as migration of the solvent throughout the pores of fibrin network, have already run out. Table 8.4 and Figure 8.4 report the effective Young's modulus for the four investigated fibrin samples.

Apart from allowing a calculation of the Young's modulus equilibrium value, the poroelastic model can be also expoited to calculate other param-

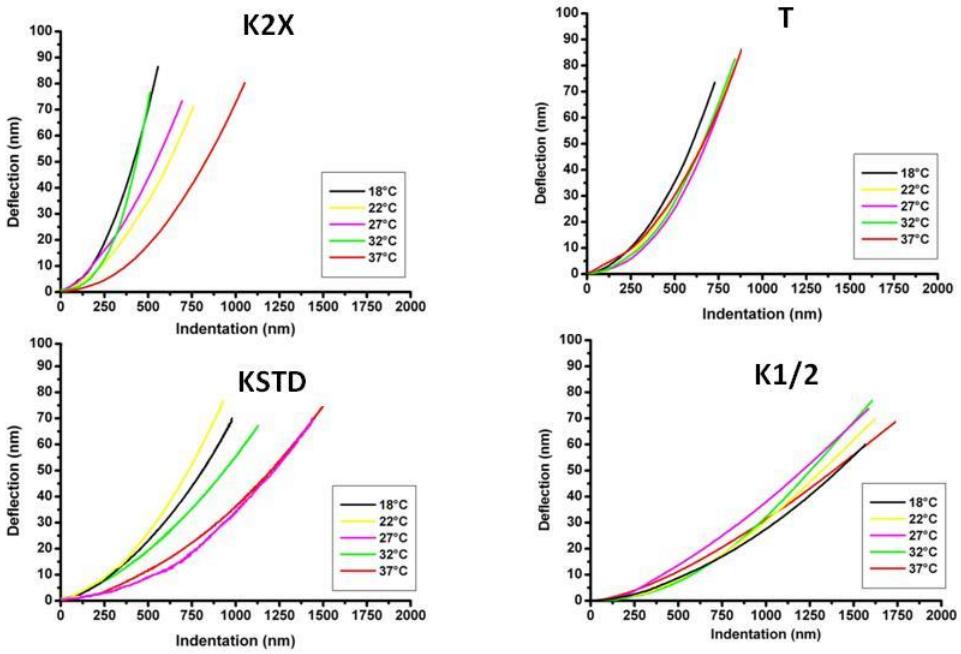

Figure 8.2: Force curves for the four investigated fibrin samples with varying temperatures. For all the samples, apart of sample T which appears very stable, the stiffness depends a lot on the temperature. All the curves are the average of at least five measurements.

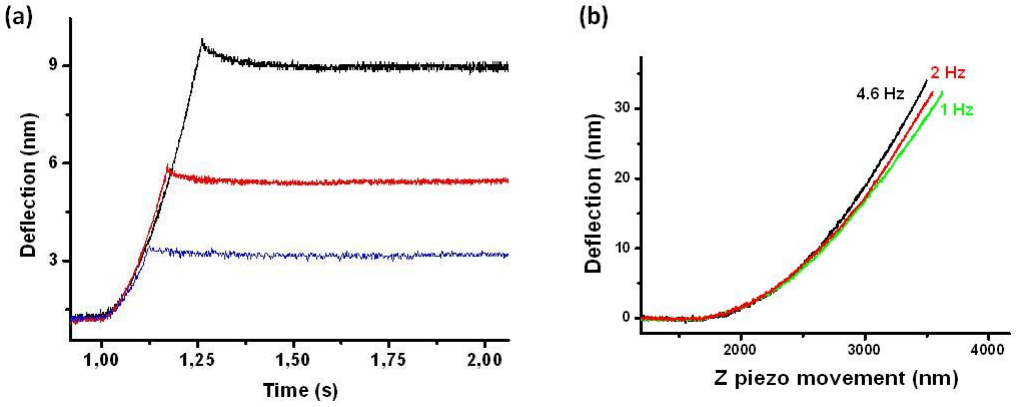

Figure 8.3: Dissipative features of fibrin; (a) Indenter force relaxation vs time; (b) The force curve is dependent on the vertical scan velocity. Both these features are characteristic of viscous materials.

Fibrin	Effective Young's modulus
K1/2	$(1.0 \pm 0.5)\ kPa$
KSTD	$(2 \pm 1)\ kPa$
T	$(5 \pm 3)\ kPa$
K2X	$(14 \pm 5)\ kPa$

Table 8.1: Effective Young's modulus for the four investigated fibrin sample. Values come from averages of at least three relaxation curves relative to different indentations. Data are relative to a pyramidal-indenter tip.

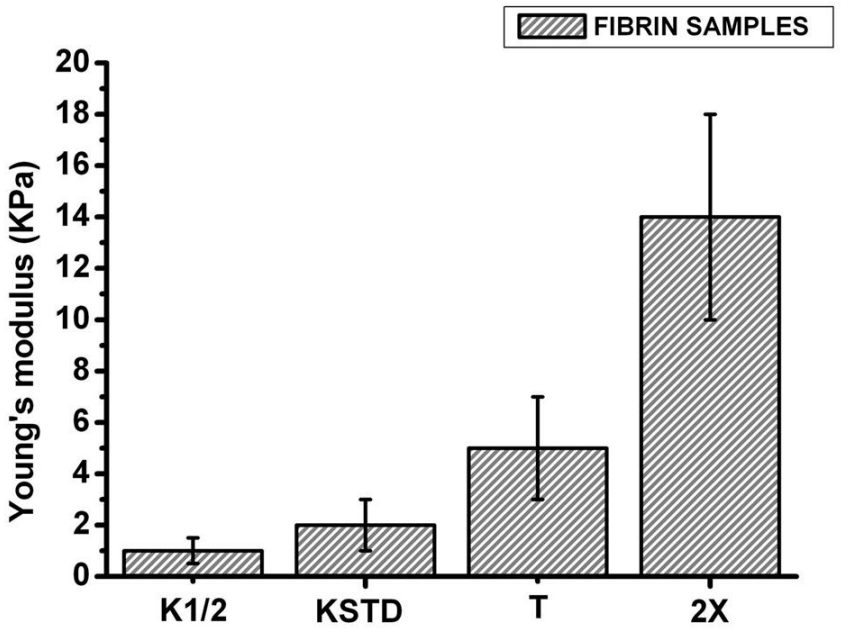

Figure 8.4: Effective Young's modulus for the four investigated fibrin samples (values of Table reported as histograms).

Fibrin	Diffusivity D (m^2/s)	Permeablity k (m^2)	Pore radius (nm)
K1/2	3×10^{-10}	3×10^{-17}	3
KSTD	9×10^{-11}	6×10^{-18}	1
T	3×10^{-11}	5×10^{-19}	0.4
K2X	2×10^{-11}	3×10^{-19}	0.2

Table 8.2: Diffusivity, permeability and pore radius desumed from the poroelastic analysis of force-relaxation curves for the four investigated fibrin samples.

eters that describe the behavior of viscoelastic materials, like the diffusivity D and the permeability k, in addition to the average pore radius (see Table 8.2). In the literature [353] it is found that permeability of fibrin clots can vary by up to five orders of magnitude in the range of $(10^{-13} \div 10^{-17}\ m^2)$ according to fibrin fibers volume fraction, with a pore size that range from 4 to 350 nm. Here we obtain quite lower values for the permeability, and consequently for the diffusivity and the pore radius, which are related to permeability through Equations 3.7 and 3.8. However, in [353] the permeability is calculated by measuring the interstitial fluid velocity through the clots at a constant pressure gradient, while here we the permeability is found by applying the poroelastic model to force-relaxation data. So, different techniques are involved and, in particular, our force-relaxation experiments may be sensitive and test the migration of the solvent only through the pores with smaller radius, i.e. low permeability, as the overall behavior was controlled by the smallest size. Neverthless it is worthwhile to note that the permeability and the pore radius do scale with the stiffness of the fibrin: lower permeability (and pore sizes) correspond to higher Young's modulus, as one can expect.

After a proper normalization of the force-relaxation curves relative to different indentation values, it is possible to test the validity of the poroelastic model by checking the overlapping of the force-normalized curves over a time-normalized scale, which takes into account the contact area between the tip and the sample. Figure 8.3 (a) shows that the measured relaxation curve strongly depends on the depth of indentation. When the force is normalized but the time is not normalized, the curves for three depths of indentation do not overlap (Figure 8.5 (a), where the force relaxation curves are reported in a semi-log scale). Consequently, the measured relaxation curve cannot be explained by viscoelasticity. When the force is normalized and the time is normalized as $\tau = t/a^2$, where a is the contact parameter, the curves for the three depths of indentation collapse into a single curve (Figure 8.5 (c)). This behavior is consistent with poroelasticity.

The poroelastic relaxation time τ is quadratic in the radius of the contact, while the viscoelastic relaxation time is size-indipendent. Our data show that the relaxation behavior of fibrin cannot be explained by pure vis-

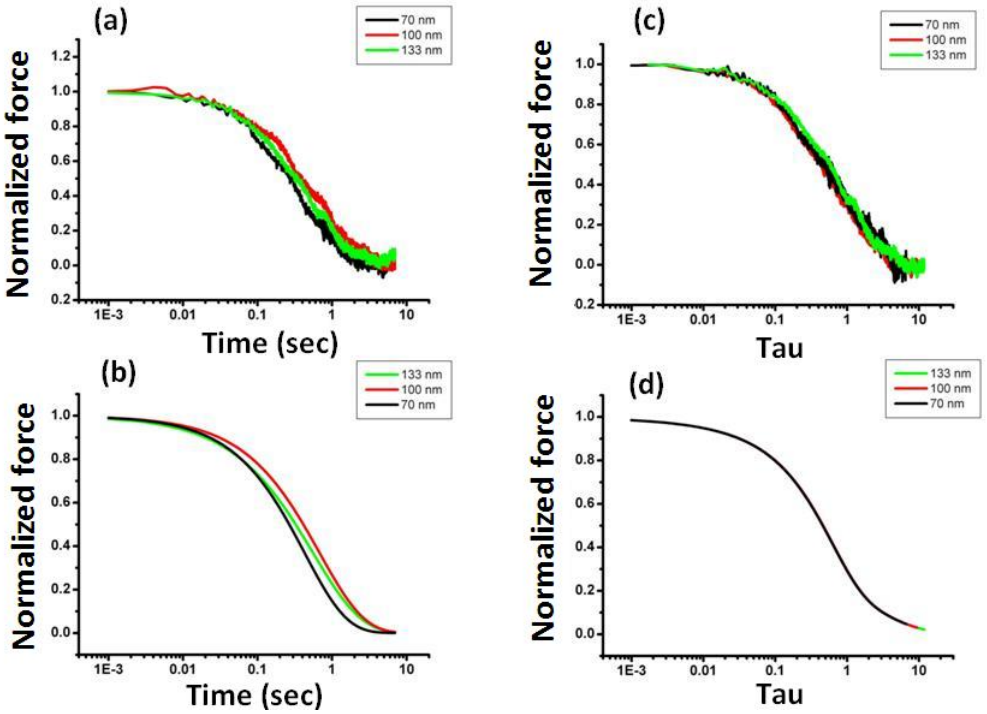

Figure 8.5: (a) Force normalized relaxation curves *vs* time; different colours mean different indentations; the plot is reported in a semi-log scale; (b) Force relaxation curves fitted with the function $g(\tau)$, that involves the tip-geometry dependent contact area a, repored as function of time; (c) Force normalized relaxation curves *vs* normalized time τ: in this case the curves do overlap, proving the validity of the applied poroelastic model; (d) The same plot as in (c) after the fitting of the curves with the function $g(\tau)$: the poroelastic model do predict the perfect overlapping of the fitted normalized curves. Data are relative to a fibrin KSTD sample.

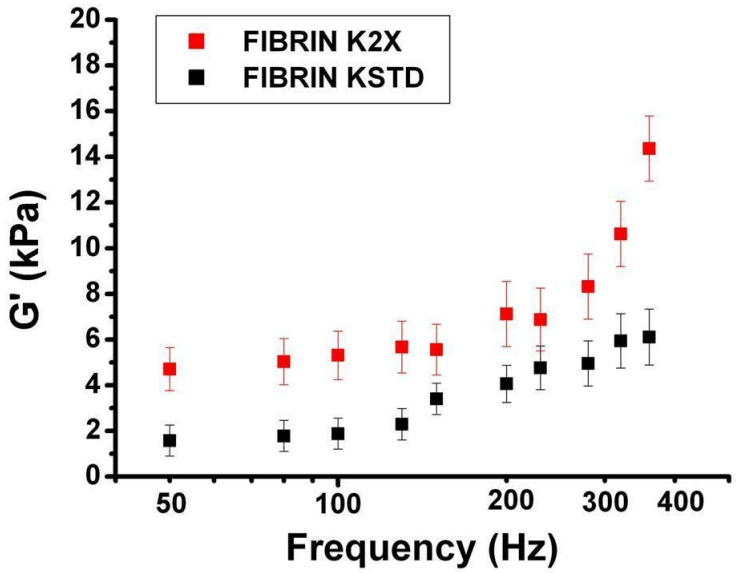

Figure 8.6: Elastic storage moduli G' reported as a function of frequency for fibrin KSTD and K2X. Data come from indentation modulation experiments where a colloidal indenter probe was employed.

coelasticity, but is consistent with poroelasticity. The combined poroelastic and viscoelastic relaxation is beyond the scope of this thesis, but in principle both contribution should be taken into account. While poroelasticity results from the diffusion of solvent through the porous polymer network, viscoelasticity results from the relaxation of polymer chains between entanglements. These two processes result in a complex time-dependent mechanical behavior that should lead to an overall stiffening with increase in frequency [354].

Figure 8.6 shows a plot where the storage elastic modulus G' for fibrin KSTD and K2X are reported as a function of frequency. Data are from indentation modulation experiments where a colloidal-probe indenter was employed. At low frequencies both the samples show a quite constant value for G' up to 150-200 Hz. Such a plateau is also observed in other force modulation studies of hydrogels [252]. This behavior could be explained as if at lower frequencies fibrin behaves as a relaxed elastic solid with complete migration of the solvent in and out the network during load cycling. The relaxation processes, such as motion of chain segments between cross-links, are relative slow, resulting in nearly frequency-indipendent moduli at lower frequencies. However, when the modulating frequencies become comparable to the poroelastic relaxation times ($f \simeq$ 150-200 Hz), it becomes harder for the solvent to migrate in and out the network, increasing the stiffness of the gel and hence the storage moduli.

8.2 Characterization of keratinocytes stem cells

8.2.1 Keratinocyte stem cells on fibrin

We performed topographical and mechanical characterizations of keratinocyte stem cells grown on fibrin substrates of different stiffness by exploiting AFM imaging and the force spectroscopy mode. We carried out two sets of experiments, namely Experiment I and Experiment II, one the doublet of the other. The same experiment was repeted twice in order to assure the replicability of the samples and to guarantee the reliability of the results, since a strict protocol has to be employed in order to permit clinical applications. Due to the intrinsic variability of this kind of systems, increasing the statistics of the experiments could obviously provide more robust results.

In each experiment we considered a pair of samples for each kind of fibrin substrate (the same as illustrated in the previous Paragraph with

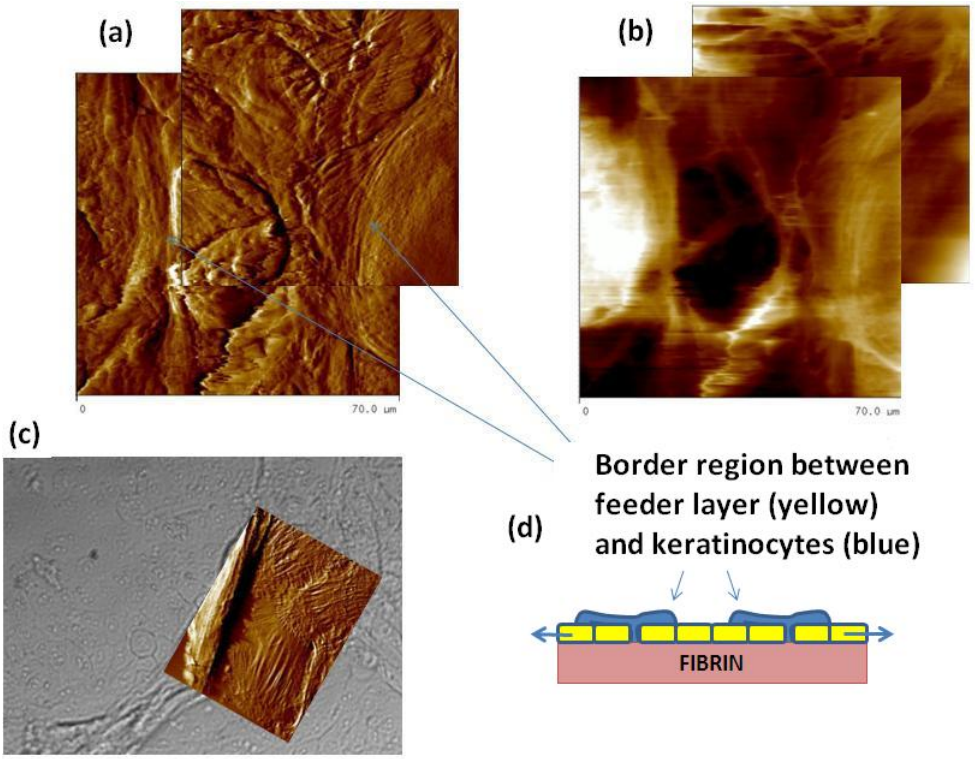

Figure 8.7: Typical example of a proliferative cells sample. (a) Overlap of two AFM topography images; (b) Overlap of two AFM error images: error images come from a derivative of the topography signal; (c) Superimposition of an optical microscopy image with the relative AFM topography. Images are from a fibrin KSTD/keratinocytes samples, but they are representative of the topographical features of the other proliferant samples; (d) cartoon where the structure of these kinds of samples is shown: the feeder layer cells are pushed away and replaced with the on-growing keratinocytes.

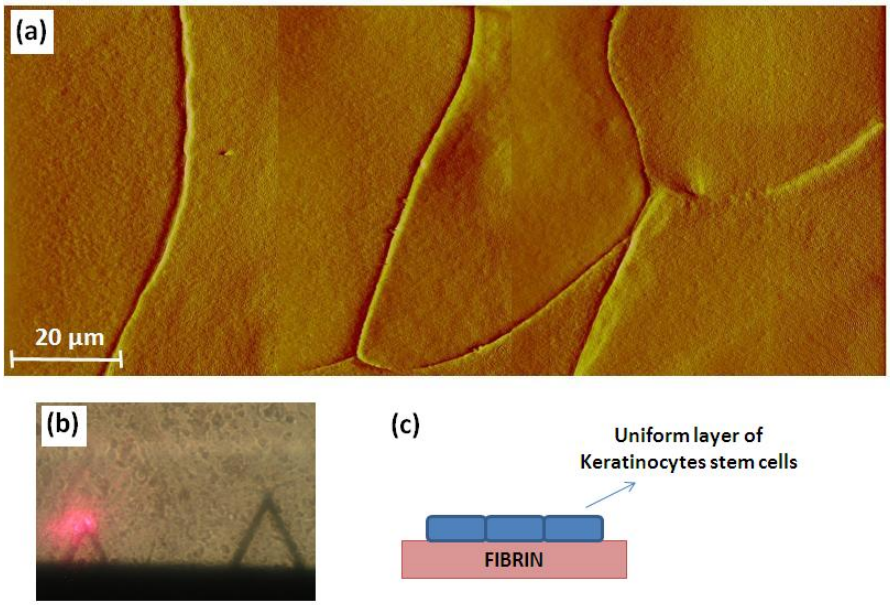

Figure 8.8: Typical example of a confluent cells sample. (a) AFM topographical image; (b) Optical microscopy image that shows the cantilever working on the sample; (c) Schematic representation on a confluent sample, where the keratinocytes form a uniform monolayer over the fibrin substrate.

the except of fibrin 2X, on which the growth of the cells is problematic), according to the proportion of the surface which is covered by the cells: proliferative (PRO) and confluent (CON). In the proliferative stage the presence of the feeder layer (3T3 irradiated fibroblast murine cells) is still evident (Figure 8.7) while in the confluent stage the keratinocytes do form a uniform carpet-like layer (Figure 8.8). In the latter case, features relative to a super-confluent state were observed, in particular Figure 8.9 shows a keratinocytes which has grown on the others.

By performing AFM force spectroscopy we were able to estimate the mechanical properies of the investigated samples in terms of Young's modulus. Initially we take an AFM topographical image of a region of interest, then we exploit the force volume (FV) mode in order to obtain a map of force curves, one for each pixel of the image. By extracting several force curves from the FV images and performing averages, we can calculate the Young's modulus of a specific region. This procedure is illustrated in Figure 8.10.

Each sample was mechanically characterized by taking into account at least five regions of different rigidity where the mechanical properties were quite uniform; for each region we considered an averaged force curve based on at least four indentations. By averaging already averaged force-curves of different regions and performing a fit (Equation 3.5) we are able to furnish a value for the Young's modulus; Table 8.3 and Figure 8.11 report the calculated Young's modulus for the investigated fibrin+keratinocytes samples, for the proliferative (PRO) and confluent (CON) stage of Experiment I. Table 8.4 and Figure 8.12 show data relative to Experiment II.

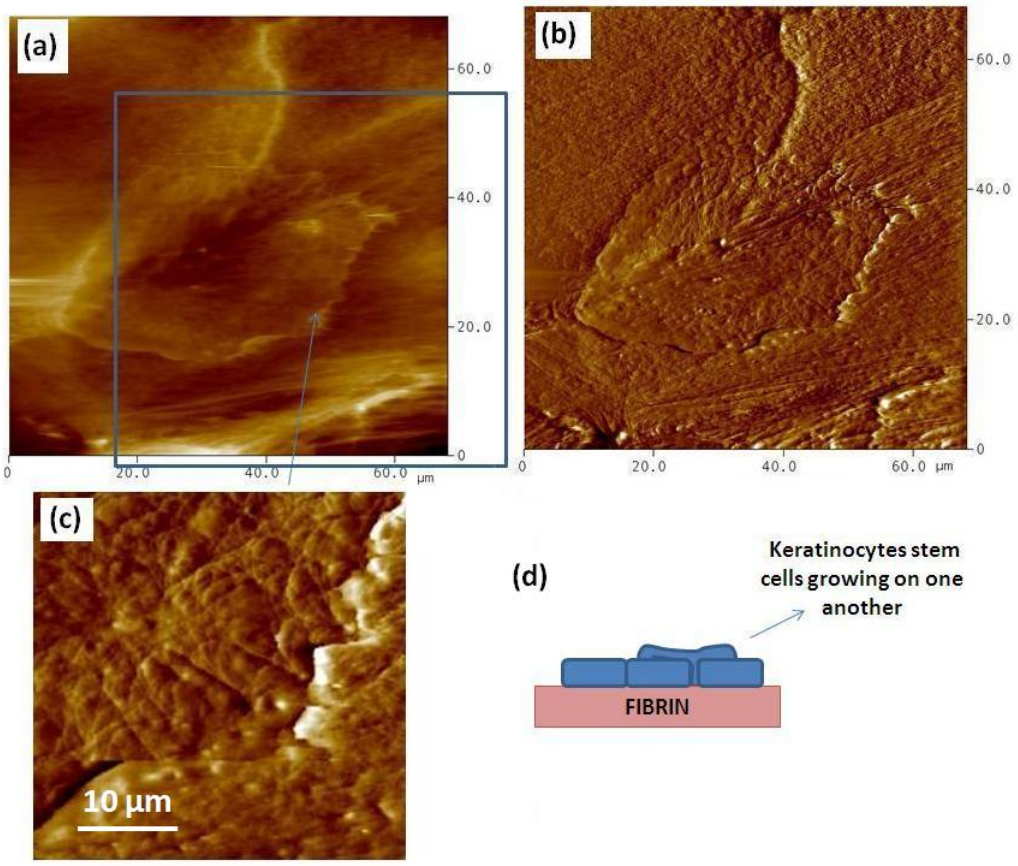

Figure 8.9: Example of a superconfluent sample; (a) AFM topographical and error (b) images of a region that shows a cell which grow on the others; (c) AFM error image of a part of the region at higher magnification: the cytoskeletal organization may be representative of a different differentiation stage; (d) schematic view of a superconfluent sample.

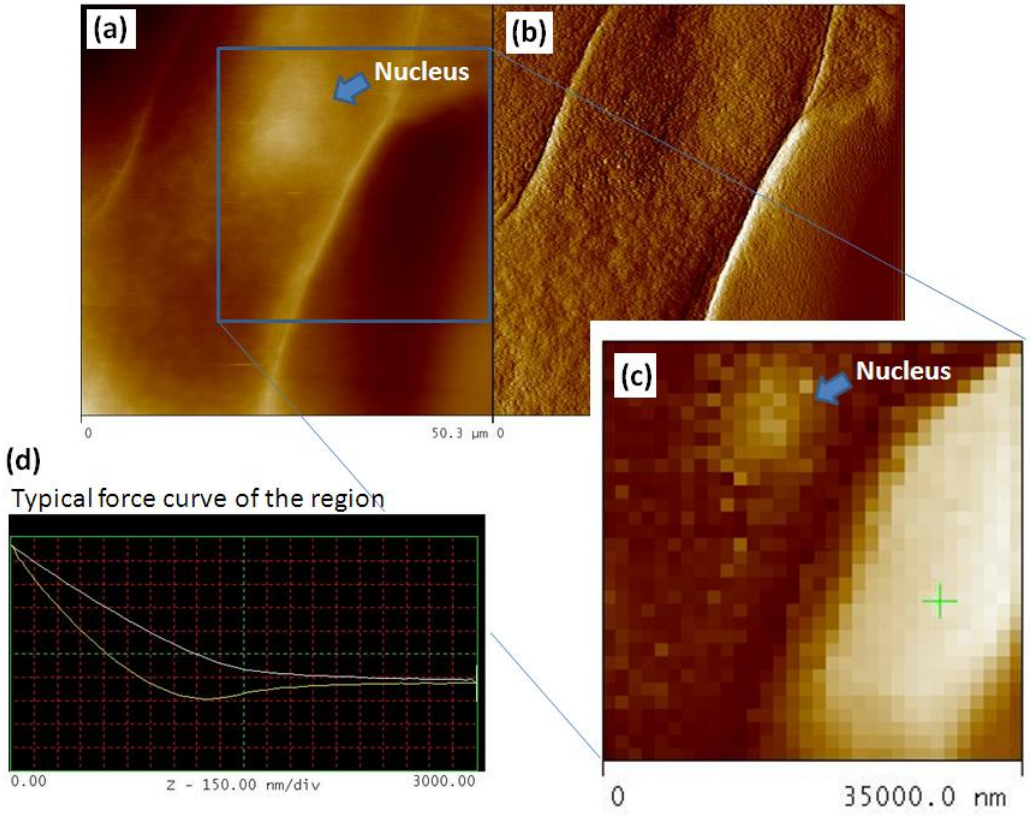

Figure 8.10: (a) AFM topographical and (b) error images of keratinocyte stem cells mechanically analyzed by AFM force spectroscopy; (c) Force volume image of the considered regions: two areas of different rigidity can be observed: A stands for the rigid one, B for the soft one; in (d) is reported a typical force curve of region B that can be extracted from the force volume image. The analyzed force curve comes from the average of several force curves extracted in the same region. In (a) and (c) the region indicated by the arrow can be interpreted as the nucleus of a cell.

Sample	Young's modulus PRO	Young's modulus CON
CELLS on K1/2	$(7 \pm 4)\ kPa$	$(5 \pm 2)\ kPa$
CELLS on KSTD	$(14 \pm 5)\ kPa$	$(10 \pm 3)\ kPa$
CELLS on T	$(13 \pm 5)\ kPa$	$(5 \pm 3)\ kPa$

Table 8.3: Young's modulus for keratinocytes stem cells grown on fibrin K1/2, KSTD, T. Values for proliferant state and confluent state are reported. Data are from Experiment I.

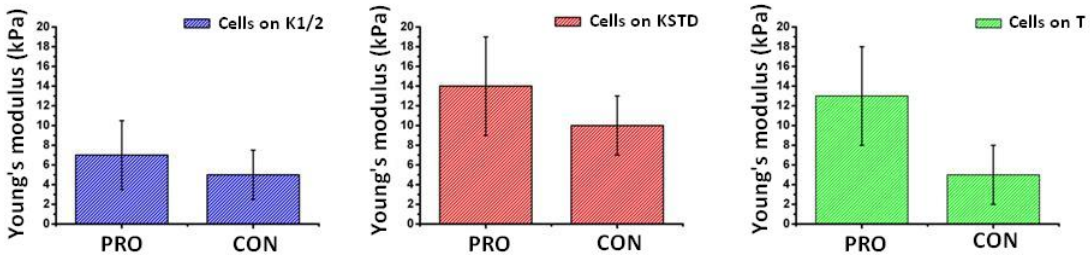

Figure 8.11: Values from Table 8.3 reported as histograms.

Sample	Young's modulus PRO	Young's modulus CON
CELLS on K1/2	$(5 \pm 3)\ kPa$	$(8 \pm 2)\ kPa$
CELLS on KSTD	$(11 \pm 5)\ kPa$	$(6 \pm 2)\ kPa$
CELLS on T	$(7 \pm 3)\ kPa$	$(9 \pm 3)\ kPa$

Table 8.4: Young's modulus for keratinocytes stem cells grown on fibrin K1/2, KSTD, T. Values for proliferant state and confluent state are reported. Data are from Experiment II.

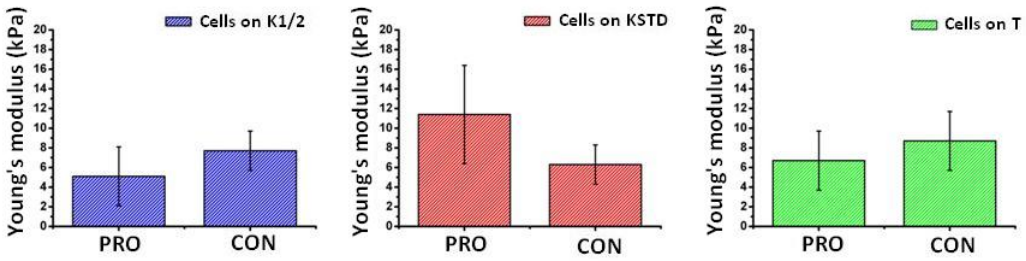

Figure 8.12: Values from Table 8.4 reported as histograms.

The main result of the mechanical analysis is that, irrespective of the different rigidity of the underlying fibrin substrate, the Young's modulus of the keratinocytes seems to converge to a constant value which is around 7-8 kPa. In our opinion this is a quite interesting result, meaning that keratinocytes stem cells are somehow able to feel and modify their environment in order to achieve an optimal mechanical condition for their growth (see Conclusions section for further discussions).

Nevertheless, as specified in Paragraph 8.1, the fibrin substrates used as supports for the keratinocytes span a quite limitated range of stiffness (from 1 to 14 kPa) and someone may properly object that obtaining a constant value of the Young's modulus for the on-growing cells should not be so surprising. For this reason we decided to test the behavior of the keratinocytes on stiffer substrates: chitin and plastic.

8.3 Keratinocytes stem cells on plastic and chitin

Chitin $(C_8H_13O5N)_n$ is a long-chain polymer of a N-acetylglucosamine, a derivative of glucose, and is found in many places throughout the natural world. It is a characteristic component of the cell walls of fungi, the esoskeletons of arthropods such as crustaceans and insects, the radulae of molluscs, and the beaks and internal shells of cephalopods. The structure of chitin is comparable to the polysaccharide cellulose, forming crystalline nanofibrils or whiskers. We performed a mechanical characterization of a funzionalized chitin substrates and we obtained an average Young's modulus of (50 ± 15) kPa which is an order of magnitude higher of the typical values for fibrin. However this value is very low if compared to the value reported in literature, which is around 200 MPa; as explained in [355] the Young's modulus for any given material typically spans several orders of magnitude if different methods of deformation are considered and this is the case because in [355] chitin was submitted to tensile deformations, while here we perform nanoindentation of few nanometers. Anyway, the stiffness of chitin in very high as compared to fibrin and this is reflected in the slope of the force curve presented in Figure 8.13. Plastic is even more stiff: values around $1GPa$ are reported in the literature [356].

Figure 8.14 shows several different features detectable in the sample which presents keratinocytes in proliferative stage on plastic. In Figure 8.14 (a) stretched fibers associated to fibroblast feeder layer cells are clearly visible; in addition, flat and deep regions can be interpreted as areas where the plastic substrate is detectable. Figure 8.14 (b) shows a very tangled region where keratinocytes are growing and probably digesting and pushing away the feeder layer cells; very large uniform areas are also present, as reported in Figure 8.14 (c), and probably these regions are the first where the confluent stage is reached. The uniform carpet-like monolayer of keratinocytes relative to the complete confluent stage on plastic is clearly present in Figure 8.15; in this image the presence of cell junctions, i.e. multiprotein complexes that provide contact between neighbouring cells or between a cell and the

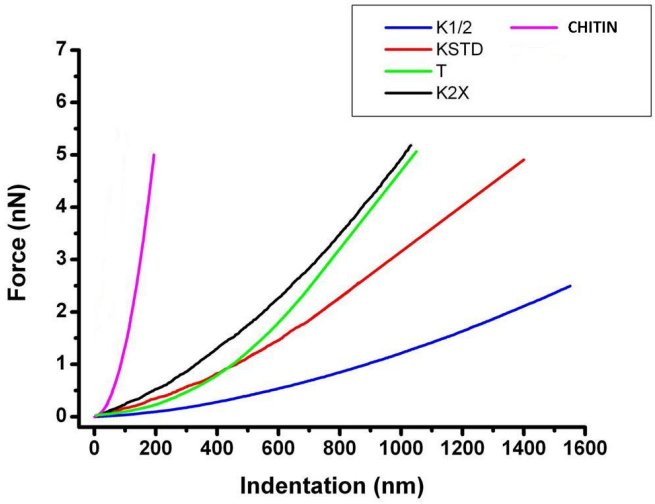

Figure 8.13: Force curves for the different materials used as substrates for keratinocytes stem cells: fibrin (K1/2, KSTD, T, 2X), chitin and plastic.

extracellular matrix, is stressed and highlighted also in comparison with a fluorescent image of keratinocyes taken from the literature [357] that shows similar features (Figure 8.15 (d)). On the other hand, cells on chitin were studied only in the confluent stage and their topographical aspects do not show particular differences with respect to other samples.

Mechanical characterization is even more interesting in this case, since we were looking for values of keratinocytes' Young's modulus to compare with those found for cells on fibrin. The results reported in Table 8.5 and Figure 8.16 are quite surprisingly, as they reproduce the outcomes found for keratinocytes on fibrin (an average Young's modulus of about 8-10 kPa), meaning that keratinocyte stem cells' Young's modulus is quite indipendent from the rigidity of the underlaying substrate. In other words, the mechanical behavior of the keratinocytes seems not to be affected by changes (here some order of magnitudes) in the stiffness of the scaffold on which they are grown. This aspects are examined in depth in the conclusion paragraph relative to this Chapter.

By contrast, at the beginning of this Chapter we stated that keratinocytes are not able to grow on fibrin 2X which is the most stiff fibrin substrate we considered. Too high rigidity of the substrate, one can guess. But in the light of the results on even more rigid substrates, where keratinocytes grow without any problem, it is evident that what prevent the growth of the keratinocytes on fibrin 2X is something else, and it probably resides in the composition/preparation of this kind of fibrin. In agreement with Centro di Medicina Rigenerativa, where every sample was prepared, we decided to study a different type of fibrin 2X with some modifications in the preparation protocol.

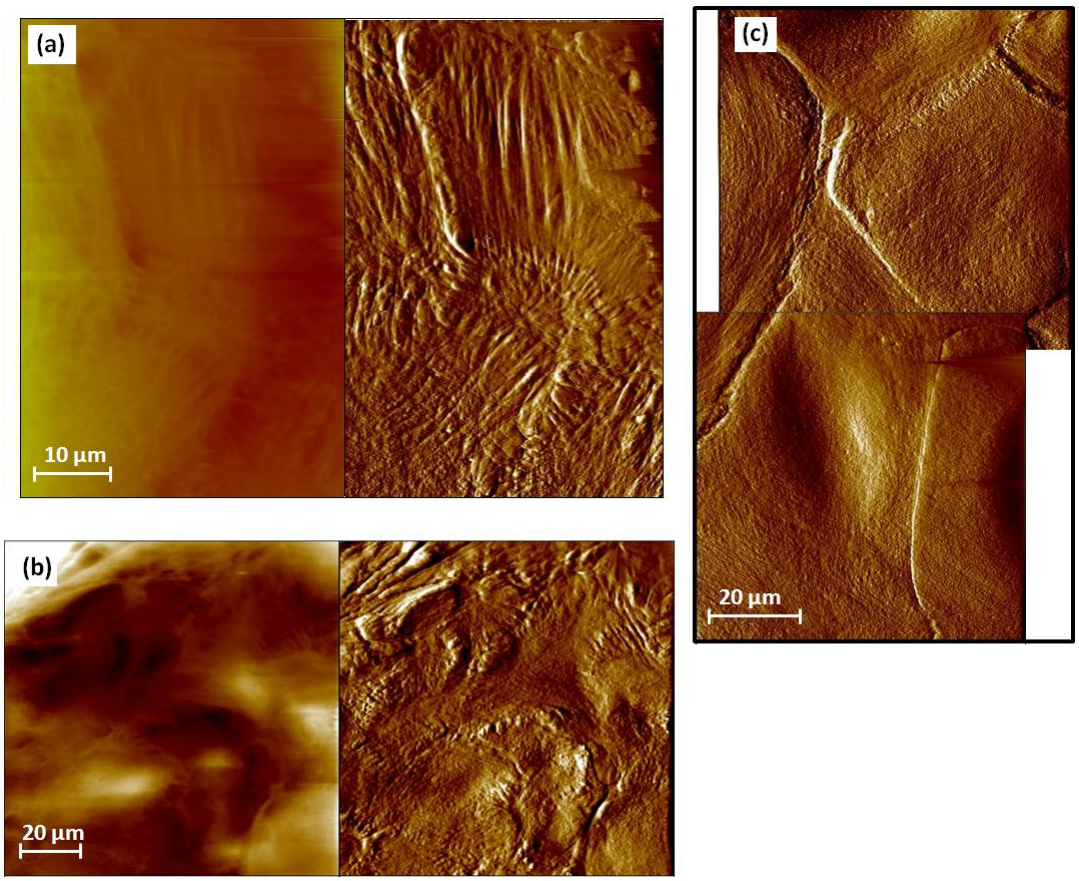

Figure 8.14: Proliferative keratinocytes on plastic; (a) AFM topographical and error images of a feeder layer region: in some points the presence of the plastic substate is detectable; (b) AFM topographical and error images of a region which shows the presence of both feeder layer cells and keratinocytes; (c) uniform region where keratinocyes have probably reached a quasi-confluent stage.

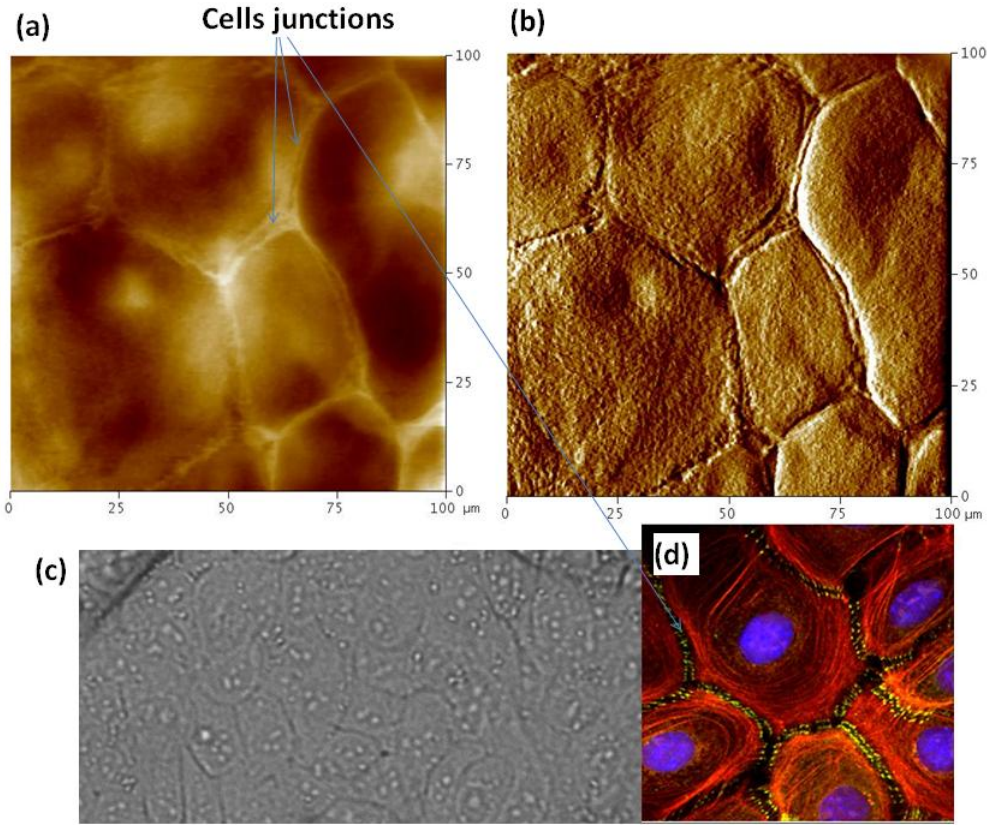

Figure 8.15: Confluent keratinocytes on plastic (a) AFM topographical and (b) error images of a uniform carpet-like monolayer of keratinocytes; (c) optical microscopy image of the investigated region; (d) fluorescent image from [357] of keratinocytes where cytoskeletal structues, in particular cell junctions, are highlighted.

Sample	Young's modulus	
	PRO	CON
CELLS on KSTD	$(6 \pm 3)\ kPa$	$(12 \pm 4)\ kPa$
CELLS on chitin	no data	$(8 \pm 3)\ kPa$
CELLS on plastic	$(30 \pm 14)\ kPa$	$(13 \pm 5)\ kPa$

Table 8.5: Young's modulus for keratinocytes stem cells grown on chitin and plastic. A control experiment of keratinocytes on fibrin KSTD was also performed for comparison. Values in the confluent stage are quite similar and do reproduce the results obtained for keratinocytes on fibrin: from this data we can conclude that keratinocyte stem cells adjust their stiffness indipendently of the rigidity of the substrate on which they grow.

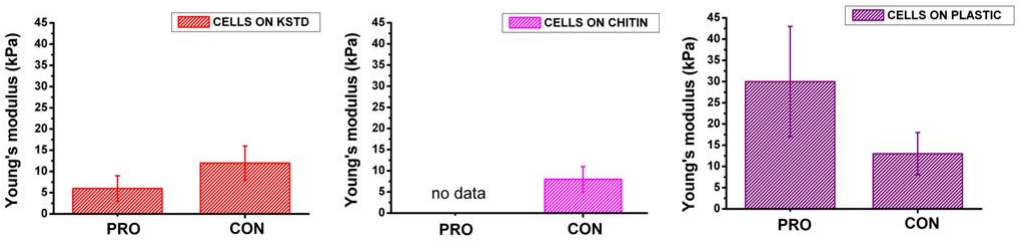

Figure 8.16: Values from Table 8.5 reported as histograms.

8.3.1 Keratinocytes stem cells on fibrin-dialysis

Two different fibrin samples, namely KSTD-dia and 2X-dia, were studied after slight modifations in the preparation protocol. The mechanical characterization provides the values reported in Table 8.6 for the Young's modulus. As we can observe, the value of the Young's moduli of KSTD-DIA and KSTD are quite similar (see Table 8.3 for comparisons) while the Young's modulus of 2X-dia is very lower with respect to the one obtained for 2X. At least mechanically, but also from a composition point of view, KSTD-DIA and 2X-DIA are more similar fibrin than the pair KSTD/2X.

In this case keratinocytes do grow on fibrin 2X-DIA and an AFM image of the confluent sample is reported in Figure 8.17. The mechanical characterization of the keratinocytes gives a value for the cells' Young's modulus that is in agreement with those found for every other sample studied in the confluent stage, i.e. $E = (6 \pm 3)\ kPa$, confirming another time our hypothesis of cells' self-adjusting stiffness.

We are currently waiting for another experiment on keratinocytes grown on KSTD-DIA substrates for comparison.

Fibrin	Young's modulus PRO
KSTD-DIA	$(2 \pm 1)\ kPa$
2X-DIA	$(3 \pm 1)\ kPa$

Table 8.6: Young's modulus for the protocol-modified fibrins KSTD and 2X. A different protocol was employed in order to allow the growth of keratinocytes stem cells also on fibrin 2X.

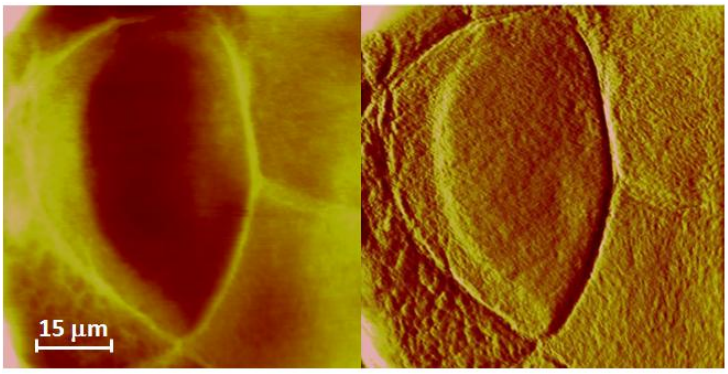

Figure 8.17: (a) AFM topographical and (b) error images of keratinocyte stem cells grown of fibrin 2X-DIA which differ from fibrin 2X by some modifications in the preparation protocol.

8.4 Viscoelastic characterization of keratinocytes stem cells

As viscoelastic materials, cells should be characterized by means of proper analysis which should take into account not only the elastic features (i.e. Young's modulus) but also the dissipative ones. In order to better describe the complete rheological behavior of keratinocyte stem cells grown on fibrin we decided to perform experiments of force relaxation. Figure 8.18 shows an example of force relaxation experiment carried on an area that presents two distinct mechanical regions: a stiff region on the left (L) and a soft region on the right (R). In Figure 8.18 (d) the curves of force relaxation relative to different values of indentation are reported. By applying the equations of the poroelastic model we calculated the diffusivity D and the permeability k, in addition to the effective Young's modulus E_∞, for the two zones of interest; values reported in Table 8.7 for region R are in substantial agreement with those found in the literature [358], where recent evidence suggests that the poroelastic model is able to well describe the cytoplasmatic rheology: the cytoplasm can be trated as a biphasic material consisting of a porous elastic solid meshwork (cytoskeleton, organelles, macromolecules) bathed in an interstitial fluid (cytosol). In this picture the rate of cellular deformation is limited by the rate at which intercellular water can redistribute within the cytoplasm. If data from region R are in

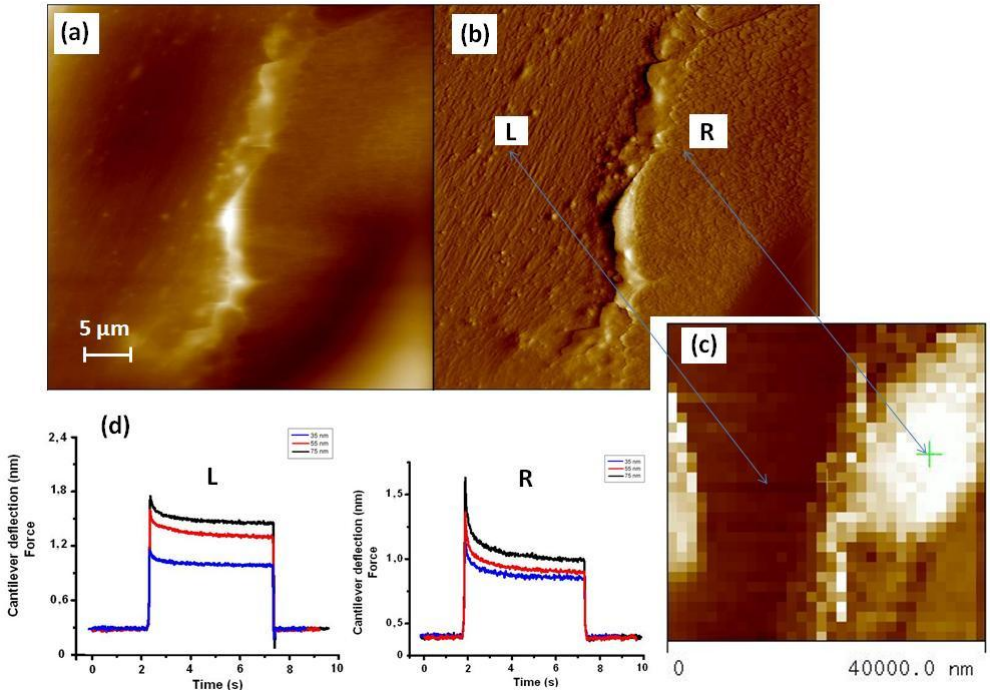

Figure 8.18: (a) AFM topographical and (b) error image of an area showing different mechanical features which are clearly detectable in the force volume image: bright regions are softer, dark regions are stiffer (c). We call L as the left-stiff area and R the right-soft area. In (d) three different force-relaxation curves corresponding to different values of indentation are reported for both the region of interest.

agreement with those ones characteristic of a cell, data from region L are quite different. The high Young's modulus and the very low permeability lead us to the conclusion that this area can be interpretated as the substrate; in particular, the elongated features clearly visible in Figure 8.18 (b) should correspond to elongated fibrin fibers which are probably stretched due to the presence of the surrounding cells. Obvioulsy, if a material is stretched its rigidity increases and its hydraulic permeability decreases due to the fact that the pores shrink.

To further characterize the rheological properties of keratinocytes we also performed an indentation modulation experiment, in which an oscillatory loading was superimposed to the AFM z-piezo signal and the relative

Region	E_∞ (kPa)	Diffusivity D (m^2/s)	Permeablity k (m^2)
L	36	1.3×10^{-13}	5.5 x 10^{-22}
R	3	2.4 x 10^{-12}	2.5 x 10^{-19}

Table 8.7: Poroelastic parameter (relaxed Young's modulus E_∞, diffusivity D and permeability k, for the left (L) and right (R) regions of Figure 8.18.

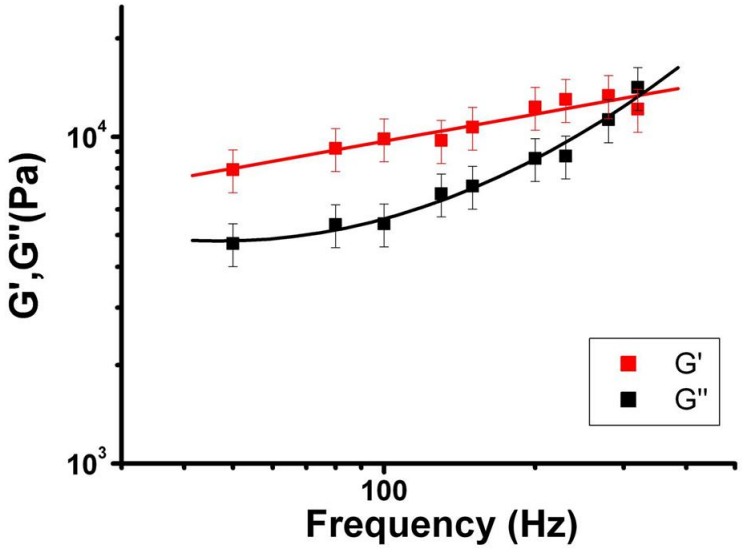

Figure 8.19: Storage and loss moduli G', G" as a function of frequency in keratinocyte stem cells subjected to oscillatory mechanical loading. Because the results are plotted on a log-log scale, the slope of G' gives the scaling exponent β which is 0.27 in this case.

oscillation response in the deflection was analyzed. By exploiting Equation 3.20 and equations 3.15, 3.16 the real and the imaginary part of the complex shear modulus G^* were calculated. Figure 8.19 shows the results of this analysis; in particular the scaling exponent β was found as the slope of the storage modulus G' reported in a log-log scale. Experiments in a variety of cell types and using various techniques for mechanical loading have demonstrated that cells exhibit a scaling exponent of around 0.2 - 0.3 [255] (in our case $\beta = 0.27$). This power-law dependence is typical of a class of materials called soft glassy materials, which includes materials such as emulsions, slurries and pastes.

8.5 Discussion

Over the last decade it has been demonstrated that a variety of tissue-forming cells can both sense the stiffness of their substrate and apply a controlled force onto that substrate. Mechanically compliant materials for studying cellular responses to substrate stiffness are typically made from synthetic polymers whose elastic moduli are indipendent of applied strain and are determined by polymer and crosslinker density. However, extracellular matrix proteins, such as fibrin, but also collagen, display non linear mechanical properties, i.e. strain stiffening. In these materials the elastic modulus of the gel increases by orders of magnitude as the applied strain increases such that the resistance that a cell feels would be a strict function of

the strain that it applies. Local strain stiffening allows an initially isotropic matrix to reinforce cell-applied mechanical anisotropy and trasmit forces between cells up to a half a millimeter apart. In this way isolated cells can create far-reaching mechanical gradients by which they can communicate with other cells [359].

In this work we found that there is no correlation (see Figure 8.20) between the mechanical properties of the substrate and the Young's modulus of the on-growing keratinocytes. The explanation of this overall result could reside in the strain-stiffening features of fibrin [134].

However, it is always important to specify the type of applied deformation, infact typical strain-stiffening is mostly associated to tensile deformations, while here deformations are related to indentation-like experiments. Due to the strain stiffening properties of fibrin, indipendently from what is the specific stiffness of the substate, the cells can deform the fibrin gel enough to sense the high strain modulus rather then the low (typically measured in our nanoindentation experiments) strain modulus of the scaffolds. In this way, if cells do apply strains large enough to enter in the strain-stiffening regime of fibrin elasticity, than they will react to fibrin as if it was stiffer matrix, like chitin or plastic. Probably this is the way the cells use to self-organize the mechanical environment to recreate their most favorable conditions to grow up and spread.

Within this view it would be very interesting to understand if the uncorrelation between the mechanical properties of the substrate and those of keratinocytes is present also at the genomical level in terms of percentage of holoclones, i.e. the mark of cells' staminality. Unfortunately, at the time of writing we are still waiting for the results from Centro di Medicina Rigenerativa and the complete discussion can not be reported here.

Some examples of images where cells exert forces and stress gradient

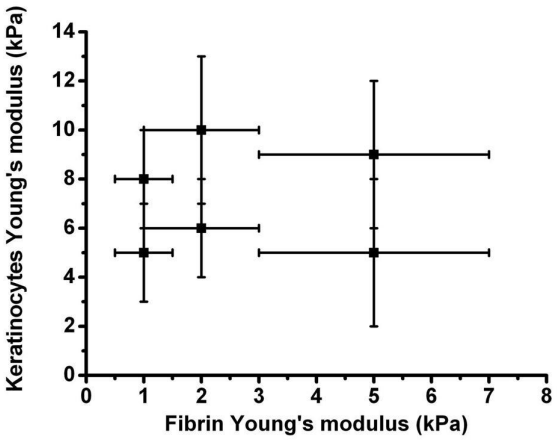

Figure 8.20: The plot reports keratinocytes Young's moduli as a function of fibrin Young's moduli. Since no trends are detectable we can state that there is no correlation between the mechanical properties of the cells and the scaffolds.

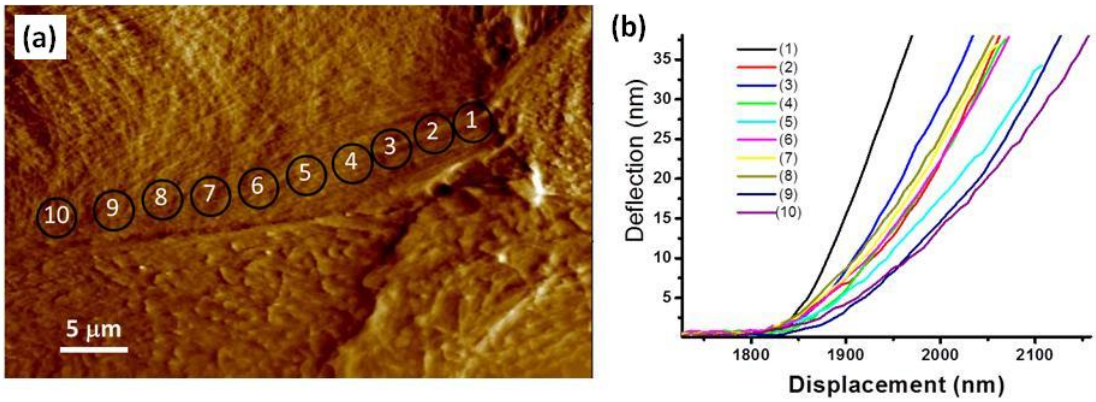

Figure 8.21: (a) High magnification AFM error image of a region where fibrin fibers are stretched due to the presence of a cell. (b) Force curves relative to the enumerated circles marked in (a). As we get far away from the cell (higher numbers), fibrin fibers become softer and sofer. This is an indication that cells are able to apply stress gradient fields.

on fibrin are reported in Figure 8.21, 8.22, 8.23, in addition to the already commentated image of Figure 8.18 where the force-relaxation experiment was performed. In particular, Figure 8.21 (a) clearly shows that fibrin's fibers are stretched and elongated due to the presence of the keratinocyte cell. As reported in Figure 8.21 (b) we are dealing with a gradient of stress applied by the cell, since the force curves acquired on the fibers become more and more compliant as they are taken at increasing distance from the cell, meaning that fibrin is softer and softer as we approach regions where the cell is not able to exercise its mechanical influence. It is worthwhile to notice that the stress gradient we are talking about is exerted in a radial way, as Figure 8.22 proves. Figure 8.23 gives a better insight in the organization of the stretched fibrin fibers, reporting an AFM image at high magnification.

Another aspect of particular interest regards the possibility of studying cytoskleton organization through AFM imaging. As keratinocytes' shape is intrinsically related to epithelial function and actin cytoskeletal organization, great effort has been put into understanding the actin reorganizatin that occurs during morphological differentiation. In epithelia, actin bundles are present as a thick circumferential ring around each cell, aligned with the cell borders [360]. In addition to the circumferential organization, a less abundant population of actin bundles also appear to terminate at sites of cell-cell contacts as assessed by electron microscopy and fluorescence (Figure 8.25). Surprisingly, there are currently no mechanistic insights into how the cytoskeleton is reorganized into the typical circumferential ring organization for mature cells as described above. In Figure 8.24 several AFM images of keratinocyte stem cells whose cytoskeleton is organized in circular shapes are presented. Since actin circumferential rings are characteristic of mature cells, we can suppose that these structures may be helpful in recognizing cells that have already undergone a differentiation process.

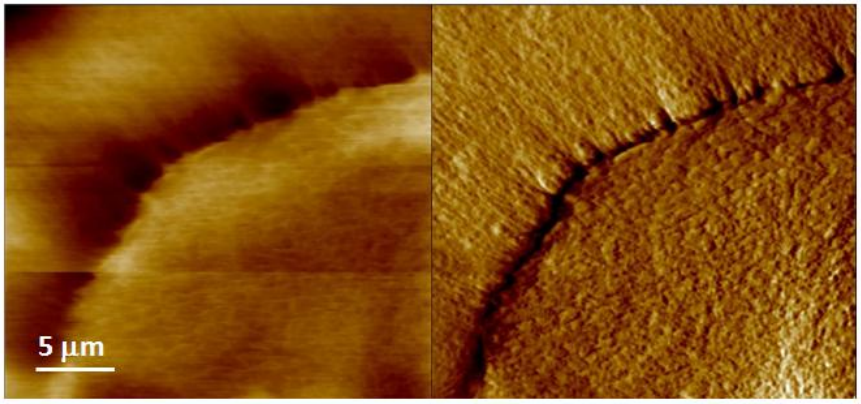

Figure 8.22: AFM topographical (a) and error (b) images of a cell applying a stress field in a radial way.

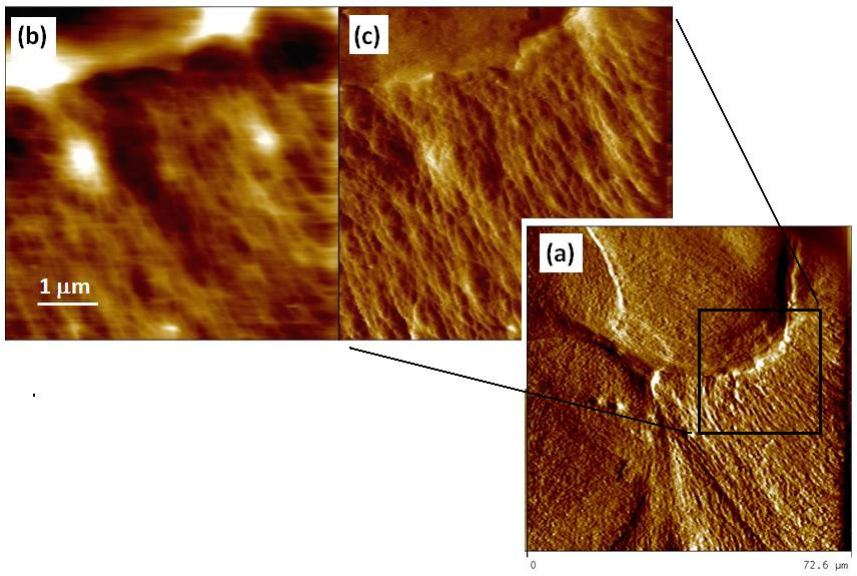

Figure 8.23: The squared region marked in (a) is reported in (b) and (c) at higher magnification in order to highlight the characteritic features of stretched fibrin fibers.

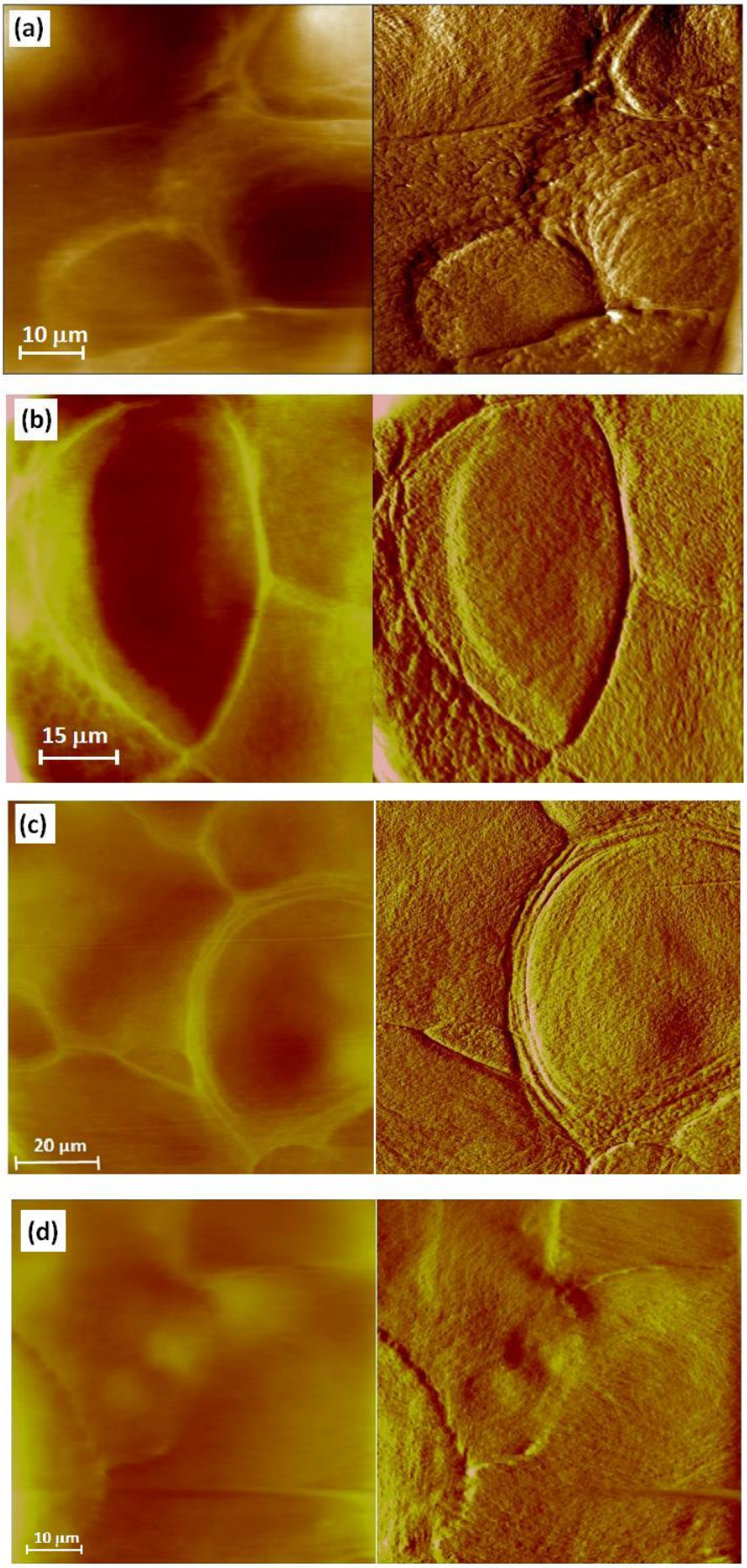

Figure 8.24: Several AFM topographical/error images of keratinocytes that present circular shape cytoskeletal structures.

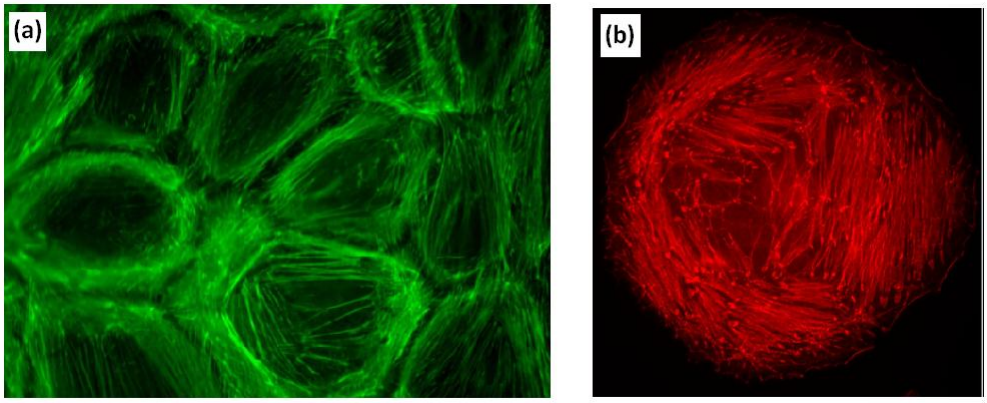

Figure 8.25: (a) Monolayer of endothelial cells in culture stained for F-actin; (b) Hela cells naturally arranged in circle stained for actin. From [361].

Chapter 9

Conclusions and future perspectives

Throughout this work, Atomic Force Microscopy and correlated techniques such as Micropipette Aspiration were employed in order to characterize the mechanical and thermodynamical properties of biological samples.

In particular, the role of neurosteroids of pharmacological interest in affecting the properties of model lipid bilayers have been pointed out. Briefly, our results showed that allopregnanolone is able to reorganize the lateral heterogeneity of the lipid bilayer by increasing the liquid disordered phase and promoting an overall softening of the system. On the other hand, isoallopregnanolone, differing from Allo only in the orientation of an OH group, has a minor effect on the properties of the membrane even if an increase in the liquid order phase was detectable. Moreover, in the case of a charged neurosteroid like pregnenolone sulfate we observed a marked change in the mechanical features of the lipid membrane, i.e. a relevant increase in the bilayer bending constant. In the lipid raft framework, all these observations endorse the importance of taking into account also the aspecific effects that drugs may have on the membrane properties in addition to the direct regulation of protein function. However, the true physical chemical mechanisms that determine membrane perturbation still remain unclear. Studies by molecular simulations can be very helpful in this context and probably they would shed light on the importance of cholesterol in the membrane lateral organization, as suggested in [300], where it is stated that aromatic compounds stabilize phase separation by partition into the liquid-disordered phase and excluding cholesterol from the disordered domain, i.e. the same overall result we obtained with allopregnanolone. Employing cholesterol enantiomer in place of cholesterol would be another interesting study to further elucidate the central role played by this molecule in determing the mechanical and thermodynamical properties of the bilayer. Experiments on *ent*-cholesterol will be carried out in the future, even if, in light of the results obtained in this work on *ent*-steroids, the lipid membrane seems to display very little enantioselectivity, at least dealing with the membrane properties we considered.

In the section relative to the effect of neurosteroids on neurons we saw that allopregnanolone exerts a weak effect in the mechanical properties of neuroblastoma cells, while dehydroepiandrosterone causes a relevant variation on them, since an increase in the shear modulus was observed by performing indentation modulation after DHEA insertion. This effect is probably related to a reorganization of the cytoskeleton that future AFM topographical images can investigate in a better way. In any case, we want to stress that in this work we were mainly interested in investigating fast responses due to neurosteroids addition at physiological concentrations; since Allo did not affect any mechanical features of NBs in a relevant way, we suppose that, for the employed concentrations, this neurosteroid can act only at the genomic level. On the other side, the rapid mechanical variations caused by DHEA are the clear signature of non-genomic effects.

Finally, dealing with the characterization of fibrin+keratinocytes stem cells we obtained quite interesting results. By investigating the mechanical features of keratinocytes we were able to point out the uncorrelation between the mechanical properties of the keratinocytes and those of the underneath fibrin scaffold. To further validate our observations, substrates of order of magnitude stiffer were employed, i.e. chitin and plastic: also in these cases the keratinocyes seemed to converge to the same Young's modulus, as if they could control and self-adjust the mechanical environment on which they grow. In the case of fibrin, this is probably due to the ability that cells have in applying strains and stretch the fibrin network enough to enter in the strain-stiffening regime of elasticity and sense the high strain modulus rather that the low one (typically measured in our nanoindentation experiments). We are currently waiting for the results from Centro di Medicina Rigenerativa, which may be helpful in clarifying the overall physiological-clinical characterization of these samples which are studied for corneas transplantation.

Bibliography

[1] Powl AM, East JM, Lee AG (2008), *Importance of direct interactions with lipids for the function of the mechanosensitive channel MscL*, Biochemistry (87), 12175-12184.

[2] Phillips R, Ursell T, Wiggins P, Sens P (2009), *Emerging roles for lipids in shaping membrane-protein function* , Nature (459), 379-385.

[3] McIntosh TJ, Simon SA (2006), *Roles of bilayer material properties in function and distribution of membrane proteins*, Biomol. Struct. (35), 177-198.

[4] Seeger HM, Aldrovandi L, Alessandrini A, Facci P (2010), *Changes in single K^+ channel behavior induced by a lipid phase transition*, Biophys. J. (99), 3675-3683.

[5] Lingwood D, Simons K (2010), *Lipid rafts as a membrane-organizing principle*, Science 327 (2010) 46-50;

[6] Pike LJ (2009), *The challenge of lipid rafts*, J. Lipid Res. (50), S323-S328;

[7] Shu HJ, Eisenman LN, Jinadasa D, Covey DF, Zorumski CF, Mennerick S (2004), *Slow actions of neuroactive steroids at GABAA receptors*, J. Neurosci. (24), 6667-6675;

[8] Akk G, Covey DF, Evers AS, Steinbach JH, Zorumski CF, Mennerick S (2009), *The influence of the membrane on neurosteroid actions at GABAA receptors*, Psychoneuroendocrynology 34:S59-S66;

[9] Hwang TC, Koeppe RE, Andersen OS (2003), *Ganistein can modulate channel function by a phosphorylation-indipendent mechanism: importance of hydrophobic mismatch and bilayer mechanics*, Biochemistry 42(46): 13646-58;

[10] Wittmer LL, Hu Y, Kalkbrenner M, Evers AS, Zorumski CF, Covey DF (1996), *Enantioselectivity of steroid-induced gamma-aminobutyric acid(A) receptor modulation and anesthesia*, Mol. Pharmacol. (50), 1581-1586;

[11] Nilsson KR, Zorumski CF, Covey DF (1998), *Neurosteroid analogues. 6. The synthesis and GABAA receptor pharmacology of enantiomers of dehydroepiandrosterone sulfate, pregnenolone sulfate, and (3 α,5 β)-3-hydroxypregnan-20-one sulfate* , J. Med.Chem. (41), 2604-2613;

[12] Cantor RS (1997), *The lateral pressure profile in membranes: a physical mechanism of general anesthesia* , Biochemistry (36) 2339-2344;

[13] Lalitha S, Kumara AS, Stine KJ, Covey DF (2001), *Chirality in Membranes: First Evidence that Enantioselective Interactions Between Cholesterol and Cell Membrane Lipids Can Be a Determinant of Membrane Physical Properties* , J. Supramol. Chem. (1) 53-61;

[14] Wang M, He Y, Eisenman LN, Fields C, Zeng C, Mathews J, Benz A, Fu T, Zorumski E, Steinbach JH, Covey DF, Zorumski CF, Mennerick S (2002), *3β-hydroxy-pregnane steroids are pregnenolone sulfate-like GABAA receptor antagonists*, J. Neurosci. (22) 3366-3375;

[15] Makriyannis A, DiMeglio CM, Fesik SW (1991), *Anesthetic steroid mobility in model membrane preparations as examined by high-resolution 1H and 2H NMR spectroscopy*, J. Med. Chem. (34) 1700-1703;

[16] Makriyannis A, Siminovitch DJ, Das Gupta SK, Griffin RG (1986), *Studies on the interaction of anesthetic steroids with phosphatidylcholine using 2H and 13C solid state NMR*, Biochim. Biophys. Acta (859) 49-55;

[17] Hosie AM, Wilkins ME, da Silva HMA, Smart TG (2006), *Endogenous neurosteroids regulate $GABA_A$ receptors via two discrete transmembrane sites*, Nature (444) 486-489;

[18] Majewska MD, Mienville JM, Vicini S (1988), *Neurosteroid pregnenolone sulfate antagonizes electrophysiological responses to GABA in neurons*, Neurosci. Lett. (90) 279-284;

[19] Park-Chung MA, Malayev RH, Gibbs PTT, Farb DH (1999), *Sulfated and unsulfated steroids modulate g-aminobutyric acidA receptor function through distinct sitesSulfated and unsulfated steroids modulate g-aminobutyric acidA receptor function through distinct sites*, Brain Res. (830) 72-87;

[20] Eisenman LN, He Y, Fields C, Zorumski CF, Mennerick S (2003), *Activation-dependent properties of pregnenolone sulfate inhibition of $GABA_A$ receptor-mediated current*, J. Physiol. (550) 679-691.;

[21] Mennerick S, Zeng CM, Benz A, Shen W, Izumi Y, Evers AS, Covey DF, Zorumski CF (2001), *Effects on g-aminobutyric acid $GABA_A$ receptors of a neuroactive steroid that negatively modulates glutamate neurotransmission and augments GABA neurotransmission*, Mol. Pharmacol. (60) 732-741;

[22] Bruner LJ (1975), *The interaction of hydrophobic ions with lipid bilayer membranes*, J. Membr. Biol. (22) 125-141;

[23] Oberhauser AF, Fernandez JM (1995), *Hydrophobic ions amplify the capacitive currents used to measure exocytotic fusion*, Biophys. J. (69) 451-459;

[24] Mennerick S, Lamberta M, Shu HJ, Hogins J, Wang C, Covey DF, Eisenman LN, Zorumski CF (2008), *Effects on Membrane Capacitance of Steroids with Antagonist Properties at $GABA_A$ Receptors*, Biophys. J. (95) 176-185;

[25] Maehle AH, Prüll CY, Halliwell RF (2002), *The emergence of the drug receptor theory*, Nat. Rev. Drug Discov. (1) 637-641;

[26] Clark AJ (1937), *General pharmacology. In: Heffner's handbuch der experimentellen pharmacologie ergänzungsband*, Band 4, Berlin: Springer-Verlag;

[27] Gaddum JH (1926), *The action of adrenaline and ergotamine on the uterus of the rabbit*, J. Physio. (61) 141-150.

[28] Ariens EJ (1954), *Affinity and intrinsic activity in the theory of competitive inhibition*, Arch. Int. Pharmacodyn. Ther. (99) 32-49;

[29] Stephenson RP (1956), *A modification of receptor theory*, Br. J. Pharmacol. (11) 379-393:

[30] Black JW, Leff P (1983), *Operational models of pharmacological agonist*, Proc. R. Soc. Lond. [Biol] (220) 141-162;

[31] Rang HP (2006), *The receptor concept: pharmacology's big idea*, Br. J. Pharmacol. (147), S9-16;

[32] BPS/IUPHAR guide to pharmacology, http://www.guidetopharmacology.org/targets.jsp (2013);

[33] Alexander SP, Mathie A, Peters JA (2011), *Guide to receptors and channels (GRAC)*, Br. J. Pharmacol. (164), S1-324;

[34] Kenakin T, Christopoulos A (2013), *Signalling bias in new drug discovery: detection, quantification and therapeutic impact*, Nat. Rev. Drug Discov. (12) 205-16;

[35] Kenakin T, Williams M (2014), *Defining and characterizing drug/compound function*, Biochem. Pharmacol. 87:40-63;

[36] Nury H, Van Renterghem C, Weng Y, Tran A, Baaden M, Dufresne V, Changeux JP, Sonner JM, Delarue M, Corringer PJ (2011), *X-ray structures of general anaesthetics bound to a pentameric ligand-gated ion channel*, Nature 469:428-431;

[37] Sonner JM, Cantor RS (2013), *Molecular mechanisms of drug action: an emerging view*, Annu. Rev. Biophys. 42:143-167;

[38] Lee DK, Albershardt DJ, Cantor RS (2015), *Exploring the mechanism of general anesthesia: kinetic analysis of $GABA_A$ receptor electrophysiology*, Biophys. J. 108(5) 1081-93;

[39] Marsh D (2008), *Protein modulation of lipids, and viceversa, in membranes*, Biochim. Biophys. Acta. 1778:1545-1575;

[40] Schmidt D, MacKinnon R (2008), *Voltagedependent K+ channel gating and voltage sensor toxin sensitivity depend on the mechanical state of the lipid membrane*, Proc. Natl. Acad. Sci. (USA) 105:19276-19281;

[41] Lundbaek JA, Collingwood SA, Ingolfsson HI, Kapoor R, Andersen OS (2010), *Lipid bilayer regulation of membrane protein function: gramicidin channels as molecular force probes*, J. R. Soc. Interface. 7:373-395;

[42] Lee AG (2003), *Lipid-protein interactions in biological membranes: a structural perspective*, Biochim. Biophys. Acta 1612:1-40;

[43] Lee AG (2004), *How lipids affect the activities of integral membrane proteins*, Biochim. Biophys. Acta 1666:62-87;

[44] Lundbaek JA, Koeppe RE, Andersen OS (2010), *Amphiphile regulation of ion channel function by changes in the bilayer spring constant*, Proc. Natl. Acad. Sci. USA 107:15427-15430;

[45] Andersen OS, Koeppe RE (2007), *Bilayer thickness and membrane protein function: an energetic perspective*, Annu. Rev. Biophys. Biomol. Struct. 36: 107-130;

[46] Janoff AS, Pringle MJ, Miller KW (1981), *Correlation of general anesthetic potency with solubility in membranes*, Biochim. Biophys. Acta 649:125-128;

[47] Cantor RS (2001), *Breaking the Meyer-Overton rule: predicted effects of varying stiffness and interfacial activity on the intrinsic potency of anesthetics*, Biophys. J. 80:2284-2297;

[48] Hemmings HC Jr., Akabas MH, Goldstein PA, Trudell JR, Orser BA, Harrison NL (2005), *Emerging molecular mechanisms of general anesthetic action*, Trends Pharmacol. Sci. 26:503-510;

[49] Urban BW, Bleckwenn M, Barann M (2006), *Interactions of anesthetics with their targets: non-specific, specific or both?*, Pharmacol. Ther. 111:729-770;

[50] Seeman P (1972), *The membrane actions of anesthetics and tranquilizers*, Pharmacol. Rev. 24:583-655;

[51] Miller KW (1985), *The nature of the site of general anesthesia*, Int. Rev. Neurobiol. 27:1-61;

[52] Koblin DD (2000), *Anesthesia, Mechanism of Action*, in R.D. Miller Ed. 48-73, Philadelphia: Churchill Livingstone;

[53] Haydon DA, Hendry BM, Levinson SR, Requena J (1977), *Anaesthesia by the N-alkanes. A comparative study of nerve impulse blockage and the properties of black lipid bilayer membranes*, Biochim. Biophys. Acta 470:17-34;

[54] Vanderkooi JM, Landesberg R, Selick H, McDonald GG (1977), *Interaction of general anesthetics with phospholipid vesicles and biological membranes*, Biochim. Biophys. Acta 464:1-18.;

[55] Galla HJ, Trudell JR (1980), *Asymmetric antagonistic effects of an inhalation anesthetic and high pressure on the phase transition temperature of dipalmitoyl phosphatidic acid bilayers*, Biochim. Biophys. Acta 599, 336-340;

[56] Tsuchiya H (2001), *Structure-specific membrane-fluidizing effect of propofol*, Clin. Exp. Pharmacol. Physiol. 28:292-299;

[57] Trudell JR (1977), *A unitary theory of anesthesia based on lateral phase separations in nerve membranes*, Anesthesiology 46:5-10;

[58] Enders A (1990), *The influence of general, volatile anesthetics on the dynamic properties of model membranes*, Biochim. Biophys. Acta 1029:43-50;

[59] Reyes J, Latorre R (1979), *Effect of the anesthetics benzyl alcohol and chloroform on bilayers made from monolayers*, Biophys. J. 28:259-279;

[60] Chisari M, Eisenman LN, Covey DF, Mennerick S, Zorumski CF (2010), *The sticky issue of neurosteroids and $GABA_A$ receptors*, Trends Neurosci. 33:299-306;

[61] Belleli D, Lambert JJ (2005), *Neurosteroids: endogenous regulators of the $GABA_A$ receptor*, Nat. Rev. Neurosci. 6:565-575;

[62] Puja G, Santi MR, Vicini S, Pritchett DB, Purdy RH, Paul SM, Seeburg PH, Costa E (1990), *Neurosteroids act on recombinant human $GABA_A$ receptors*, Neuron 4:759-765;

[63] Mienville JM, Vicini S (1989), *Pregnenolone sulfate antagonizes $GABA_A$ receptor-mediated currents via a reduction of channel opening frequency*, Brain Res. 489:190-194;

[64] Mennerick S, He Y, Jiang X, Manion BD, Wang M, Shute A, Benz A, Evers AS, Covey DF, Zorumski CF (2004), *Selective antagonism of 5α-reduced neurosteroid effect at GABAA receptors*, Mol. Pharm. 65:1191-1197;

[65] Hosie AM, Wilkins ME, Smart TG (2004), *Neurosteroid binding sites on GABAA receptors*, Pharmacol. Ther. 116:7-19;

[66] Hosie AM, Clarke L, da Silva H, Smart TG (2009), *Conserved site for neurosteroid modulation of $GABA_A$ receptors*, Neuropharmacology 56:149-154;

[67] Chisari M, Eisenman LN, Krishnan K, Bandyopadhyaya AK, Wang C, Taylor A, Benz A, Covey DF, Zorumski CF, Mennerick S (2009), *The influence of neuroactive steroid lipophilicity on $GABA_A$ receptor modulation: evidence for a low-affinity interaction*, J. Neurophysiol. 102:1254-1264;

[68] Majewska MD (1992), *Neurosteroids: endogenous bimodal modulators of the $GABA_A$ receptor. Mechanism of action and physiological significance*, Prog. Neurobiol. 38:379-395;

[69] Shu HJ, Eisenman LN, Jinadasa D, Covey DF, Zorumski CF, Mennerick S (2004), *Slow actions of neuroactive steroids at GABAA receptors*, J. Neurosci. 24:6667-6675;

[70] Olsen RW, DeLorey TM (1999), *GABA receptor physiology and pharmacology*, in Basic neurochemistry: molecular, cellular and medical aspects. 6th edition, Lippincott-Raven, Philadelphia;

[71] Engelman DM (2005), *Membranes are more mosaic than fluid*, Nature 438: 578-580;

[72] Levental I, Lingwood D, Grzybek M, Coskun U, Simons K (2010), *Palmitoylation regulates raft affinity for the majority of integral raft protein*, Proc. Natl. Acad. Sci. USA 107:22050-22054;

[73] Veatch SL, Cicuta P, Sengupta P, Honerkamp-Smith A, Holowka D, Bairds B (2008), *Critical fluctuations in plasma membrane vesicles*, ACS Chem. Biol. 3:287-293;

[74] Gray E, Karslake J, Machta BB, Veatch SL (2013), *Liquid general anesthetics lower critical temperatures in plasma membrane vesicles*, Biophys. J. 105:2751-2759;

[75] Sackmann E (1984), *Physical basis for trigger processes and membrane structures*, in D.Chapman (Ed.), Biological Membranes, Academic Press, London, 1984, 105-143;

[76] Mouritsen OG, Bloom M (1984), *Mattress model of lipid-protein interactions in membranes*, Biophys. J. 46, 141-153;

[77] Simons K, Ikonen E (1997), *Functional rafts in cell membranes*, Nature 387: 569-572;

[78] Martinac B, Adler J, Kung C (1990), *Mechanosensitive ion channels of E. coli activated by amphipaths*, Nature 348:261-263;

[79] Yethiraj A, Weisshaar JC (2007), *Why are lipid rafts not observed in vivo?*, Biophys. J. 93: 3113-3119;

[80] Eggeling C, Ringemann C, Medda R, Schwarzmann G, Sandhoff K, Polyakova S, Belov VN, Hein B, von Middendorff C, Schonle A, Hell SW (2097), *Direct observation of the nanoscale dynamics of membrane lipids in a living cell*, Nature 26: 457(7233);

[81] Hirst LS, Uppamoochikkal P, Chai L (2011), *Phase separation and critical phenomena in biomimetic ternary lipid mixtures*, Liq. Cryst. 38: 1735-1747;

[82] Veatch SL, Keller SL (2005), *Seeing spots: complex phase behavior in simple membranes*, Biochim. Biophys. Acta 1746: 172-185;

[83] Honerkamp-Smith AR, Veatch SL, Keller SL (2009), *An introduction to critical points for biophysicists; observations of compositional heterogeneity in lipid membranes*, Biochim. Biophys. Acta 1788: 53-63.

[84] Ueda I, Tatara T, Chiou JS, Krishna PR, Kamaya H (1999), *Structure selective anesthetic action of steroids: anesthetic potency and effects on lipid and protein*, Anesth. Analg. 78:718-725;

[85] Covey DF, Nathan D, Kalkbrenner M, Nilsson KR, Hu Y, Zorumski CF, Evers AS (2000), *Enantioselectivity of pregnanolone-induced γ-aminobutyric acidA receptor modulation and anesthesia*, J. Pharmacol. Exp. Ther. 293: 1009-1116;

[86] Crossley R (1995), *Chirality and the biological activity of drugs*, Boca Raton: CRC Press;

[87] Covey DF (2009), *Ent-steroids: novel tools for studies of signaling pathways*, Steroids 74: 577-585;

[88] Zorumski CF, Wittmer LL, Isenberg KE, Hu Y, Covey DF (1996), *Effects of neurosteroid and benzeindene enantiomers on $GABA_A$ receptor in cultured hippocampal neurons and transfected HEK-293 cells*, Neuropharmacology 35:1161-8;

[89] Antkowiak B (2001), *How do general anesthetics work?*, Naturwissenschaften 88: 201-213;

[90] Ueda I, Yoshida T (1999), *Hydration of lipid membranes and action mechanisms of anesthetics and alcohols*, Chem. Phys. Lipids 101: 65-79;

[91] Oliver D, Lien CC, Soom M, Baukrowitz T, Jonas P, Fakler B (2004), *Functional conversion between A-type and delayed rectifier K^+ channels by membrane lipids*, Science 304: 265-270;

[92] Cafiso DS (1998), *Dipole potentials and spontaneous curvature: membrane properties that could mediate anesthesia*, Toxicol. Lett. 100-101: 431-439;

[93] Dickinson B, Franks NP, Lieb WR (1994), *Can the stereoselective effects of the anesthetic isoflurane be accounted for by lipid solubility?*, Biophys. J. 66: 2019-2023;

[94] Tomlin SL, Jenkins A, Lieb WR, Franks NP (1998), *Stereoselective effects of etomidate optical isomers on gamma-aminobutyric acid type A receptors and animals*, Anesthesiology 88: 708-717;

[95] Baulieu EE (1997), *Neurosteroids: of the nervous system, by the nervous system, for the nervous system*, Recent Prog. Horm. Res. 52:1-32;

[96] Brinton RD (2013), *Neurosteroids as regenerative agents in the brain: therapeutic implications*, Nature Reviews 1-10;

[97] Baulieu EE, Robel P (1995), *Dehydroepiandrosterone (DHEA) and DHEA sulfate as neuroactive neurosteroids*, Proc. Natl. Acad. Sc.i USA 95: 4089-4091;

[98] Compagnone NA, Mellon SH (2000), *Neurosteroids: biosynthesis and function of these novel neuromodulators*, Front Neuroendocrinol. 21: 1-56;

[99] Sanchez AM, Flamini MI, Polak K, Palla G, Spina S, Mannella P, Genazzani AD, Simoncini T (2011), *Actin Cytoskeleton Remodelling by Sex Steroids in Neurones*, J. Of Neuroendocrinology, 24:195-201;

[100] Kolodkin AL, Tessier-Lavigne M (2011), *Mechanisms and molecules of neuronal wiring: a primer*, Cold Spring Harb. Perspect. Biol. 3:a001727;

[101] Tojima T, Hines JH, Henley JR, Kamiguchi H. (2011), *Second messengers and membrane trafficking direct and organize growth cone steering*, Nat. Rev. Neurosci. 12:191-203;

[102] Addae-Mensah K, Wikswo JP (2008), *Measurement techniques for cellular biomechanics in vitro*, Exp. Biol. Med. (Maywood). 233:792-809;

[103] Hochmuth RM (2000), *Micropipette aspiration of living cells*, J. Biomech. 33(1): 15-22;

[104] Schmid-Schönbein GW, Sung KL, Tözeren H, Skalak R, Chien S (1981), *Passive mechanical properties of human leukocytes*, Biophys. J. 36:243-256;

[105] Bausch AR, Möller W, Sackmann E (1999), *Measurement of local viscoelasticity and forces in living cells by magnetic tweezers*, Biophys. J. 76:573-579;

[106] Hénon S, Lenormand G, Richert A, Gallet F (1999), *A new determination of the shear modulus of the human erythrocyte membrane using optical tweezers*, Biophys. J. 76:1145-1151;

[107] Kim KS, Cho CH, Park EK, Jung MH, Yoon KS, Park HK (2012), *AFM-detected apoptotic changes in morphology and biophysical property caused by paclitaxel in Ishikawa and HeLa cells*, PLoS One 7(1), e30066;

[108] Li QS, Lee YH, Ong CN, Lim CT (2008), *AFM indentation study of breast cancer cells*, Biochem. Biophys. Res. Commun. 374:609-613;

[109] Alcarez J, Buscemi L, Grabulosa M, Trepat X, Fabry B, Farré R, Vanajas D (2008), *Microrheology of human lung epithelial cells measured by atomic force microscopy*, Biophys. J. 84:2071-2079;

[110] Radmacher M (2002), *Measuring the elastic properties of living cells by atomic force microscope*, Met. Cells Biol. 68: 67-90;

[111] Yang R, Xi N, Lai KW, Zhong BH, Fung CK, Qu CG, Wang DH (2011), *Nanomechanical analysis of insulinoma cells after glucose and capsaicin stimulation using atomic force microscopy*, Acta Pharmacol. Sin. 32:853-860;

[112] Yang R, Chen JY, Xi N, Lai KW, Qu C, Fung CK, Penn LS, Xi J (2012), *Characterization of mechanical behavior of an epithelial monolayer in response to epidermal growth factor stimulation*, Exp. Cell Res. 318:521-526;

[113] Yang R, Xi N, Lai KW, Patterson KC, Chen H, Song B, Qu C, Zhong B, Wang DH (2013), *Cellular biophysical dynamics and ion channel activities detected by AFM-based nanorobotic manipulator in insulinoma β-cells*, Nanomedicine 9:636-645;

[114] Fung CK, Seiffert-Sinha K, Lai KW, Yang R, Panyard D, Zhang J, Xi N, Sinha AA (2010), *Investigation of human keratinocyte cell adhesion using atomic force microscopy*, Nanomedicine 6:191-200;

[115] Kasas S, Wang X, Hirling H, Marsault R, Huni B, Yersin A, Regazzi R, Grenningloh G, Riederer B, Forro L, Dietler G, Catsicas S (2005), *Superficial and deep changes of cellular mechanical properties following cytoskeleton disassembly*, Cell Motil. Cytoskeleton 62, 124-132;

[116] Kuipers HF, Rappert AA, Mommaas AM, van der Valk P, Boddeke HW, Biber KP, van der Elsen PJ (2006), *Simvastatin affects cell motility and actin cytoskeleton distribution of microglia*, Glia 53: 115-123;

[117] Stamenović D, Ingber DE (2002), *Models of cytoskeletal mechanics of adherent cells*, Biomech. Model. Mechanobiol. 1: 95-108;

[118] Matus A (2000), *Actin-based plasticity in dendritic spines*, Science 290: 754-758;

[119] Woolley CS, McEwen BS (1993), *Roles of estradiol and progesterone in regulation of hippocampal dendritic spine density during the estrous cycle in the rat*, J Comp Neurol 336: 293-306;

[120] Srivastava DP, Woolfrey KM, Liu F, Brandon NJ, Penzes P (2010), *Estrogen receptor's activity modulates synaptic signaling and structure*, J Neurosci 30: 13454-13460;

[121] Arnold AP, Gorski RA (1984), *Gonadal steroid induction of structural sex differences in the central nervous system*, Annu Rev Neurosci 7: 413-442;

[122] Foy MR, Baudry M, Akopian GK, Thompson RF (2010), *Regulation of hippocampal synaptic plasticity by estrogen and progesterone*, Vitam Horm 82: 219-239;

[123] Hojo Y, Murakami G, Mukai H, Higo S, Hatanaka Y, Ogiue-Ikeda M, Ishii H, Kimoto T, Kawato S (2008), *Estrogen synthesis in the brain-role in synaptic plasticity and memory*, Mol Cell Endocrinol 290: 31-43;

[124] Hung AJ, Stanbury MG, Shanabrough M, Horvath TL, Garcia-Segura LM, Naftolin F (2003), *Estrogen, synaptic plasticity and hypothalamic reproductive aging*, Exp Gerontol 38: 53-59;

[125] Bruel-Jungerman E, Davis S, Laroche S (2007), *Brain plasticity mechanisms and memory: a party of four*, Neuroscientist 13: 492-505;

[126] Duffau H (2006), *Brain plasticity: from pathophysiological mechanisms to therapeutic applications*, J Clin Neurosci 13: 885-897;

[127] Henderson VW (2007), *Alzheimer's disease and other neurological disorders*, Climacteric 10(Suppl. 2): 92-96;

[128] Sherwin BB, Henry JF (2008), *Brain aging modulates the neuroprotective effects of estrogen on selective aspects of cognition in women: a critical review*, Front Neuroendocrinol 29: 88-113;

[129] Foy MR (2011), *Ovarian hormones, aging and stress on hippocampal synaptic plasticity*, Neurobiol Learn Mem 95: 134-144;

[130] Eriksson PS, Perfilieva E, Bjork-Eriksson T, Alborn AM, Nordborg C, Peterson DA, Gage FH (1998), *Neurogenesis in the adult human hippocampus*, Nat. Med. 4, 1313-1317;

[131] Engler AJ, Sen S, Sweeney HL, Discher DE (2006), *Matrix elasticity directs stem cell lineage specification*, Cell 126, 677-689;

[132] Catelas I, Sese N, Wu B, Dunn J, Helgerson S, Tawil B (2006), *Human mesenchymal stem cells proliferation and osteogenic differentiation in fibrin gels in vitro*, Tissue Engineering 12(8), 1-9;

[133] Brouwers J (2002), *Influence of fibrinogen concentration on the Young's modulus in fibrin gel*, Master Thesis;

[134] Shah JV, Janmay PA (1997), *Strain hardening of fibrin gels and plasma clots*, Rheol Acta 36:262-268;

[135] Weisel JW (2004), *The mechanical properties of fibrin for basic scientists and clinicians*, Biophysical Chemistry 112:267-276;

[136] David Hui-Kang Ma, Arvin Chi-Chin Sun, Jui-Yang Lai and Han-Kan Chen (2008), *A Review of Corneal Epithelial Stem Cell Therapy*, Progress in Stem Cell Applications, Faraday AV, Dyer JY, pp.13-56;

[137] Gallico GG, O'Connor NE, Compton CC, et al. (1984), *Permanent coverage of large burn wounds with autologous cultured human epithelium*, N.Engl.J.Med. 311:448-51;

[138] Pellegrini G, De Luca M, Arsenijevic Y (2007), *Towards therapeutic application of ocular stem cells*, Semin.Cell.Dev.Biol. 18(6): 805-18;

[139] Pellegrini G, Traverso CE, Franzi AT, et al. (1997), *Long-term restoration of damaged corneal surfaces with autologous cultivated corneal epithelium*, Lancet 349:990-3;

[140] van Susante JL, Buma P, Schuman L et al. (1999), *Resurfacing potential of heterologous chondrocytes suspended in fibrin glue in large full-thickness defects of femoral articular cartilage: an experimental study in the goat*, Biomaterials. 20:1167-75;

[141] Ye Q, Zund G, Benedikt O, et al. (1999), *Fibrin gel as a three dimensional matrix in cardiovascular tissue engineering*, Eur.J.Cardiothorac.Surg. 17:587-91;

[142] Kaiser HW, Stark GB, Kopp J, et al. (1994), *Cultured autologous keratinocytes in fibrin glue suspension, esclusively and combinated with STS-allograft (preliminary clinical and histological report of a new technique)*, Burns 20:23-9;

[143] Pellegrini G, Ranno R, Stracuzzi G, et al. (1999), *The control of epidermal stem cells (holoclones) in the treatment of massive full-thickness burns with autologous keratinocytes cultured on fibrin*,Transplantation. 1999; 68:868-79;

[144] Hianik T (2006), *Structure and physical properties of biomembranes and model membranes*, Acta Physica Slovaca vol. 56(6): 687-805;

[145] Gorter E, Grendel F (1925), *On bimolecular layers of lipoids on the chromocytes of the blood*, The Journal of Experimental Medicine, 41(4): 439-443;

[146] Danielli JF, Davson H (1935), *A contribution to the theory of permeability of thin films*, Journal of cellular and comparative physiology, 5(4):495-508;

[147] Singer SJ, Nicolson GL (1972), *The fluid mosaic model of the structure of cell membranes*, Science, 175(4023): 720-731;

[148] Blicher A (2011), *Electrical aspects of lipid membranes*, PhD thesis, Niels Bohr Institute, Copenhagen University.

[149] Heimburg T (2007), *Thermal biophysics of membranes*, Wiley-VCH;

[150] Coster HGL (2003), *The physics of cell membranes*, J. of Biol. Phys. 29(4):363-399;

[151] Luzzati V, Spegt PA (1967), *Polymorphism of lipids*, Nature, 215:701-704;

[152] Cullis PR, De Kruij B (1979), *Lipid polymorphism and the functional roles of lipids in biological membranes*, Biochimica et Biophysica Acta (BBA) - Reviews on Biomembranes, 559(4):399-420;

[153] Tamm LK, McConnell HM (1985), *Supported phospholipid bilayers*, Biophys. J. 47 (1985) 105-113;

[154] McConnell HM, Watts TH, Weis RM, Brian AA (1986), *Supported planar membranes in studies of cell-cell recognition in the immune system*, Biochim. Biophys. Acta 864: 95-106;

[155] Castellana ET, Cremer PS (2006), *Solid supported lipid bilayers: from biophysical studies to sensor design*, Surf. Sci. Rep. 61, 429-444;

[156] Dufr^ene YF, Barger WR, Green JBD, Lee GU (1997), *Nanometer-scale surface properties of mixed phospholipid monolayers and bilayers*, Langmuir 13, 4779-4784;

[157] Brian AA, McConnell HM (1984), *Allogeneic stimulation of cytotoxic T cells by supported planar membranes*, Proc. Natl. Acad. Sci. USA 81, 6159-6163;

[158] Picas L, Suarez-Germa C, Teresa Montero M, Hernandez-Borrell J (2010), *Force spectroscopy study of Langmuir-Blodgett asymmetric bilayers of phosphatidylethanolamine and phosphatidylglycerol*, J. Phys. Chem. B 114: 3543-9;

[159] Crane JM, Kiessling V, Tamm LK (2005), *Measuring lipid asymmetry in planar supported bilayers by fluorescence interference contrast microscopy*, Langmuir, 21: 1377-88;

[160] KimJ, Kim G, Cremer PS (2001), *Investigations of water structure at the solid/liquid interface in the presence of supported lipid bilayers by vibrational sum frequency spectroscopy*, Langmuir, 17: 7255-7260;

[161] Alessandrini A, Facci P (2009), *Nanoscale mechanical properties of lipid bilayers and their relevance in biomembrane organization and function*, Micron, 43(12): 1212-23;

[162] Bangham AD, Horne RW (1964), *Negative staining of phospholipids and their structural modification by surface active agents as observed in the electron microscope*, Journal of Molecular Biology 8: 660-668;

[163] Lasic DD (1988), *The mechanism of vescicle formation*, Biochemical Journal. 256: 1-11;

[164] Szoka F, Papahadjopoulos D (1980), *Comparative Properties and Methods of Preparation of Lipid Vesicles (Liposomes)*, Annual Review of Biophysics and Bioengineering. 9: 467-508;

[165] Trimble WS, Cowan DM, Scheller RH (1988), *VAMP-1: a synaptic vesicle-associated integral membrane protein*, Proceedings of the National Academy of Sciences of the United States of America, 85: 4538-4542;

[166] Papahadjapoulos D, Miller N (1967), *Phospholipid Model Membranes I. Structural characteristics of hydrated liquid crystals*, Biochimica et Biophysica Acta, 135: 624-638;

[167] Trauble H, Haynes H (1971), *The volume change in lipid bilayer lamellae at the crystalline-liquid crystalline phase transition*, Chem. Phys. Lipids. 7: 324-335;

[168] Popplewell J, Swann M, Freeman N, McDonnell C, Ford R (2007), *Quantifying of the Effects of Mellitin on Liposomes*, Biochimica et Biophysica Acta, 1768: 13-20;

[169] Guohua L, Macdonald RC (2003), *Lipid bilayer vesicle fusion: Intermediates captured by high-speed microfluorescence spectroscopy*, Biophysical Journal. 85, 1585-1599;

[170] Dietrich C, Bagatolli LA, Volovyk ZN, Thompson NL (2001), *Lipid rafts reconstituted in model membranes*, Biophysical Journal. 80: 1417-1428;

[171] Dimitrov DS, Angelova MI (1988), *Lipid swelling and liposome formation mediated by electric fields*, Bioelectrochem. Bioenerg. 19: 323-336;

[172] Baulieu EE, Robel P (1990), *Neuroactive steroids, a new brain function?*, The Journal of Steroid Biochemistry and Molecular Biology. 37: 395-403;

[173] Lambert JJ, Belelli D, Peden DRm Vardi AW, Peters JA (2003), *Neurosteroid modulation of GABAA receptors*, Progress in Neurobiology. 2003; 71: 67-80;

[174] Reddy DS (2003), *Pharmacology of endogenous neuroactive steroids*, Critical Reviews in Neurobiology. 2003; 15:197-234;

[175] Miller PS, Aricescu AR (2014), *Crystal structure of a human GABAA receptor*, Nature, 512:270-5;

[176] Genazzani AR, Petraglia F, Bernardi F, Casarosa E, Salvestroni C, Tonetti A, Nappi RE, Luisi S, Palumbo M, Purdy RH, Luisi M (1998), *Circulating levels of allopregnanolone in humans: gender, age, and endocrine influences*, J. Clin. Endocrinol. Metab. 83: 2099-2103;

[177] Irwin RW, Solinsky CM, Brinton RD (2014), *Frontiers in the therapeutic development of allopregnanolone for Alzheimer's disease and other neurological disorders*, Frontiers in cellular neuroscience 8

[178] Lundgren P, Strömberg J, Bäckström T, Wang M (2003), *Allopregnanolone-stimulated GABA-mediated chloride ion flux is inhibited by 3β-OH-5a-pregnan-20-one (isoallopregnanolone)*, Brain Res. 982: 45-53;

[179] Gyemek L, Iriarte J, Crabbe P (1968), *Structure-activity relationship of some steroidal hypnotic agents*, J. Med. Chem. 11: 117-125;

[180] Gee KW, Chang WC, Briton RE, McEwen BS (1987), *GABA-dependent modulation of Cl- ionophore by steroids in rat brain*, Eur. J. Pharmacol. 136: 419-23;

[181] Wang MD, Bäckström T, Lundgren S (2000), *The inhibitory effects of allopregnanolone and pregnanolone on the population spike, evoked in the rat hippocampal CA1 stratum pyramidale in vitro, can be blocked selectively by epiallopregnanolone*, Acta Physiol. Scand. 169: 333-341;

[182] Bäckstrom T, Wahlstrom G, Wahlstrom K, Zhu D, Wang MD (2005), *Isoallopregnanolone: an antagonist to anaesthetic effect of allopregnanolone in male rats*, Eur. J. Pharmacol. 512: 15-21;

[183] Falany CN (1997), *Enzymology of human cytosolic sulfotransferases*, FASEB J. 11: 206-216;

[184] Strott CA (2002), *Sulfonation and molecular action*, Endocr. Rev. 23: 703-732;

[185] Wang MD, Wahlstrom G, Backstrom T (1997), *The regional brain distribution of the neurosteroids pregnenolone and pregnenolone sulfate following intravenous infusion*, T. Journal of Steroid Biochemistry and Molecular Biology 62: 299-306;

[186] Geyer J, Wilke T, Petzinger E (2006), *The solute carrier family SLC10: more than a family of bile acid transporters regarding function and phylogenetic relationships*, Naunyn Schmiedebergs Arch. Pharmacol. 372: 413-431;

[187] Akk G, Bracamontes J, Steinbach JH (2001), *Pregnenolone sulfate block of GABA-A receptors, mechanism and involvement of a residue in the M2 region of the subunit*, Journal of Physiology 532: 673-684;

[188] Gibbs TT, Russek SJ, Farb DH (2006), *Sulfated steroids as endogenous neuromodulators*, Pharmacology Biochemistry and Behavior 84: 555-567;

[189] (Darnaudery M, Koehl M, Piazza PV, Le Moal M, Mayo W (2000), *Pregnenolone sulfate increases hippocampal acetylcholine release and spatial recognition*, Brain Research 852: 173-179;

[190] Darbra S, George O, Bouyer JJ, Piazza PV, Le Moal M, Mayo W (2004), *Sleepwake states and cortical synchronization control by pregnenolone sulfate into the pedunculopontine nucleus*, Journal of Neuroscience Research 76: 742-747;

[191] Reddy DS, Kulkarni SK (1998), *The effects of neurosteroids on acquisition and retention of a modified passive-avoidance learning task in mice*, Brain Research 791: 108-116;

[192] Tchernof A, Labrie F (2004), *Dehydroepiandrosterone, obesity and cardiovascular disease risk: A review of human studies*, European Journal of Endocrinology, 151: 1-14;

[193] Bastianetto S, Ramassamy C, Poirier J, Quirion R (1999), *Dehydroepiandrosterone (DHEA) protects hippocampal cells from oxidative stress-induced damage*, Brain Res. Mol. Brain Res. 66: 35-41;

[194] Imrich R (2002), *The role of neuroendocrine system in the pathogenesis of rheumatic diseases*, Endocr. Regul. 37(1): 45-6.

[195] Thijs L, Fagard R, Forette F, et al. (2003), *Are low dehydroepiandrosterone sulphate levels predictive for cardiovascular diseases? A review of prospective and retrospective studies*, Acta Cardiol. 58(5): 403-10;

[196] Chen CC, Parker CR Jr (2004), *Adrenal androgens and the immune system*, Semin. Reprod. Med. 22(4): 369-77;

[197] Dharia S, Parker CR Jr. (2004), *Adrenal androgens and aging*Semin. Reprod. Med. 22(4): 361-68;

[198] Rosmond R (2006), *Androgen excess in women-a health hazard?*, Med Hypotheses 67(2): 229-34.

[199] Bergfeld WF (2000), *Hirsutism in women: Effective therapy that is safe for long-term use*, Postgrad. Med. 107(7): 93-4.

[200] Krobath PD, Salek FS, Pittenger AL et al. (1999), *DHEA and DHEA-S: A reviews*, J. Clin. Pharmacol. 39: 327-48;

[201] Campbell B (2006), *Adrenarche and the evolution of human life history*, Am. J. Hum. Biol., 18: 569-89;

[202] Widstrom R, Dillon JS (2004), *Is there a receptor for dehydroepiandrosterone or dehydroepiandrosterone sulfate?*, Semin. Repro. Med., 22(4): 289-98;

[203] Dillon JS (2005), *Dehydroepiandrosterone, dehydroepiandrosterone sulfate and related steroids: Their role in inflammatory, allergic and immunological disorders*, Current Drug Targets Inflam Allergy, 4: 377-85;

[204] Franze K, Janmey PA, Guck J (2013) *Mechanics in neuronal development and repair*, Annu. Rev. Biomed. Eng., 15: 227-51;

[205] *www.educarer.org*, 2006;

[206] Biedler JL, Helson L, Spengler BA (1973), *Morphology and growth, tumorigenicity, and cytogenetics of human neuroblastoma cells in continuous culture*, Cancer Res. 33(11): 2643-52;

[207] Biedler JL, Roffler-Tarlov S, Schachner M, Freedman LS (1978), *Multiple neurotransmitter synthesis by human neuroblastoma cell lines and clones*, Cancer Res. 38(11): 3751-7;

[208] La Quagli MO, Manchester KM (1996), *A comparative analysis of neuroblastic and substrate-adherent human neuroblastoma cell lines*, J. of Ped. Surg. 31(2): 315-318;

[209] *www.qb.fcen.uba.ar/nicolaspregi*;

[210] Janmey PA, Winer JP, Weisel JW (2009), *Fibrin gels and their clinical and bioengineering applications*,J. R. Soc. Interface 6: 1-10;

[211] Di Stasio E, Nagaswami C, Weisel JW, Di Cera E (1998), *ClK regulates the structure of the fibrin clot*, Biophys. J. 75: 1973-79;

[212] Ferry JD, Morrison PR (1947), *Preparation and properties of serum and plasma proteins. VIII. The conversion of human fibrinogen to fibrin under various conditions*, J. Am. Chem Soc. 69: 388-400;

[213] Weisel JW, Nagaswami C, Makowski L (1987), *Twisting of fibrin fibers limits their radial growth*, Proc. Natl Acad. Sci. USA 84: 8991-8995;

[214] Ryan EA, Mockros LF, Weisel JW, Lorand L (1999), *Structural origins of fibrin clot rheology*, Biophys. J. 77, 2813-2826;

[215] Ferry JD (1980), *Viscoelastic Properties of Polymers*, John Wiley, New York;

[216] Roberts WW, Lorand L, Mockros LF (1973), *Viscoelastic properties of fibrin clots*, Biorheology 10: 29-42;

[217] Janmey PA, Amis E, Ferry J (1983), *Rheology of fibrin clots. VI. Stress relaxation, creep and differential dynamic modulus of fine clots in large shearing deformations*, J. Rheol. 27: 135-153;

[218] MacKintosh FC, Kas J, Janmey PA (1995), *Elasticity of semiflexible biopolymer networks*, Phys. Rev. Lett. 75: 4425-4428;

[219] Didonna B, Lubensky T (2005), *Nonaffinity and nonlinearity in random elastic networks*, Phys. Rev. E 72, 066 619;

[220] Onck PR, Koeman T, van Dillen T, van der Giessen E (2005), *Alternative explanation of stiffening in cross-linked semiflexible networks*, Phys. Rev. Lett. 95: 178 102;

[221] Storm C, Pastore JJ, MacKintosh FC, Lubensky TC, Janmey PA (2005), *Nonlinear elasticity in biological gels*, Nature 435, 191-194;

[222] Heussinger C, Schaefer B, Frey E (2007), *Nonaffine rubber elasticity for stiff polymer networks*, Phys. Rev. E Stat. Nonlin. Soft Matter Phys. 76 031 906;

[223] Huisman EM, van Dillen T, Onck PR, Van der Giessen E (2007), *Three-dimensional cross-linked F-actin networks: relation between network architecture and mechanical behavior*, Phys. Rev. Lett. 99, 208 103;

[224] Flory PJ (1969), *Statistical mechanics of chain molecules*, Interscience Publishers, New York;

[225] Brown AE, Litvinov RI, Discher DE, Weisel JW (2007), *Forced unfolding of coiled-coils in fibrinogen by single-molecule AFM*, Biophys. J. 92: L39-L42;

[226] Rheinwal JG,Green H (1975), *Serial cultivation of strains of human epidermal keratinocytes: the formation of keratinizing colonies from single cells*, Cell 6: 317-330;

[227] Barrandon Y, Green H (1987), *Three clonal types of keratinocyte with different capacities for multiplication*, PNAS USA 84(8): 2302-2306;

[228] Pellegrini G, Bondanza S, Guerra L, De Luca M (1998), *Cultivation of human keratinocyte stem cells: current and future clinical applications*, Med. And Biol. Eng. And Comp. 36(6): 778-790;

[229] Meyer G, Amer NM (1988), *Novel optical approach to atomic force microscopy*, Appl. Phys. Lett. 53: 1045-7;

[230] Alessandrini A, Facci P (2005), *Atomic force microscope: a versatile tool in biophysics*, Meas. Sci. Technol. 16: R65-R92;

[231] Ebenstein DM, Pruitt LA (2006), *Nanoindentation of biological materials*, Nanotoday 1(3): 26-33;

[232] Tranchida D, Piccarolo S, Soliman M (2006), *Nanoscale mechanical characterization of polymers by AFM nanoindentations: critical approach to the elastic characterization*, Macromolecules 39: 4547;

[233] Sader JE, White L (1993), *Theoretical analysis of the static deflection of plates for atomic force microscope applications*, J. Appl. Phys. 74, 1-9;

[234] Senden TJ, Ducker WA (1994), *Experimental determination of spring constants in atomic force microscopy*, Langmuir 10: 1003-4;

[235] Sader JE, Larson I, Mulvaney P, White LR (1995), *Method for calibration of atomic force microscope cantilevers*, Rev. Sci. Instrum. 66 3789-98;

[236] Hutter JL, Bechhoefer J (1993), *Calibration of atomic-force microscope tips*, Rev Sci Instrum 64: 1868-73;

[237] Cleveland JE, Manne S, Bocek D, Hansma PK (1993), *A non destructive method for determining the spring constant of cantilevers for scanning force microscopy*, Rev. Sci. Instrum. 64 403-5;

[238] Radmacher M,Cleveland JP, Fritz M, Hansma HG, Hansma PK (1994), *Mapping interaction forces with the atomic force microscope*, Biophys. J 66: 2159-65;

[239] Tao NJ, Lindsay S, Mand Lees S (1992), *Measuring the microelastic properties of biological material*, Biophys. J. 63: 1165-9;

[240] Costa KD, Yin FCP (1999), *Analysis of indentation: implications for measuring mechanical properties with atomic force microscopy*, J. Biomech. Eng. 121: 462-71;

[241] Vinckier A, Semenza G (1998), *Measuring elasticity of biological materials by atomic force microscopy*, FEBS Lett 430: 12-6;

[242] Hertz HR (1882) *On the contact of rigid elastic solids*, in Gesammelte Werke, vol.1, Leipzig, Germany;

[243] *www.imagemet.com*;

[244] Bilodeau G (1992), *Regular pyramid punch problem*, J. Appl. Mech. 59: 519-523;

[245] Heinz WF, Hoh JH (1999), *Spatially resolved force spectroscopy of biological surfaces using the atomic force microscope*, Trends Biotechnol. 17: 143-50;

[246] Radmacher M (1997), *Measuring the elastic properties of biological samples with the AFM*, IEEE Eng. Med. Biol. Mag. 16: 47-57;

[247] Baro A, Reifenberger RG (2012), *Atomic force microscopy in liquid: biological applications*, Wiley, p.20;

[248] Tsukruk VV, Gorbunov VV (2002), *Nanomechanical analysis of polymer surfaces*, Probe Microscopy 241: 3-4;

[249] McConney ME, Singamaneni S, Tsukruk VV (2010), *Probing soft matter with the atomic force microscopies: Imaging and Force Spectroscopy*, Polymer Reviews 50: 235-28;

[250] Ducker WA, Senden TJ, Pashley RM (1991), *Direct measurement of colloidal forces using an atomic force microscope*, Nature, 353: 239-241;

[251] McConney ME, Anderson KD, Brott LL, Naik RR, Tsukruk VV (2009), *Bio-inspired material approaches to sensing*, Advanced Functional Materials, 19: 2527-2544;

[252] Mahaffy RE, Park S, Gerde E, Kas Jand Shih CK (2004), *Quantitative analysis of the viscoelastic properties of thin regions of fibroblasts using atomic force microscopy*, Biophys. J. 86: 1777-93;

[253] Hu Y, Zhao X, Vlassak JJ, Suo Z (2010), *Using indentation to characterize the poroelasticity of gels*, Appl. Phys. Lett. 96, 121904;

[254] Carr Jr ME, Hardin CL (1987), *Fibrin has larger pores when formed in the presence of erythrocytes*, Am. J. of Physiol. 253: H1069-H1073;

[255] Fabry B, Maksym GN, Butler JP, Glogauer M, Navajas D, Fredberg JJ (2001), *Scaling the microrheology of living cells*, Phys. Rev. Lett. 87: 148102;

[256] Mahaffy RE, Shih CK, MacKintosh FC, Kas J (2000), *Scanning probe-based frequency-dependent microrheology of polymer gels and biological cells*, Phys. Rev. Lett. 85: 880-883;

[257] Landau LD, Lifshitz (1986), *Theory of elasticity*, Pergamon Press, Oxford;

[258] Findley W, Lai J, Onaran K (1976), *Creep and relaxation of nonlinear viscoelastic materials*, Dover Publications, Inc., New York;

[259] Okajima T (2015), *Atomic force microscopy: imaging and rheology of living cells*, in Nano/Micro Science and Technology in Biorheology, Springer;

[260] Oh MJ, Kuhr F, Byfield F, Levitan I (2012), *Micropipette Aspiration of Substrate-attached Cells to Estimate Cell Stiffness*, J. Vis. Exp. 67: e3886;

[261] Mitchinson JM, Swann MM (1954), *The Mechanical Properties of the Cell Surface: I. The Cell Elastimeter*, J. of Experimental Biology. 31: 443-460;

[262] Rand RP (1964), *Mechanical properties of the red cell membrane*, Biophys. J. 4(4):303-316;

[263] Longo ML, Waring AJ, Hammer DA (1997), *Interaction of the influenza hemagglutinin fusion peptide with lipid bilayers: area expansion and permeation*, Biophys. J. 73: 1430-1439;

[264] Sun Y, Lee CC, Hung WC, Chen FY, Lee MT, Huang HW (2008), *The bound states of amphipathic drugs in lipid bilayers: study of curcumin*, Biophys. J. 95: 2318-2324;

[265] Rawicz W, Olbrich KC, McIntosh T, Needham D, Evans E (2000), *Effect of chain length and unsaturation on elasticity of lipid bilayers*, Biophys. J., 79: 328-339;

[266] Seeger HM, Marino G, Alessandrini A, Facci P (2009), *Effect of physical parameters on the main phase transition of supported lipid bilayers*, Biophys. J. 97: 1067-1076;

[267] Nicolini C, Kraineva J, Khurana M, Periasamy N, Funari SS, Winter R (2006), *Temperature and pressure effects on structural and conformational properties of POPC/SM/cholesterol model raft mixtures - a FT-IR, SAXS, DSC, PPC and Laurdan fluorescence spectroscopy study*,Biochim Biophys Acta. 1758: 248-58;

[268] Veatch SL, Keller SL (2003), *A closer look at the canonical raft mixture in model membrane studies*, Biophys. J. 84:725-726;

[269] Bagatolli LA (2012), *Membrane domains and their relevance to the organization of the biological membranes*, Compr. Biophys. 5: 16-36;

[270] Connell SD, Heath G, Olmsted PD, Kisi A (2013), *Critical point fluctuations in supported lipid membranes*, Faraday Discuss. 161: 91-111;

[271] Petruzielo RS, Heberle FA, Drazba P, Katsaras J, Feigenson GW (2013), *Phase behavior and domain size in sphingomyelin-containing lipid bilayers*, Biochim. Biophys.Acta 1828: 1302-13013;

[272] Veatch SL, Polozov IV, Gawrisch K, Keller SL (2004), *Liquid domains in vesicles investigated by NMR and fluorescence microscopy*, Biophys. J. 86: 2910-2922;

[273] Zhao J, Wu J, Shao H, Kong F, Jain N, Hunt G, Feigenson G (2007), *Phase studies of model biomembranes: macroscopic coexistence of L_d + L_o, with light induced coexistence of L_d + L_o phases*, Biochim. Biophys. Acta 1768: 2777-2786;

[274] Balleza D, Sacchi M, Vena G, Galloni D, Puia G, Facci P, Alessandrini A (2015), *Effects of neurosteroids on a model membrane including cholesterol: a micropipette aspiration study*, Biochim. Biophys. Acta 1848(5): 1268-76;

[275] Sacchi M, Balleza D, Vena G, Puia G, Facci P, Alessandrini A (2015), *Effects of neurosteroids on a model lipid bilayer including cholesterol: an Atomic Force Microscopy study*, Biochim. Biophys. Acta 1848(5): 1258-67;

[276] Bhatia T, Husen P, Ipsen JH, Bagatolli LA, Simonsen AC (2014), *Fluid domain patterns in free-standing membranes captured on a solid support*, Biochim. Biophys. Acta 1838. 2503-2510,

[277] Gedig M, Faiss S, Janshoff A (2008), *Melting and interdigitation of microstructured solid supported membranes quantified by imaging ellipsometry*, Biointerphases 3: FA51;

[278] Akk G, Shu HJ, Wang C, Steinbach JH, Zorumski CF, Covey DF, Mennerick S (2005), *Neurosteroid access to the GABAA receptor*, J. Neurosci. 25: 11605-11613.

[279] Sooksawate T, Simmonds MA (2001), *Influence of membrane cholesterol on modulation of the GABAA receptor by neuroactive steroids and other potentiators*, Br. J. Pharmacol. 134: 1303-1311;

[280] Sooksawate T, Simmonds MA (1998), *Increased membrane cholesterol reduces the potentiation of GABAA currents by neurosteroids in dissociated hippocampal neurons*, Neuropharmacology 37: 1103-1110;

[281] Sooksawate T, Simmonds MA (2001), *Effects of membrane cholesterol on the sensitivity of the GABAA receptor to GABA in acutely dissociated rat hippocampal neurons*, Neuropharmacology 40: 178-184;

[282] Honerkamp-Smith AR, Cicuta P, Collins MD, Veatch SL, den Nijs M, Schick M, Keller SL (2008), *Line tensions, correlation lengths, and critical exponents in lipid membranes near critical points*, Biophys. J. 95: 236-246;

[283] Davis JH, Schmidt ML (2014), *Critical behavior in DOPC/DPPC/cholesterol mixtures: Static 2H NMR line shapes near the critical point*, Biophys. J. 106: 1970-1978;

[284] Nicolini C, Kraineva J, Khurana M, Periasamy N, Funari SS, Winter R (2006), *Temperature and pressure effects on structural and conformational properties of POPC/SM/cholesterol model raft mixtures: a FT-IR, SAXS, DSC, PPC and Laurdan fluorescence spectroscopy study*, Biochim. Biophys. Acta 1758: 248-258;

[285] Filippov A, Orädd G, Lindblom G However (2006), *Sphingomyelin structure influences the lateral diffusion and raft formation in lipid bilayers*, Biophys J. 90: 2086-92;

[286] Alessandrini A, Facci P (2014), *Phase transitions in supported lipid bilayers studied by AFM*, Soft Matter 10: 7145-7164;

[287] Ly HV, Longo ML (2004), *The influence of short-chain alcohols on interfacial tension,mechanical properties, area/molecule and permeability of fluid lipid bilayers*, Biophys. J. 87: 1013-1033;

[288] Zhelev DV (1998), *Material property characteristics for lipid bilayers containing lysolipid*, Biophys. J. 75: 321-330;

[289] Fa N, Lins L, Courtoy PJ, Dufrene Y, Van Der Smissen P, Brasseur R, Tyteca D, Mingeot-Leclercq MP (2007), *Decrease of elastic moduli of DOPC bilayers induced by a macrolide antibiotic, azithromycin*, Biochim. Biophys. Acta 1768: 1830-1838;

[290] Zhou Y, Raphael RM (2005), *Effect of salicylate on the elasticity, bending stiffness, and strength of SOPC membranes*, Biophys. J. 89: 1789-1801;

[291] Evans EA, Rawicz W (1990), *Entropy-driven tension and bending elasticity in condensedfluid membranes*, Phys. Rev. Lett. 64: 2094-2097;

[292] Evans EA, Needham D (1987), *Physical properties of surfactant bilayer-membranes: thermal transitions, elasticity, rigidity, cohesion and colloidal interactions*, J. Phys. Chem. 91: 4219-4228;

[293] Bagatolli LA, Needham D (2014), *Quantitative optical microscopy and micromanipulation studies on the lipid bilayer membranes of giant unilamellar vesicles*, Chem. Phys. Lipids 181: 99-120;

[294] Henriksen JR, Ipsen JH (2004), *Measurement of membrane elasticity by micro-pipette aspiration*, Eur. Phys. J. E 14: 149-167;

[295] Rawicz W, Smith BA, McIntosh TJ, Simon SA, Evans E (2008), *Elasticity, strength, and water permeability of bilayers that contain raft microdomain-forming lipids*, Biophys. J. 94: 4725-4736;

[296] Tierney KJ, Block DE, Longo ML (2005), *Elasticity and phase behavior of DPPC membrane modulated by cholesterol, ergosterol, and ethanol*, Biophys. J. 89: 2481-2493;

[297] Rawicz W, Olbrich KC, McIntosh T, Needham D, Evans E (2000), *Effect of chain length and unsaturation on elasticity of lipid bilayers*, Biophys. J. 79: 328-339;

[298] Yoon YZ, Hale JP, Petrov PG, Cicuta P (2010), *Mechanical properties of ternary lipid membranes near a liquid-liquid phase separation boundary*, J. Phys. Condens. Matter 22: 062101;

[299] Song Y, Guallar V, Baker NA (2005), *Molecular dynamics simulations of salicylate effects on the micro- and mesoscopic properties of a dipalmitoylphosphatidylcholine bilayer*, Biochemistry 44: 13425-13438;

[300] Barnoud J, Rossi G, Marrink SJ, Monticelli L (2014), *Hydrophobic compounds reshape membrane domains*, PLoS Comput Biol 10(10): e1003873;

[301] Dufrene YF, Boland T, Schneider JW, Barger WR, Lee GU (1998), *Characterization of the physical properties of model biomembranes at the nanometer scale with the atomic force microscope*, Faraday Discuss. 111: 79-94;

[302] Garcia-Manyes S Redondo-Morata L, Oncins G, Sanz F (2010), *Nanomechanics of lipid bilayers: Heads or tails?*, J. Am. Chem. Soc. 132: 12874-12886;

[303] Garcia-Manyes S, Oncins G, Sanz F, Garcia-Manyes, S, Oncins G, Sanz F (2005), *Effect of ion-binding and chemical phospholipid structure on the nanomechanics of lipid bilayers studied by force spectroscopy*, Biophys. J. 2005: 89: 1812-1826;

[304] Garcia-Manyes S, Oncins G, Sanz F (2005), *Effect of temperature on the nanomechanics of lipid bilayers studied by force spectroscopy*, Biophys. J. 89: 4261-4274;

[305] Redondo-Morata L, Oncins G, Sanz F (2012), *Force spectroscopy reveals the effect of different ions in the nanomechanical behavior of phospholipid model membranes: The case of potassium cation*, Biophys. J. 102, 66-74;

[306] Picas L, Montero MT, Morros A, Cabanas ME, Seantier B, Milhiet PE, Hernandez-Borrell J.(2009), *Calcium-induced formation of subdomains in phosphatidylethanolamine-phosphatidylglycerol bilayers: a combined DSC, (31)P NMR, and AFM study*, J. Phys.Chem. B, 113: 4648-4655;

[307] Redondo-Morata L, Giannotti MI, Sanz F (2012), *Influence of cholesterol on the phase transition of lipid bilayers: a temperature-controlled force spectroscopy study*, Langmuir 28: 12851-12860;

[308] Veatch SL, Gawrisch K, Keller SL (2006), *Closed-Loop Miscibility Gap and Quantitative Tie-Lines in Ternary Membranes Containing Diphytanoyl PC*, Biophys. J. 90: 4428-4436;

[309] Reiner GN, Fraceto LF, de Paula E, Perillo MA, Garcia (2013), *Effects of gabaergic phenols on phospholipid bilayers as evaluated by 1H NMR*, J. Biomater. Nanobiotechnol. 4: 28-34;

[310] Henriksen JR, Ipsen JH (2002), *Thermal undulations of quasi-spherical vescicles stabilized by gravity*, Eur. Phys. J. E9: 365-74;

[311] Vitkova V, Genova J, Mitov MD, Bivas I (2006), *Sugars in the aqueous phase change the mechanical properties of lipid mono- and bilayers*, Mol. Cryst. Liq. Cryst. 449: 95-106;

[312] Genova J, Zheliaskova A, Mitov MD (2006), *The influence of sucrose on the elasticity of DOPC lipid membrane studied by the analysis of thermally induced shape fluctuations*, Colloids Surf. A283: 420-2;

[313] Shchelokovsky P, Tristram-Nagle S, Dimova R (2011), *Effect of the HIV-1 fusion peptide on the mechanical properties and leaflet coupling of lipid bilayers*, New J Phys. 13: 25004;

[314] Eisenman LN, Shu HJ, Akk G, Wang C, Manion BD, Kress GJ, Evers AS, Steinbach JH, Covey DF, Zorumski CF, Mennerick S (2007), *Anticonvulsant and anesthetic effects of a fluorescent neurosteroid analog activated by visible light*, Nat Neurosci. 10(4):523-30;

[315] Sun TL, Sun Y, Lee CC, Huang HW (2013), *Membrane permeability of hydrocarbon-cross-linked peptides*, Biophys J. 104(9): 1923-32;

[316] Hansen AH, Sorensen KT, Mathieu R, Serer A, Duelund L, Khandelia H, Hansen PL, Simonsen AC (2013), *Propofol modulates the lipid phase transition and localizes near the headgroup of membranes*, Chem Phys Lipids 175-176:84-91;

[317] Palmieri B, Yamamoto T, Brewster RC, Safran SA (2014), *Line active molecules promote inhomogeneous structures in membranes: theory, simulations and experiments*, Adv Colloid Interface Sci. 208:58-65;

[318] Soubias O, Teague WE Jr, Hines KG, Mitchell DC, Gawrisch K (2010), *Contribution of membrane elastic energy to rhodopsin function*, Biophys J. 99(3):817-24;

[319] Iversen L, Mathiasen S, Larsen JB, Stamou D (2015), *Membrane curvature bends the laws of physics and chemistry*, Nat Chem Biol. 11(11): 822-5;

[320] Zhou Y, Raphael RM (2007), *Solution pH alters mechanical and electrical properties of phosphatidylcholine membranes: relation between interfacial electrostatics, intramembrane potential, and bending elasticity*, Biophys J. 92(7): 2451-62;

[321] Winterhalter M, Helfrich W (1992), *Bending Elasticity of Electrically Charged Bilayers: Coupled Monolayers, Neutral Surfaces, and Balancing Stresses*, J. Phys. Chem. 96(1): 327-330;

[322] Winterhalter M, Helfrich W (1992), *Bending Elasticity of Electrically Charged Bilayers: Coupled Monolayers, Neutral Surfaces, and Balancing Stresses*, J. Phys. Chem. 96(1): 327-330;

[323] Lekkerkerker HNW (1989), *Contribution of the electric double layer to the curvature elasticity of charged amphiphilic monolayers*, Physica A: Statistical Mechanics and its Applications, 159(3): 319-328;

[324] Winterhalter M, Helfrich W (1988), *Effect of Surface Charge on the Curvature Elasticity of Membranes*, J. Phys. Chem. 92: 6865-6867;

[325] Vitkova V, Cenova J, Finogenova O, Mitov MD, Ermakov Y, Bivas I (2004), *Surface Charge Effect on the Bending Elasticity of Lipid Bilayers*, Comptes Rendus de l'Academie Bulgare des Sciences 57: 11-25;

[326] Mitkova D, Stoyanova-Ivanova A, Ermakov Yu A, Vitkova V (2012), *Experimental study of the bending elasticity of charged lipid bilayers in aqueous solutions with pH5*, Journal of Physics: Conference Series 398: 012028;

[327] Alakoskela JM, Covey DF, Kinnunen PK (2014), *Lack of enantiospecifity in the effects of anesthetic steroids on lipid bilayers* Biochim. Biophys. Acta 1768(1): 131-45;

[328] Ingber D, Dike L, Hansen L, Karp S, Liley H, Maniotis A et al. (1994), *Cellular tensegrity: exploring how mechanical changes in the cytoskeleton regulate cell growth, migration and tissue pattern during morphogenesis*, International Review of Cytology, 50: 173;

[329] Ingber D (1993), *Cellular tensegrity: defining new rules of biological design that govern the cytoskeleton*, Journal of Cell Science, 104: 613-627;

[330] Wang N, Butler J, Ingber D (1993), *Mechanotransduction across the cell surface and through the cytoskeleton*, Science, 260: 1124-1127;

[331] Ingber D (2003), *Cellular tensegrity revisited: I. Cell structure and hierarchical system biology*, Journal of Cell Science, 116: 1157-1163;

[332] Ingber D (1997), *Tensegrity: The architectural basis of cellular mechanotransduction*, Annu. Rev. Physiol, 59: 575-599;

[333] Amos L, Amos W (1991), *Molecules of the Cytoskeleton*, Guilford Press, New York.

[334] Gittes F, Mickey B, Nettlelton J, Howard J (1993), *Flexural rigidity of microtubules and actin filaments measured from thermal fluctuations shape*, J. Cell Biol, 120: 923-934;

[335] Fletcher DA, Mullins RD (2010), *Cell mechanics and the cytoskeleton*, Nature 463: 485-492;

[336] Stamenovic D, Mijailovich S, Norrelkykke I, Chen J, Wang N (2002), *Cell Prestress. II. Contribution of microtubules*, The American Physiological Society, 282: C617-C624;

[337] Desai A, Mitchison TJ (1997), *Microtubule polymerization dynamics*, Annu. Rev. Cell Dev. Biol. 13, 83-117;

[338] Odde DJ, Ma L, Briggs AH, DeMarco A, Kirschner MW (1999), *Microtubule bending and breaking in living fibroblast cells*, J. Cell Sci. 112: 3283-3288;

[339] Hu X, Viesselmann C, Nam S, Merriam E, Dent EW (2008), *Activity-dependent dynamic microtubule invasion of dendritic spines*, J. Neurosci. 28: 13094-13105.

[340] Jaworski J et al (2009), *Dynamic microtubules regulate dendritic spine morphology and synaptic plasticity*, Neuron 61: 85-100;

[341] Stamenovic D, Wang N (2000), *Engineering approaches to cytoskeletal mechanics*, J Appl Physiol, 89: 2085-2090;

[342] Lee MK, Cleveland DW (1996), *Neuronal intermediate filaments*, Annu. Rev. Neurosci. 19: 187-217;

[343] Wolf OT, Kirschbaum C (1999), *Actions of dehydroepiandrosterone and its sulfate in the central nervous system: effects on cognition and emotion in animals and humans*, Brain Res Rev 30(3): 264-88;

[344] Murakami K, Fellous A, Baulieu EE, Robel P (2000), , Proc. Natl. Acad. Sci. USA 97: 3579-3584;

[345] Gehrig-Burger K, Lemck S (2000), *Rapid Effects of Sex Steroids on the Cytoskeleton of Neuroblastoma Cells*, Institute of Biochemistry, University of Mainz, Germany;

[346] Lemcke S, Hönnscheidt C, Waschatko G, Bopp A, Lutjohann D et al (2000), *DHEA-Bodipy: a functional fluorescent DHEA analog for live cell imaging*, Molecular and Cellular Endocrinology, Elsevier: 314 (1): 31-40;

[347] Compagnone NA, Mellon SH (1998), *Dehydroepiandrosterone: a signalling molecule for neocortical organization during development*, Proc. Natl. Acad. Sci. USA, 95 : 4678-4683;

[348] Laurine E, Lafitte D, Gregoire C, Seree E, Loret E, Douillard et al. (2003), *Specific Binding of Dehydroepiandrosterone to the N Terminus of the Microtubule-associated Protein MAP2*, The J. of Biological Chem. 278(32): 29979-86;

[349] Charalampopoulos I, Dermitzaki E, L. Vardouli, C. Tsatsanis, C. Stournaras, Margioris AN, Gravanis A (2005), *Dehydroepiandrosterone Sulfate and Allopregnanolone Directly Stimulate Catecholamine Production via Induction of Tyrosine Hydroxylase and Secretion by Affecting Actin Polymerization*, Endocrinology 146(8):3309-3318;

[350] Perego C, Di Cairano ES, Ballabio M, Magnaghi V (2011), *Neurosteroid Allopregnanolone regulates EAAC1-mediated glutamate uptake*

and triggers actin changes in Schwann cells, J. Cell. Phys. 227: 1740-1751;

[351] Lösel R, Wehling M (2003), *Nongenomic actions of steroid hormones*, Nat Rev Mol Cell Biol 4(1): 46-56;

[352] Fang Y, Iu CYY, Lui CNP, Zou Y, Fung CKM, Li HW, Xi N, Young KKL, Lai WC (2014), *Investigating dynamic structural and mechanical changes of neuroblastoma cells associated with glutamate-mediated neurodegeneration*, Scientific Reports 4:1-10;

[353] Wufsus AR, Macera NE, Neeves KB (2013), *The hydraulic permeability of blood clots as a function of fibrin and platelet density*, Biophys. J. 104: 1812-23;

[354] Nalam PC, Gosvami NN, Caporizzo MA, Composto RJ, Carpick RW (2015), *Nano-rheology of hydrogels using direct drive force modulation atomic force microscopy*, The Royal Soc. of Chem.;

[252] Mahaffy RE, Shih CK, MacKintosh FC, Kas J (2000), *Scanning probe-based frequency-dependent microrheology of polymer gels and biological cells*, Phys. Rev. Lett. 85: 880-883;

[355] McKee CT, Last JA, Russel P, Murphy CJ (2013), *Indentation vs tensile measurements of Young's modulus for soft biological tissues* , Tissue Engineering BB, 17 (3): 155-164;

[356] *www.materials.eng.cam.ac.uk.html*;

[357] *www.a-star.edu.sg*;

[358] Moeendarbary E, Valon L, Fritzsche M, Harris AR, Moulding DA, Thrasher AJ, Stride E, Mahadevan L, Charras GT (2013), *The cytoplasm of cells behaves as a poroelastic materials*, Nature Mat. 12: 253-261;

[359] Winer JP, Oake S, Janmey PA (2013), *Non-linear elasticity of extracellular matrices enables contractile cells to communicate local position and orientation*, PLoS ONE, 4(7): e6382;

[360] Owaribe K, Kodama R, Eguchi G (1981), *Demonstration of contactility of circumferential actin bundles and its morphogenetic significance in pigmented epithelium in vitro and in vivo*, J. Cell. Biol. 90: 507-514;

[361] *www.celladhesionlab.com*, imagine by Megha Rao, Mechanobiology Institute Singapore and department of Biomedical Engineering, National University of Singapore.